



THE HONG KONG
POLYTECHNIC UNIVERSITY

香港理工大學

Pao Yue-kong Library

包玉剛圖書館

Copyright Undertaking

This thesis is protected by copyright, with all rights reserved.

By reading and using the thesis, the reader understands and agrees to the following terms:

1. The reader will abide by the rules and legal ordinances governing copyright regarding the use of the thesis.
2. The reader will use the thesis for the purpose of research or private study only and not for distribution or further reproduction or any other purpose.
3. The reader agrees to indemnify and hold the University harmless from and against any loss, damage, cost, liability or expenses arising from copyright infringement or unauthorized usage.

IMPORTANT

If you have reasons to believe that any materials in this thesis are deemed not suitable to be distributed in this form, or a copyright owner having difficulty with the material being included in our database, please contact lbsys@polyu.edu.hk providing details. The Library will look into your claim and consider taking remedial action upon receipt of the written requests.

The Hong Kong Polytechnic University

Department of Building Services Engineering

AEROACOUSTICS OF MERGING
FLOWS AT DUCT JUNCTIONS

Garret, Chi Yan, LAM

A thesis submitted in partial fulfilment of the requirements for
the degree of Doctor of Philosophy

December 2011

Garret, Chi Yan, LAM: *Aeroacoustics of Merging Flows at Duct Junctions*, A thesis submitted in partial fulfilment of the requirements for the degree of Doctor of Philosophy, © December 2011

CERTIFICATE OF ORIGINALITY

I hereby declare that this thesis is my own work and that, to the best of my knowledge and belief, it reproduces no material previously published or written, nor material that has been accepted for the award of any other degree or diploma, except where due acknowledgement has been made in the text.

Hong Kong, December 2011

Garret, Chi Yan, LAM

Dedicated to my wife, Sharen.

ABSTRACT

This thesis involves a numerical and experimental investigation of aeroacoustics of merging flow at duct junctions, which are composed of a main duct and a side branch with the same duct width. Since the aeroacoustics of internal flow is complicated, the flow dynamic and acoustic disturbances generated are always mixed. It is very difficult to differentiate their evolutions experimentally, so a numerical tool is developed to investigate the duct junction aeroacoustics. This tool is based on the Conservation Element and Solution Element method, which solves the unsteady compressible Navier-Stokes equations and the ideal gas law, to perform direct aeroacoustic simulation. To account for the effects of flow turbulence, implicit LES strategy is adopted by combining the MILES approach and wall modeling derived from the classical logarithm wall law. The numerical code is verified fully with both external and internal benchmark aeroacoustic problems.

The numerical investigations are performed in two dimensions (2D) with Reynolds number (Re) based on duct width equal to 10^5 . The cases under investigation are defined by different combinations of the ratio of side-branch to main duct flow velocities, VR ($= 0.5, 0.67, 1.0, 2.0$) and merging angle, θ ($= 30^\circ, 45^\circ, 60^\circ, 90^\circ$). The numerical investigation continues with a three dimensional (3D) calculation ($VR = 1$ and $\theta = 90^\circ$) due to limited computational resources available. The general aeroacoustics of 2D merging flow and its variations with VR and θ are discussed. The acoustic power generated is found to increase with VR and θ , leading to the noisiest case at $VR = 2.0$ with $\theta = 90^\circ$. The numerical results of both 2D and 3D studies are compared and discussed.

A test rig is developed for investigating different combinations of VR ($0.5, 0.67, 1.0, 2.0$) and θ ($45^\circ, 90^\circ$) in experiments. Due to the limited capability

of facilities available, a smaller maximum Re is attained (10^4). The merging flow was driven by using a two-fan system. The velocity of the flow and pressure fluctuations were measured by a cobra probe and a probe microphone respectively. The experimental results are discussed and compared with the numerical results, which provide us the insights in the aeroacoustics generated by the merging flow at duct junction.

PUBLICATIONS

Some ideas and figures have appeared previously in the following publications:

1. Lam, G. C. Y., Leung, R. C. K. & Tang, S. K., 'Aeroacoustics of Merging Flow at T-Junction', *The Journal of the Acoustical Society of America*. (Submitted).
2. Lam, G. C. Y., Leung, R. C. K., Tang, S. K. & Seid, K. H., 'Space-Time CE/SE Method for low Mach number direct aeroacoustic simulation', *Computers & Fluids*. (Submitted).
3. Tang, S. K. & Lam, G. C. Y., 'On sound propagation from a slanted side branch into an infinitely long rectangular duct', *The Journal of the Acoustical Society of America* **124**(4), 2008, 1921-1929.
4. Lam, G. C. Y., Leung, R. C. K. & Tang, S. K., Aeroacoustics of Low Mach Number Merging Flows at Duct Junction, *in '17th International Congress on Sound and Vibration'*, Cairo, Egypt, 2010, pp. 1-8.
5. Lam, G. C. Y., Tang, S. K. Leung, R. C. K., Aeroacoustics of Merging Flow at Duct Junction, *in '10th International Conference on Theoretical and Computational Acoustics'*, Taipei, Taiwan, 2011, pp. 1-10.
6. Lam, G. C. Y., Leung, R. C. K., Yu, K. F., Tang, S. K., Computational Aeroacoustics Using CE/SE Method, *in '15th International Congress on Sound and Vibration'*, Daejeon, Korea, 2008, pp. 1-8.
7. Lam, G. C. Y., Leung, R. C. K., Yu, K. F., Tang, S. K., Computational Aeroacoustics Using CE/SE Method, *in '14th AIAA/CEAS Aeroacoustics Conference'*, Vancouver, 2008, pp. 1-12.

*We have seen that computer programming is an art,
because it applies accumulated knowledge to the world,
because it requires skill and ingenuity, and especially
because it produces objects of beauty.*

— Donald E. Knuth (Knuth 1974)

ACKNOWLEDGMENTS

First of all, I would like to praise God, the Almighty for providing me this opportunity and the capability to complete this. I also thank Him for granting me the strength to proceed when the road in front of me seemed unclear, opening the way for me when it seemed blocked. Without the assistance and guidance of several people, this thesis cannot be finished definitely; thus I would like to offer my sincere thanks to all of them.

I have met two generous men as my supervisors, Prof. Tang and Dr. Leung. They not only provide me a strong support in terms of equipments, but also most importantly great guidance in both research and life.

Furthermore, I would like to thank my wife and my parents for their continuing encouragement and support. I would not pursue my PhD. degree if they did not encourage and support me.

Moreover, when I encountered the huge obstacle in my research that was very difficult to overcome, Dr. Joseph Yen generously shared his experiences in both theory and implementation on numerical simulation, which was a great help in developing the *CE/SE code* for my investigations.

Many thanks should be given to my colleagues who helped me in the experiment. Finally, support received from the Research Grants Council of the HKSAR Government through grant PolyU 5278/06E, PolyU 5230/09E and from the Hong Kong Polytechnic University through grant J-BB2C is gratefully acknowledged.

CONTENTS

1	INTRODUCTION	1
1.1	Literature Survey	2
1.2	Objectives and Research Scope	5
1.3	Approach of Investigations	6
1.4	Organization of the Thesis	9
2	THE SPACE TIME CONSERVATION ELEMENT AND SOLUTION ELEMENT METHOD	11
2.1	Introduction	11
2.2	Two Dimensional Formulation of CE/SE Method	14
2.2.1	Definition of Conservation Element (CE) & Solution Element (SE)	17
2.2.2	Time Marching of Solution in CE/SE Method	19
2.3	Three Dimensional Formulation of CE/SE Method	28
2.3.1	Definition of CE & SE in 3D	32
2.3.2	Time Marching of Solution in 3D CE/SE Method	35
2.4	Treatment of Boundary Condition in CE/SE Method	39
2.4.1	Non-Reflecting Boundary Condition (NRBC)	41
2.4.2	Slip Wall Boundary Condition (SLWBC)	42
2.4.3	No-slip Wall Boundary Condition (NSWBC)	43
2.5	Turbulence Modeling	43
2.5.1	MILES Approach	45
2.5.2	Wall Modeling	46
2.6	Code Development	50
2.7	Concluding Remarks	51
3	VALIDATION OF CE/SE METHOD FOR DAS	53
3.1	Spatial Resolution of CE/SE Method	53

3.1.1	Method of Assessment	54
3.1.2	Results	55
3.2	Two Dimensional Cases	56
3.2.1	Flow Past Backward Facing Step	56
3.2.2	Acoustic Propagation Through Duct Junction	60
3.2.3	Aeolian Tone of a Square Cylinder	63
3.2.4	Acoustic Absorption Through Orifice	68
3.3	Three Dimensional Cases	72
3.3.1	Supersonic Flow Over Wedge	73
3.3.2	Propagation of Acoustic, Vortex and Entropy Pulses in Uniform Flow	76
3.3.3	Flow Past Backward Facing Step	78
3.4	Concluding Remarks	82
4	TWO DIMENSIONAL MERGING FLOW AT DUCT JUNCTIONS	85
4.1	Formulation of the Problem	85
4.2	Aeroacoustics of Merging Flow	89
4.2.1	Mean Flow	90
4.2.2	Unsteady Flow Dynamics	95
4.2.3	Sound Generation	109
4.3	Influence of Velocity Ratio, VR	124
4.3.1	Mean Flow	125
4.3.2	Unsteady Flow Dynamics	126
4.3.3	Sound Generation	130
4.4	Effect of Merging Angle, θ	130
4.4.1	Mean Flow	131
4.4.2	Unsteady Flow Dynamics	134
4.4.3	Sound Generation	138
4.5	Concluding Remarks	139
5	EXPERIMENTAL INVESTIGATION OF MERGING FLOW AT DUCT JUNC- TIONS	143
5.1	Experimental Setup	143

5.1.1	Test Rig Design and Instrumentations	144
5.1.2	Flow Conditions	150
5.2	Experimental Results	152
5.2.1	Inlet Flow Profile	152
5.2.2	Mean Flow	153
5.2.3	Flow Unsteadiness	154
5.2.4	Acoustic Propagation	159
5.3	Concluding Remarks	162
6	THREE DIMENSIONAL MERGING FLOW AT DUCT JUNCTIONS	167
6.1	Formulation of the Flow Problem	167
6.2	Aeroacoustics of Three Dimensional Merging Flow	169
6.2.1	Mean Flow	170
6.2.2	Unsteady Flow Dynamics	174
6.2.3	Sound Generation	184
6.3	Concluding Remarks	186
7	CONCLUSIONS	189
7.1	Summary of Important Achievements	189
7.2	Suggestions for Future Work	191
	BIBLIOGRAPHY	193

LIST OF FIGURES

Figure 1.1	Merging flow at duct junction.	1
Figure 1.2	Geometry for current investigations.	6
Figure 2.1	An arbitrary space-time region for a two dimensional problem.	13
Figure 2.2	Decomposition of computational domain.	17
Figure 2.3	Geometrical definitions of CE & SE.	18
Figure 2.4	Geometrical definitions of $P_i, i = 1, 2, 3$.	24
Figure 2.5	The numerical domain and analytical domain of dependence.	26
Figure 2.6	Typical hexahedron in spatial computational domain.	32
Figure 2.7	3D Numerical and analytical domain of dependence.	37
Figure 2.8	Boundary cell and ghost cell.	40
Figure 3.1	Schematic of a plane wave propagation in duct with slip wall.	54
Figure 3.2	Comparison of spatial resolution with different scheme.	55
Figure 3.3	Configuration of backward facing step flow.	57
Figure 3.4	Profiles of x-velocity at various downstream location to the step.	58
Figure 3.5	Reattachment length of recirculation zone behind the step.	59
Figure 3.6	Second recirculating zone near the upper wall at $Re = 500$.	60
Figure 3.7	The configuration of T-duct acoustics case.	61
Figure 3.8	Wave pattern at duct junction at different excitation frequencies.	61

Figure 3.9	Amplitude of plane waves in main duct and vertical duct sections. 62
Figure 3.10	Configuration of flow past a square cylinder. 63
Figure 3.11	CE/SE results and vorticity distributions. 65
Figure 3.12	Instantaneous pressure fluctuation and directivity. 66
Figure 3.13	Decay of acoustic fluctuation. 68
Figure 3.14	Configuration of sound past through orifice. 69
Figure 3.15	Snapshot of CE/SE results at the start and end of a half cycle. 70
Figure 3.16	Comparison of acoustics impedance. 71
Figure 3.17	Configuration of supersonic flow over wedge. 75
Figure 3.18	Snapshots of CE/SE results. 76
Figure 3.19	Schematic of supersonic flow over wedge. 77
Figure 3.20	Snapshots of results from CE/SE at different time. 79
Figure 3.21	Comparison of CE/SE results with analytical solution at $y = 0$. 80
Figure 3.22	Streamwise velocity, u and recirculation zones from CE/SE calculations. 81
Figure 4.1	Schematic of the merging flow problem. 86
Figure 4.2	Mean velocity profile of the inflows at I_1 . 87
Figure 4.3	Different regions in the merging flow problem. 89
Figure 4.4	Mean flow for N-1.0-90. 90
Figure 4.5	Profile of u_{mean} over the domain for different cases. BL denotes the approximated boundary layer. RZ1 and RZ2 denote the first and second recirculating zones respectively. 91
Figure 4.6	Mean vorticity ω_{mean} near the duct junction for different cases. 93
Figure 4.7	Snapshots of vorticity. 97
Figure 4.8	Snapshots of vorticity. 98
Figure 4.9	Snapshots of vorticity. 99

- Figure 4.10 Spectra of pressure fluctuation calculated at a location between $(x_{dj} + 1, -0.2)$ and $(x_{dj} + 2, -0.2)$. 100
- Figure 4.11 Vortex shedding frequency of different cases, $f_{s,RZ1}$. SL marks the frequency of vortex roll-up at SL respectively. 102
- Figure 4.12 Streamwise velocity profile u along $x = 0.05$. Both N-0.67-45 and N-0.5-90 have large velocity gradient at SL (near $y = 0$), leading to vortex shedding at SL. The other two cases have a small velocity gradient at SL, thus no vortex shedding occurs at SL. 102
- Figure 4.13 Distribution of $\overline{u'u'}/u_{eq}^2$ in different selected cases. The one with the smallest fluctuation is N-0.5-30 and the one with largest fluctuation is N-2.0-90. 104
- Figure 4.14 Distribution of $\overline{v'v'}/u_{eq}^2$ in different selected cases. The one with the smallest fluctuation is N-0.5-30 and the one with largest fluctuation is N-2.0-90. 105
- Figure 4.15 Distribution of $\overline{u'v'}/u_{eq}^2$ in different selected cases. The one with the smallest fluctuation is N-0.5-30 and the one with largest fluctuation is N-2.0-90. 106
- Figure 4.16 Distributions of $(p'_{wall})_{rms} / \rho_0 u_{eq}^2$ in various cases. 108
- Figure 4.17 Setting of two point method. 111
- Figure 4.18 Variation of phase difference along the selected lines (N-1.0-90). Red circles denote the results in DS and the black triangles represent those in SB and US. 113
- Figure 4.19 Typical phase difference between the streamwise velocity and pressure. The demonstration is N-0.5-90. 114
- Figure 4.20 Time histories of pressure fluctuation at different points in US, SB and DS of case N-1.0-90. 115
- Figure 4.21 Snapshots of density fluctuations. 116
- Figure 4.22 $p(k_x, f)$ spectrum at $y = -0.2$ in DS. 121
- Figure 4.23 $p(k_x, f)$ spectrum at $y = -0.2$ in DS. 122

- Figure 4.24 $p(k_x, f)$ spectrum at $y = -0.2$ in DS. 122
- Figure 4.25 Acoustic disturbances shown in filtered $p(k_x, f)$ spectrum at $y = -0.2$. 123
- Figure 4.26 Variation of reattachment length L_{RZ1} and separation length L_2 with VR ($\theta = 30^\circ, 90^\circ$). 125
- Figure 4.27 Variation of α_{SL} with VR ($\theta = 90^\circ$). 126
- Figure 4.28 Snapshots of vorticity at $t = 34$ in all $\theta = 90^\circ$ cases. 127
- Figure 4.29 Variation of vortex shedding frequency $f_{s,RZ1}$ with VR ($\theta = 30^\circ$). 128
- Figure 4.30 Distributions of $(p'_{wall})_{rms} / \rho_0 u_{eq}^2$ for various VR at $\theta = 90^\circ$. 129
- Figure 4.31 The variation of acoustic efficiency η with VR ($\theta = 30^\circ$ and 90°). 130
- Figure 4.32 Mean streamwise velocity profile (u) at $VR = 1$. 131
- Figure 4.33 Mean vorticity with streamlines at $VR = 1$. 132
- Figure 4.34 Variation of reattachment length L_{RZ1} with θ . 132
- Figure 4.35 Variation of separation length L_{RZ2} with θ . 133
- Figure 4.36 Variation of α_{SL} with θ . 133
- Figure 4.37 Snapshots of vorticity in all $\theta = 90^\circ$ cases at $t = 34$. 134
- Figure 4.38 Variation of vortex shedding frequency, $f_{s,RZ1}$, with θ . 135
- Figure 4.39 Variation of vortex shedding frequency, $f_{s,SL}$ with θ . 135
- Figure 4.40 Mean Reynolds stress $(\overline{u'v'} / u_{eq}^2)$ at $VR = 1$. 136
- Figure 4.41 Distributions of $(p'_{wall})_{rms} / \rho_0 u_{eq}^2$ for various θ ($VR = 1.0$). 137
- Figure 4.42 Variation of η_{SB} , η_{US} and $\eta_{DS,acoustic}$ with different θ . 138
- Figure 4.43 Scaling law of η and F_{rms} for all cases. 142
- Figure 5.1 Schematic of duct system used. Two turns are required in the side branch due to the limitation of space available in laboratory, so an expansion chamber is added before the flow entering the junction. 145
- Figure 5.2 Various components of duct system used. 146

- Figure 5.3 Duct junction applied in experimental setup. 147
- Figure 5.4 Cobra probe used in experimental study. 148
- Figure 5.5 Schematic of data acquisition system in measurements. 149
- Figure 5.6 XY table. 149
- Figure 5.7 Snapshot of measurement. 150
- Figure 5.8 Streamwise velocity profile u_s before flows are merged for case E-1.0-90. 152
- Figure 5.9 Coordinate system adopted in this discussion. 154
- Figure 5.10 Velocity at the measurement region for different cases. 155
- Figure 5.11 Comparison of velocity with 2D numerical study for different cases. (—) is the calculated results and (□) represents the experimental results. 156
- Figure 5.12 Reynolds shear stresses at the measurement region for different cases. 158
- Figure 5.13 Root mean square of pressure fluctuation p_{rms} of experimental study in selected cases. The solid lines shown are the contours of rejected zone obtained from velocity measurements. 159
- Figure 5.14 Root mean square of pressure fluctuation p_{rms} obtained from numerical study in selected cases. 160
- Figure 5.15 Auto-spectra of pressure fluctuations for E-0.5-90 and N-0.5-90. 161
- Figure 5.16 Auto-spectra of pressure fluctuations, G_{pp} , at $(x_{dj} + 1, -0.2)$ of both experimental and 2D numerical study for different cases. 161

- Figure 5.17 Auto-spectra of pressure fluctuations, G_{pp} , at $(x_{dj} + 1, -0.2)$ of both experimental and 2D numerical simulations with frequency scaling for different cases. Red dashed lines highlight the corresponding pairs of the dominant peaks in experimental and 2D numerical results. Shaded region: system noise dominant. a) $f_{system} / (f_{1st\ peak})_{experiment} = 0.6$; b) $f_{system} / (f_{1st\ peak})_{experiment} = 0.428$. 163
- Figure 5.18 Spectra of pressure fluctuations, G_{pp} , at $(x_{dj} + 1, -0.2)$ of both experimental and 2D numerical simulations with frequency scaling for different cases. Red dashed lines highlight the corresponding pairs of the dominant peaks in experimental and 2D numerical results. Shaded region: system noise dominant. a) $f_{system} / (f_{1st\ peak})_{experiment} = 0.75$; b) $f_{system} / (f_{1st\ peak})_{experiment} = 0.5$. 164
- Figure 6.1 Schematic of the merging flow problem in three dimensional case. 168
- Figure 6.2 Mean flow over the domain for N-1.0-90-3D (Not to scale in z axis). 171
- Figure 6.3 Comparison of u in N-1.0-90 (red dashed line) and N-1.0-90-3D (black solid line). 172
- Figure 6.4 $\omega_{mean,z}$ in N-1.0-90-3D on $z = 0.05$. 173
- Figure 6.5 Mean vorticity ω_{mean} obtained in N-1.0-90-3D (Not to scale in z axis). 175
- Figure 6.6 Snapshots of ω_z and λ_2 on $z = 0.05$ at $t = 50$. 176
- Figure 6.7 Snapshots of vortical structures educed by λ_2 -criterion. 177
- Figure 6.8 Snapshots of vortical structures educed by λ_2 -criterion. 178
- Figure 6.9 Spectrum of pressure fluctuation at $(x_{dj} + 3, -0.5)$. 179
- Figure 6.10 Spectrum of pressure fluctuation at $(x_{dj} + 6, -0.5)$. 180

Figure 6.11	Comparison of the auto-spectra of pressure fluctuations between the experimental, 2D and 3D numerical simulations with frequency scaling for $VR = 1, \theta = 90^\circ$. Green dashed lines highlight the corresponding groups of the dominant peaks in experimental, 2D and 3D numerical results. Shaded region: fan noise dominant. $f_{fan} / (f_{1st\ peak})_{experiment} = 0.428.$	181
Figure 6.12	Reynolds stresses over the domain for N-1.0-90-3D.	182
Figure 6.13	Distributions of $(p'_{wall})_{rms} / \rho_0 u_{eq}^2$ in 2D and 3D cases.	183
Figure 6.14	$p(k_x, f)$ spectrum at centerline of DS.	184

LIST OF TABLES

Table 3.1	Reference parameters adopted in the plane wave propagation.	54
Table 3.2	Reference parameters adopted in flow past BFS.	57
Table 3.3	Reference parameters adopted in T-duct acoustics	60
Table 3.4	Reference parameters adopted in aeolian tone.	64
Table 3.5	Comparison of C_L and C_D metrics.	65
Table 3.6	Reference parameters adopted in orifice case.	69
Table 3.7	Reference parameters adopted in supersonic flow over wedge.	75
Table 3.8	Reference parameters adopted in 3D pulses case.	78
Table 4.1	Reference parameters adopted in this chapter.	86
Table 4.2	Variation of projection of side branch opening x_{dj} with θ .	87
Table 4.3	Description of simulated cases.	88

Table 4.4	Selected cases for illustrating the general aeroacoustic features. 89
Table 4.5	Reattachment length L_{RZ1} for selected cases. 94
Table 4.6	Separation length L_{RZ2} for selected cases. 95
Table 4.7	The initial angle between the shear layer and the main duct, α_{SL} . 95
Table 4.8	The frequency of vortex rolling up at SL $f_{s,SL}$. 103
Table 4.9	The acoustic efficiency η_{US} in US. Shown in the brackets are the relative order of difference $O(\eta/\eta_{max})$ when compared with the maximum η obtained. 118
Table 4.10	The acoustic efficiency η_{SB} in SB. Shown in the brackets are the relative order of difference $O(\eta/\eta_{max})$ when compared with the maximum η obtained. 118
Table 4.11	The acoustic efficiency η_{DS} in DS. Shown in the brackets are the relative order of difference $O(\eta/\eta_{max})$ when compared with the maximum η obtained. Note that the calculation of this acoustic efficiency actually includes the contribution of acoustic and flow dynamic disturbances in DS. 119
Table 4.12	The acoustic efficiency $\eta_{DS,acoustic}$ in DS. Shown in the brackets are the relative order of difference $O(\eta/\eta_{max})$ when compared with the maximum η obtained. 124
Table 4.13	Selected cases for illustrating the effect of the velocity ratio, VR . 125
Table 5.1	Reference parameters adopted in experiment. 151
Table 5.2	Description of experimental cases. 151
Table 5.3	Boundary layer thickness δ_d and δ_m for different cases. 153
Table 6.1	Reference parameters adopted in this research. 169
Table 6.2	Sizes of various flow features for N-1.0-90 and N-1.0-90-3D. 173

Table 6.3 Acoustic efficiency η for N-1.0-90 and N-1.0-90-3D. 185

ACRONYMS

CE/SE The Conservtion Element and Solution Element Method

CFD Computational Fluid Dynamics

DAS Direct Aeroacoustic Simulation

DNS Direct Numerical Simulation

MILES Monotonically Integrated Large Eddy Simulation

N-S Navier-Stokes

INTRODUCTION

Duct work is one of the fundamental components in various fluid transporting systems, ranging from the large air-ventilation systems in buildings, to small intake or exhaust systems in automobile. When air flows inside these systems, sound may be generated by the unsteady flow dynamics occurred in the system and then propagates inside these duct works. Nevertheless, in many engineering applications, this sound generated is undesirable except in musical instruments and thus it is regarded as noise.

Duct junction is commonly found inside the duct works of these transporting systems. In order to minimize the sound generation and transmission inside the duct work, it is essential to understand the aeroacoustics occurred at duct junction. In many practical applications, different configurations of flows occur at duct junctions, e. g., a merging flow as illustrated in [Figure 1.1](#). The flows enter the duct junction at rectangular duct inlets I_1 and I_2 of the same size. These two flows merge at the duct junction, creating a shear layer between them owing to the velocity gradient across the flow. Similar to the case in mixing layer ([Thomas \(1991\)](#)), this shear layer locally behaves as a

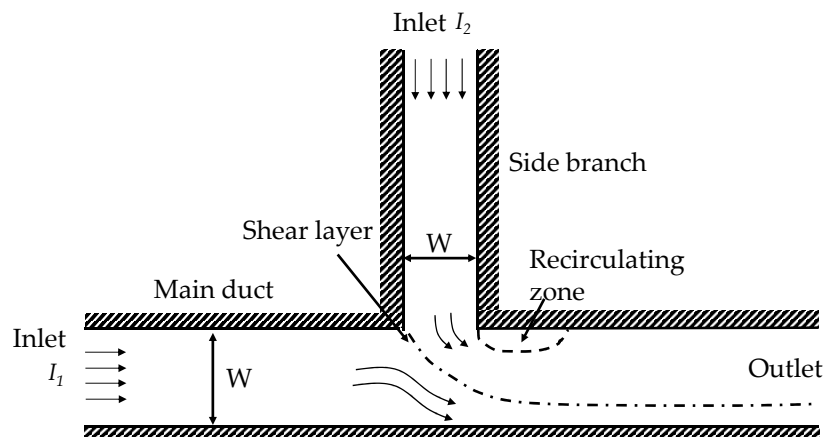


Figure 1.1: Merging flow at duct junction.

mixing layer and may roll up to form vortices, which are believed to be the sources of sound. Furthermore, a recirculating region is usually formed downstream of the corner of duct junction. It may be so unstable such that vortices are also shed there. Therefore, duct junction plays an important role not only in the sound transmission, but also the aeroacoustics when fluid flows through it.

1.1 LITERATURE SURVEY

In the past century, numerous researches were performed associated with the duct junction in a duct work. These researches can be generally divided into three categories - flow, acoustics, and aeroacoustics. The steady flow is the earliest one that attracts the researchers' attention. Later on, attentions have also been drawn to the acoustics at duct junction. Only in the last few decades, the aeroacoustics at duct junction begins to be investigated.

In the early days (1920s), studies were mainly focused on the steady flow behavior at duct junction. Most of them concerned the pressure loss across the duct junction such as [Vogel \(1928\)](#), [McNown \(1954\)](#), [Blaisdell & Manson \(1963\)](#). [Miller \(1971\)](#) and [Ito & Imai \(1973\)](#) later contributed to the experimental database of this pressure loss. While the aforementioned studies assumed incompressible flow, [Abou-Haidar & Dixon \(1992\)](#) and [Pérez-Garcia et al. \(2010\)](#) extended these investigations to the compressible flow. On the other hand, the flow behavior at duct junction has also been studied extensively for both bifurcation and merging flows. Some of the studies on bifurcation at duct junction were [Anagnostopoulos & Mathioulakis \(2004\)](#), [Miranda et al. \(2008\)](#), [Moshkin & Yambangwi \(2009\)](#), in which they adopted the numerical approach. In the case of the merging flow, [Krijger et al. \(1990\)](#) examined this numerically by applying conformal mapping when solving the Navier-Stokes equations. [Brücker \(1997\)](#) studied the merging flow at junction with two circular pipes experimentally using three dimensional scanning particle image

velocimetry (3D SPIV). The unsteady flow dynamics in both cases showed a strong secondary horseshoe vortex induced by the flow in side branch, similar to the case of jet impinging a crossflow (Kelso et al. (1998)). Wu (2003) also investigated the flow structures in the merging flow with circular side branch joining rectangular main duct. Thomas & Ameel (2010) investigated the mixing of impinging flow at duct junction experimentally. Usually, these studies covered the regime of laminar flow only. For higher Reynolds number flow regime, Hirota et al. (2006, 2010) studied the mixing of cold and hot air streams at duct junction experimentally. Since their major focus was the heat transfer between the inlet flows, rather than the flow behavior, only a few flow characteristics were discussed in their paper. According to their results, the mean flow pattern was similar to the one shown in Figure 1.1. They also found that the highest turbulent fluctuations occurred at the edge of the recirculating zone.

In the aspect of acoustics at duct junction, Miles (1947) evaluated the sound transmission across duct junction at low frequency. Bruggeman (1987) also studied the propagation of low frequency sound at T-junction with experiments. Dubos et al. (1999) applied modal decomposition to investigate this problem. Tang & Li (2003) investigated the prediction of plane wave theory on the sound transmission loss across the duct junction. Tang (2004) also studied the resonance of T-junction and the length correction required for the prediction of using plane wave theory. However, in conducting these researches, no flows were assumed inside these duct works, which was not the usual situation encountered in the applications with a duct work.

In the past two decades, more and more research attentions have been drawn to the aeroacoustics at duct junction. These researches generally can be separated into two categories. The first category can be viewed as an extension of the aforementioned acoustic researches. They study the sound transmission at duct junction with the presence of mean flow, i. e., the scattering effect. The second one is related to the sound generation caused by the unsteady flow dynamics at duct junction.

In these two areas of research, most of them focused on the first category, e. g., [Bruggeman et al. \(1991\)](#), [Dequand et al. \(2003\)](#), [Martínez-Lera et al. \(2009\)](#), [Tonon et al. \(2010\)](#) and [Karlsson & Åbom \(2010\)](#). Nearly all of them studied the acoustic excitation or the whistling potential of bifurcation at duct junction, i. e., the grazing flow. This is because the possible sound amplification occurred in this case are the suspect of whistling occurred at duct junction. In these researches, the time averaged acoustic power proposed by [Howe \(1998\)](#) was applied to calculate the aeroacoustic responses of the flow, i. e.,

$$\langle P \rangle = -\rho_0 \int_V \langle (\boldsymbol{\omega} \times \mathbf{v}) \cdot \mathbf{u}' \rangle dV, \quad (1.1)$$

where the angle bracket $\langle \rangle$ denotes the time averaged quantities, $\boldsymbol{\omega}$ is the vorticity vector, \mathbf{v} is the total velocity vector and \mathbf{u}' is the acoustic velocity vector (from excitation). There were two main approaches for estimating $\boldsymbol{\omega} \times \mathbf{v}$ in the calculation of the aeroacoustic responses of duct junction. The first one was the adoption of vortex model in calculating the acoustic power generated by vortical motions excited by the oncoming acoustic waves ([Bruggeman et al. 1991](#), [Dequand et al. 2003](#) and [Karlsson & Åbom 2010](#)). [Bruggeman et al. \(1991\)](#) proposed a theoretical model for such self-sustained pulsation at duct junction from the convected wave equation. [Dequand et al. \(2003\)](#) derived another analytical model to improve the prediction of the amplitudes of pulsations. This model was based on the vortex model proposed by [Nelson et al. \(1983\)](#), in which the shear layer was treated as a chain of point vortices convecting at a constant speed. [Karlsson & Åbom \(2010\)](#) adopted the same vortex model as [Bruggeman et al. \(1991\)](#). They treated the T-junction as an active acoustic three-port. The sound transmission and the sound generation by unsteady flow dynamics were modeled as the passive acoustic properties and the source vector respectively. Based on this model, the whistling potential was evaluated. In the second approach, $\boldsymbol{\omega} \times \mathbf{v}$ was obtained from the numerical simulations using the incompressible Navier-Stokes equations. [Martínez-Lera et al. \(2009\)](#) combined this approach and the system identification technique proposed

by Polifke et al. (2001) to calculate the transfer function relating the output source pressure differences to the input fluctuating velocities under a slow mean flow ($M \sim 0.05$). It is worthwhile to note that the excitation amplitude was also comparable to the mean flow in this study. Tonon et al. (2010) further extended this method to study the whistling of a pipe system with multiple side branches.

On the contrary, research effort is seldom devoted in the second category, i. e., studying the sound generation by the merging flow at duct junctions, especially at high Reynolds number. One example is the work of Karlsson & Åbom (2010). As mentioned by Hirota et al. (2006), this flow is very complex in nature, which consists of three dimensional flow, separation and reattachment. Little are known for these complex unsteady flow structures. The sound generation may also be very complicated. Thus, it is essential to investigate them for the minimization of sound generation. In addition, these studies are restricted to the T-junction; other angles between the side branch and main duct have not been studied. This implies that the important role of such flow in sound generation at different merging angles is not thoroughly studied. Thus, this research is motivated to investigate the present aspect.

1.2 OBJECTIVES AND RESEARCH SCOPE

In this research, identification of the sound generation mechanisms of the merging flow at duct junctions is attempted at Reynolds numbers commonly encountered in practical situations, i. e., up to $O(5)$. Furthermore, the relationship between the flow dynamics and the sound generated is also studied. The effects of different velocity ratio between the inlet flows and the merging angle between the flows are also focused. From this research, the fundamental knowledge on the flow dynamics and aeroacoustics acquired will deepen our understanding of the physics for this type of flow.

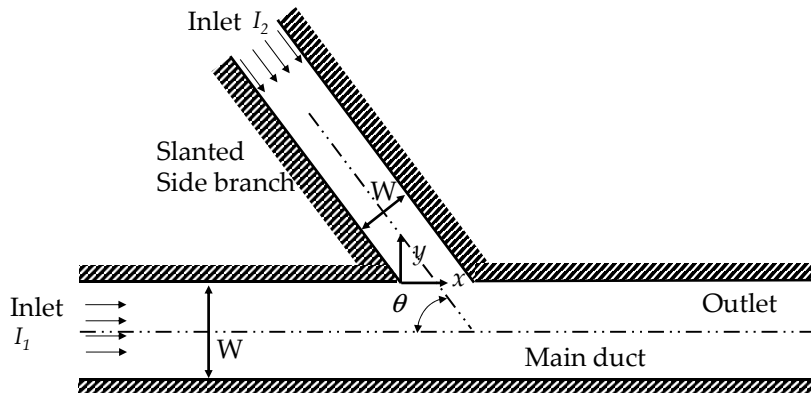


Figure 1.2: Geometry for current investigations.

However, in this research, only the duct junction geometry shown in [Figure 1.2](#) is investigated. The straight side branch of the same width joins the straight main duct at an angle θ . The flows enter the duct junction at duct inlets I_1 and I_2 , whereas turbulent profiles are assumed in this investigations.

1.3 APPROACH OF INVESTIGATIONS

The investigation of aeroacoustics of the merging flow at duct junctions is divided into two parts. The first part is a two dimensional numerical study. The second part is a three dimensional investigation, which involves both the numerical and experimental efforts. Since the aeroacoustics in internal flows is very complicated, the flow and acoustic disturbances are always mixed in the internal flow, inducing great difficulty to differentiate their evolutions experimentally. Furthermore, due to the high mesh requirement for simulating turbulent flow, the computational resources available are not sufficient to perform a full three dimensional numerical study. Thus, the present investigation starts with the two dimensional study. A numerical tool is developed and applied in order to give further directions for the three dimensional investigations, in which we try to capture the evolution of large coherent structures.

In the aforementioned literature, a hybrid approach is adopted for the investigation. This approach essentially separates the calculation of the flow

field and acoustic field individually, so the interaction between them is ignored. With such complex merging flow at duct junction, it is not appropriate to adopt the simplified vortex model like Bruggeman et al. (1991). Since the unsteady flow structures are not clearly understood, the adopted approach should be able to reveal the flow structures and their sound generation. Therefore, the numerical approach adopted in the present research is the direct aeroacoustic simulation (DAS). In contrast with hybrid approach, in which the acoustics is studied by the existing computational flow field and yields the acoustic radiation in the far field, DAS is based on the simultaneous calculation of the flow dynamic and acoustic fields obtained by solving the unsteady compressible Navier-Stokes (N-S) equations and the perfect gas equation of state. In addition to the acoustics in the far field, DAS can further provide a deeper insight of the sound source mechanisms. Furthermore, it would also provide the link between unsteady flow and the acoustics. Numerous researches (Freund 2001, Rowley et al. 2002, Gloorfelt et al. 2003) have already demonstrated its success in dealing with jet and cavity flow aeroacoustic problems. Therefore, it is a feasible approach to estimate far field sound and its source mechanisms in the study of aeroacoustic problems. However, this success is obtained at the expense of serious numerical issues that may be difficult to overcome as pointed out by Tam (1995).

In fact, these serious numerical issues arise from the large disparity of scales between the aerodynamic and acoustic field, such as length and energy. According to Curle (1955), for a flow with Mach number M and the presence of a rigid wall, the acoustic efficiency η which is the ratio of the acoustic power P_{acoust} to the flow power injected to the system P_{aero} , is proportional to M^3 . Thus, at low Mach number, say $M = 0.1$, $\eta = P_{acoust}/P_{aero} \sim 10^{-3}$. Furthermore, the propagating speed of the acoustic and flow disturbances are greatly different by M . Therefore, many researches (such as Tam 1995, Lele 1992, Bogey 2004) indicate that a low-dispersive and a low-dissipative numerical scheme is required if the acoustic waves propagating in the computational domain are to be preserved correctly in DAS. Conventionally, the

DAS is carried out by a high order compact finite difference scheme such as that of Tam (1993). Nevertheless, its general applicability is hindered by the huge computational resources demand.

In the present research, the space-time conservation element and solution element (CE/SE) scheme proposed by Chang (1995) is adopted as the numerical tools due to its high accuracy and low dissipation. It meets the aforementioned numerical requirement of DAS. Since its inception, the CE/SE scheme has been successfully attempted in calculating different incompressible and low supersonic flows of practical interest such as unsteady viscous and Euler flows, traveling and interacting shocks, supersonic jet noise, as well as acoustic wave propagation (Loh, Chang & Hultgren (2001), Loh (2005), Loh & Hultgren (2006), Venkatachari et al. (2008), Guo et al. (2004)). These researches demonstrate its great capability in solving the aeroacoustics. This high-resolution scheme takes entirely different concept and approach from conventional schemes (e.g. finite-difference, finite-volume, etc.). Its construction of numerical framework relies solely on the physical law and emphasizes on the unified treatment in both space and time. It also reveals several unique features in its solution formulation in addition to the unified treatment of space and time. They are (i) treatment of both flow variables and their spatial derivatives as independent unknowns, (ii) introduction of conservation element and solution element for space-time flux conservation calculation at interfaces without an interpolation or extrapolation procedure, (iii) enforcement of both local and global space-time flux conservation conforming consistently to the conservation nature of the physics of flow, (iv) capturing shock without solving the Riemann problem, (v) schemes built from a non-dissipative core scheme allowing for control of numerical dissipation effectively established with mathematical and/or physical arguments. Equipping with these superior features, the CE/SE scheme is capable to yield consistent formulation for incompressible to supersonic flow regimes where the solution procedure does not require any pre-conditioning method or Riemann-solver based shock capturing technique. In addition, it can be easily

adapted in unstructured mesh which is often a necessity for solving real-life problems.

After determining the location of dominant flow unsteadiness from the two dimensional study, the three dimensional study at the region is performed to compare the differences between the two and three dimensional studies. It consists of both numerical and experimental investigations. The numerical method adopted is the three dimensional CE/SE method. In the experimental investigations, due to the existence of three dimensional flow structures (Hirota et al. (2006)), equipments that can measure three dimensional velocity fluctuation should be used. However, since the non-intrusive equipment is unavailable, the experiment is carried out by intrusive apparatus. Cobra probe is adopted in experiment as it can measures the three dimensional velocities and their fluctuations. The boundary layer of the inlet flows are measured by a hot wire due to its good spatial resolution. The experimental study is carried out using the quiet flow facility consisting of two fans, the necessary duct work and the silencer. Furthermore, the mean flow profile and the pressure fluctuation is examined near the location of dominant flow unsteadiness for the acoustic investigations.

1.4 ORGANIZATION OF THE THESIS

This thesis is divided into three parts. The first part is the introduction and the methodology adopted in this research (chapter 1, chapter 2 and chapter 3). The second part is the two dimensional investigation of the merging flow at duct junctions (chapter 4). The third part is its three dimensional investigation (chapter 5 and chapter 6). It then comes to the conclusion and some suggestions of future work (chapter 7).

In chapter 2, the implementation of the CE/SE method on the Navier-Stokes equation for the DAS is focused. The two dimensional case is first described by introducing the two dimensional Navier-Stokes Equations and

the implementation of CE/SE method on them. Then, the text drives us to the three dimensional situation and discuss its implementation. Similarly, a three dimensional CE/SE method is also developed for this study. Afterwards, the boundary condition applied for the CE/SE method is introduced. Since the investigations of this research involve the turbulent flows, the turbulent modeling adopted is also discussed. Finally, the code development of the CE/SE method incorporated with the turbulence modeling and various boundary conditions is mentioned.

In [chapter 3](#), the credibility of the CE/SE method is established through a series of aeroacoustic problems. These cases are some typical cases encountered in the aeroacoustics. Similar to [chapter 2](#), the validation is also divided into two and three dimensional case.

The investigation of merging flow at duct junctions begins with the two dimensional numerical study in [chapter 4](#). The general aeroacoustics of this flow is discussed together with the effects of the velocity ratio and the merging angle between the side branch and main duct on it. Furthermore, since the calculated signals in the downstream part of main duct are mixed with both flow and acoustic disturbances, an approach of acoustic extraction is proposed and discussed in this chapter.

In the third part of thesis, the focus is the three dimensional investigation of this flow. In [chapter 5](#), the focus is on the experimental study, which gives some comparisons between the simulation and the experiment. The experimental setup is first described, followed by the comparison of its results with those obtained in the two dimensional study.

The three dimensional numerical study in [chapter 6](#) try to address the differences between the two dimensional and the three dimensional study. Its setup is described first and the obtained aeroacoustics are then compared with those of two dimensional study.

Finally, the investigation is summarized in [chapter 7](#) together with the suggestion of improving the present study and the direction of future study.

THE SPACE TIME CONSERVATION ELEMENT AND SOLUTION ELEMENT METHOD

In this chapter, the development of a numerical solver for conservation laws, the space-time Conservation Element and Solution Element (CE/SE) Method, which was first proposed by [Chang \(1995\)](#), is described. Implementation of this method to the Navier-Stokes (N-S) equations in both two and three dimensions will be described, followed by the treatment of boundary condition. In addition, since many practical applications involve turbulent flows, the implementation of turbulence modeling (MILES and wall modeling) is also discussed. Finally, the code development of CE/SE method is described.

2.1 INTRODUCTION

As mentioned in [chapter 1](#), the DAS always requires a N-S solver with high accuracy and little dissipation due to the large disparity in scales such as energy scales, length scales, especially in low Mach number flow. Therefore, it is very essential to choose a suitable N-S solver as excessive numerical dissipation will kill the small acoustic quantities throughout the calculations. Traditionally, very high order (> 5 th, e. g., [Lele 1992](#), or even up to 15th nowadays, e. g., [Tam 2006](#)) numerical methods such as finite difference method, spectral method, are applied in such simulations. However, these solvers are usually based on some criteria which are rather difficult to attain in reality or even unphysical for certain cases, e. g., smoothness in physical solution. The only conventional method that follows the physical governing law is the finite volume method, which enforces the flux conservations derived from the original equations. It, nevertheless, relies on the flux reconstruction at the interfaces that require

extrapolation or interpolation according to the characteristic-based technique such as dimensional splitting. These techniques are complicated and more importantly, difficult to extend to the multidimensional cases (computational burden is very heavy).

Motivated by the challenge of overcoming the aforementioned limitations of conventional numerical methods, the development of CE/SE method relies heavily on the physical laws according to [Chang \(1995\)](#). It considers the physical conservation laws as the conservation of flux in space and time, which is a uniqueness to other numerical methods. To illustrate this concept, consider a differential form of conservation law, with $\mathbf{Q} = (F, G)$

$$\frac{\partial \mathbf{U}}{\partial t} + \nabla \cdot \mathbf{Q} = 0, \quad (2.1)$$

By applying Gauss's divergence theorem to Eq.(2.1), it results in the integral form of conservation law,

$$\oint_{S(V)} \mathbf{K} \cdot d\mathbf{s} = 0, \quad (2.2)$$

where $\mathbf{K} = (F, G, U)$, $S(V)$ is the surface of an space-time arbitrary region V and $d\mathbf{s} = d\sigma \mathbf{n}$, where $d\sigma$ is the area and \mathbf{n} is the unit outward normal of the surface element on $S(V)$. Taking a two dimensional case as an example, V is a just 3-dimensional Euclidean region, E_3 and other variables are as defined in [Figure 2.1](#). Here $\mathbf{K} \cdot d\mathbf{s}$ is defined as the space-time flux leaving the surface $S(V)$, thus in CE/SE method, the conservation laws are regarded as all the space-time flux leaving $S(V)$ are balanced. This concept is very important to CE/SE method as the evolution of flow depends on this idea.

In order to march the solution in time, the CE/SE method defines two important cornerstones, the *conservation element* (CE) and *solution element* (SE). The CE is a control space-time volume like V in [Figure 2.1](#) to handle the flux conservation while the SE is used to calculate the space-time flux across the

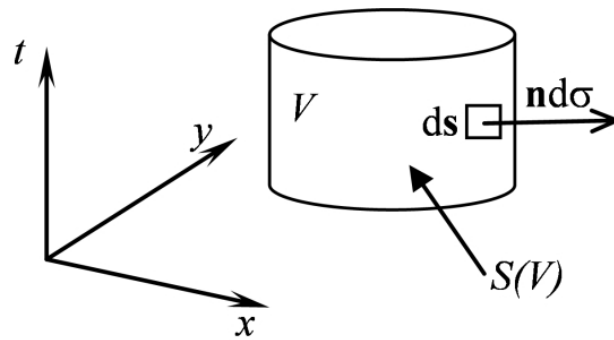


Figure 2.1: An arbitrary space-time region for a two dimensional problem.

boundary. By constructing the CE and SE wisely, the flux reconstruction at the cell interface can be avoided, unlike in finite volume method.

One can see that the CE/SE method is built on an entirely different philosophy that is unique to other conventional numerical methods. It i) unifies the treatment of both space and time derivatives of flow variables; ii) conserves the space-time flux globally and locally; iii) introduces the CE and SE to eliminate the need of flux reconstruction, thus it is capable in capturing shock without Riemann solver; iv) is truly multi-dimensional scheme; v) is a non-dissipative core scheme allowing the control of dissipation based on the rigorous physical and mathematical arguments. Furthermore, it can be easily adapted to complex geometries in both structured or unstructured mesh, which is often encountered in real situations. All these novel features make it an excellent candidate for the DAS because it can be applied to a wide range of flow problems from very low subsonic flow to supersonic flow with minimum of artificial intervention such as filtering, Riemann solver. This is also confirmed by the successful applications of CE/SE method in different types of flow problems, e. g., viscous flow, vortex-shock interactions, supersonic jet noise and acoustic wave propagation (Guo et al. (2004), Loh, Chang & Hultgren (2001), Loh, Himansu & Wang (2001), Loh (2005), Venkatachari et al. (2008)).

The following sections will show the implementation of this method to the N-S equations. However, before going into the details of the implementation of CE/SE method on the N-S equations, some notations are mentioned

here for enhancing the foregoing presentations and they will be used throughout this text. First, all the geometrical points are represented by Roman letter. Second, since the CE/SE method involves geometry of several time levels, the geometrical point with superscript '' and ' represent them at $(n + 1/2)$ -th and n -th time level respectively while the point with no superscript denote it at $(n - 1/2)$ -th time level. Finally, all the variables with hat denote the dimensional quantities while their dimensionless counterparts are denoted by the variables without hat.

2.2 TWO DIMENSIONAL FORMULATION OF CE/SE METHOD

The present aeroacoustic problem of low Mach number is governed by N-S equations together with ideal gas law for calorically perfect gas and the flow scale is the most suitable to be scaling parameter. Thus, by choosing the appropriate reference length \hat{L}_0 , reference velocity \hat{u}_0 , reference time, \hat{t}_0 , density $\hat{\rho}_0$, pressure $\hat{\rho}_0 \hat{u}_0^2$, temperature \hat{T}_0 and viscosity $\hat{\mu}_0$, the two dimensional normalized N-S equations without source can be written in the strong conservation form as

$$\frac{\partial \mathbf{U}}{\partial t} + \frac{\partial (\mathbf{F} - \mathbf{F}_v)}{\partial x} + \frac{\partial (\mathbf{G} - \mathbf{G}_v)}{\partial y} = 0, \quad (2.3)$$

where

$$\mathbf{U} = \begin{bmatrix} U_1 \\ U_2 \\ U_3 \\ U_4 \end{bmatrix} = \begin{bmatrix} \rho \\ \rho u \\ \rho v \\ \rho E \end{bmatrix},$$

$$\begin{aligned}
\mathbf{F} &= \begin{bmatrix} f_1 \\ f_2 \\ f_3 \\ f_4 \end{bmatrix} = \begin{bmatrix} \rho u \\ \rho u^2 + p \\ \rho uv \\ (\rho E + p) u \end{bmatrix}, \quad \mathbf{G} = \begin{bmatrix} g_1 \\ g_2 \\ g_3 \\ g_4 \end{bmatrix} = \begin{bmatrix} \rho v \\ \rho uv \\ \rho v^2 + p \\ (\rho E + p) v \end{bmatrix}, \\
\mathbf{F}_v &= \begin{bmatrix} f_{v1} \\ f_{v2} \\ f_{v3} \\ f_{v4} \end{bmatrix} = C_1 \begin{bmatrix} 0 \\ \tau_{xx} \\ \tau_{xy} \\ \tau_{xx}u + \tau_{xy}v - q_x \end{bmatrix}, \\
\mathbf{G}_v &= \begin{bmatrix} g_{v1} \\ g_{v2} \\ g_{v3} \\ g_{v4} \end{bmatrix} = C_1 \begin{bmatrix} 0 \\ \tau_{xy} \\ \tau_{yy} \\ \tau_{xy}u + \tau_{yy}v - q_y \end{bmatrix}, \\
\tau_{xx} &= \frac{2}{3}\mu \left(2\frac{\partial u}{\partial x} - \frac{\partial v}{\partial y} \right), \quad \tau_{xy} = \mu \left(\frac{\partial u}{\partial y} + \frac{\partial v}{\partial x} \right), \\
\tau_{yy} &= \frac{2}{3}\mu \left(2\frac{\partial v}{\partial y} - \frac{\partial u}{\partial x} \right), \quad E = \frac{p}{\rho(\gamma-1)} + \frac{u^2+v^2}{2}, \quad p = \frac{\rho T}{\gamma C_2}, \\
q_x &= -\frac{\mu}{(\gamma-1)PrC_2} \frac{\partial T}{\partial x}, \quad q_y = -\frac{\mu}{(\gamma-1)PrC_2} \frac{\partial T}{\partial y},
\end{aligned}$$

with the specific heat ratio $\gamma = 1.4$, Mach number $M = \hat{u}_o / \hat{c}_o$, $\hat{c}_o = \sqrt{\gamma \hat{R} \hat{T}_o}$, the specific gas constant for air $\hat{R} = 287.058 \text{ J / (kgK)}$, Reynolds number $Re = \hat{\rho}_o \hat{u}_o \hat{L}_o / \hat{\mu}_o$, Prandtl number $Pr = \hat{c}_{p,o} \hat{\mu}_o / \hat{k}_o = 0.71$, $C_1 = 1/Re$ and $C_2 = M^2$. Sometimes it is more appropriate to take the acoustic speed as the reference speed when facing the problem dominated by the acoustic propagation. In such situation, $C_1 = M/Re$ and $C_2 = 1$. The viscosity and the temperature are also related by Sutherland's Law, i. e.,

$$\mu = T^{\frac{3}{2}} \left(\frac{1 + \hat{S}_{su} / \hat{T}_{su}}{\hat{T}_{su} + \hat{S}_{su} / \hat{T}_{su}} \right), \quad (2.4)$$

where $\hat{S}_{su} = 110.2^\circ\text{C}$ at $\hat{T}_{su} = 20^\circ\text{C}$. If the reference velocity is changed to the speed of sound, \hat{c}_o , then the coefficients of \mathbf{F}_v and \mathbf{G}_v are replaced by $\frac{M}{Re}$;

the equations of p , q_x and q_y are also replaced by $p = \frac{\rho T}{\gamma}$, $q_x = -\frac{\mu}{(\gamma-1)Pr} \frac{\partial T}{\partial x}$ and $q_y = -\frac{\mu}{(\gamma-1)Pr} \frac{\partial T}{\partial y}$. However, the following discussion keeps using the characteristic speed of flow, \hat{u}_o as the reference velocity. Expressing all these quantities in terms of \mathbf{U} and introducing $\beta \equiv \gamma - 1$, it yields

$$\mathbf{F} = \begin{bmatrix} U_2 \\ \frac{U_2^2}{U_1} - A_1 + \beta U_4 \\ \frac{U_2 U_3}{U_1} \\ \frac{\gamma U_2 U_4}{U_1} + \beta U_2 \frac{U_2^2 + U_3^2}{2U_1^2} \end{bmatrix}, \quad \mathbf{G} = \begin{bmatrix} U_3 \\ \frac{U_2 U_3}{U_1} \\ \frac{U_3^2}{U_1} - A_1 + \beta U_4 \\ \frac{\gamma U_3 U_4}{U_1} + \beta U_3 \frac{U_2^2 + U_3^2}{2U_1^2} \end{bmatrix},$$

$$T = \frac{\gamma Ma^2 \beta}{U_1} \left(U_4 - \frac{U_2^2 + U_3^2}{2U_1} \right),$$

$$\tau_{xx} = \frac{2}{3} \mu \left[2 \left(\frac{1}{U_1} \frac{\partial U_2}{\partial x} - \frac{U_2}{U_1^2} \frac{\partial U_1}{\partial x} \right) - \left(\frac{1}{U_1} \frac{\partial U_3}{\partial y} - \frac{U_3}{U_1^2} \frac{\partial U_1}{\partial y} \right) \right],$$

$$\tau_{xy} = \frac{2}{3} \mu \left[\left(\frac{1}{U_1} \frac{\partial U_2}{\partial y} - \frac{U_2}{U_1^2} \frac{\partial U_1}{\partial y} \right) + \left(\frac{1}{U_1} \frac{\partial U_3}{\partial x} - \frac{U_3}{U_1^2} \frac{\partial U_1}{\partial x} \right) \right],$$

$$\tau_{yy} = \frac{2}{3} \mu \left[2 \left(\frac{1}{U_1} \frac{\partial U_3}{\partial x} - \frac{U_3}{U_1^2} \frac{\partial U_1}{\partial x} \right) - \left(\frac{1}{U_1} \frac{\partial U_2}{\partial y} - \frac{U_2}{U_1^2} \frac{\partial U_1}{\partial y} \right) \right],$$

where $A_1 = \beta \frac{U_2^2 + U_3^2}{2U_1^2}$. Furthermore, the Jacobian matrices, $\frac{\partial \mathbf{F}}{\partial \mathbf{U}}$, $\frac{\partial \mathbf{G}}{\partial \mathbf{U}}$ and $\frac{\partial T}{\partial \mathbf{U}}$ will be used in the derivation of 2D CE/SE method and they are written as

$$\begin{aligned} \frac{\partial \mathbf{F}}{\partial \mathbf{U}} &= \begin{bmatrix} 0 & 1 & 0 & 0 \\ A_1 - \frac{U_2^2}{U_1^2} & (3-\gamma) \frac{U_2}{U_1} & -\beta \frac{U_3}{U_1} & \beta \\ -\frac{U_2 U_3}{U_1^2} & \frac{U_3}{U_1} & \frac{U_2}{U_1} & 0 \\ \frac{U_2}{U_1} A_2 & A_3 - \beta \frac{U_2^2}{U_1^2} & -\beta \frac{U_2 U_3}{U_1^2} & \gamma \frac{U_2}{U_1} \end{bmatrix}, \\ \frac{\partial \mathbf{G}}{\partial \mathbf{U}} &= \begin{bmatrix} 0 & 0 & 1 & 0 \\ -\frac{U_2 U_3}{U_1^2} & \frac{U_3}{U_1} & \frac{U_2}{U_1} & 0 \\ A_1 - \frac{U_3^2}{U_1^2} & -\beta \frac{U_2}{U_1} & (3-\gamma) \frac{U_3}{U_1} & \beta \\ \frac{U_3}{U_1} A_2 & -\beta \frac{U_2 U_3}{U_1^2} & A_3 - \beta \frac{U_3^2}{U_1^2} & \gamma \frac{U_3}{U_1} \end{bmatrix}, \\ \frac{\partial T}{\partial \mathbf{U}} &= \frac{\gamma Ma^2 \beta}{U_1} \begin{bmatrix} -\frac{U_4}{U_1} + \frac{U_2^2 + U_3^2}{U_1^2} & -\frac{U_2}{U_1^2} & -\frac{U_3}{U_1^2} & 1 \end{bmatrix}, \end{aligned} \tag{2.5}$$

where $A_2 = \gamma \frac{u_4}{u_1^2} + \beta \frac{u_2^2 + u_3^2}{u_1^2}$, $A_3 = \gamma \frac{u_4}{u_1} - \beta \frac{u_2^2 + u_3^2}{2u_1^2}$.

2.2.1 Definition of Conservation Element (CE) & Solution Element (SE)

Let $\mathbf{X} = (x, y, t)$ be a coordinate of a 3-dimensional Euclidean space E_3 . After applying Gauss Divergence Theorem, Eq.(2.3) takes the form of Eq.(2.2), with $\mathbf{K} \equiv [F - F_v, G - G_v, \mathbf{U}]$. Next, the computational domain is decomposed into non-overlapping triangles as shown in Figure 2.2. Points B, F, and D are the mesh points that form a triangular mesh with point G being its centroid. Similarly, point A, C and E are the centroids of the adjacent triangles. The point G^* is the centroid of ABCDEF and is taken as the solution point. In general, G^* and G are not the same point.

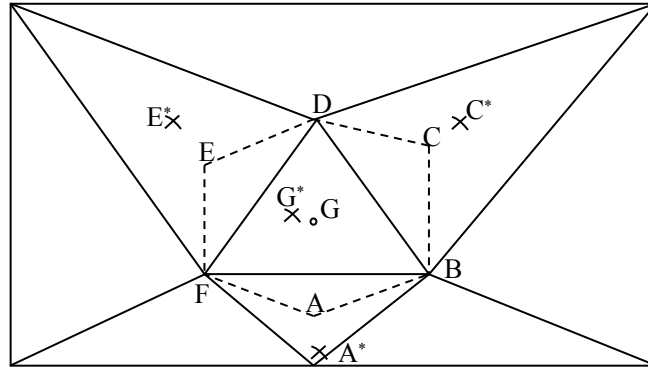


Figure 2.2: Decomposition of computational domain.

The definition of CE is shown in Figure 2.3. Three basic CEs, $CE_i(G^*, n)$, $i = 1, 2, 3$, are defined by the hexahedra $ABGFA'B'G'F'$, $CDGBC'D'G'B'$ and $EFGDE'F'G'D'$ respectively. The union of these three basic CEs forms the combined CE, which is denoted as $CE(G^*, n)$, where G^* is its *spatial* location and n denotes the n -th time level. Conservation of flux is enforced in $CE(G^*, n)$, in which the flux leaves through its 8 surfaces $A'ABB'$, $B'BCC'$, $C'CDD'$, $D'DEE'$, $E'EFF'$, $ABCDEF$ and $A'B'C'D'E'F'$.

On the other hand, the solution element of spatial location G^* at n th time level denoted by $SE(G^*, n)$ is formed by the planes $A'B'C'D'E'F'$, $BB''G''G$, $DD''G''G$ and $FF''G''G$. Its solution is represented by the value at the solution point G^* . For any location \mathbf{X} within $SE(G^*, n)$, the flow variables, $\phi(\mathbf{X}) =$

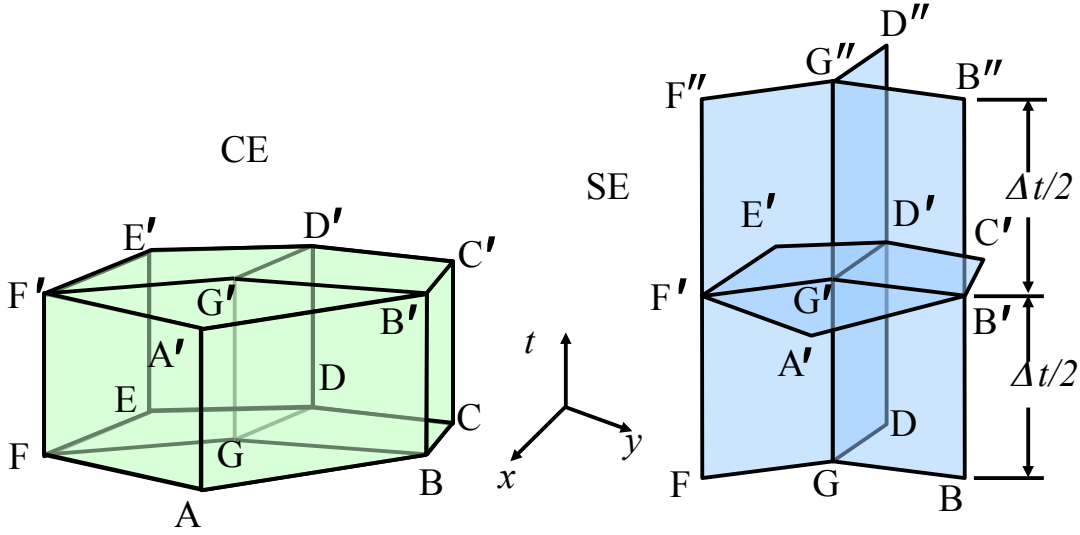


Figure 2.3: Geometrical definitions of CE & SE.

$\mathbf{U}(\mathbf{X})$, $F(\mathbf{X})$, or $G(\mathbf{X})$ at this location can be approximated by applying the first order Taylor expansions at the solution point G^* , i. e.,

$$\phi(\mathbf{X})_{G^*} = \phi_{G^*} + \delta x (\phi_x)_{G^*} + \delta y (\phi_y)_{G^*} + \delta t (\phi_t)_{G^*}, \quad (2.6)$$

where $\delta x = (x - x_{G^*})$, $\delta y = (y - y_{G^*})$, $\delta t = (t - t^i)$, the subscripts x , y are the spatial gradients in x and y direction respectively. Furthermore, according to Eq.(2.5), these gradients can be calculated by chain rule as

$$\begin{aligned} (\phi_x)_{G^*} &= \frac{\partial \phi}{\partial \mathbf{U}} (\mathbf{u}_x)_{G^*}, \\ (\phi_y)_{G^*} &= \frac{\partial \phi}{\partial \mathbf{U}} (\mathbf{u}_y)_{G^*}, \\ (\phi_t)_{G^*} &= \frac{\partial \phi}{\partial \mathbf{U}} (\mathbf{u}_t)_{G^*}. \end{aligned} \quad (2.7)$$

Moreover, the viscous terms F_v and G_v in Eq.(2.3) are approximated by $F_v(\mathbf{X})_{G^*}$ and $G_v(\mathbf{X})_{G^*}$ respectively and are assumed to be constant within $SE(G^*, n)$. Thus, the N-S equations inside $SE(G^*, n)$ can be expressed as,

$$(\mathbf{u}_t)_{G^*} = - (F_x)_{G^*} - (G_y)_{G^*}. \quad (2.8)$$

Moreover, \mathbf{K} at \mathbf{X} within $SE(G^*, n)$ are approximated by \mathbf{K}^\dagger at \mathbf{X} , i. e.,

$$\mathbf{K}^\dagger(\mathbf{X})_{G^*} \equiv [F(\mathbf{X})_{G^*} - F_v(\mathbf{X})_{G^*}, G(\mathbf{X})_{G^*} - G_v(\mathbf{X})_{G^*}, \mathbf{U}(\mathbf{X})_{G^*}], \quad (2.9)$$

where $F(\mathbf{X})_{G^*} - F_v(\mathbf{X})_{G^*}$ is the approximated $F - F_v$ at location \mathbf{X} by applying Taylor expansion at solution point G^* and similar interpretation can be applied to $G(\mathbf{X})_{G^*} - G_v(\mathbf{X})_{G^*}$ and $\mathbf{U}(\mathbf{X})_{G^*}$. Thus, all the approximated flux and flow variables can be expressed in terms of the independent variables, \mathbf{U} , \mathbf{U}_x and \mathbf{U}_y , whose updating will be discussed in Section 2.2.2.

2.2.2 Time Marching of Solution in CE/SE Method

The updating of solution \mathbf{U} , \mathbf{U}_x and \mathbf{U}_y in CE/SE method can be divided into three parts. The first part involves the calculation of \mathbf{U} through the conservation of space-time flux in CE for each element. The second part proceeds to the calculation of \mathbf{U}_x and \mathbf{U}_y with various schemes. In this project, the simplified Courant Number Insensitive Scheme (CNIS) introduced by [Yen & Wagner \(2005\)](#) is employed due to its compact stencils required while minimizing the dissipation for the large elements in highly non-uniform meshes. The last part is the assignment of the boundary condition, which will be detailed in later section.

Hereafter, for any flow variables $\phi_{G^*}^n$, the superscript n denotes the n -th time level while G^* denotes the position where ϕ is taken.

Calculation of \mathbf{U}

From [Figure 2.3](#), $CE(G^*, n)$ is surrounded by the external faces of $CE_i(G^*, n)$, $i = 1, 2, 3$, and the top face $A'B'C'D'E'F'$. Therefore, the total flux leaving it can be separated into four parts, the flux associated with the top face and $CE_i(G^*, n)$, $i = 1, 2, 3$. In the flux calculation, the flux associated with $CE_i(G^*, n)$, $i = 1, 2, 3$, are assigned to $SE(A^*, n - 1/2)$, $SE(C^*, n - 1/2)$ and $SE(E^*, n)$ respectively, where A^* , C^* and E^* are the solution points of adjacent

elements illustrated in [Figure 2.2](#). The determination of U at the new time level depends on the enforcement of the flux conservation, i. e., within $CE(G^*, n)$. Due to the flux cancellation between the interfaces of $CE_i(G^*, n)$, $i = 1, 2, 3$, the updating procedure of U^n , only requires to calculate the flux leaving $CE(G^*, n)$ at its surfaces and these are illustrated as follows.

First, consider $CE_1(G^*, n)$, the flux leaves it through $A'ABB'$, $F'FAA'$ and $ABGF$. According to [Eq.\(2.9\)](#), the flux leaving $CE_1(G^*, n)$ (ignoring the interfaces) can be expressed as,

$$\mathbf{T}_1^{n-\frac{1}{2}} = \mathbf{T}_{A'ABB'} + \mathbf{T}_{F'FAA'} + \mathbf{T}_{ABGF}, \quad (2.10)$$

where

$$\mathbf{T}_{A'ABB'} = \mathbf{K}^\dagger (\mathbf{X}_{A'ABB'})_{A^*} \cdot \mathbf{S}_{A'ABB'},$$

$$\mathbf{T}_{F'FAA'} = \mathbf{K}^\dagger (\mathbf{X}_{F'FAA'})_{A^*} \cdot \mathbf{S}_{F'FAA'},$$

$$\mathbf{T}_{ABGF} = \mathbf{K}^\dagger (\mathbf{X}_{ABGF})_{A^*} \cdot \mathbf{S}_{ABGF}.$$

$\mathbf{X}_{A'ABB'} = \left(\frac{x_A+x_B}{2}, \frac{y_A+y_B}{2}, t^{n-\frac{1}{4}} \right)$, $\mathbf{X}_{F'FAA'} = \left(\frac{x_F+x_A}{2}, \frac{y_F+y_A}{2}, t^{n-\frac{1}{4}} \right)$, $\mathbf{X}_{ABGF} = \left(x_1, y_1, t^{n-\frac{1}{2}} \right)$ are the centroids of faces $A'ABB'$, $F'FAA'$ and $ABGF$ respectively while

$$\mathbf{S}_{A'ABB'} = \frac{\Delta t}{2} (y_B - y_A, x_A - x_B, 0),$$

$$\mathbf{S}_{F'FAA'} = \frac{\Delta t}{2} (y_A - y_F, x_F - x_A, 0),$$

$$\mathbf{S}_{ABGF} = \frac{\Delta t}{2} (0, 0, -S_1),$$

where S_1 is the area of face $ABGF$, are their outward normals respectively. Furthermore, from [Eq.\(2.6\)](#) and [Eq.\(2.9\)](#) with T denoting the transpose of matrix,

$$\mathbf{K}^\dagger (\mathbf{X}_{A'ABB'})_{A^*} = \begin{bmatrix} \mathbf{F} (\mathbf{X}_{A'ABB'})_{A^*} - \mathbf{F}_v (\mathbf{X}_{A'ABB'})_{A^*} \\ \mathbf{G} (\mathbf{X}_{A'ABB'})_{A^*} - \mathbf{G}_v (\mathbf{X}_{A'ABB'})_{A^*} \\ \mathbf{U} (\mathbf{X}_{A'ABB'})_{A^*} \end{bmatrix}^T, \quad (2.11)$$

$$\mathbf{K}^\dagger(\mathbf{X}_{F'FAA'})_{A^*} = \begin{bmatrix} F(\mathbf{X}_{F'FAA'})_{A^*} - F_v(\mathbf{X}_{F'FAA'})_{A^*} \\ G(\mathbf{X}_{F'FAA'})_{A^*} - G_v(\mathbf{X}_{F'FAA'})_{A^*} \\ \mathbf{U}(\mathbf{X}_{F'FAA'})_{A^*} \end{bmatrix}^T, \quad (2.12)$$

$$\mathbf{K}^\dagger(\mathbf{X}_{ABGF})_{A^*} = \begin{bmatrix} F(\mathbf{X}_{ABGF})_{A^*} - F_v(\mathbf{X}_{ABGF})_{A^*} \\ G(\mathbf{X}_{ABGF})_{A^*} - G_v(\mathbf{X}_{ABGF})_{A^*} \\ \mathbf{U}(\mathbf{X}_{ABGF})_{A^*} \end{bmatrix}^T, \quad (2.13)$$

where all F , G and \mathbf{U} can be evaluated by Eq.(2.6) at $SE(A^*, n - 1/2)$. All the viscous terms are assumed to be equal to the value calculated at A^* at $(n - 1/2)$ -th time level, i. e.,

$$F_v(\mathbf{X}_{A'ABB'})_{A^*} = F_v(\mathbf{X}_{F'FAA'})_{A^*} = F_v(\mathbf{X}_{ABGF})_{A^*} = (F_v)_{A^*} \quad (2.14)$$

and

$$G_v(\mathbf{X}_{A'ABB'})_{A^*} = G_v(\mathbf{X}_{F'FAA'})_{A^*} = G_v(\mathbf{X}_{ABGF})_{A^*} = (G_v)_{A^*}. \quad (2.15)$$

Thus, the flux leaving $CE_1(G^*, n)$, $\Upsilon_1^{n-\frac{1}{2}}$, can be fully expressed in terms of the solution at A^* at $n - 1/2$ th time level.

Next, consider $CE_2(G^*, n)$, the flux leaving it is through $B'BCC'$, $C'CDD'$ and $CDGB$. From Eq.(2.9), the flux leaving $CE_2(G^*, n)$ (ignoring the interfaces) can be expressed as,

$$\Upsilon_2^{n-\frac{1}{2}} = \Upsilon_{B'BCC'} + \Upsilon_{C'CDD'} + \Upsilon_{CDGB}, \quad (2.16)$$

where

$$\boldsymbol{\Upsilon}_{B'BCC'} = \mathbf{K}^\dagger(\mathbf{X}_{B'BCC'})_{A^*} \cdot \mathbf{S}_{B'BCC'},$$

$$\boldsymbol{\Upsilon}_{C'CDD'} = \mathbf{K}^\dagger(\mathbf{X}_{C'CDD'})_{A^*} \cdot \mathbf{S}_{C'CDD'},$$

$$\boldsymbol{\Upsilon}_{CDGB} = \mathbf{K}^\dagger(\mathbf{X}_{CDGB})_{A^*} \cdot \mathbf{S}_{CDGB}.$$

$\mathbf{X}_{B'BCC'} = \left(\frac{x_B+x_C}{2}, \frac{y_B+y_C}{2}, t^{n-\frac{1}{4}} \right)$, $\mathbf{X}_{C'CDD'} = \left(\frac{x_C+x_D}{2}, \frac{y_C+y_D}{2}, t^{n-\frac{1}{4}} \right)$, $\mathbf{X}_{CDGB} = \left(x_2, y_2, t^{n-\frac{1}{2}} \right)$ are the centroids of faces $B'BCC'$, $C'CDD'$ and $CDGB$ respectively while

$$\mathbf{S}_{B'BCC'} = \frac{\Delta t}{2} (y_C - y_B, x_B - x_C, 0),$$

$$\mathbf{S}_{C'CDD'} = \frac{\Delta t}{2} (y_D - y_C, x_C - x_D, 0),$$

$$\mathbf{S}_{CDGB} = \frac{\Delta t}{2} (0, 0, -S_2),$$

where S_2 is the area of face $CDGB$, are their outward normals respectively. All the calculations of these terms are obtained similar to those in $CE_1(G^*, n)$ with faces $A'ABB'$, $F'FAA'$ and $ABGF$ replaced by faces $B'BCC'$, $C'CDD'$ and $CDGB$ respectively. Thus, the flux leaving $CE_2(G^*, n)$, $\boldsymbol{\Upsilon}_2^{n-\frac{1}{2}}$, can be fully expressed in terms of the solution at C^* at $(n - 1/2)$ -th time level.

Third, consider $CE_3(G^*, n)$, the flux leaving it is through $D'DEE'$, $E'EFF'$ and $EFGD$. According to Eq.(2.9), the flux leaving $CE_3(G^*, n)$ (ignoring the interfaces) can be expressed as,

$$\boldsymbol{\Upsilon}_3^{n-\frac{1}{2}} = \boldsymbol{\Upsilon}_{D'DEE'} + \boldsymbol{\Upsilon}_{E'EFF'} + \boldsymbol{\Upsilon}_{EFGD}, \quad (2.17)$$

where

$$\boldsymbol{\Upsilon}_{D'DEE'} = \mathbf{K}^\dagger(\mathbf{X}_{D'DEE'})_{A^*} \cdot \mathbf{S}_{D'DEE'},$$

$$\boldsymbol{\Upsilon}_{E'EFF'} = \mathbf{K}^\dagger(\mathbf{X}_{E'EFF'})_{A^*} \cdot \mathbf{S}_{E'EFF'},$$

$$\boldsymbol{\Upsilon}_{EFGD} = \mathbf{K}^\dagger(\mathbf{X}_{EFGD})_{A^*} \cdot \mathbf{S}_{EFGD}.$$

$\mathbf{X}_{D'DEE'} = \left(\frac{x_D+x_E}{2}, \frac{y_D+y_E}{2}, t^{n-\frac{1}{4}} \right)$, $\mathbf{X}_{E'EFF'} = \left(\frac{x_E+x_F}{2}, \frac{y_E+y_F}{2}, t^{n-\frac{1}{4}} \right)$, $\mathbf{X}_{EFGD} = \left(x_3, y_3, t^{n-\frac{1}{2}} \right)$ are the centroids of faces $D'DEE'$, $E'EFF'$ and $EFGD$ respectively while

$$\mathbf{S}_{D'DEE'} = \frac{\Delta t}{2} (y_E - y_D, x_D - x_E, 0),$$

$$\mathbf{S}_{E'EFF'} = \frac{\Delta t}{2} (y_F - y_E, x_F - x_E, 0),$$

$$\mathbf{S}_{EFGD} = \frac{\Delta t}{2} (0, 0, -S_3),$$

where S_3 is the area of face EFGD, are their outward normals respectively. Similarly, all the calculations of these terms are obtained in the same way as those in $CE_1(G^*, n)$ with faces $A'ABB'$, $F'FAA'$ and $ABGF$ replaced by faces $D'DEE'$, $E'EFF'$ and $EFGD$ respectively. Therefore, the flux leaving $CE_3(G^*, n)$, $\mathbf{\Upsilon}_3^{n-\frac{1}{2}}$, can be fully expressed in terms of the solution at E^* at $(n - 1/2)$ -th time level and this completes all the calculations of flux leaving $CE(G^*, n)$ at the side faces and the bottom faces.

Finally, consider the top face $A'B'C'D'E'F'$ with its outward normal being $(0, 0, S_1 + S_2 + S_3)$, the flux leaving through it at n th time level, $\mathbf{\Upsilon}_{top}^n$ is written as,

$$\mathbf{\Upsilon}_{top}^n = (S_1 + S_2 + S_3) \mathbf{U}_{G^*}^n. \quad (2.18)$$

By the conservation of flux over $CE(G^*, n)$, i. e., Eq.(2.2),

$$\mathbf{\Upsilon}_{top}^n + \mathbf{\Upsilon}_1^{n-\frac{1}{2}} + \mathbf{\Upsilon}_2^{n-\frac{1}{2}} + \mathbf{\Upsilon}_3^{n-\frac{1}{2}} = 0. \quad (2.19)$$

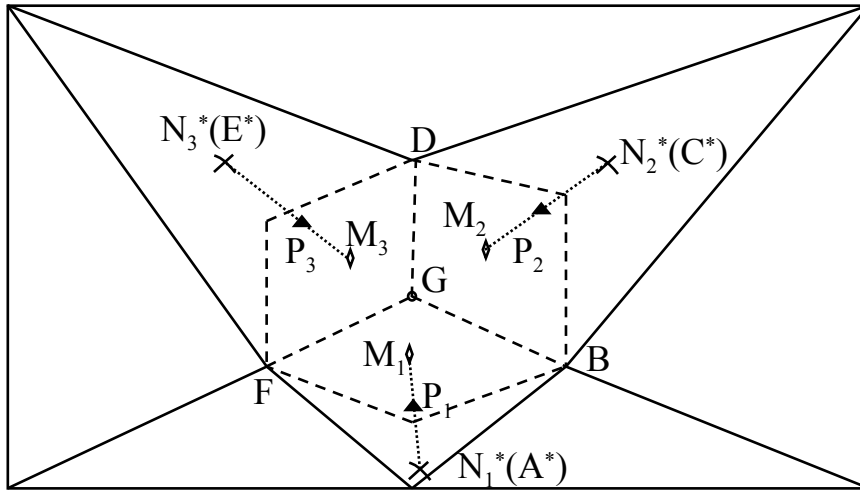
Thus,

$$\mathbf{U}_{G^*}^n = -\frac{\mathbf{\Upsilon}_1^{n-\frac{1}{2}} + \mathbf{\Upsilon}_2^{n-\frac{1}{2}} + \mathbf{\Upsilon}_3^{n-\frac{1}{2}}}{S_1 + S_2 + S_3}. \quad (2.20)$$

Hence, $\mathbf{U}_{G^*}^n$ can be determined from the solutions of the neighboring elements and their spatial derivatives at $(n - 1/2)$ -th time level. Next the spatial gradient at the n -th time level, \mathbf{U}_x^n and \mathbf{U}_y^n will be updated based on \mathbf{U}^n .

Calculation of U_x and U_y

In CE/SE method, the original scheme for calculating the spatial gradient of \mathbf{U} is called "a" scheme, which solves these gradients with the solution

Figure 2.4: Geometrical definitions of P_i , $i = 1, 2, 3$.

vector \mathbf{U} simultaneously with the solutions at the centroids of basic CEs approximated by the neighboring cells at $(n - 1/2)$ -th time level. This scheme is non-dissipative in nature according to Chang (1995) and so it cannot be applied to a physical process that is irreversible. Thus, another scheme with dissipation called “c” scheme was developed by Chang (1999). It calculates these gradients through a central differencing scheme with the solutions at the solution points of neighboring elements calculated at $(n - 1/2)$ -th time level. Due to the properties of CE/SE method as stated by Chang (2002), the “c” scheme will become highly dissipative when the Courant number $v_t \ll 1$ and this always occurs when a highly non-uniform mesh is used, e.g., in turbulent flow simulation with no-slip walls. To cope with this problem, Courant Number Insensitive scheme (CNIS) was introduced by Chang (2002), which is based on a dissipation controlling parameter, the local Courant number, σ . Later, Yen & Wagner (2005) further improved it to a simplified version (SCNIS) in finding σ , which is adopted in this research. For triangular mesh in 2D, these schemes are quite similar except the points adopted for the calculations and the procedure are illustrated in the followings.

Consider [Figure 2.4](#). P_i , $i = 1, 2, 3$, denoted by black triangle, lays between the centroid of basic CE, M_i and the adjacent solution point, N_i^* and can be written as

$$P_i = M_i + \kappa (N_i^* - M_i), \quad (2.21)$$

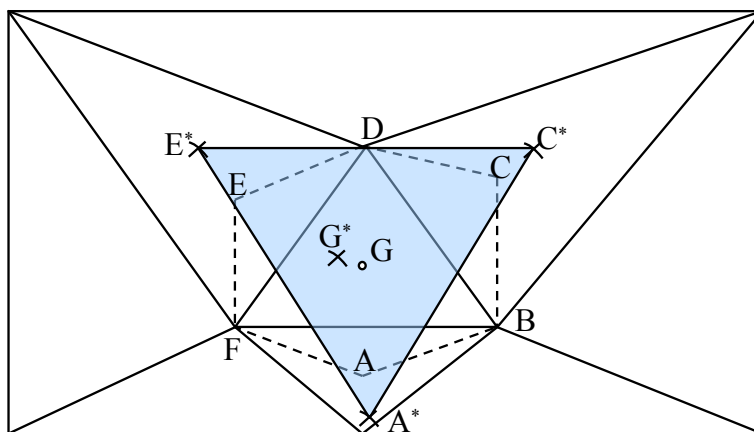
where κ is the parameter controlling the location of P_i . Taking [Figure 2.4](#) as an example, N_1^* , N_2^* and N_3^* are A^* , C^* and E^* respectively. In the original “a” scheme, $\kappa = 0$ while $\kappa = 1$ for “c” scheme. In the *CNIS* or *SCNIS*, κ is set by the local Courant number, σ . Since both schemes utilize the same stability criterion, only the adopted one, i. e. simplified version, is listed here in details. [Figure 2.5a](#) shows the numerical domain of dependence of G^* and a numerical solution is stable if the analytical domain of dependence falls completely inside this numerical domain of dependence. The analytical domain of dependence is the backward characteristic projection of the solution at G^* from n th time level to $(n - 1/2)$ -th time level. Taking the present location of G^* as origin, it is a circle centered at $(-\frac{u\Delta t}{2}, -\frac{v\Delta t}{2})$ of radius $\frac{c\Delta t}{2}$ with $c = \sqrt{\gamma p/\rho}$ as the local sound speed showed in [Figure 2.5b](#). Without loss of generality, the flow speed u and v are assumed to be positive in the discussion. The stability criterion requires that the time step Δt should be so small such that the numerical domain of dependence includes all the analytical domains of dependence. Consider the side A^*C^* first, this criterion is equivalent to

$$\sigma_1 = \frac{|G^*J| + |JH|}{|G^*Q|} = \frac{\Delta t \sqrt{u^2 + v^2} \cos(\phi_1 - \alpha) + c}{2 |G^*Q|}. \quad (2.22)$$

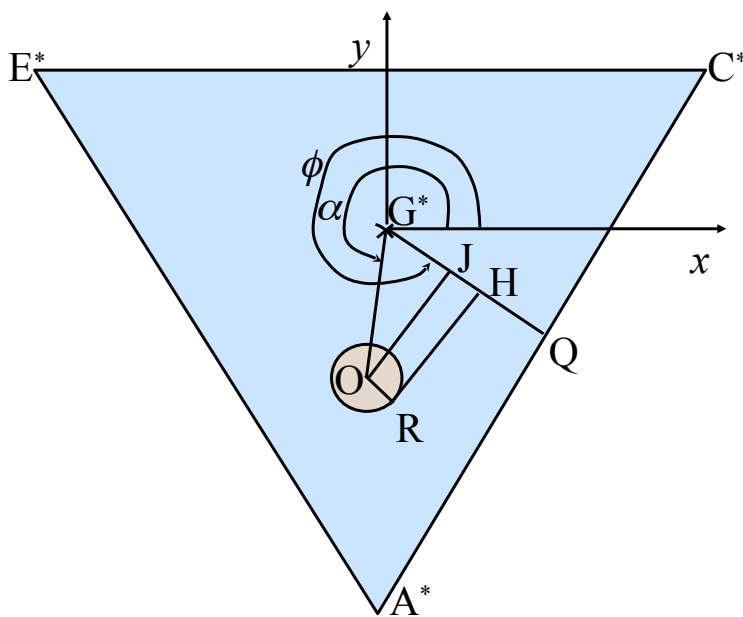
In a similar manner, σ_2 and σ_3 can be determined for the sides C^*E^* and E^*A^* respectively. Then the local CFL number σ is calculated by

$$\sigma = \max(\sigma_1, \sigma_2, \sigma_3). \quad (2.23)$$

In the original *CNIS*, the above procedure is projected at a whole Δt time level rather than $\frac{\Delta t}{2}$ time level, so this requires the information of all the



(a) The numerical domain of dependence.



(b) The stability criterion.

Figure 2.5: The numerical domain and analytical domain of dependence.

neighborhoods of $SE(A^*, n)$, $SE(C^*, n)$ and $SE(E^*, n)$. On the other hand, the simplified one only needs these three SEs. Thus, memory footprint is much smaller in the *SCNIS*.

After σ is calculated, P_i can then be determined by Eq.(2.21). The centroid of the triangle formed by $P_1P_2P_3$ in general does not coincide with the solution point G^* , this triangle is translated to a new position $\underline{P}_1\underline{P}_2\underline{P}_3$ such that the centroid of this new position coincides with G^* . Therefore, for $i = 1, 2, 3$,

$$\underline{P}_i = P_i + \left(G^* - \frac{P_1 + P_2 + P_3}{3} \right). \quad (2.24)$$

Hence, the solution vector of \underline{P}_i at n th time level can be written as

$$\mathbf{u}_{\underline{P}_i}^n = \mathbf{u}_{N_i^*}^{n-\frac{1}{2}} + \delta x_{\underline{P}_i} (\mathbf{u}_x)_{N_i^*}^{n-\frac{1}{2}} + \delta y_{\underline{P}_i} (\mathbf{u}_y)_{N_i^*}^{n-\frac{1}{2}} + \frac{\Delta t}{2} (\mathbf{u}_t)_{N_i^*}^{n-\frac{1}{2}}, \quad (2.25)$$

where $\delta x_{\underline{P}_i} = x_{\underline{P}_i} - x_{N_i^*}$ and $\delta y_{\underline{P}_i} = y_{\underline{P}_i} - y_{N_i^*}$. Then a central differencing scheme as described below is applied to calculate the spatial gradient \mathbf{u}_x^n and \mathbf{u}_y^n . For $i = 1, 2, 3$, denote

$$\left(\mathbf{u}_x^i \right)_{G^*}^n = \frac{\Delta_x^i}{\Delta^i}, \quad \left(\mathbf{u}_y^i \right)_{G^*}^n = \frac{\Delta_y^i}{\Delta^i}, \quad (2.26)$$

where

$$\begin{aligned} \Delta^1 &= \begin{vmatrix} \delta x_G^1 & \delta y_G^1 \\ \delta x_G^2 & \delta y_G^2 \end{vmatrix}, \Delta^2 = \begin{vmatrix} \delta x_G^2 & \delta y_G^2 \\ \delta x_G^3 & \delta y_G^3 \end{vmatrix}, \Delta^3 = \begin{vmatrix} \delta x_G^3 & \delta y_G^3 \\ \delta x_G^1 & \delta y_G^1 \end{vmatrix}, \\ \Delta_x^1 &= \begin{vmatrix} \delta \mathbf{u}_G^1 & \delta y_G^1 \\ \delta \mathbf{u}_G^2 & \delta y_G^2 \end{vmatrix}, \Delta_x^2 = \begin{vmatrix} \delta \mathbf{u}_G^2 & \delta y_G^2 \\ \delta \mathbf{u}_G^3 & \delta y_G^3 \end{vmatrix}, \Delta_x^3 = \begin{vmatrix} \delta \mathbf{u}_G^3 & \delta y_G^3 \\ \delta \mathbf{u}_G^1 & \delta y_G^1 \end{vmatrix}, \\ \Delta_y^1 &= \begin{vmatrix} \delta \mathbf{u}_G^1 & \delta x_G^1 \\ \delta \mathbf{u}_G^2 & \delta x_G^2 \end{vmatrix}, \Delta_y^2 = \begin{vmatrix} \delta \mathbf{u}_G^2 & \delta x_G^2 \\ \delta \mathbf{u}_G^3 & \delta x_G^3 \end{vmatrix}, \Delta_y^3 = \begin{vmatrix} \delta \mathbf{u}_G^3 & \delta x_G^3 \\ \delta \mathbf{u}_G^1 & \delta x_G^1 \end{vmatrix}, \end{aligned}$$

and $\delta x_G^i = x_{\underline{P}_i} - x_{G^*}$, $\delta y_G^i = y_{\underline{P}_i} - y_{G^*}$, $\delta \mathbf{u}_G^i = \mathbf{u}_{\underline{P}_i}^n - \mathbf{u}_{G^*}^n$. $\left(\mathbf{u}_x^i \right)_{G^*}^n$ and $\left(\mathbf{u}_y^i \right)_{G^*}^n$ actually represent the spatial gradients with respect to the solution

point G^* and corresponding \underline{P}_i . Defining $\frac{A}{B}$ to be the element-wise division of column matrix, the spatial gradients are then given by

$$(\mathbf{u}_x)_{G^*}^n = \frac{\sum_{i=1}^3 (\mathbf{w}_k^i)^\alpha (\mathbf{u}_x^i)_{G^*}^n}{\sum_{i=1}^3 (\mathbf{w}_k^i)^\alpha}, \quad (2.27)$$

and

$$(\mathbf{u}_y)_{G^*}^n = \frac{\sum_{i=1}^3 (\mathbf{w}_k^i)^\alpha (\mathbf{u}_y^i)_{G^*}^n}{\sum_{i=1}^3 (\mathbf{w}_k^i)^\alpha}, \quad (2.28)$$

where $\alpha \geq 0$, $\mathbf{w}_k^1 = \zeta_2 \zeta_3$, $\mathbf{w}_k^2 = \zeta_1 \zeta_3$, $\mathbf{w}_k^3 = \zeta_1 \zeta_2$ and

$$\zeta_i = \sqrt{\left[(\mathbf{u}_x^i)_{G^*}^n \right]^2 + \left[(\mathbf{u}_y^i)_{G^*}^n \right]^2},$$

for $i = 1, 2, 3$.

2.3 THREE DIMENSIONAL FORMULATION OF CE/SE METHOD

The CE/SE method can be readily extended to the three dimensional case by constructing a new four dimensional CE and SE. First, using the same reference parameters as in Section 2.2, the three dimensional normalized N-S equations without source are written in the strong conservation form as

$$\frac{\partial \mathbf{U}}{\partial t} + \frac{\partial (\mathbf{F} - \mathbf{F}_v)}{\partial x} + \frac{\partial (\mathbf{G} - \mathbf{G}_v)}{\partial y} + \frac{\partial (\mathbf{H} - \mathbf{H}_v)}{\partial z} = 0, \quad (2.29)$$

where

$$\begin{aligned}
 \mathbf{U} &= \begin{bmatrix} \rho \\ \rho u \\ \rho v \\ \rho w \\ \rho E \end{bmatrix}, \quad \mathbf{F} = \begin{bmatrix} \rho u \\ \rho u^2 + p \\ \rho uv \\ \rho uw \\ (\rho E + p)u \end{bmatrix}, \quad \mathbf{G} = \begin{bmatrix} \rho v \\ \rho uv \\ \rho v^2 + p \\ \rho vw \\ (\rho E + p)v \end{bmatrix}, \\
 \mathbf{H} &= \begin{bmatrix} \rho w \\ \rho uw \\ \rho vw \\ \rho w^2 + p \\ (\rho E + p)w \end{bmatrix}, \quad \mathbf{F}_v = C_1 \begin{bmatrix} 0 \\ \tau_{xx} \\ \tau_{xy} \\ \tau_{zx} \\ \tau_{xx}u + \tau_{xy}v + \tau_{zx}w - q_x \end{bmatrix}, \\
 \mathbf{G}_v = C_1 &\begin{bmatrix} 0 \\ \tau_{xy} \\ \tau_{yy} \\ \tau_{yz} \\ \tau_{xy}u + \tau_{yy}v + \tau_{yz}w - q_y \end{bmatrix}, \quad \mathbf{H}_v = C_1 \begin{bmatrix} 0 \\ \tau_{zx} \\ \tau_{yz} \\ \tau_{zz} \\ \tau_{zx}u + \tau_{yz}v + \tau_{zz}w - q_z \end{bmatrix}, \\
 \tau_{xx} &= \frac{2}{3}\mu \left(2\frac{\partial u}{\partial x} - \frac{\partial v}{\partial y} - \frac{\partial w}{\partial z} \right), \quad \tau_{xy} = \mu \left(\frac{\partial u}{\partial y} + \frac{\partial v}{\partial x} \right), \\
 \tau_{yy} &= \frac{2}{3}\mu \left(2\frac{\partial v}{\partial y} - \frac{\partial u}{\partial x} - \frac{\partial w}{\partial z} \right), \quad \tau_{yz} = \mu \left(\frac{\partial v}{\partial z} + \frac{\partial w}{\partial y} \right), \\
 \tau_{zz} &= \frac{2}{3}\mu \left(2\frac{\partial w}{\partial z} - \frac{\partial u}{\partial x} - \frac{\partial v}{\partial y} \right), \quad \tau_{zx} = \mu \left(\frac{\partial w}{\partial x} + \frac{\partial u}{\partial z} \right), \\
 E &= \frac{p}{\rho\beta} + \frac{1}{2} (u^2 + v^2), \quad p = \frac{\rho T}{\gamma C_2}, \\
 q_x &= \frac{-\mu}{\beta Pr C_2} \frac{\partial T}{\partial x}, \quad q_y = \frac{-\mu}{\beta Pr C_2} \frac{\partial T}{\partial y}, \quad q_z = \frac{-\mu}{\beta Pr C_2} \frac{\partial T}{\partial z},
 \end{aligned}$$

with M , Re and Pr being the Mach number, Reynolds number and the Prandtl number calculated from the reference parameters respectively, $\beta \equiv \gamma - 1$, $C_1 = 1/Re$ and $C_2 = M^2$. The lengths, velocities, density, pressure, temperature and viscosity are also normalized by the reference parameters \hat{L}_0 , \hat{u}_0 , $\hat{\rho}_0$, \hat{p}_0 , \hat{T}_0 , $\hat{\mu}_0^2$,

\widehat{T}_0 and $\widehat{\mu}_0$ respectively. The viscosity and the temperature are still related by Sutherland's Law, i. e., Eq.(2.4). Furthermore, if the speed of sound is chosen as the reference speed, the corresponding terms in the above equations can be modified similar to those in the two dimensional case. Next, the above terms are all expressed in terms of \mathbf{U} , U_x , U_y and U_z , i. e.,

$$\begin{aligned}
 \mathbf{F} &= \begin{bmatrix} U_2 \\ \frac{U_2^2}{U_1} - A_4 + \beta U_5 \\ \frac{U_2 U_3}{U_1} \\ \frac{U_2 U_4}{U_1} \\ \frac{\gamma U_2 U_5}{U_1} + U_2 A_4 \end{bmatrix}, \quad \mathbf{G} = \begin{bmatrix} U_3 \\ \frac{U_2 U_3}{U_1} \\ \frac{U_3^2}{U_1} - A_4 + \beta U_5 \\ \frac{U_3 U_4}{U_1} \\ \frac{\gamma U_3 U_5}{U_1} + U_3 A_4 \end{bmatrix}, \\
 \mathbf{H} &= \begin{bmatrix} U_4 \\ \frac{U_2 U_4}{U_1} \\ \frac{U_3 U_4}{U_1} \\ \frac{U_4^2}{U_1} - A_4 + \beta U_5 \\ \frac{\gamma U_4 U_5}{U_1} + U_4 A_4 \end{bmatrix}, \quad T = \frac{\gamma \text{Ma}^2 \beta}{U_1} \left(U_5 - \frac{A_4 U_1}{\beta} \right), \\
 \tau_{xx} &= \frac{2}{3} \mu \left[2 \left(\frac{1}{U_1} \frac{\partial U_2}{\partial x} - \frac{U_2}{U_1^2} \frac{\partial U_1}{\partial x} \right) - \left(\frac{1}{U_1} \frac{\partial U_3}{\partial y} - \frac{U_3}{U_1^2} \frac{\partial U_1}{\partial y} \right) \right. \\
 &\quad \left. - \left(\frac{1}{U_1} \frac{\partial U_4}{\partial z} - \frac{U_4}{U_1^2} \frac{\partial U_1}{\partial z} \right) \right], \\
 \tau_{xy} &= \frac{2}{3} \mu \left[\left(\frac{1}{U_1} \frac{\partial U_2}{\partial y} - \frac{U_2}{U_1^2} \frac{\partial U_1}{\partial y} \right) + \left(\frac{1}{U_1} \frac{\partial U_3}{\partial x} - \frac{U_3}{U_1^2} \frac{\partial U_1}{\partial x} \right) \right], \\
 \tau_{yy} &= \frac{2}{3} \mu \left[2 \left(\frac{1}{U_1} \frac{\partial U_3}{\partial y} - \frac{U_3}{U_1^2} \frac{\partial U_1}{\partial y} \right) - \left(\frac{1}{U_1} \frac{\partial U_2}{\partial x} - \frac{U_2}{U_1^2} \frac{\partial U_1}{\partial x} \right) \right. \\
 &\quad \left. - \left(\frac{1}{U_1} \frac{\partial U_4}{\partial z} - \frac{U_4}{U_1^2} \frac{\partial U_1}{\partial z} \right) \right], \\
 \tau_{yz} &= \frac{2}{3} \mu \left[\left(\frac{1}{U_1} \frac{\partial U_3}{\partial z} - \frac{U_3}{U_1^2} \frac{\partial U_1}{\partial z} \right) + \left(\frac{1}{U_1} \frac{\partial U_4}{\partial y} - \frac{U_4}{U_1^2} \frac{\partial U_1}{\partial y} \right) \right], \\
 \tau_{zz} &= \frac{2}{3} \mu \left[2 \left(\frac{1}{U_1} \frac{\partial U_4}{\partial z} - \frac{U_4}{U_1^2} \frac{\partial U_1}{\partial z} \right) - \left(\frac{1}{U_1} \frac{\partial U_3}{\partial y} - \frac{U_3}{U_1^2} \frac{\partial U_1}{\partial y} \right) \right. \\
 &\quad \left. - \left(\frac{1}{U_1} \frac{\partial U_2}{\partial x} - \frac{U_2}{U_1^2} \frac{\partial U_1}{\partial x} \right) \right], \\
 \tau_{zx} &= \frac{2}{3} \mu \left[\left(\frac{1}{U_1} \frac{\partial U_4}{\partial x} - \frac{U_4}{U_1^2} \frac{\partial U_1}{\partial x} \right) + \left(\frac{1}{U_1} \frac{\partial U_2}{\partial z} - \frac{U_2}{U_1^2} \frac{\partial U_1}{\partial z} \right) \right],
 \end{aligned}$$

where $A_4 = \beta \frac{U_2^2 + U_3^2 + U_4^2}{2U_1^2}$. Similarly, the Jacobian matrices, $\frac{\partial F}{\partial \mathbf{U}}$, $\frac{\partial G}{\partial \mathbf{U}}$, $\frac{\partial H}{\partial \mathbf{U}}$ and $\frac{\partial T}{\partial \mathbf{U}}$ will be used in the derivation of 3D CE/SE method and they are written as

$$\frac{\partial F}{\partial \mathbf{U}} = \begin{bmatrix} 0 & 1 & 0 & 0 & 0 \\ A_4 - \frac{U_2^2}{U_1^2} & (3 - \gamma) \frac{U_2}{U_1} & -\beta \frac{U_3}{U_1} & -\beta \frac{U_4}{U_1} & \beta \\ -\frac{U_2 U_3}{U_1^2} & \frac{U_3}{U_1} & \frac{U_2}{U_1} & 0 & 0 \\ -\frac{U_2 U_4}{U_1^2} & \frac{U_4}{U_1} & 0 & \frac{U_2}{U_1} & 0 \\ \frac{U_2}{U_1} A_5 & A_6 - \beta \frac{U_2^2}{U_1^2} & -\beta \frac{U_2 U_3}{U_1^2} & -\beta \frac{U_2 U_4}{U_1^2} & \gamma \frac{U_2}{U_1} \end{bmatrix},$$

$$\frac{\partial G}{\partial \mathbf{U}} = \begin{bmatrix} 0 & 0 & 1 & 0 & 0 \\ -\frac{U_2 U_3}{U_1^2} & \frac{U_3}{U_1} & \frac{U_2}{U_1} & 0 & 0 \\ A_4 - \frac{U_3^2}{U_1^2} & -\beta \frac{U_2}{U_1} & (3 - \gamma) \frac{U_3}{U_1} & -\beta \frac{U_4}{U_1} & \beta \\ -\frac{U_3 U_4}{U_1^2} & 0 & \frac{U_4}{U_1} & \frac{U_3}{U_1} & 0 \\ \frac{U_3}{U_1} A_5 & -\beta \frac{U_2 U_3}{U_1^2} & A_6 - \beta \frac{U_3^2}{U_1^2} & -\beta \frac{U_3 U_4}{U_1^2} & \gamma \frac{U_3}{U_1} \end{bmatrix},$$

$$\frac{\partial H}{\partial \mathbf{U}} = \begin{bmatrix} 0 & 0 & 0 & 1 & 0 \\ -\frac{U_2 U_4}{U_1^2} & \frac{U_4}{U_1} & 0 & \frac{U_2}{U_1} & 0 \\ -\frac{U_3 U_4}{U_1^2} & 0 & \frac{U_4}{U_1} & \frac{U_3}{U_1} & 0 \\ A_4 - \frac{U_4^2}{U_1^2} & -\beta \frac{U_2}{U_1} & -\beta \frac{U_3}{U_1} & (3 - \gamma) \frac{U_4}{U_1} & \beta \\ \frac{U_4}{U_1} A_5 & -\beta \frac{U_2 U_4}{U_1^2} & -\beta \frac{U_3 U_4}{U_1^2} & A_6 - \beta \frac{U_4^2}{U_1^2} & \gamma \frac{U_4}{U_1} \end{bmatrix},$$

$$\frac{\partial T}{\partial \mathbf{U}} = \frac{\gamma Ma^2 \beta}{U_1} \begin{bmatrix} -\frac{U_5}{U_1} + \frac{U_2^2 + U_3^2 + U_4^2}{U_1^2} & -\frac{U_2}{U_1^2} & -\frac{U_3}{U_1^2} & -\frac{U_4}{U_1^2} & 1 \end{bmatrix}, \quad (2.30)$$

where $A_4 = \beta \frac{U_2^2 + U_3^2 + U_4^2}{2U_1^2}$, $A_5 = \gamma \frac{U_5}{U_1} + \beta \frac{U_2^2 + U_3^2 + U_4^2}{U_1^2}$, $A_6 = \gamma \frac{U_5}{U_1} - \beta \frac{U_2^2 + U_3^2 + U_4^2}{2U_1^2}$.

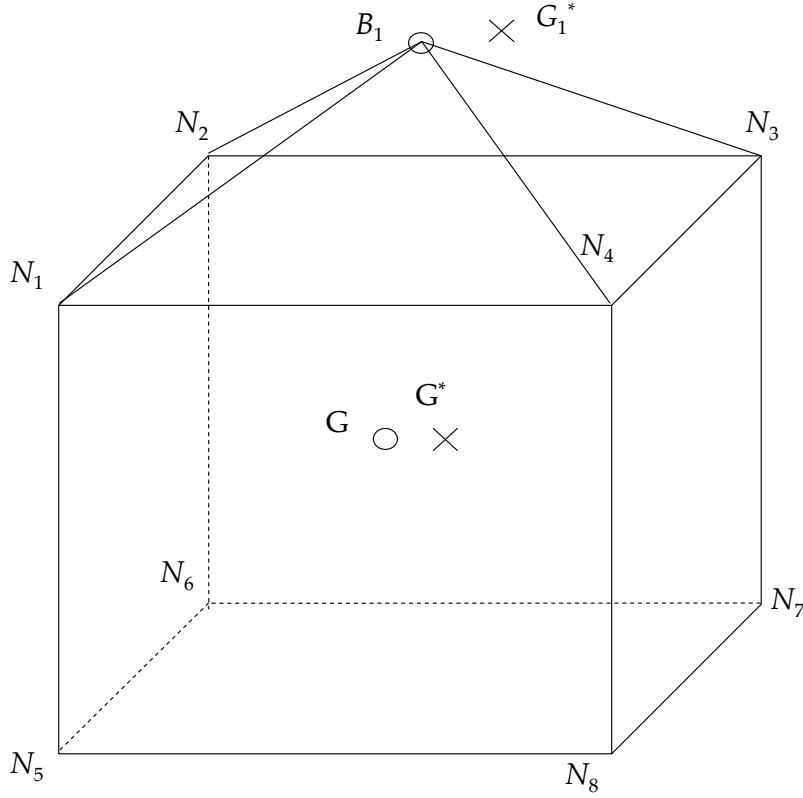


Figure 2.6: Typical hexahedron in spatial computational domain.

2.3.1 Definition of CE & SE in 3D

In this research, hexahedral mesh is used for the three dimensional calculation, so the computational domain is decomposed into non-overlapping hexahedrons. One typical element is shown in Figure 2.6. The open circles are the centroids of the hexahedral mesh and they help in constructing the CEs and SEs. The nodes of the elements are denoted as N_k for $k = 1 - 8$ and the centroids of the m -th neighboring elements are also denoted as B_i for $i = 1 - 6$. Furthermore, the centroid of this hexahedron is denoted as G and the solution point G^* is the centroid of the polyhedron $N_1N_2N_3N_4N_5N_6N_7N_8B_1B_2B_3B_4B_5B_6$, or in short denoted by $N_{1 \rightarrow 8}B_{1 \rightarrow 6}$. Similarly, G_m^* s are the centroids of m -th neighboring element. The cross in Figure 2.6 marks the centroid of the first neighboring element G_1^* .

Let $\mathbf{X} = (x, y, z, t)$ be a coordinate of a 4-dimensional Euclidean space \mathbf{E}_4 . After applying Gauss Divergence Theorem, Eq.(2.3) takes the form of Eq.(2.2), with $\mathbf{K} \equiv [F - F_v, G - G_v, H - H_v, \mathbf{U}]$. Hereafter, hyperplane in \mathbf{E}_4 is called

as hyperplane unless otherwise stated. Since the three dimensional CE and SE extend in the time dimension, they are bounded regions of hyperplanes and can be written in the form as

$$a_1x + a_2y + a_3z + a_4t + a_5 = 0 \quad (2.31)$$

with $a_1^2 + a_2^2 + a_3^2 + a_4^2 \neq 0$ and its unit normal \mathbf{n} is expressed as

$$\mathbf{n} = \pm \frac{(a_1, a_2, a_3, a_4)}{\sqrt{a_1^2 + a_2^2 + a_3^2 + a_4^2}}. \quad (2.32)$$

In the CE/SE method, two types of hyperplanes are normally used. The first type of hyperplane is formed by the extension of a volume in the three dimensional spatial domain in the time axis while the second type is created by a surface in the three dimensional spatial domain extending in the time axis.

Firstly, regarding the CE of G^* at n -th time level, $CE(G^*, n)$ for hexahedral mesh, its vertices are the space-time mesh points N_k , N'_k , B_i and B'_i for $k = 1 - 8$ and $i = 1 - 6$. It is the region bounded by the “top” face, the “bottom” face and the “side” faces. The “top” face $(\Xi^n)_{G^*}$ and the “bottom” face $(\Xi^{n-\frac{1}{2}})_{G^*}$ are the space-time hyperplanes formed by $N'_{1 \rightarrow 8}B'_{1 \rightarrow 6}$ and $N_{1 \rightarrow 8}B_{1 \rightarrow 6}$ respectively. They are analogue to $A'B'C'D'E'F'$ and $ABCDEF$ in [Figure 2.3](#) respectively. The superscripts represent the time level of the faces. These two faces belong to the first type of hyperplane. The “side” faces of $CE(G^*, n)$ are the extensions of triangles in time axis, which are formed by B_i and two vertices N_k adjacent to B_i for $i = 1 - 6$, such as $B_1N_3N_4B'_1N'_3N'_4$, $B_1N_1N_2B'_1N'_1N'_2$. They are analogue to $ABB'A'$ in [Figure 2.3](#). Obviously, they are the second type of hyperplane. In this CE, there are 24 triangles in total forming the “side” faces of $CE(G^*, n)$. For ease in further discussion, the “side” faces of $CE(G^*, n)$ are denoted as $(\Lambda_{i,l}^{n-\frac{1}{2}})_{G^*}$, which means the l th face formed with B_i extended from the $(n - 1/2)$ -th time level to n -th time level for $l = 1 - 4$ and $i = 1 - 6$.

Secondly, the SE of G^* at n th time level, $SE(G^*, n)$ also consists of $(\Xi^n)_{G^*}$ and $(\Gamma_j^n)_{G^*}$, which is the j -th hyperplane generated from the spatial triangles formed by G and the neighboring vertices N_k extending from $(n - 1/2)$ -th time level to $(n + 1/2)$ -th time level for $j = 1 - 12$, e. g., $GN_3N_7G_1''N_3''N_7''$. $(\Gamma_j^n)_{G^*}$ for $j = 1 - 12$ also belong to the second type of hyperplanes. Similar to the 2D formulation, for any location \mathbf{X} within $SE(G^*, n)$, the flow variables, $\boldsymbol{\phi}(\mathbf{X}) = \mathbf{U}(\mathbf{X}), F(\mathbf{X}), G(\mathbf{X})$ or $H(\mathbf{X})$, at this location can be written as

$$\boldsymbol{\phi}(\mathbf{X})_{G^*} = \boldsymbol{\phi}_{G^*} + \delta x (\boldsymbol{\phi}_x)_{G^*} + \delta y (\boldsymbol{\phi}_y)_{G^*} + \delta z (\boldsymbol{\phi}_z)_{G^*} + \delta t (\boldsymbol{\phi}_t)_{G^*}, \quad (2.33)$$

where $\delta x = (x - x_{G^*})$, $\delta y = (y - y_{G^*})$, $\delta z = (z - z_{G^*})$, $\delta t = (t - t^n)$, and the subscripts x, y, z denote the spatial gradients in x, y, z direction respectively. Furthermore, according to Eq.(2.5), these gradients can be calculated by the chain rule as

$$\begin{aligned} (\boldsymbol{\phi}_x)_{G^*} &= \frac{\partial \boldsymbol{\phi}}{\partial \mathbf{U}} (\mathbf{U}_x)_{G^*}, & (\boldsymbol{\phi}_y)_{G^*} &= \frac{\partial \boldsymbol{\phi}}{\partial \mathbf{U}} (\mathbf{U}_y)_{G^*}, \\ (\boldsymbol{\phi}_z)_{G^*} &= \frac{\partial \boldsymbol{\phi}}{\partial \mathbf{U}} (\mathbf{U}_z)_{G^*}, & (\boldsymbol{\phi}_t)_{G^*} &= \frac{\partial \boldsymbol{\phi}}{\partial \mathbf{U}} (\mathbf{U}_t)_{G^*}. \end{aligned} \quad (2.34)$$

Moreover, the viscous terms F_v, G_v and H_v in Eq.(2.3) is approximated by $F_v(\mathbf{X})_{G^*}, G_v(\mathbf{X})_{G^*}$ and $H_v(\mathbf{X})_{G^*}$ respectively and are also assumed to be constant within $SE(G^*, n)$. Thus, the N-S equations inside $SE(G^*, n)$ can be expressed as,

$$(\mathbf{U}_t)_{G^*} = - (F_x)_{G^*} - (G_y)_{G^*} - (H_z)_{G^*}. \quad (2.35)$$

Moreover, \mathbf{K} at \mathbf{X} within $SE(G^*, n)$ are approximated by \mathbf{K}^+ , i. e.,

$$\mathbf{K}^+(\mathbf{X})_{G^*} \equiv \begin{bmatrix} F(\mathbf{X})_{G^*} - F_v(\mathbf{X})_{G^*}, G(\mathbf{X})_{G^*} - G_v(\mathbf{X})_{G^*}, \\ H(\mathbf{X})_{G^*} - H_v(\mathbf{X})_{G^*}, \mathbf{U}(\mathbf{X})_{G^*} \end{bmatrix}, \quad (2.36)$$

where $F(\mathbf{X})_{G^*} - F_v(\mathbf{X})_{G^*}$ is the approximated $F - F_v$ at location \mathbf{X} by applying Taylor expansion at solution point G^* and similar interpretation can be

applied to $G(\mathbf{X})_{G^*} - G_v(\mathbf{X})_{G^*}$, $H(\mathbf{X})_{G^*} - H_v(\mathbf{X})_{G^*}$ and $\mathbf{U}(\mathbf{X})_{G^*}$. Thus, all the approximated flux and flow variables can be expressed in terms of the independent variables, \mathbf{U} , \mathbf{U}_x , \mathbf{U}_y and \mathbf{U}_z , whose updating will be discussed in the next section.

2.3.2 Time Marching of Solution in 3D CE/SE Method

One can notice that according to aforementioned definitions, the CEs are bounded by SEs in \mathbf{E}_4 . In other words, part of $\left(\Lambda_{i,l}^{n-\frac{1}{2}}\right)_{G^*}$ overlaps with $\left(\Gamma_j^{n-\frac{1}{2}}\right)_{G_i^*}$ for $i = 1 - 6$. The basic CEs $CE_i(G^*, n)$ for $i = 1 - 6$ combine to form $CE(G^*, n)$ in the evaluation of flux. Moreover, the "bottom" face of i -th basic CE is denoted as $\left(\Xi_i^{n-\frac{1}{2}}\right)_{G^*}$. Similar to 2D formulation, the evaluation of flux leaving $\left(\Xi_i^{n-\frac{1}{2}}\right)_{G_i^*}$ and $\left(\Lambda_{i,l}^{n-\frac{1}{2}}\right)_{G^*}$ are assigned to $SE(G_i^*, n - \frac{1}{2})$ for $i = 1 - 6$ and $l = 1 - 4$, while that leaving the "top" face $(\Xi^n)_{G^*}$ is still assigned to $SE(G^*, n)$. With the help of Eq.(2.2), Eq.(2.33) to Eq.(2.36), $\mathbf{U}_{G^*}^n$ can be expressed in terms of $\mathbf{U}_{G_i^*}^n$, $(\mathbf{U}_x)_{G_i^*}^n$, $(\mathbf{U}_y)_{G_i^*}^n$ and $(\mathbf{U}_z)_{G_i^*}^n$ for $i = 1 - 6$.

Calculation of \mathbf{U} (3D)

Since the fluxes passing through interfaces between $CE_i(G^*, n)$ cancel out each other, only the fluxes leaving its external faces are taken into account. For each $CE_i(G^*, n)$, the flux leaving through the external face, $\mathbf{T}_i^{n-\frac{1}{2}}$ can be written as

$$\mathbf{T}_i^{n-\frac{1}{2}} = \mathbf{T}_{\Xi_i} + \mathbf{T}_{\Lambda}, \quad (2.37)$$

where

$$\begin{aligned} \mathbf{T}_{\Xi_i} &= \mathbf{K}^+(\mathbf{X}_i)_{G_i^*} \cdot \mathbf{S}_i, \\ \mathbf{T}_{\Lambda} &= \sum_{l=1}^4 \mathbf{K}^+(\mathbf{X}_{i,l})_{G_i^*} \cdot \mathbf{S}_{i,l}, \end{aligned} \quad (2.38)$$

\mathbf{X}_i and $\mathbf{X}_{i,l}$ are the centroids of $\left(\Xi_i^{n-\frac{1}{2}}\right)_{G^*}$ and $\left(\Lambda_{i,l}^{n-\frac{1}{2}}\right)_{G^*}$ respectively, $\mathbf{S}_i = (0, 0, 0, -V_i)$ with V_i being the volume of $\left(\Xi_i^{n-\frac{1}{2}}\right)_{G^*}$, $\mathbf{S}_{i,l} = (x_{c,i,l}, y_{c,i,l}, z_{c,i,l}, 0)$ with $(x_{c,i,l}, y_{c,i,l}, z_{c,i,l})$ being the spatial area vector of $\left(\Lambda_{i,l}^{n-\frac{1}{2}}\right)_{G^*}$. $\forall i$, $\mathbf{K}^+(\mathbf{X}_i)_{G_i^*}$ can be calculated from Eq.(2.36). On the other hand, the flux leaving the ‘‘top’’ face of $CE(G^*, n)$, $\mathbf{r}_{G^*}^n$ can be expressed as

$$\mathbf{r}_{G^*}^n = \mathbf{K}^+(\mathbf{X}_t)_{G^*} \cdot \mathbf{S}_t = \mathbf{U}_{G^*}^n \cdot V, \quad (2.39)$$

where \mathbf{X}_t is the centroid of $(\Xi^n)_{G^*}$, $\mathbf{S}_t = (0, 0, 0, V)$ and V is the spatial volume of $(\Xi^n)_{G^*}$. Therefore, according to Eq.(2.2), the total flux leaving $CE(G^*, n)$ is canceled, i. e.,

$$\mathbf{r}_{G^*}^n + \sum_{i=1}^6 \mathbf{r}_i^{n-\frac{1}{2}} = 0, \quad (2.40)$$

Thus,

$$\mathbf{U}_{G^*}^n = -\frac{1}{V} \sum_{i=1}^6 \mathbf{r}_i^{n-\frac{1}{2}}. \quad (2.41)$$

Calculation of U_x , U_y and U_z

Yen et al. (2006) further extended Simplified Courant Number Insensitive scheme (SCNIS) to the three dimensional manner, which is adopted in the present code for the evaluation of spatial gradient $(\mathbf{U}_x)_{G_i^*}^n$, $(\mathbf{U}_y)_{G_i^*}^n$ and $(\mathbf{U}_z)_{G_i^*}^n$ due to the reasons mentioned in 2D formulation. The numerical and analytical domain of dependence are now extended into the three dimensional geometries, which are shown in Figure 2.7. The numerical domain of dependence is an octahedron formed by G_i^* for $i = 1 - 6$ and the analytical one is the sphere of radius $\frac{c\Delta t}{2}$ centered at $\mathbf{R} = \left(-\frac{u\Delta t}{2}, -\frac{v\Delta t}{2}, -\frac{w\Delta t}{2}\right)$ with G^* as the origin. Here $c = \sqrt{\gamma p/\rho}$ is the local sound speed. The stability criterion is the still same as that for the two dimensional case, i. e., the solution is stable if the analytical domain of dependence falls inside the numerical one completely.

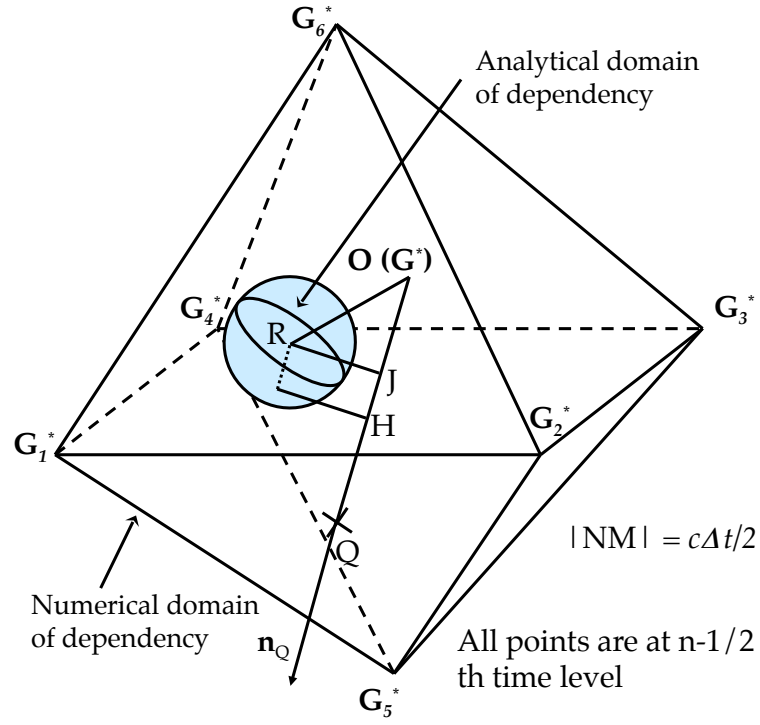


Figure 2.7: 3D Numerical and analytical domain of dependency.

Without loss of generality, the flow speed u , v and w are assumed to be positive in the discussion. Consider the plane $G_1^*G_2^*G_3^*$ first, the above criterion is equivalent to

$$\sigma_1 = \frac{|G^*J| + |JH|}{|G^*Q|} = \frac{\Delta t \mathbf{R} \cdot \mathbf{n}_Q + c}{2 |G^*Q|}, \quad (2.42)$$

where Q is the projection of G^* on the plane $G_1^*G_2^*G_3^*$ and \mathbf{n}_Q is the outward normal of the plane $G_1^*G_2^*G_3^*$. In a similar manner, σ_2 to σ_6 can be determined for the other planes bounded by G_i^* , $i = 2 - 6$. Eventually, σ is set by

$$\sigma = \max(\sigma_1, \sigma_2, \sigma_3, \sigma_4, \sigma_5, \sigma_6). \quad (2.43)$$

Same as the procedure in the two dimensional case, the locations for calculating gradient, P_i can then be determined by Eq.(2.21) for $i = 1 - 6$. The centroid of the octahedron formed by $P_1P_2P_3P_4P_5P_6$ in general does not coincide with the solution point G^* , so it is translated to a new position

$\underline{P}_1\underline{P}_2\underline{P}_3\underline{P}_4\underline{P}_5\underline{P}_6$ such that the centroid at this new position coincides with G^* .

Therefore, for $i = 1 - 6$,

$$\underline{P}_i = P_i + (G^* - P_c), \tag{2.44}$$

where P_c is the centroid of the octahedron $P_1P_2P_3P_4P_5P_6$. Then, the solution vector of \underline{P}_i at n -th time level can be written as

$$\mathbf{u}_{\underline{P}_i}^n = \mathbf{u}_{G_i^*}^{n-\frac{1}{2}} + \delta x_{\underline{P}_i} (\mathbf{u}_x)_{G_i^*}^{n-\frac{1}{2}} + \delta y_{\underline{P}_i} (\mathbf{u}_y)_{G_i^*}^{n-\frac{1}{2}} + \delta z_{\underline{P}_i} (\mathbf{u}_z)_{G_i^*}^{n-\frac{1}{2}} + \frac{\Delta t}{2} (\mathbf{u}_t)_{G_i^*}^{n-\frac{1}{2}}, \tag{2.45}$$

where $\delta x_{\underline{P}_i} = x_{\underline{P}_i} - x_{G_i^*}$, $\delta y_{\underline{P}_i} = y_{\underline{P}_i} - y_{G_i^*}$ and $\delta z_{\underline{P}_i} = z_{\underline{P}_i} - z_{G_i^*}$. Then a central differencing scheme as described below is applied to calculate the spatial gradient \mathbf{u}_x^n , \mathbf{u}_y^n and \mathbf{u}_z^n . For each N_k , there are 3 \underline{P}_i s connecting to it and these \underline{P}_i s are denoted as $\underline{P}_{k,j}$ for $j = 1, 2, 3$ in order to simplify the expression. Furthermore, $(\mathbf{u}_x^k)_{G^*}^n$, $(\mathbf{u}_y^k)_{G^*}^n$ and $(\mathbf{u}_z^k)_{G^*}^n$ are defined as

$$(\mathbf{u}_x^k)_{G^*}^n = \frac{\Delta_x^k}{\Delta^k}, \quad (\mathbf{u}_y^k)_{G^*}^n = \frac{\Delta_y^k}{\Delta^k}, \quad (\mathbf{u}_z^k)_{G^*}^n = \frac{\Delta_z^k}{\Delta^k}, \tag{2.46}$$

where

$$\Delta^k = \begin{vmatrix} \delta x_G^1 & \delta y_G^1 & \delta z_G^1 \\ \delta x_G^2 & \delta y_G^2 & \delta z_G^2 \\ \delta x_G^3 & \delta y_G^3 & \delta z_G^3 \end{vmatrix}, \quad \Delta_x^k = \begin{vmatrix} \delta \mathbf{u}_G^1 & \delta y_G^1 & \delta z_G^1 \\ \delta \mathbf{u}_G^2 & \delta y_G^2 & \delta z_G^2 \\ \delta \mathbf{u}_G^3 & \delta y_G^3 & \delta z_G^3 \end{vmatrix},$$

$$\Delta_y^k = \begin{vmatrix} \delta x_G^1 & \delta \mathbf{u}_G^1 & \delta z_G^1 \\ \delta x_G^2 & \delta \mathbf{u}_G^2 & \delta z_G^2 \\ \delta x_G^3 & \delta \mathbf{u}_G^3 & \delta z_G^3 \end{vmatrix}, \quad \Delta_z^k = \begin{vmatrix} \delta x_G^1 & \delta y_G^1 & \delta \mathbf{u}_G^1 \\ \delta x_G^2 & \delta y_G^2 & \delta \mathbf{u}_G^2 \\ \delta x_G^3 & \delta y_G^3 & \delta \mathbf{u}_G^3 \end{vmatrix},$$

and $\delta x_G^j = x_{\underline{P}_{k,j}} - x_{G^*}$, $\delta y_G^j = y_{\underline{P}_{k,j}} - y_{G^*}$, $\delta z_G^j = z_{\underline{P}_{k,j}} - z_{G^*}$, $\delta \mathbf{u}_G^j = \mathbf{u}_{\underline{P}_{k,j}}^n - \mathbf{u}_{G^*}^n$ for $j = 1, 2, 3$. $(\mathbf{u}_x^k)_{G^*}^n$, $(\mathbf{u}_y^k)_{G^*}^n$ and $(\mathbf{u}_z^k)_{G^*}^n$ actually represent the spatial

gradients with respect to the solution point G^* and the corresponding $\underline{P}_{k,m}$. Finally, the spatial gradients at n th time level are given by

$$(\mathbf{u}_x)_{G^*}^n = \frac{\sum_{k=1}^8 (\mathbf{W}_k)^\alpha (\mathbf{u}_x^i)_{G^*}^n}{\sum_{k=1}^3 (\mathbf{W}_k)^\alpha}, \quad (\mathbf{u}_y)_{G^*}^n = \frac{\sum_{k=1}^8 (\mathbf{W}_k)^\alpha (\mathbf{u}_y^i)_{G^*}^n}{\sum_{k=1}^3 (\mathbf{W}_k)^\alpha}, \quad (2.47)$$

and

$$(\mathbf{u}_z)_{G^*}^n = \frac{\sum_{k=1}^8 (\mathbf{W}_k)^\alpha (\mathbf{u}_z^i)_{G^*}^n}{\sum_{k=1}^3 (\mathbf{W}_k)^\alpha}, \quad (2.48)$$

where $\alpha \geq 0$, \mathbf{W}_k is the product of $\zeta_1, \zeta_2, \dots, \zeta_8$ excluding ζ_k and

$$\zeta_k = \sqrt{\left[(\mathbf{u}_x^k)_{G^*}^n \right]^2 + \left[(\mathbf{u}_y^k)_{G^*}^n \right]^2 + \left[(\mathbf{u}_z^k)_{G^*}^n \right]^2}.$$

2.4 TREATMENT OF BOUNDARY CONDITION IN CE/SE METHOD

Undoubtedly, boundary condition is a very important issue in every field of numerical simulation. While the physical domain has nearly no bounds, the computational resources cannot afford to simulate such a nearly infinite region. In every simulation, only the incidents in a very small portion of physical domain are investigated. Boundary condition then provides the information of the environment outside the simulated region to the calculation. Furthermore, it is also a mean to express the physical boundary and its behavior into the mathematical equations used in the simulation e. g., the solid boundary. Wrong boundary condition can be fatal in the calculation as it provides incorrect information to the calculation causing completely different results. Thus, it is very important for the boundary condition to be consistent with the physics.

One of the most popular method adopted in DAS is the characteristic-based technique e. g., [Poinsot & Lele \(1992\)](#) and [Colonius et al. \(1993\)](#). This

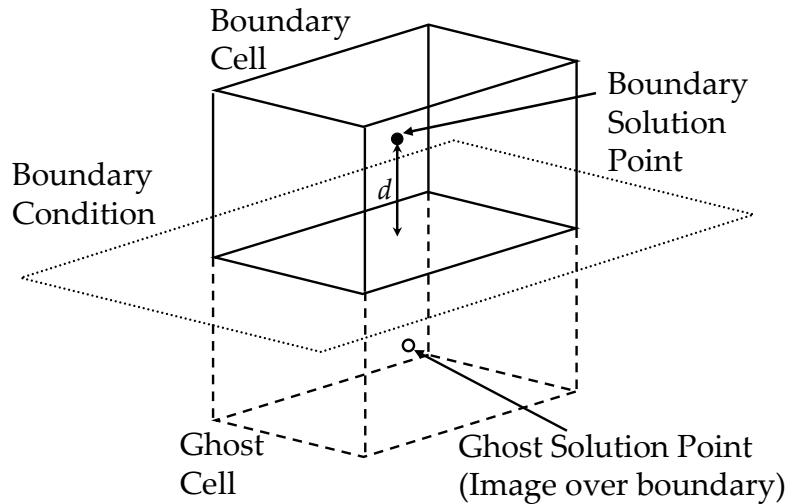


Figure 2.8: Boundary cell and ghost cell.

method derives the boundary conditions for the algorithm from the physical laws i. e., N-S equations, so as to reveal the true effect of a physical boundary in numerical simulations. A characteristic analysis is first applied on the N-S equations to recast the system of governing equations with the characteristic waves. The amplitudes of these waves (both incoming and outgoing) are then determined from the flow near the boundary. Eventually, the flow variables at the boundary are estimated by substituting the amplitudes of these waves back to the recasted systems of N-S equations. Therefore, this approach is consistent with the physical law, but it is very complicated in the implementation especially for multi-dimensional cases.

On the contrary, the implementation of boundary condition in CE/SE method is very simple compared with the characteristic-based technique. The numerical boundary condition in CE/SE method usually adopts the ghost cell approach, in which a ghost cell is created by mirroring the boundary cell at the boundary interface as shown in [Figure 2.8](#). Based on the type of boundary condition, appropriate solution values together with their spatial gradients are then assigned to the solution point of the ghost cell for the calculation of flux. One should note that no complicated recasting of the governing equations like in the characteristic-based technique is involved. These have been discussed

in details by Loh (2003) and Chang (2006), whose literature also reveals its consistency with the physical law despite its simplicity.

In the following sections, the implementations in CE/SE method are discussed in the three dimensional situation as the concept is the same as that in the two dimensional case. Hereafter unless stated otherwise, the subscript 'b' and 'g' denote the boundary cell and ghost cell respectively.

2.4.1 Non-Reflecting Boundary Condition (NRBC)

Non-reflecting boundary condition (NRBC) is one of the most important conditions as it determines the amount of the non-physical reflection at the boundary to the environment, which can contaminate the solution in the interested domain seriously if it is too excessive. In CE/SE method, there are mainly two types of NRBC and Loh (2003) provided a rigorous mathematical validation of these implementation.

Type I NRBC (NRBC-I)

Consider Figure 2.8 and the flow exits at the boundary. The solution vector \mathbf{U} and its spatial derivatives \mathbf{U}_x , \mathbf{U}_y and \mathbf{U}_z are set by

$$\mathbf{U}_g = \mathbf{U}_b, \quad (2.49)$$

and

$$(\mathbf{U}_x)_g = (\mathbf{U}_x)_b, (\mathbf{U}_y)_g = (\mathbf{U}_y)_b, (\mathbf{U}_z)_g = (\mathbf{U}_z)_b. \quad (2.50)$$

This type of NRBC is very suitable to the supersonic flow simulation as shown by Loh, Himansu & Wang (2001), Loh (2005), Loh & Hultgren (2006). This is mainly because in such aeroacoustic problem, the propagation speed of the information, mainly acoustics, is slower than the flow speed, which implies the information never goes back to the domain interior once it exits

at the NRBC. In other words, the simulation of this supersonic flow does not require the acoustic information outside the domain whereas the above formulation truly reflects this physical requirement.

Type II NRBC (NRBC-II)

On the contrary, in the subsonic flow simulation, the acoustic information outside the boundary is very essential to the computational domain as the propagation speed of acoustic information is higher than the characteristic flow speed. The acoustic information downstream can influence the upstream region. Since the external information is blocked by the use of Type I NRBC, the mean of \mathbf{U} may be shifted. In order to solve this problem, a variant, Type II of NRBC, is applied and is implemented by setting

$$\rho_g = \rho_o, p_g = p_o, u_g = u_b, v_g = v_b, w_g = w_b \quad (2.51)$$

and the spatial gradient is still set by Eq.(2.50).

2.4.2 Slip Wall Boundary Condition (SLWBC)

Slip wall boundary condition is commonly applied in the flow with sliding solid wall surface. Wang & Chang (1999) proposed this condition as the symmetry condition at the interface in CE/SE method and is done by the following equations. Without loss of generality, the normal of the slip wall is assumed pointing to z axis. This boundary condition is set by

$$\begin{aligned} \rho_g &= \rho_b, p_g = p_{xb}, u_g = u_b, v_g = v_b, w_g = -w_b, \\ \rho_{xg} &= \rho_{xb}, p_{xg} = p_{xb}, u_{xg} = u_{xb}, v_{xg} = v_{xb}, w_{xg} = -w_{xb}, \\ \rho_{yg} &= \rho_{yb}, p_{yg} = p_{yb}, u_{yg} = u_{yb}, v_{yg} = v_{yb}, w_{yg} = -w_{yb}, \\ \rho_{zg} &= -\rho_{zb}, p_{zg} = -p_{zb}, u_{zg} = -u_{zb}, v_{zg} = -v_{zb}, w_{zg} = w_{zb}. \end{aligned} \quad (2.52)$$

2.4.3 No-slip Wall Boundary Condition (NSWBC)

No-slip wall boundary condition always represents the no-slip solid wall boundary in the N-S simulation. There are various types of no-slip wall boundary conditions in the CE/SE method such as unified wall boundary condition (NSWBC-U) developed by [Chang et al. \(2001\)](#). In this research, near wall approach (NSWBC-NW) introduced by [Chang \(2007\)](#) is employed in simulation and it is expressed as

$$\rho_g = \rho_o, p_g = p_o, u_g = u_w, v_g = v_w, w_g = w_w, \quad (2.53)$$

where u_w, v_w and w_w are the velocities at the wall. As the distance of the solution point to the boundary, $d \rightarrow 0$, $(u, v, w) \rightarrow (u_w, v_w, w_w)$. Thus, this is an approximation to the actual no-slip wall in the physical sense. One should note that NSWBC-NW is the isothermal wall condition.

2.5 TURBULENCE MODELING

Dynamics of turbulent flow is still a popular research area in CFD because literally all flows of practical interest are turbulent in nature. In general, there are two approaches simulating these flows. The first one is the direct numerical simulation (DNS), which solves the N-S equations directly using a sufficiently fine mesh to resolve all the involved scales of energy in the flow, e. g., from the finest turbulence ($O(10^{-6})$) to the very large-scale vortical structures ($O(1)$). Therefore, the computational resources required are extremely high. Even with the advanced computer technology nowadays, it is still too demanding to perform a three dimensional DNS for real flows with low Reynolds number, not to mention the case with high Reynolds number in which the required mesh is much finer than the former.

On the contrary, the second strategy adopts modeling of the effects of turbulence, which reduces the required computational resources. Reynolds-averaged Navier-Stokes (RANS) and Large Eddy Simulation (LES) are two common types of turbulence modeling. The former studies the time-averaged behavior of the flow and introduces the Reynolds stresses for estimating the turbulent stresses through modeling such as Boussinesq hypothesis, Reynolds stress model (RSM). While the model of Boussinesq's type may not yield accurate results in resolving multiple-scale aeroacoustic problem, the model of RSM type requires lots of resources to solve such problem. Furthermore, it is important to check whether such assumed model is compatible with the actual flows or not, which may be complicated for general application in aeroacoustics. Thus, RANS is not chosen in this research.

The LES investigates only large coherent structures in the flows while neglecting smallest eddies in the flows. In this methodology, the flow variables are decomposed into two parts

$$f = \tilde{f} + f', \quad (2.54)$$

where f , \tilde{f} and f' are the unfiltered, filtered and unresolved flow variables respectively. Using these variables, a set of filtered N-S equations capable of resolving the energy fluctuations down to the Kolmogorov scale can be obtained. All other unresolved scales are represented by a subgrid scale model and believed to have little influences on the large, resolved fluid motions. This strategy is supported by the fact that the finest scale of energy does not affect the large-scale coherent structures strongly as pointed out by Reynolds (1989). Through a series of priori testings between DNS and LES models, he found that their results on the statistical structures (usually large-scale structures) in the flow were very similar, though little correlation was found between the unresolved scales.

In actual implementation, the dissipations of energy in all unresolved scales are represented by adding a turbulent dissipation to the original viscous

dissipation through the application of subgrid scale (SGS) model. Smagorinsky Turbulence Model (Smagorinsky (1963)) is one such classic SGS model. It uses an adhoc constant parameter to estimate the turbulent dissipation of the mesh, but this may not be good for all cases. For instance, it cannot correctly predict the turbulent fields in rotating flows, flows near wall region etc. as indicated by Germano et al. (1991). Since it is not the methodology adopted in the present study, they will not be covered in details here. The adopted approach of turbulence modeling is Monotonically Integrated Large Eddy Simulation (MILES), which was first purposed by Boris et al. (1992).

2.5.1 MILES Approach

MILES relies on the numerical dissipation to mimic the turbulent dissipation in the flows. No SGS model is needed in this model, so it further reduces the required resources. Various researches show that this is a good approach to tackle the turbulent simulations by producing excellent agreement with the experimental results. Fureby (2002) applied this model to study the free shear jet ($Re = 8.5 \times 10^4 \sim 2.2 \times 10^5$) and channel flow ($Re \sim 10^4$) and reported that the key aerodynamic fields including the turbulent velocity fluctuations were correctly captured as compared with experiments and DNS. Larchevêque et al. (2003) further extended its application to investigate the aeroacoustics of compressible turbulent flow past a backward facing steps. Their numerical results showed little differences on the large coherent vortical structures generated at the cavity when compared with the existing experimental and LES results. The agreement in the predicted velocity and Reynolds stresses were very good too. Furthermore, Loh, Chang, Wang & Jorgenson (2001) studied the gap noise of automobile body using MILES approach in CE/SE method and correctly captured the resonant frequency of the flow. All these indicate that MILES is a good alternative to the conventional LES model for investigating the aeroacoustic of flow problems.

However, one has to note that not all numerical schemes can accommodate MILES. The suitable scheme must possess the five properties, i. e., global conservations, monotonicity, positivity, causality and locality. Global conservation ensures that the total quantities are preserved over the computational domain independent of the adopted integration scheme. Monotonicity means that the scheme does not bring up non-physical oscillation of density except Gibbs phenomenon. Positivity indicates that the scheme does not have negative density. Causality means that when a fluid element is convected from location A to location B, its path must be continuous between A and B. Finally, locality ensures no non-physical action is induced at a short distance as in the real world the region that the fluid action are limited to a small region. When a numerical method contains all the above properties, MILES can then be adopted to this method. [Loh & Hultgren \(2006\)](#) have already demonstrated that CE/SE method is one such scheme. Thus, the MILES approach is adopted in this research.

2.5.2 *Wall Modeling*

Since the mesh requirement of the LES is still very demanding in terms of the computational resources, wall model, which accommodates the viscous effect happening at the near wall region, is applied to further reduce the mesh requirement. This is done by introducing the addition of wall shear and its heat dissipation to the viscous terms in the N-S equations, which is only applicable in the region adjacent to the wall. Region further away from the wall does not need the wall model. This wall modeling is implemented as a new boundary condition in the present code, which has not been attempted in the CE/SE method.

Denoting τ_w and q_w as the wall shear and the heat flux due to the turbulence modeling through wall, the definition of F_v , G_v and H_v can then be modified to

$$\begin{aligned}
 F_v &= \frac{1}{Re} \begin{bmatrix} 0 \\ \tau_{xx} \\ \tau_{xy} + \tau_{w,y} \\ \tau_{zx} + \tau_{w,z} \\ \tau_{xx}u + (\tau_{xy} + \tau_{w,y})v + (\tau_{zx} + \tau_{w,z})w - q_x - q_{wx} \end{bmatrix}, \\
 G_v &= \frac{1}{Re} \begin{bmatrix} 0 \\ \tau_{xy} + \tau_{w,x} \\ \tau_{yy} \\ \tau_{yz} + \tau_{w,z} \\ (\tau_{xy} + \tau_{w,x})u + \tau_{yy}v + (\tau_{yz} + \tau_{w,z})w - q_y - q_{wy} \end{bmatrix}, \\
 H_v &= \frac{1}{Re} \begin{bmatrix} 0 \\ \tau_{zx} + \tau_{w,x} \\ \tau_{yz} + \tau_{w,y} \\ \tau_{zz} \\ (\tau_{zx} + \tau_{w,x})u + (\tau_{yz} + \tau_{w,y})v + \tau_{zz}w - q_z - q_{wz} \end{bmatrix},
 \end{aligned} \tag{2.55}$$

where the subscripts x , y , z of τ_w and q_w represent their component in the x -, y - and z - direction respectively. The next step is to evaluate τ_w and q_w and this is done by inverting the classical log law profile with compressibility correction for the cell nearest to wall. This correction is achieved by the Van Driest's transformation on velocity profile. [Fernholz & Finley \(1980\)](#) showed that the incompressible log law profile is retained by using Van Driest's Transformation on the velocity profile. [Huang et al. \(1993\)](#) further extended this idea to a general approach in constructing the mean velocity profiles for

compressible turbulent boundary layer and got satisfactory results compared with DNS. The theoretical background and procedure are outlined below.

Firstly, according to [Huang & Coleman \(1994\)](#), the convection can be neglected and the shear stress is assumed to be equal to the wall shear stress near the solid wall. Without loss of generality, assume that the wall normal direction is y axis. The energy equation can then be integrated with respect to y and gives

$$\hat{q} = \hat{q}_w + \hat{u}\hat{\tau}_w, \quad (2.56)$$

where $\hat{q} = -(\hat{\mu}_t \hat{c}_p / Pr_t) (\partial \hat{T} / \partial \hat{y})$ and $\hat{\tau}_w = \hat{\mu}_t (\partial \hat{u} / \partial \hat{y})$. Thus,

$$\hat{q}_w = -(\hat{\mu}_t \hat{c}_p / Pr_t) (\partial \hat{T} / \partial \hat{y}) - \hat{u} \hat{\mu}_t (\partial \hat{u} / \partial \hat{y}). \quad (2.57)$$

Before further discussion, $M_\tau = \frac{\hat{u}_\tau}{\hat{c}_w} = \frac{u_\tau}{c_w}$ and $B_q = \frac{\hat{q}_w}{\hat{\rho}_w \hat{c}_p \hat{u}_\tau \hat{T}_w}$ are defined, where $\hat{c}_w = \sqrt{\beta \hat{c}_p \hat{T}_w}$ is the speed of sound in air at wall, $\hat{\rho}_w$ is the density of air at wall, $\hat{u}_\tau = \sqrt{\hat{\tau}_w / \hat{\rho}_w}$ is the friction velocity, \hat{T}_w is the wall temperature and $\beta \equiv \gamma - 1$. Furthermore, another scale is introduced in describing the behavior of turbulent boundary layer, i. e., the wall unit $y^+ = \hat{y} \hat{\rho}_w \hat{u}_\tau / \hat{\mu}_w = y \rho_w u_\tau Re / \mu_w$, $u^+ = \hat{u} / \hat{u}_\tau = u / u_\tau$ and $T^+ = T / T_w$.

The Van Driest law of wall for compressible flow can then be written as

$$\frac{du^+}{dy^+} = \frac{(\hat{\rho}_w / \hat{\rho}_{av})^{0.5}}{\kappa y^+}, \quad (2.58)$$

and

$$\frac{dT^+}{dy^+} = - \left(B_q + \beta u^+ M_\tau^2 \right) Pr_t \frac{(\hat{\rho}_w / \hat{\rho}_{av})^{0.5}}{\kappa y^+}, \quad (2.59)$$

where $\hat{\rho}_{av}$ is the local mean value of density, Pr_t is the turbulent Prandtl number taken as 0.9, and κ is the von Karman constant taken as 0.41. Combining Eq.(2.58) and Eq.(2.59), then integrating them with respect to y^+ yields

$$T^+ = C_w - Pr_t B_q u^+ - \frac{1}{2} Pr_t \beta u^+ M_\tau^2, \quad (2.60)$$

and

$$u_{vd}^+ = \frac{1}{\kappa} \ln y^+ + C, \quad (2.61)$$

where $C_w = 1$ and $C = 5.0$. The Van Driest's transformation is given by

$$u_{vd}^+ = \int \left(\frac{\rho}{\rho_w} \right)^{\frac{1}{2}} du^+ \approx \sqrt{\hat{D}_1} \left[\sin^{-1} \left(\frac{\hat{D}_2 + u^+}{\hat{D}_3} \right) - \sin^{-1} \left(\frac{\hat{D}_2}{\hat{D}_3} \right) \right], \quad (2.62)$$

where $\hat{D}_1 = \frac{2\hat{c}_p \hat{T}_w}{Pr_t \hat{u}_\tau^2} = \frac{2\hat{c}_w^2}{(\gamma-1)Pr_t \hat{u}_\tau^2}$, $\hat{D}_2 = \frac{\hat{q}_w}{\hat{\tau}_w \hat{u}_\tau} = \frac{\hat{q}_w}{\hat{\rho}_w \hat{u}_\tau^3}$, $\hat{D}_3 = \frac{1}{\hat{u}_\tau} \sqrt{\hat{D}_1 + \hat{D}_2^2}$. Applying the original reference scales as in Section 2.2, Eq.(2.57), Eq.(2.60) and Eq.(2.61) become

$$q_w = q - \beta u \rho_w u_\tau^2 Pr Re M^2, \quad (2.63)$$

$$T = T_w - Pr_t \frac{q_w}{\tau_w} \frac{u}{Pr Re} - \frac{1}{2} Pr_t \beta u^2 M^2, \quad (2.64)$$

$$u_{vd} \approx \sqrt{D_1} \left[\sin^{-1} \left(\frac{D_2 + u}{D_3} \right) - \sin^{-1} \left(\frac{D_2}{D_3} \right) \right], \quad (2.65)$$

where

$$D_1 = \frac{2T_w}{Pr_t} \frac{1}{\beta M^2}, \quad (2.66)$$

$$D_2 = \frac{q_w}{\tau_w} \frac{1}{\beta Re Pr M^2} = \frac{T_w - T}{Pr_t M^2 \beta u} - \frac{u}{2} \quad (2.67)$$

and

$$D_3 = \sqrt{D_1 + D_2^2}. \quad (2.68)$$

From Eq.(2.66) and Eq.(2.67), D_1 and D_2 can be explicitly expressed in terms of u , T and T_w , which are all known in the calculations. Therefore, u_{vd} can then be estimated from Eq.(2.65). Afterwards, the friction velocity, u_τ can be evaluated from Eq.(2.61) by an iterative Newton process. Finally, since D_1 and u_τ are calculated, the wall heat flux q_w can be obtained from Eq.(2.67) and this completes the evaluation of the turbulence effect on the flow exerted by the no-slip wall.

2.6 CODE DEVELOPMENT

The CE/SE method and all the mentioned models are all programmed in C++ language. Moreover, in addition to the mentioned hexahedral mesh, the tetrahedral mesh is also built into the program for the three dimensional case while only triangular mesh is adopted for the two dimensional case. C++ is chosen for its decent features offered through the object oriented programming, which greatly enhances the ease in coding and the debugging processes. Furthermore, in order to speed up the computations, parallelized computations are required. Fortunately since the CE/SE method is an explicit scheme, parallelization of the *CE/SE code* can be readily achieved. This is attained by adopting the OpenMP Application Program Interface (API), which can fully utilize the computation power of a machine with shared-memory platform such as multi-cores desktop computer while keeping minimum

coding effort due to the simplicity of the program structure in *CE/SE code*. The speed-up is roughly 3.2 times for a 4-core computation.

2.7 CONCLUDING REMARKS

In this chapter, the formulation of CE/SE method for DAS is discussed. It is developed according to the physical conservation laws, which is very essential for solving the flow physics correctly. The CE/SE method is also implemented to solve the N-S equations for the DAS in both two and three dimensions. The treatment of boundary conditions in CE/SE method is rather simple, leading to the reduction of required computational resources for DAS. However, this method is not free of some shortcomings. Firstly, due to its conservation in space-time flux, some useful numerical remedies in other numerical method may not be applied. For example, a damping function such as PML (Hu et al. 2008) is usually applied in the buffer zone to absorb the incoming/outgoing waves when finite volume or finite difference is adopted. In the CE/SE method, this damping function creates a sink in the buffer zone because of its conservation in both time and space, which may influence the solution inside the domain. The effect of numerical remedies on the CE/SE method needs to be studied. Secondly, compared to other high order finite difference or finite volume scheme (Lele 1992), it is relatively low resolution and this will be assessed in the next chapter.

In simulating the turbulent flow, very fine mesh is required for LES to accurately calculate the problem. In order to reduce the numerical burdens, MILES and wall modeling are chosen for the turbulence modeling due to their relatively light weights and good results demonstrated by Larchevêque et al. (2003) and Loh & Hultgren (2006). The CE/SE method together with these boundary conditions and turbulence modeling are implemented in the *CE/SE code* as the numerical tools for DAS.

As mentioned in Section 1.3, the capability of resolving scale disparity is important in any DAS solver, it is very essential to verify the capability of the proposed CE/SE method in simulating the aeroacoustical physics correctly before it is used to tackle realistic aeroacoustic problems. In the literature, only a few aeroacoustic investigation adopted the CE/SE method and they all mainly focused on the supersonic flow region. Therefore, the method has not been assessed in solving the aeroacoustic problem. This chapter will discuss the assessment of the CE/SE method. The spatial resolution of this method is first assessed. Then both the two and three dimensional aeroacoustic problems will be considered. The validity of the method is established when it can pass all the validation tests using carefully selected benchmark cases. Note that the key is to resolve disparate scales in aeroacoustic problems.

3.1 SPATIAL RESOLUTION OF CE/SE METHOD

Popescu & Shyy (2002) have assessed the CE/SE method and compared to the high-order finite difference DRP scheme (Tam 1993). It is found that the CE/SE method is formally second order accurate in space and time despite its first order in nature. This implies that CE/SE method is an efficient scheme compared to DRP scheme, which is only $2(N - 1)$ order accurate with the number of stencil $2N + 1$. However, the spatial resolutions of these two methods are not compared in their work. The spatial resolution of a scheme affects the number of mesh points required for correctly capturing the acoustic waves of certain frequency. Therefore, in this section, the spatial

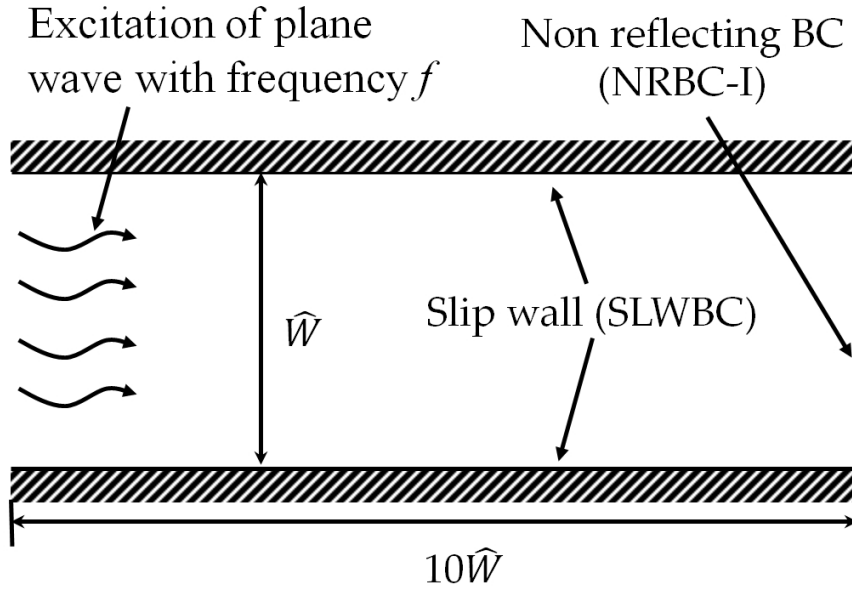


Figure 3.1: Schematic of a plane wave propagation in duct with slip wall.

REFERENCE PARAMETERS	PHYSICAL VARIABLES
Length, \hat{L}_0	The width of duct, \hat{W}
Velocity, \hat{u}_0	Acoustic speed, \hat{c}_0
Time, \hat{t}_0	\hat{W}/\hat{c}_0
Density, $\hat{\rho}_0$	Density at inlet, $\hat{\rho}_{in}$
Pressure, $\hat{\rho}_0 \hat{u}_0^2$	Inlet pressure, $\hat{\rho}_{in} \hat{c}_0^2$

Table 3.1: Reference parameters adopted in the plane wave propagation.

resolution of the CE/SE method is assessed and compared to other finite difference scheme.

3.1.1 Method of Assessment

To assess the spatial resolution, a simple plane wave propagating in a duct with slip walls is simulated, whose schematic is shown in Figure 3.1. The width and the length of duct are \hat{W} and $10\hat{W}$ respectively. Plane wave is excited at the left inlet of the duct and exit at the right outlet. NRBC-I is applied for this outlet while SLWBC is applied at the wall. The reference parameters applied are shown in Table 3.1. Uniform mesh size with $\Delta x = \Delta y = 0.05$ is applied

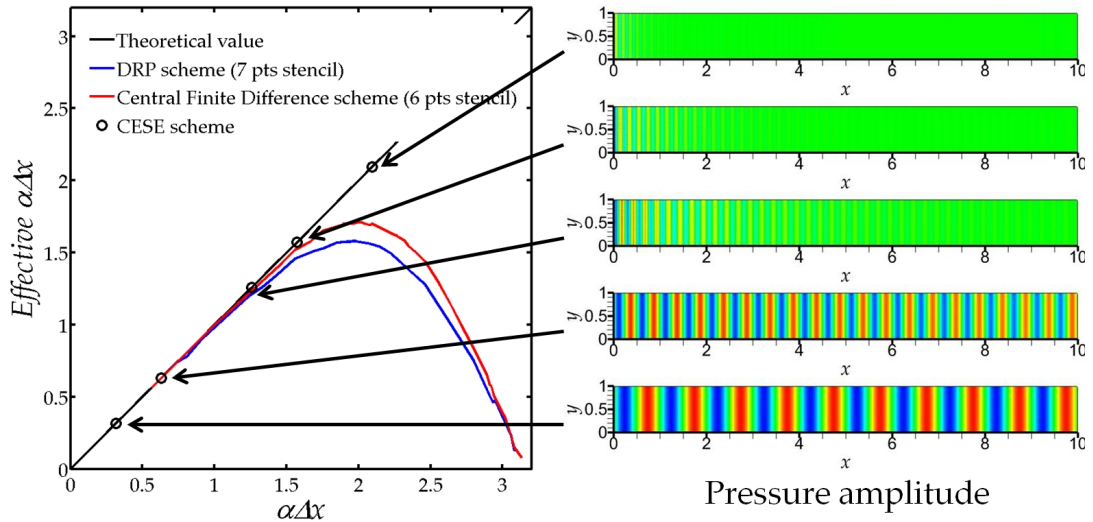


Figure 3.2: Comparison of spatial resolution with different scheme.

for the computational domain. The wavelength of excitation simulated λ is 0.15, 0.2, 0.25, 0.5 and 1.0 with an amplitude of 10^{-4} . The simulations last for a period of 10.

3.1.2 Results

Figure 3.2 show the results calculated by the present *CE/SE code* and the comparison with other high order finite difference schemes (Central finite difference with 6-point stencil and DRP scheme with 7-point stencil). $\alpha = 2\pi/\lambda$ is the wave number of the excited acoustic wave and Δx is the mesh size. The effective α is the actual wave number resolved by a scheme under the excitation of wave number α with mesh size Δx . Therefore, this figure represents the actual spatial resolution of a numerical scheme. In this figure, the CE/SE method can resolve the actual wave number even for a large $\alpha\Delta x > 2$ and this is higher than other high order finite difference schemes do. However, the pressure amplitude of excitation with $\alpha\Delta x > 1$ decays very quickly. This indicates that a severe dissipation occurs when the number of cells per wavelength is less than 5. This also implies that the CE/SE method can capture the acoustics very well when $\alpha\Delta x \leq \pi/5$, i.e. the number of cells per wavelength is at least 10. Therefore, a good accuracy of aeroacoustic

solution can be obtained when the interested frequency range lies in that region.

3.2 TWO DIMENSIONAL CASES

In the two dimensional cases, the assessment of the CE/SE method is divided into two stages with different level of complexity. At the first stage, its performance in capturing the individual aerodynamic and acoustic fields is examined; this can be tested by two benchmark cases, namely, the flow past backward facing step and acoustic propagation through duct junction respectively. It is important for an DAS scheme to resolve these fields correctly before its application in resolving their interactions. Once the capability of the CE/SE method in these two areas are established, the interactions between the aerodynamic and the acoustic fields are then examined by two aeroacoustic problems, namely, the aeolian tone due to a flow past a rectangular cylinder, and the acoustic absorption by an in-duct orifice. The former reveals the acoustics generation by the unsteady aerodynamics while the latter illustrates the aerodynamic unsteadiness initiated by an acoustic wave impinging onto sharp edges. The validity of the method is established when it passes all the above tests.

3.2.1 *Flow Past Backward Facing Step*

Flow past backward facing step (BFS) has been studied extensively and is a prototypical case for code validation e. g., [Guo et al. \(2004\)](#). [Armaly et al. \(1983\)](#) provided a rich experiment database, in which the hydraulic diameter of the inlet duct, the average inlet flow speed were chosen as the reference length and velocity respectively. His experimental results reveal that the flow is characterized by the recirculation zone just behind the step. Moreover, at Reynolds number less than 400 based on the above reference parameters,

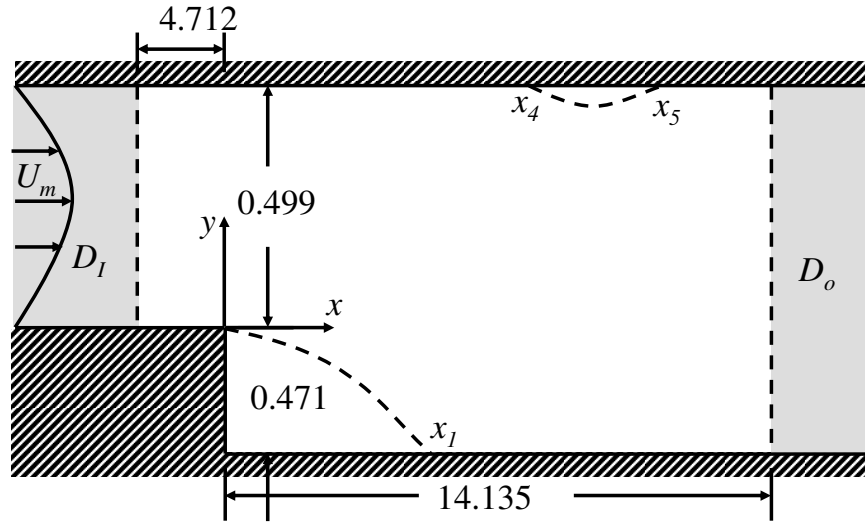


Figure 3.3: Configuration of backward facing step flow.

REFERENCE PARAMETERS	PHYSICAL VARIABLES
Length, \hat{L}_0	the hydraulic diameter of inlet duct, \hat{D}_H
Velocity, \hat{u}_0	Average velocity of inlet, \hat{u}_{av}
Time, \hat{t}_0	\hat{L}_0 / \hat{u}_0
Density, $\hat{\rho}_0$	Density at inlet, $\hat{\rho}_{in}$
Pressure, $\hat{\rho}_0 \hat{u}_0^2$	Inlet pressure, $\hat{\rho}_{in} \hat{u}_{max}^2$

Table 3.2: Reference parameters adopted in flow past BFS.

this flow is found to be a two-dimensional phenomenon. When the Reynolds number is increased above the range, the flow is strongly three-dimensional and the recirculation zones are developed in both upper wall and lower wall, which may be due to the instability of the initial recirculation zone behind the steps.

The setup of the case is shown in [Figure 3.3](#) and [Table 3.2](#) summarizes the reference parameters applied in this case. In this problem, the hydraulic diameter of inlet duct (~ 2.12 times the step height \hat{H}) is chosen as the reference length, but the reference velocity is still the mean velocity of the parabolic inlet profile, u_{av} . The Reynolds number, Re , and the Mach number, M , are

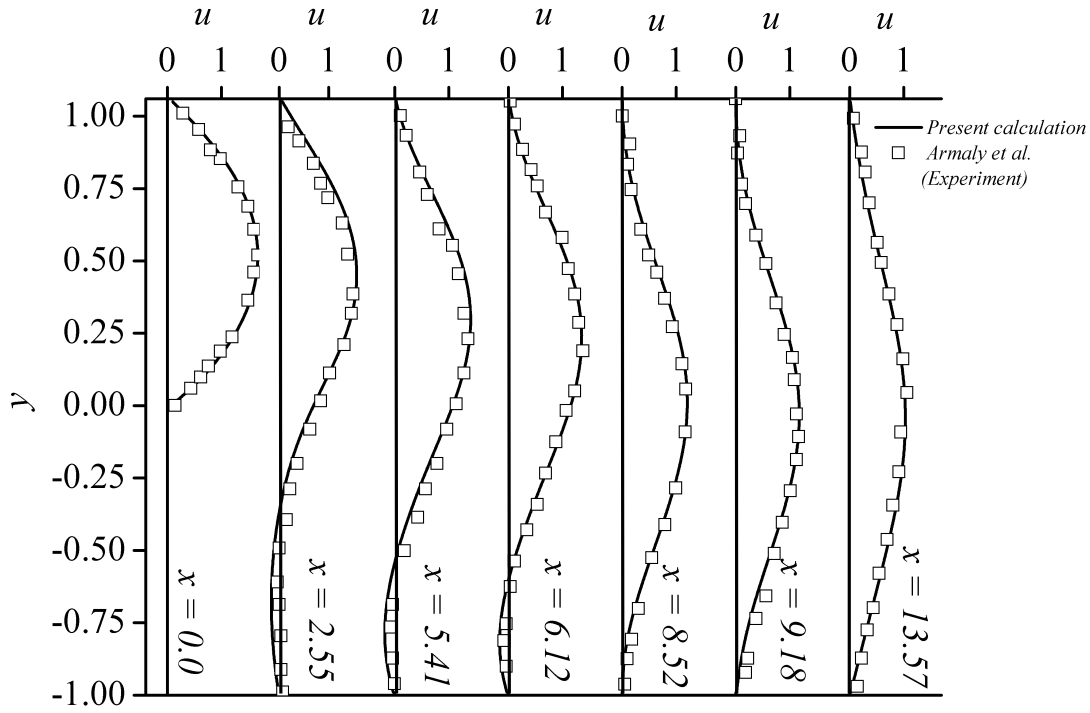


Figure 3.4: Profiles of x -velocity at various downstream location to the step.

calculated based on these parameters. In these studies, M is equal to 0.2 and the tested Re is taken as 155.6, 389 and 500.

The parabolic velocity profile is applied to the left inlet boundary condition with density, $\rho = \rho_0 = 1$ and pressure, $p = p_0 = 1/M^2$. At the outlet boundary on the right of the domain, NRBC-II is applied, whereas the density and pressure are fixed at their reference values while the velocities are taken as those in the boundary cells. All other wall boundary conditions are NSWBC-NW.

The size of the computational domain is $-4.712 < x < 14.135$ by $-0.471 < y < 0.499$ and the edge of step is located at the origin. Buffer zones $D_I = D_O = 4.712$ are also appended to the inlet and exit of the domain. The mesh points are uniform in both x and y directions with $\Delta x = 0.02356$ and $\Delta y = 0.01178$. Grid stretching is applied for the buffer zones in the x direction only. The time step Δt is 10^{-4} and the simulating time T is 150, beyond which the flow reaches its steady state.

After the time stationary solution is obtained, the velocity profiles downstream of the step are plotted with the experimental results of [Armaly et al. \(1983\)](#) in [Figure 3.4](#). The simulated velocity profiles match with experimental

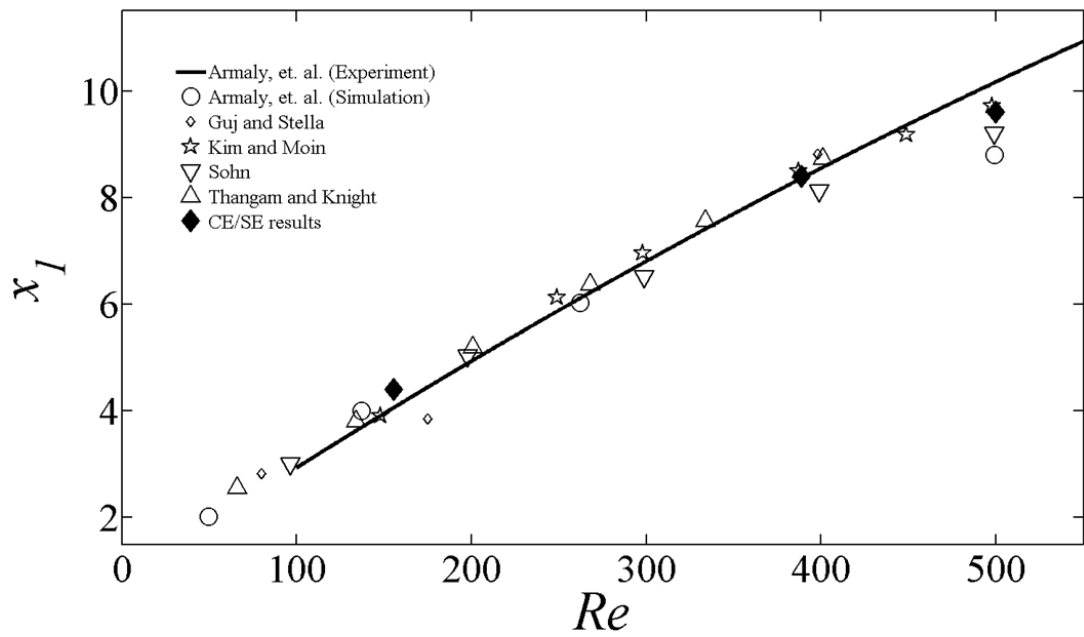


Figure 3.5: Reattachment length of recirculation zone behind the step.

data very well. Furthermore, according to the experiments of [Armaly et al. \(1983\)](#), the flow is characterized by different recirculating zones downstream of the step depending on the Reynolds number, whereas the primary recirculating zone is at x_1 as shown in [Figure 3.3](#). Therefore, it is important that the solver can predict the reattachment length x_1 well in order to show it as a suitable tool to simulate such problem. The reattachment length is determined by the location where the shear stress changes sign and the results are plotted in [Figure 3.5](#) together with experimental and incompressible simulation results from [Armaly et al. \(1983\)](#), [Guj & Stella \(1988\)](#), [Kim & Moin \(1985\)](#), [Sohn \(1988\)](#) and [Thangam & Knight \(1990\)](#). From [Figure 3.5](#), it is found that x_1 calculated by the CE/SE method agrees excellently with the experimental results of [Armaly et al. \(1983\)](#) and other numerical results (incompressible codes) when the Reynolds number is below 400. However, similar to other two dimensional incompressible simulations, the predicted x_1 deviates from the experimental result for $Re > 400$ because the flow transits to the three dimensional nature according to [Armaly et al. \(1983\)](#). In this situation, a secondary recirculating zone (from x_4 to x_5 in [Figure 3.3](#)) is generated at the upper wall illustrated in [Figure 3.6](#). Thus, the results for $Re = 500$ are not included in the validation of

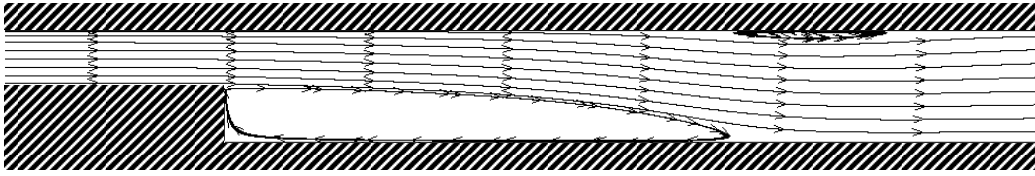


Figure 3.6: Second recirculating zone near the upper wall at $Re = 500$.

REFERENCE PARAMETERS	PHYSICAL VARIABLES
Length, \hat{L}_o	Width of duct, \hat{W}
Velocity, \hat{u}_o	Speed of sound, \hat{c}_o
Time, \hat{t}_o	\hat{W}/\hat{c}_o
Density, $\hat{\rho}_o$	Density at inlet, $\hat{\rho}_{in}$
Pressure, $\hat{\rho}_o \hat{u}_o^2$	Inlet pressure, $\hat{\rho}_{in} \hat{c}_o^2$

Table 3.3: Reference parameters adopted in T-duct acoustics

present scheme. Therefore, these results prove that the CE/SE method can correctly capture the characteristics of the flow at $Re < 400$.

3.2.2 Acoustic Propagation Through Duct Junction

Tang & Lam (2008) investigated the acoustic transmission inside ductwork and aimed at identifying the influence of geometry, which included the angle between side branch and main duct and their sizes, on the acoustic transmission at the duct junction. They applied finite element method to solve the Helmholtz equation in the frequency domain. In this problem, acoustic plane waves of different frequencies are excited at the inlet of the side branch. When the sound reaches the duct junction in the absence of a mean flow, it reflects, transmits, or even converts to non-planar duct modes at the duct junction depending on the relative length of excited wavelength to the size of the duct in both sections. Thus, the sound propagation at T-ducts serves as a good testing case due to its complexity.

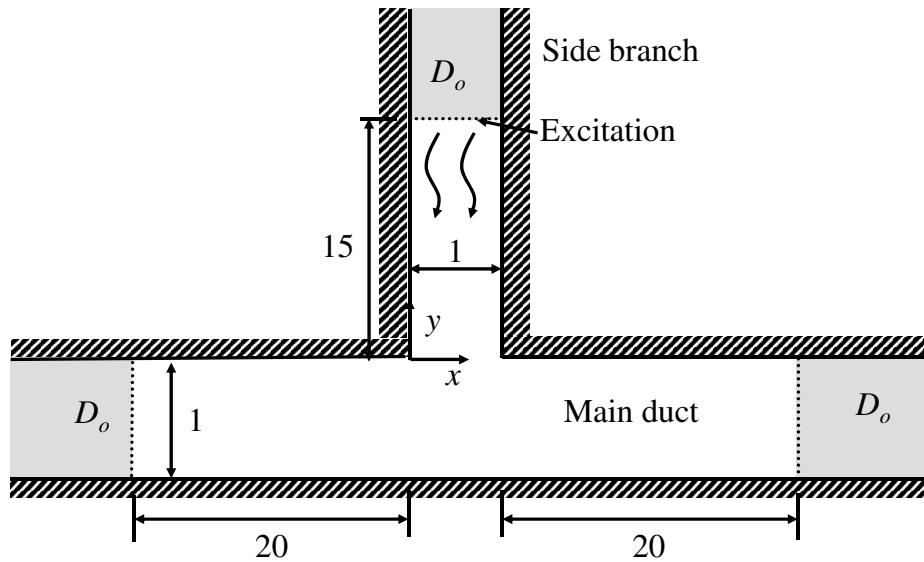


Figure 3.7: The configuration of T-duct acoustics case.

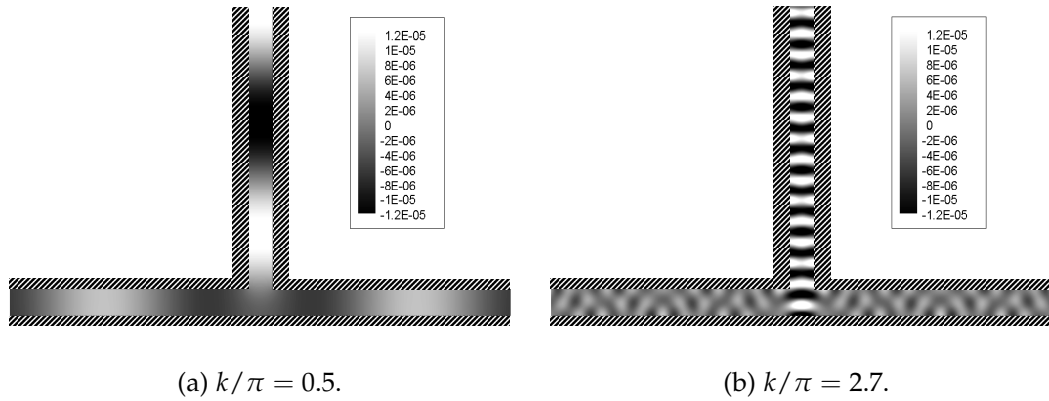


Figure 3.8: Wave pattern at duct junction at different excitation frequencies.

In this problem, the reference parameters applied is illustrated in [Table 3.3](#). and the schematic is shown in [Figure 3.7](#), where two ducts of the same width join at 90 degree, and the origin is located at the left upper corner of the duct junction. The normalized length L of each section are 20. The domain is discretized in uniform mesh with $\Delta x = \Delta y = 0.025$ and buffer zones D_o of length 10 with grid stretching are added to the end of each duct section. The acoustic waves are excited in the vertical duct ($y = 20$) with $k/\pi = 0.25, 0.5, 0.667, 0.75, 0.9, 1.25, 1.5, 1.75, 2, 2.25, 2.5, 2.7$ and 3.2, where k is the wave number, and the excited amplitude is about $p_{ex} = 10^{-5}$. Type I NRBC is applied to the outlet while the wall boundary conditions are SLWBC. The time step Δt is 0.001 and the simulation lasts for 60 normalized time.

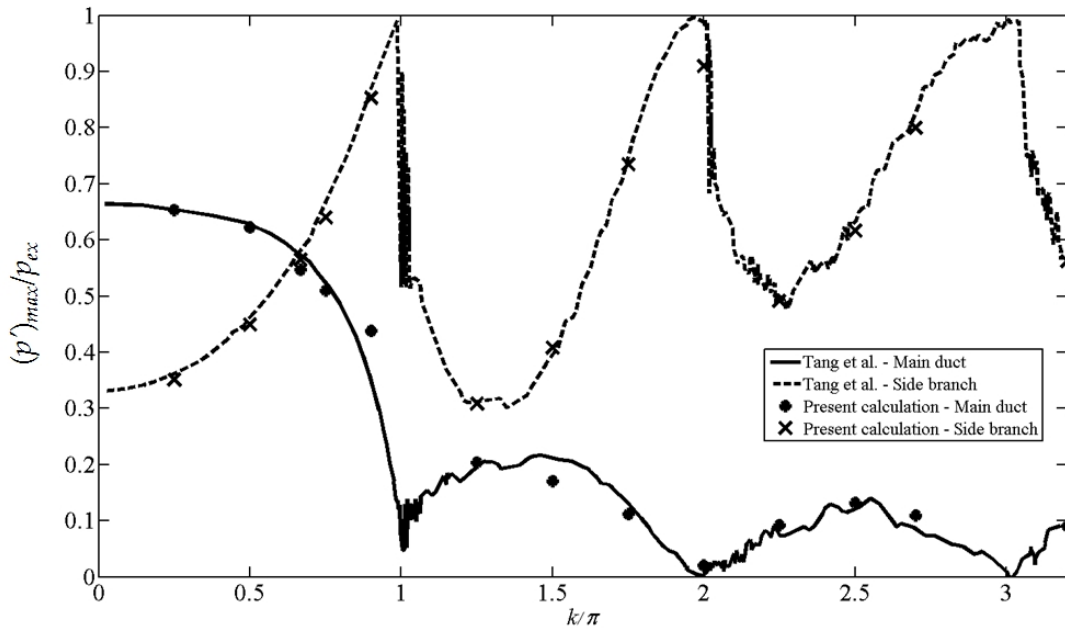


Figure 3.9: Amplitude of plane waves in main duct and vertical duct sections.

When the wavelength of the excited plane wave is larger than the duct width e.g., in Figure 3.8a, less than half of plane wave splits up into two parts. With one part travels downstream while the other part is reflected back to the side branch. In this situation, the plane wave is still kept without conversion to non-planar mode of sound wave. On the contrary, when the wavelength of the excited plane wave is smaller than the duct width e.g., in Figure 3.8b, significant acoustics propagates to downstream and less than 20% of excitations are reflected back to the side branch. Those downstream propagation is mainly in non-planar mode rather than plane wave mode.

The sound transmission coefficients of the plane wave amplitudes are then calculated and presented in Figure 3.9. These are also compared with the numerical results of Tang & Lam (2008) and the results are very satisfactory. The CE/SE method not only correctly calculated the amplitudes of plane wave transmitted and reflected, but also captured the conversion of plane wave to non-planar duct mode at duct junction. This illustrates the excellence of the CE/SE method in capturing the acoustic behavior.

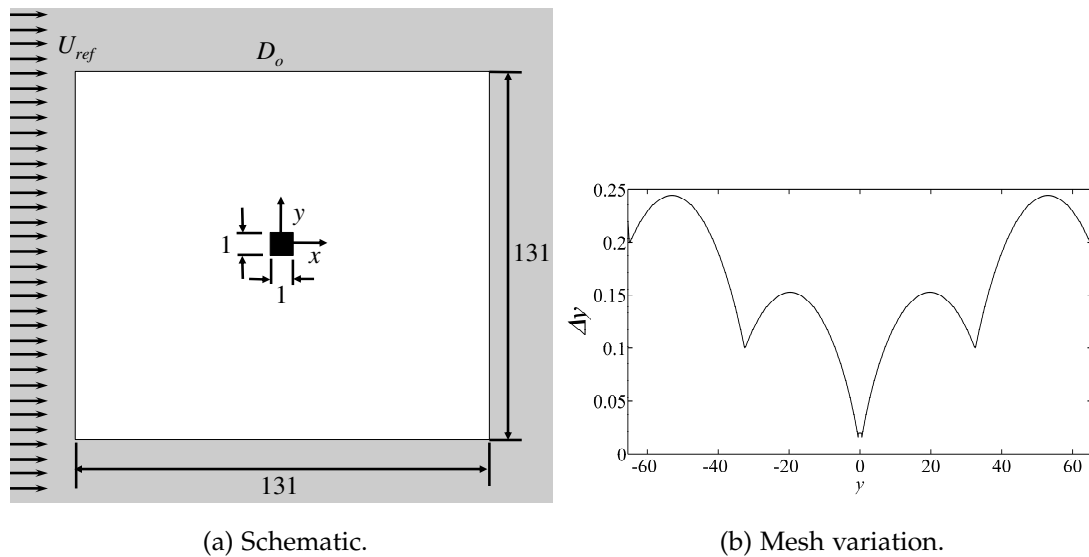


Figure 3.10: Configuration of flow past a square cylinder.

3.2.3 Aeolian Tone of a Square Cylinder

Extensive investigations were carried out to study aeolian tone of a uniform flow past a cylinder as its utmost importance in understanding the physics for fluid-structure interaction e. g., [Inoue & Hatakeyama \(2002\)](#). This flow often experiences the separation of boundary layer at the downstream corners of the square cylinder alternatively. At sufficiently large Reynolds number, the boundary layer then rolls up into vortices, which are convected to the wake region created behind the cylinder. Furthermore, the lift and drag fluctuations at the cylinder surfaces are also induced by this vortex shedding. The alternating vortex shedding creates a chain of alternating positive pressure and negative pulses. This pressure fluctuation propagates to the far field in the form of acoustics due to the compressibility of air and eventually forms a lift dipole. The acoustic generation (lift dipole) from the sole aerodynamic cause (unsteady vortex shedding) makes it an excellent case for code validation in aeroacoustics.

Consider a computational domain of $-65.5 < x < 65.5$ by $-65.5 < y < 65.5$ with a square cylinder of size 1 centered at the origin as shown in Figure 3.10a. Buffer zones D_O of length 95 are applied to the four sides of the domain. The mesh points are clustered near the cylinder and its wake region.

REFERENCE PARAMETERS	PHYSICAL VARIABLES
Length, \hat{L}_o	Length of cylinder, \hat{L}_o
Velocity, \hat{u}_o	Inlet velocity, \hat{u}_{in}
Time, \hat{t}_o	\hat{L}_o / \hat{u}_{in}
Density, $\hat{\rho}_o$	Density at inlet, $\hat{\rho}_{in}$
Pressure, $\hat{\rho}_o \hat{u}_o^2$	Inlet pressure, $\hat{\rho}_{in} \hat{u}_{in}^2$

Table 3.4: Reference parameters adopted in aeolian tone.

The minimum x and y are 0.02 and their maxima are 0.2 as illustrated in Figure 3.10b. The reference parameters are shown in Table 3.4. Uniform inlet flow with Mach number $M = 0.2$ is applied at the left boundary condition and the Reynolds number based on the reference parameters is 200. The outlet boundary conditions are NRBC-II and the solid surfaces of the cylinder are prescribed by NSWBC-NW. The duration of simulation T is 240, which has already included 20 periods of simulation after the solution reaches its steady state.

The time histories of lift coefficient C_L and drag coefficient C_D are illustrated in Figure 3.11a and 3.11b respectively, in which C_L fluctuates with a dominant Strouhal number $St = 0.1476$ and is double that of C_D . Moreover, the vorticity distributions at the beginning ($t = 203.95$) and end ($t = 207.35$) of a half cycle of C_L are shown in Figures 3.11c and 3.11d. From these figures, the fluctuation of C_L is definitely induced by the regular vortex shedding from the cylinder. In addition, Table 3.5 shows a comparison of the present calculations with existing experimental results and numerical results obtained from incompressible flow calculations. It demonstrates that the present calculation with the CE/SE method successfully captures all key aerodynamic features of the flow with good accuracy.

As mentioned in chapter 1, the pressure fluctuation in acoustics is usually much smaller than that in the aerodynamics e. g., in this case. Therefore, to

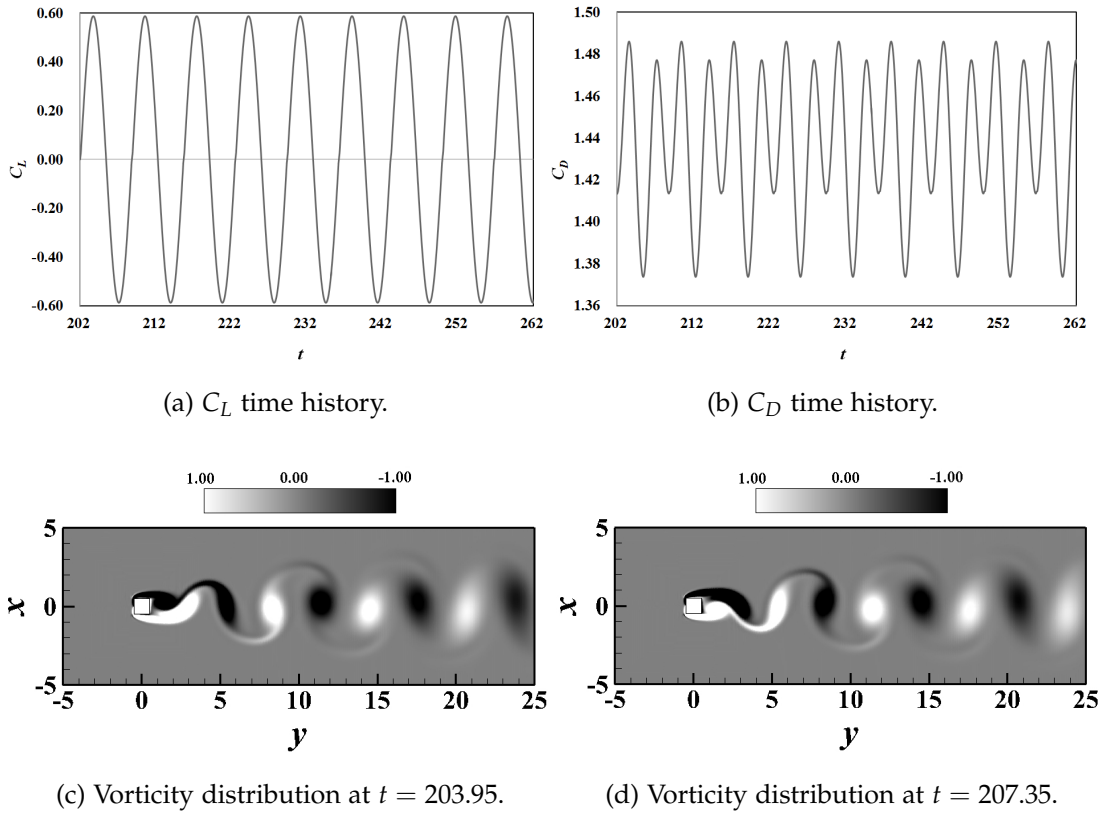
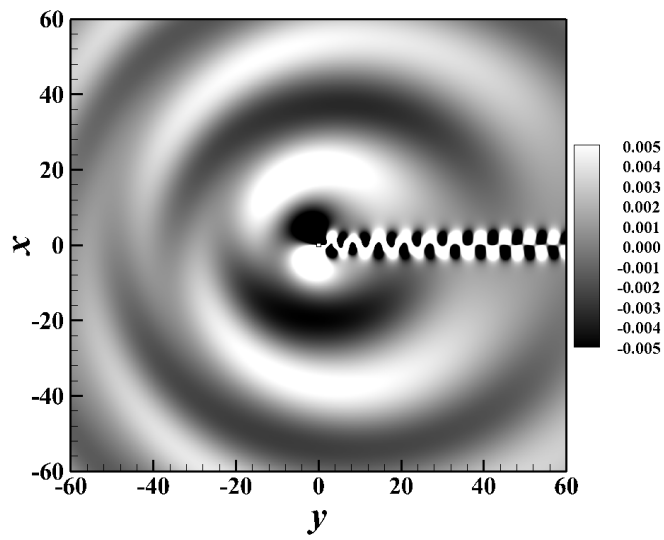


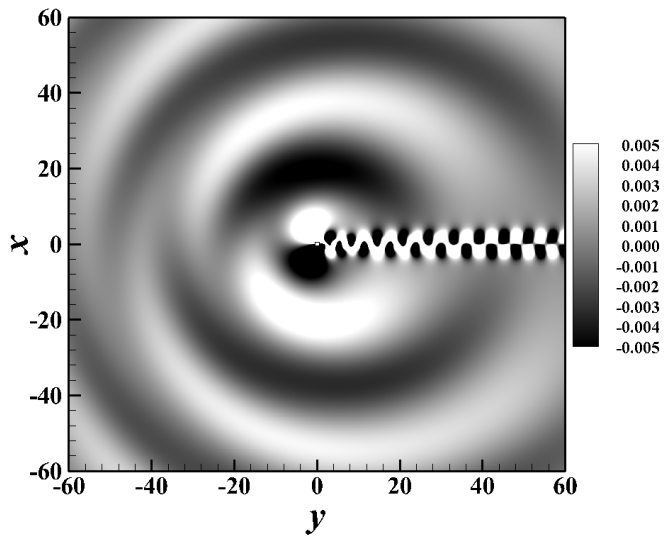
Figure 3.11: CE/SE results and vorticity distributions.

RESULTS	St	$(C_L)_{rms}$	$(C_L)_{max}$	$(C_L)_{min}$	$(C_D)_{rms}$	$(C_D)_{max}$	$(C_D)_{min}$
Okajima (2006) (Experiment)	0.140 – 0.148	-	-	-	1.450	-	-
Sohankar et al. (1998) (Numerical Simulation)	0.148	0.377	-	-	1.462	-	-
Jan & Sheu (2004) (Numerical Simulation)	0.150	-	-	-	-	-	-
Cheng et al. (2007) (Numerical Simulation)	0.150	0.372	0.600	-0.600	1.450	1.500	1.390
Present Study	0.148	0.359	0.589	-0.589	1.447	1.487	1.374

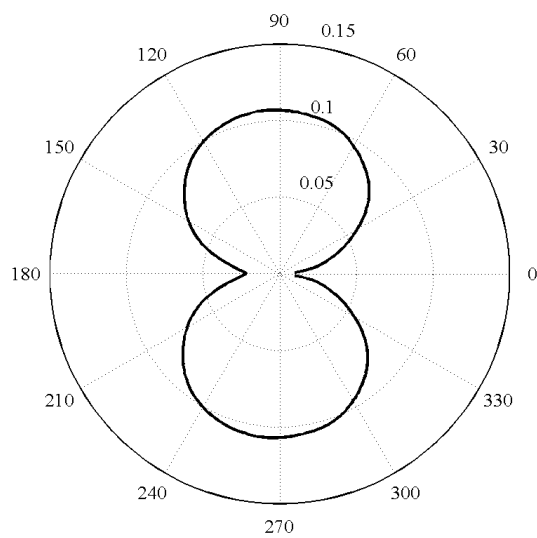
Table 3.5: Comparison of C_L and C_D metrics.



(a) Snapshots of p' at $t = 203.95$.



(b) Snapshots of p' at $t = 207.35$.



(c) Directivity of rms pressure fluctuation at $r = 60$.

Figure 3.12: Instantaneous pressure fluctuation and directivity.

reveal this acoustic pressure, it needs to be separated out from the total pressure by taking the pressure fluctuation

$$p'(x, y, t) = p(x, y, t) - p_{mean}(x, y), \quad (3.1)$$

where (x, y) is the location and $p_{mean}(x, y)$ is the time averaged pressure at (x, y) . [Figure 3.12](#) shows the instantaneous pressure fluctuation at $t = 203.95$ and $t = 207.35$. It clearly illustrates two distinct regions. The first one is the downstream region of the cylinder, where is dominated by a chain of vortex convecting with the flow speed. The other one is the acoustic region, whereas a nearly circular wave pattern propagates outward from the cylinder with the sound speed ($c = 1/M = 5$ in this case). Evidently the upper and the lower side of the cylinder are out of phase in the fluctuation. [Figure 3.12c](#) shows the root mean square of acoustic pressure p'_{rms} at $r = \sqrt{x^2 + y^2} = 60$ and further reveals that the acoustics is lift dipole as the major propagating direction is in the lift direction (vertical). For a lift dipole, the decay rate of acoustic pressure in the far field is given by

$$p' \propto \frac{M^5}{\sqrt{r}}. \quad (3.2)$$

where $r = \sqrt{x^2 + y^2}$. [Figure 3.13](#) demonstrates the variation of peak value of p' with r along $y < 0$. It clearly shows that the slope of the decay curve reaches a constant value of -0.501 at $r \geq 33.88$, which is approximately equal to the wavelength λ of the acoustics pressure and it is in excellent agreement with [Eq.\(3.2\)](#). From this fact, we can deduce that the far field definition for this case is at least region further than λ which is consistent with existing aeroacoustic theories e. g., [Inoue & Hatakeyama \(2002\)](#). This concludes the success of the CE/SE method in capturing this flow induced acoustics.

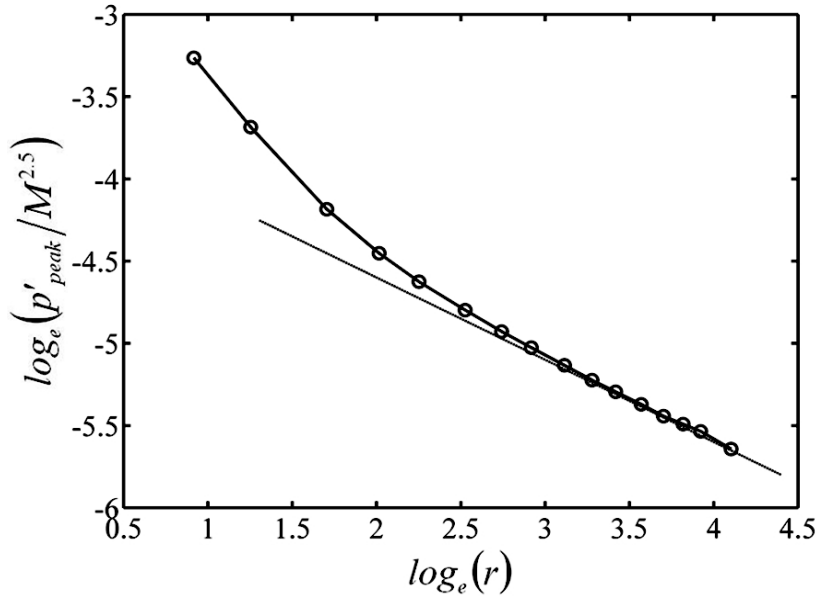
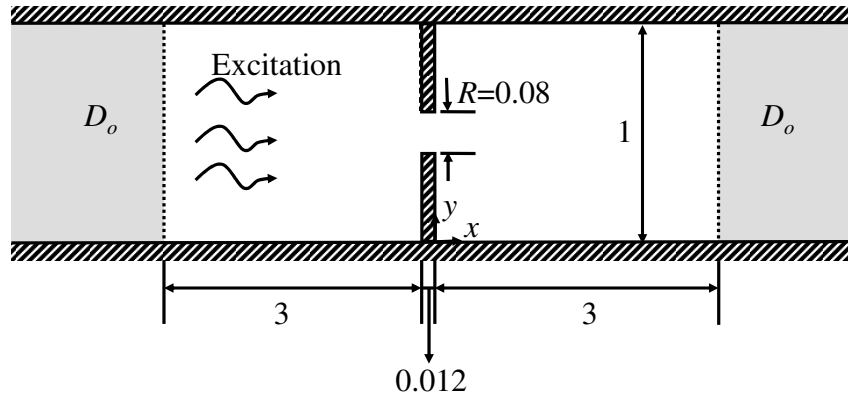


Figure 3.13: Decay of acoustic fluctuation.

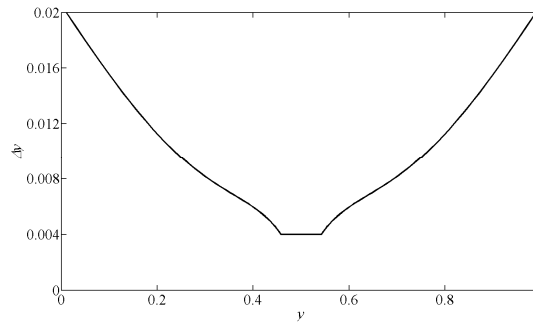
3.2.4 Acoustic Absorption Through Orifice

Acoustic absorption through orifice is a classic example of acoustics induced dynamics, which is originated from Helmholtz resonators in reducing the noise level in ducts. When the sound with sufficient power is introduced into a duct and reaches the orifice, part of the sound is reflected while some portions are transmitted to the other side of orifice. Throughout this process, vortices are shed at the orifice and convected to the other side. Then these vortices are dissipated by the action of air viscosity, so the acoustic power is adsorbed. The phase of the transmitted sound is also changed as a result of the non-linear acoustic behavior of an orifice. Moreover, this absorption is frequency dependent. Therefore, the capability of resolving the acoustically induced aerodynamic motions of the CE/SE method can be established if it is capable of capturing the nonlinear acoustic absorption processes as well as the absorption spectrum.

In the present simulation, the case is set up as shown in Figure 3.14a, which is a two dimensional replica to the model used in the experiment of Jing & Sun (2002). The reference parameters are listed in Table 3.6. The computational domain is $-3 < x < 8$ by $0 < y < 1$. The opening of the orifice



(a) Schematic.



(b) Mesh variation in y .

Figure 3.14: Configuration of sound past through orifice.

REFERENCE PARAMETERS	PHYSICAL VARIABLES
Length, \hat{L}_o	Width of duct, \hat{W}
Velocity, \hat{u}_o	Speed of sound, \hat{c}_o
Time, \hat{t}_o	\hat{L}_o/\hat{c}_o
Density, $\hat{\rho}_o$	Density at inlet, $\hat{\rho}_{in}$
Pressure, $\hat{\rho}_o\hat{u}_o^2$	Pressure at inlet, $\hat{\rho}_{in}\hat{c}_o^2$

Table 3.6: Reference parameters adopted in orifice case.

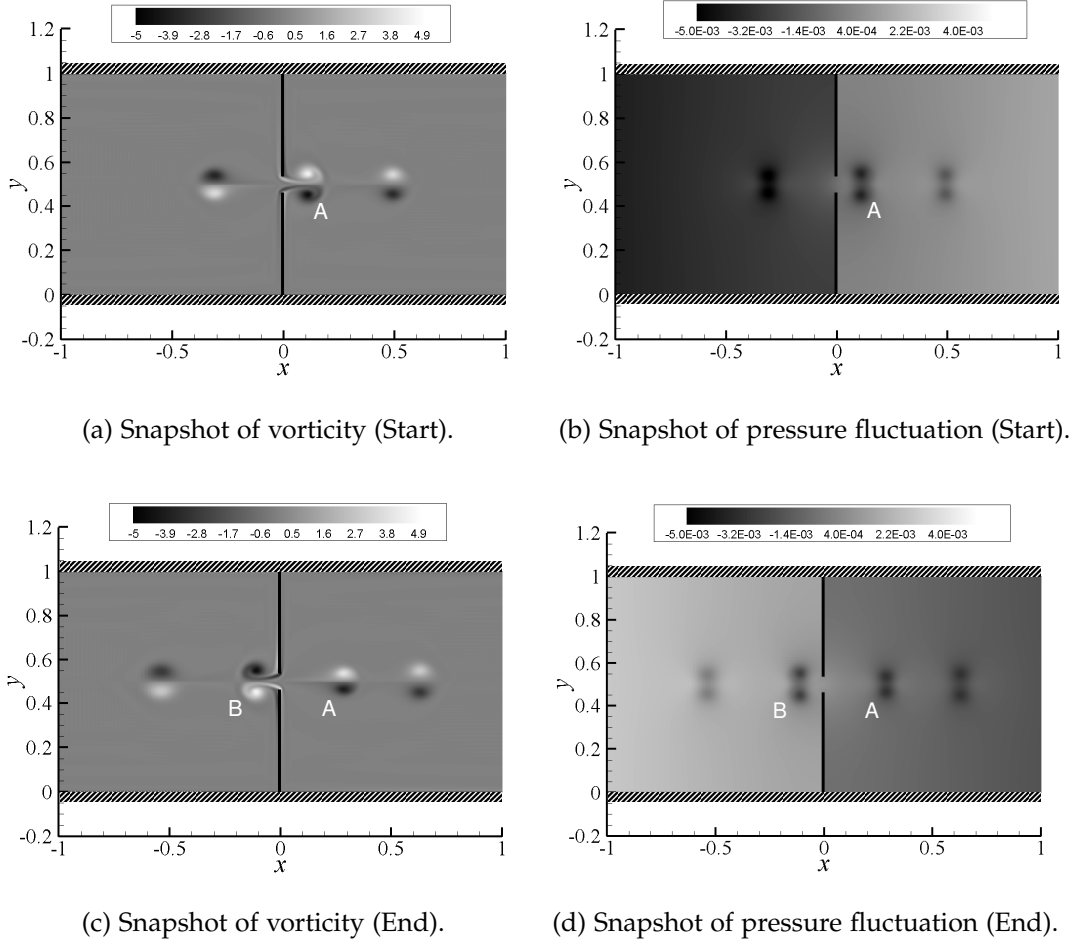


Figure 3.15: Snapshot of CE/SE results at the start and end of a half cycle.

is 0.08 with a thickness of 0.012. The mesh points are uniform in x direction with $\Delta x = 0.005$ and the mesh is clustered near the orifice in y direction with $\Delta y_{min} = 0.004$ and $\Delta y_{max} = 0.02$ as illustrated in Figure 3.14b. Sound with amplitude p_{ex} is excited at $x = -3$ in all calculations with normalized sound pressure level $p\omega/R^2$ ranging from 2.30 to 46.03, where $\omega = 2\pi f_{ex}$ is the angular frequency of the excitations. The excitation frequencies f_{ex} are arbitrarily chosen as 0.0588 and 0.147. The boundary condition of the walls is NSWBC-NW. Furthermore, the outlet condition at left and right sides NRBC-I. Buffer zones D_o of size 10 are applied to the ends of the duct. The time step size is set to $\Delta t = 5 \times 10^{-4}$ and the calculations last until $T = 88$ to attain time-stationary solutions.

Figure 3.15 show the instantaneous vorticity and pressure fluctuation of the CE/SE results and it demonstrates the mechanism of acoustic absorption

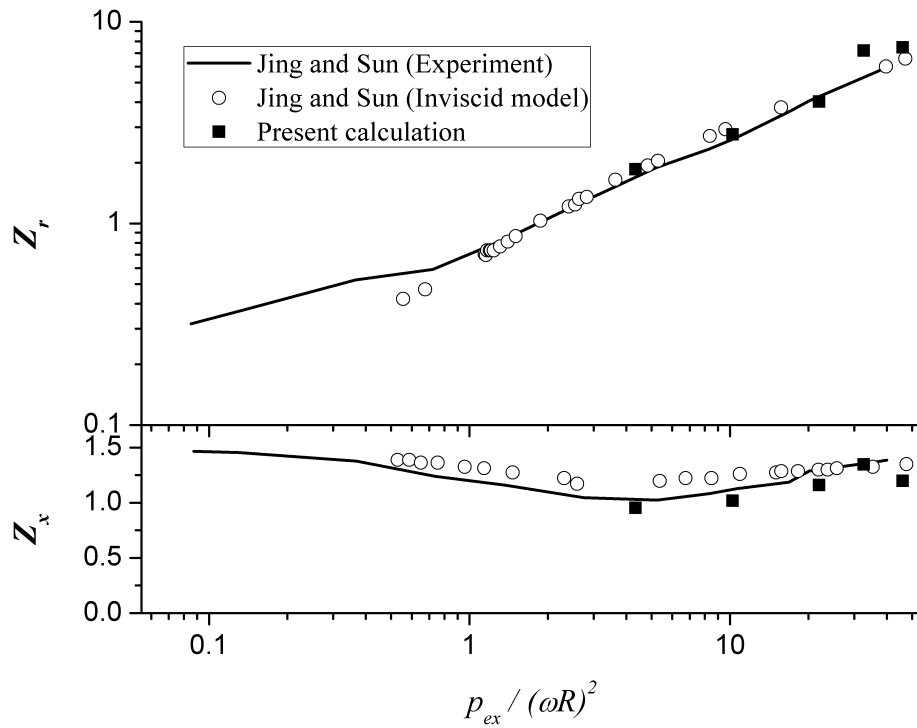


Figure 3.16: Comparison of acoustics impedance.

through orifice. When the positive part of acoustics wave (compression) reaches the orifice from the left, a vortex pair A with size comparable to the opening of orifice is shredded to the right section of the orifice as shown in Figure 3.15a and one can note that the phase of the acoustic wave is also changed significantly according to Figure 3.15b. On the other hand, when the negative part of the wave (rarefaction) reaches the orifice from the left, another vortex pair B is shredded in the opposite direction depicted in Figure 3.15a. Phase changing in the left and right section of the orifice is also observed for this case as shown in Figure 3.15d. These figures also show that the vortex suffered from significant dissipation due to the viscous effect of the air. Moreover, the normalized acoustic impedance $Z_x = z_x / f_{ex}$ and normalized acoustic resistance $Z_r = z_r / f_{ex}$ of the orifice are calculated from the CE/SE method and compared with the experimental results of [Jing & Sun \(2002\)](#) and their inviscid model in Figure 3.16. It shows that the CE/SE results matched excellently with the experiment especially for the acoustic resistance. For the acoustic reactance, our calculation is closer to their experiment than their inviscid model, suggesting that the viscous effect of the air or wall have to be

accounted for accurate predictions. Finally, these results prove that the CE/SE method can also capture the acoustics induced flow extremely well.

3.3 THREE DIMENSIONAL CASES

The successful validation in the two dimensional cases has already established the capability of the CE/SE method in dealing with the aeroacoustic problems. The validation of the CE/SE method in the three dimensional situation should also be carried out in the similar fashion. However, due to the requirement of high resolution in the spanwise direction in these cases and the lack of computational resources (The flows can only be calculated using a server with a dual 6-core CPU), it is not possible to simulate all the attempted two dimensional cases in three dimensions. Thus, other three dimensional validation cases requiring less computational resources are selected.

The first step in the validation is to check if the CE/SE method solves the compressible N-S equation in three dimensions correctly. This can be done by simulating a supersonic flow over a wedge. When the supersonic flow reaches the wedge, it is forced to change direction immediately. Since the air is compressible, an oblique shock is generated at the corner of the wedge and this process is irreversible, leading to the increase in the entropy of the entire system. As a shock is formed, the incompressible form of Bernoulli's solution cannot be applied as the total pressure jump across the shock. However, the original integral form of N-S equations is still valid. Thus, this serves as a good case to check the capability of the CE/SE method in three dimensions.

Secondly, one of the most important features required for a DAS solver is the capability of distinguishing the flow dynamic and acoustic quantities despite their large disparity in scales such as length and energy as pointed out by Tam (1995). Furthermore, the speed of propagation must be accurately captured because this is the most distinguished characteristics of any aeroacoustic problem. For instance, the acoustic wave propagates at sonic

speed while flow disturbance propagates at nearly the characteristic flow speed. The solver must be able to differentiate these two different types of signals. Therefore, a benchmark CAA Workshop problem Category 3 Problem 1 proposed by [Hardin et al. \(1994\)](#) is selected for assessing the capability of differentiation of disparate scales in three dimensions. Despite its simplicity, it can reveal the capability of a solver in handling the above important issue. In this problem, an acoustic pulse with small amplitude travels with a vortex pulse and entropy pulse in a uniform flow. One notes that these pulses are Gaussian and non-dispersive in nature, which can also be used to test the dispersive error of a DAS solver. If the CE/SE method can accurately capture these propagations, its capability of resolving disparate scales with several order difference simultaneously is established. This requirement is fundamental for resolving the interaction between the flow dynamics and acoustics.

Finally, it is essential to check the CE/SE method against a three dimensional case similar to the merging flow at duct junction, so the flow past backward facing step is revisited. In this case, the recirculation zone is completely determined by the flow dynamics, which is a good indicator for capturing the flow physics in three dimensions. A BFS flow with $Re > 400$ is chosen for the validation as the three dimensional effect becomes stronger under this circumstance. In addition, it can be simulated with less computational resources. Thus, it is chosen for the validations.

3.3.1 *Supersonic Flow Over Wedge*

The schematic and the mesh of this problem are illustrated in [Figure 3.17](#). In this calculation, a supersonic uniform flow enters the domain from the left and meets a wedge. An oblique shock is then formed at the wedge. The

CE/SE method is used to capture this shock. This flow problem is governed by N-S equations which, according to Babu (2008), can be simplified to

$$\begin{aligned}\rho_1 u_{n,1} &= \rho_2 u_{n,2}, \\ p_1 + \rho_1 u_{n,1}^2 &= p_2 + \rho_2 u_{n,2}^2, \\ h_1 + \frac{1}{2} u_{n,1}^2 &= h_2 + \frac{1}{2} u_{n,2}^2,\end{aligned}\tag{3.3}$$

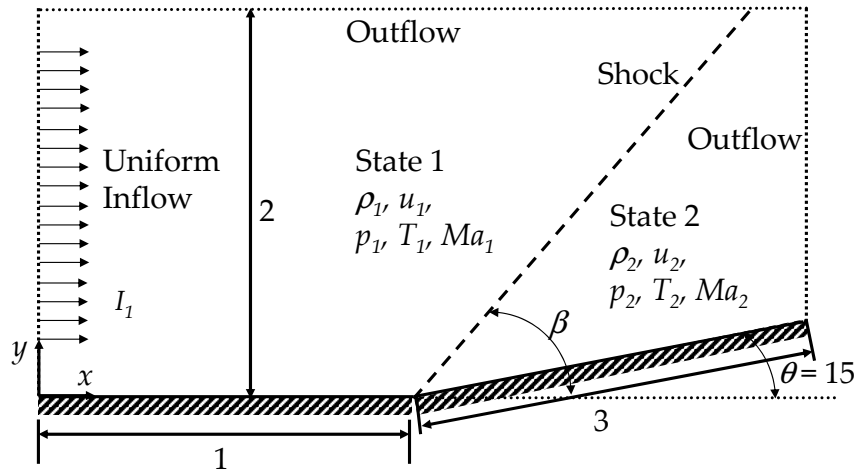
where h is the enthalpy of the flow, the subscript n denotes the normal direction to the shock, the subscripts 1 and 2 denote the states of the flow upstream and downstream of the shock respectively. By substituting $u_n = u \sin \beta$, the relationship between θ , β and M_1 , where M_1 is the Mach number of state 1 can be expressed as

$$\tan \theta = 2 \cot \beta \frac{M_1^2 \sin^2 \beta - 1}{M_1^2 (\gamma + \cos(2\beta)) + 2},\tag{3.4}$$

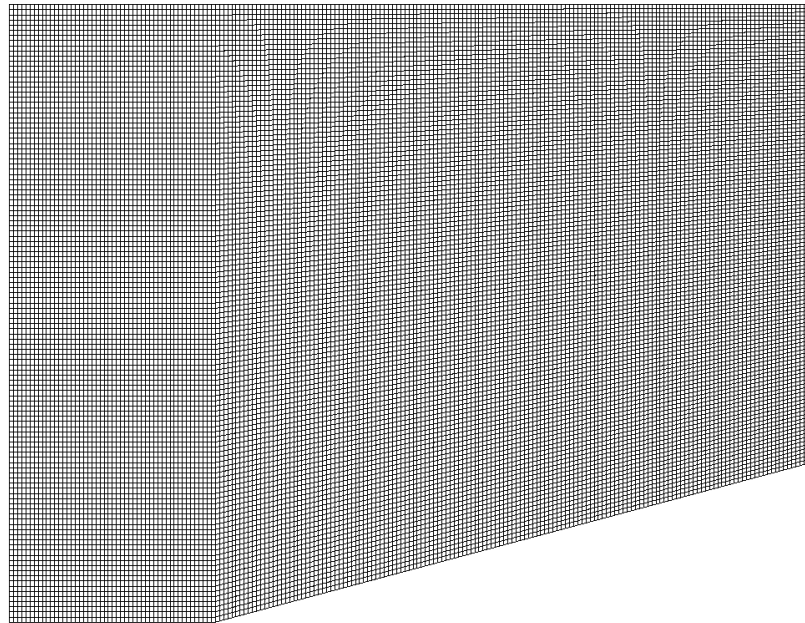
where γ is the ratio of specific heat.

The reference parameters are listed in Table 3.7. The computational domain is $0 < x < 3.9$ by $0 < y < 2$ by $0 < z < 0.1$. A uniform, supersonic air stream flows over a sliding horizontal wall of length \hat{L} and reaches the wedge of angle 15° at $x = 1$. A tetrahedral mesh is then built from uniform hexahedral mesh across the domain of size $\Delta x = \Delta y = \Delta z = 0.05$. Uniform flow of $M = 2.5$ is specified at left inlet boundary condition with density, $\rho = \rho_0 = 1$ and pressure, $p = p_0 = 1/\gamma$. SLWBC is applied to all the walls and the uniform flow is specified at the inlet. The outlet condition is NRBC-I for supersonic flow and in z (spanwise) direction, SLWBC is also prescribed as an symmetry condition. The initial condition is setup as stationary with density $\rho = \rho_0 = 1$ and pressure $p = p_0 = 1/\gamma$. The time step Δt is 5×10^{-5} and the case is simulated until it reaches its time stationary state, i. e., about after a nondimensional duration 10.

A snapshot of Mach number is shown in Figure 3.18a. The abrupt change in the Mach number contour clearly shows the location of the shock,



(a) Schematic.



(b) Hexahedral mesh before dividing into uniform tetrahedral mesh.

Figure 3.17: Configuration of supersonic flow over wedge.

REFERENCE PARAMETERS	PHYSICAL VARIABLES
Length, \hat{L}_o	Length of horizontal plate, \hat{L}
Velocity, \hat{u}_o	Velocity of inlet, \hat{c}_{in}
Time, \hat{t}_o	\hat{L}/\hat{c}_{in}
Density, $\hat{\rho}_o$	Density at inlet, $\hat{\rho}_{in}$
Pressure, $\hat{\rho}_o \hat{u}_o^2$	Inlet pressure, $\hat{\rho}_{in} \hat{c}_{in}^2$

Table 3.7: Reference parameters adopted in supersonic flow over wedge.

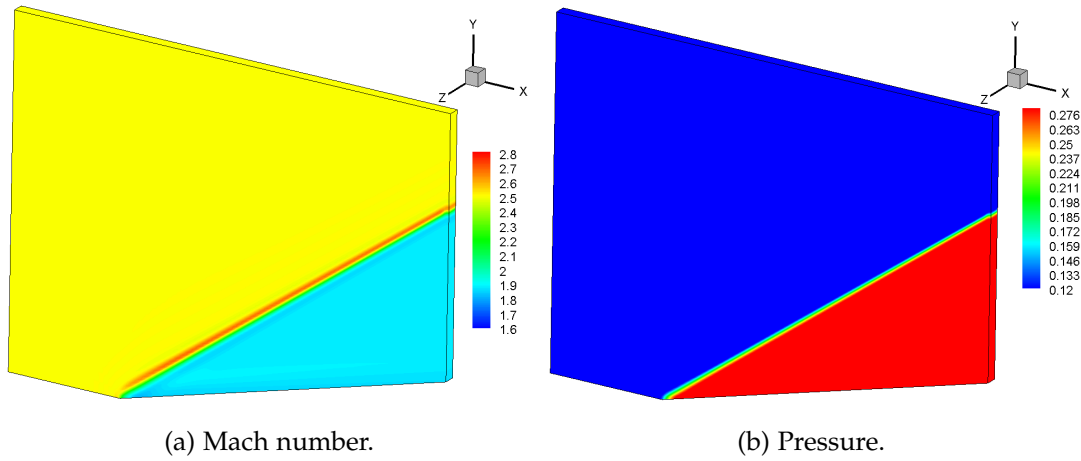


Figure 3.18: Snapshots of CE/SE results.

which makes an angle of $\sim 36.89^\circ$. This matches with the theoretical value of 36.92° very well. The difference is only 0.08%. The pressure variation is also illustrated in Figure 3.18b and the pressure ratio p_2/p_1 is found to be 2.467, which is in excellent agreement with the theoretical value determined by 2.469. This shows that the CE/SE method correctly solves the N-S equations.

3.3.2 Propagation of Acoustic, Vortex and Entropy Pulses in Uniform Flow

The schematic of the case is demonstrated in Figure 3.19. The reference parameters are also shown in Table 3.8. This computational domain is reduced to $-50 < x < 50$ by $-50 < y < 50$ by $0 < z < 2.5$ to speed up computation. Furthermore, the vorticity pulse and entropy pulse are relocated at $x = 33$ such that the acoustic pulse will reach the domain boundary $x = 50$ with the other two pulses at the same time to show their interactions. The tetrahedral mesh is built from uniform structured hexahedral mesh with mesh size of 0.5 in all directions. The uniform flow enters the domain at $M = 0.5$. NRBC-I is applied at the outflow boundaries. SLWBC is also specified as the

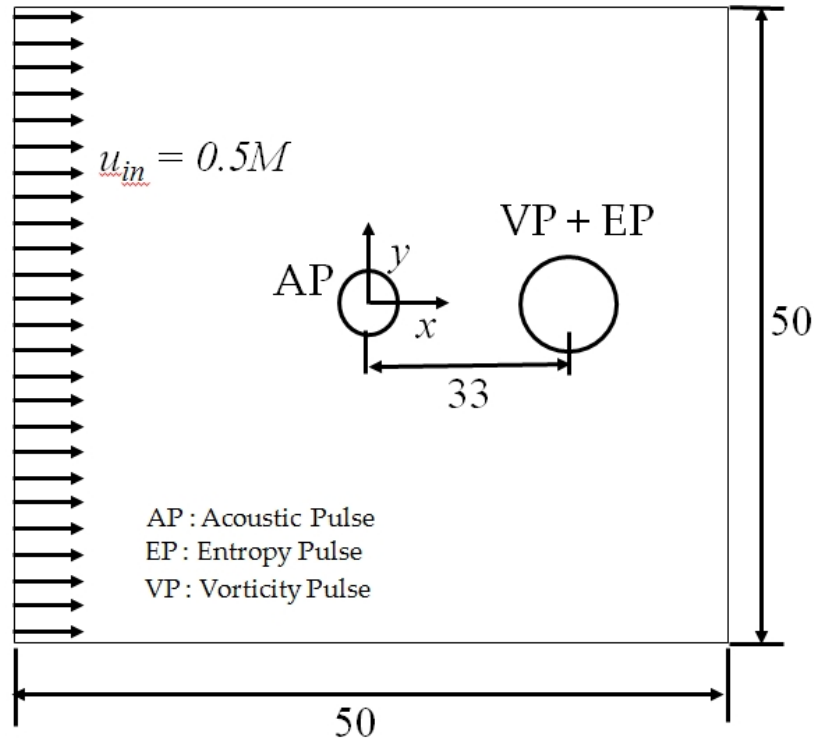


Figure 3.19: Schematic of supersonic flow over wedge.

symmetry condition in the z direction. Finally, the initial condition is given by

$$\begin{aligned}
 \rho &= \rho_{in} + \delta \exp(-\alpha_1 r_1^2) + 0.1\delta \exp(-\alpha_2 r_2^2), \\
 u &= u_{in} + 0.04\delta y \exp(-\alpha_2 r_2^2), \\
 v &= -0.04\delta x \exp(-\alpha_2 r_2^2), \\
 p &= p_o + \delta \exp(-\alpha_1 r_1^2),
 \end{aligned} \tag{3.5}$$

where $\rho_{in} = 1$, $p_o = 1/\gamma$, $\delta = 10^{-3}$, $r_1^2 = x^2 + y^2$, $r_2^2 = (x - 67)^2 + y^2$, $\alpha_1 = -\ln(2) / (3\hat{L})^2$, $\alpha_2 = -\ln(2) / (5\hat{L})^2$ and \hat{L} is the 1/3 half-width of the acoustic Gaussian pulse. The amplitudes of all these pulses are very small compared with the mean uniform flow. The time step Δt is set to 5×10^{-3} and the simulation is calculated up to nondimensional time 60.

Figure 3.20 shows the snapshots of the fluctuations in ρ and u at time $t = 10$ and 30. The density fluctuation $\rho'(x, y, z) = \rho(x, y, z) - \rho_{in}$ and that of u , $u'(x, y, z) = u(x, y, z) - u_{in}$. The acoustic pulse propagates at a normalized speed 1 which is the same as the speed of sound $c = 1$ in this calculation. On

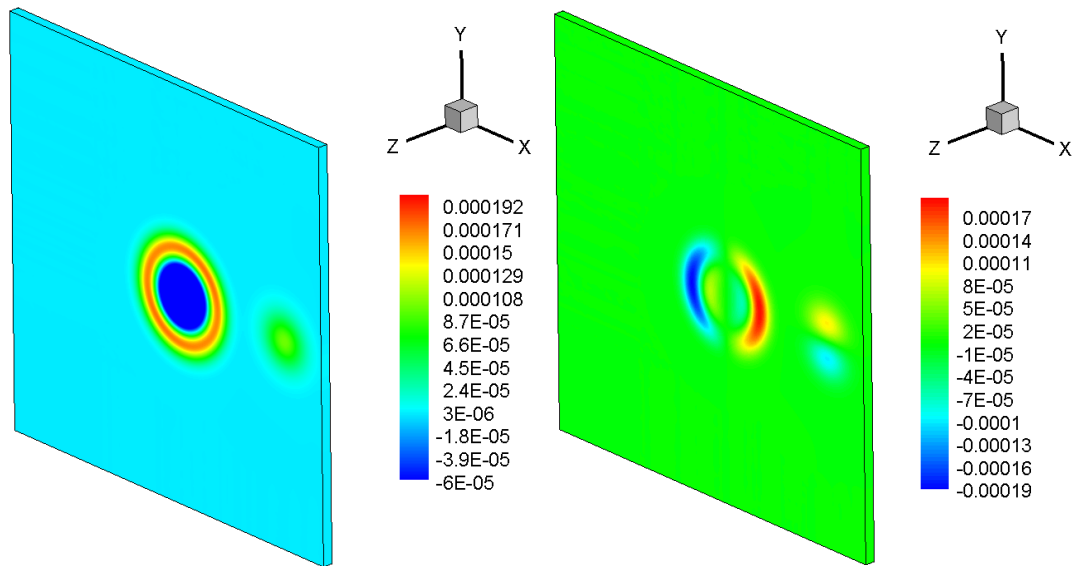
REFERENCE PARAMETERS	PHYSICAL VARIABLES
Length, \hat{L}_o	1/3 half-width of acoustic Gaussian pulse, \hat{L}
Velocity, \hat{u}_o	Acoustic speed, \hat{c}_{in}
Time, \hat{t}_o	\hat{L}/\hat{c}_{in}
Density, $\hat{\rho}_o$	Density at inlet, $\hat{\rho}_{in}$
Pressure, $\hat{\rho}_o \hat{u}_o^2$	Inlet pressure, $\hat{\rho}_{in} \hat{c}_{in}^2$

Table 3.8: Reference parameters adopted in 3D pulses case.

the other hand, the vorticity pulse and entropy pulse travel at the flow speed u_{in} without any dispersion as expected. [Figure 3.21](#) compares the CE/SE results with the analytical results of [Tam \(1993\)](#) at $y = 0$ and it shows that both results are very close. This proves the correctness of the CE/SE method in solving the speed of propagation and in differentiating different types of weak signals in a strong mean flow.

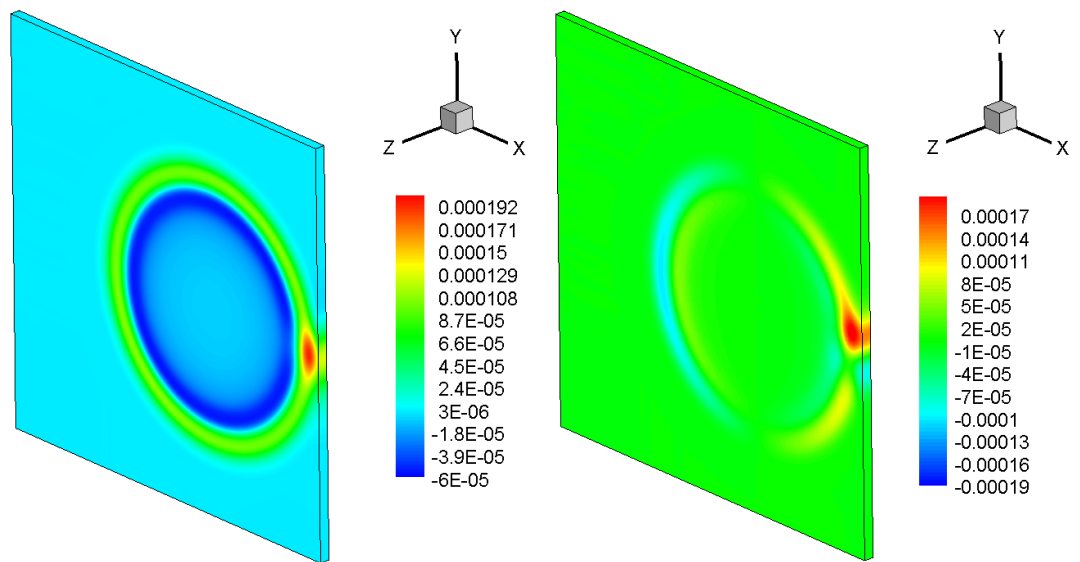
3.3.3 Flow Past Backward Facing Step

Similar to the two dimensional case, backward facing step flow is chosen as a validation case. However, due to the highly limited computational resource available, only a small part around the step rather than whole duct in experiment was simulated. The setup is the same as the one in the two dimensional validation ([Figure 3.3](#)). The size of the computational domain is $-4.713 < x < 14.135$ by $-0.471 < y < 0.499$ by $0 < z < 0.0471$ and the edge of step is located at the origin. The mesh points are clustered near the wall region and the step with minimum mesh $\Delta_{min} = 0.00589$ and the maximum $\Delta_{max} = 0.01178$ located the center of the duct for both x and y direction. In the z direction, uniform mesh size is applied with $\Delta z = 0.01178$ for 10 cells. All the lengths and the velocities are normalized with the height of inflow



(a) Density fluctuation at $t = 10$.

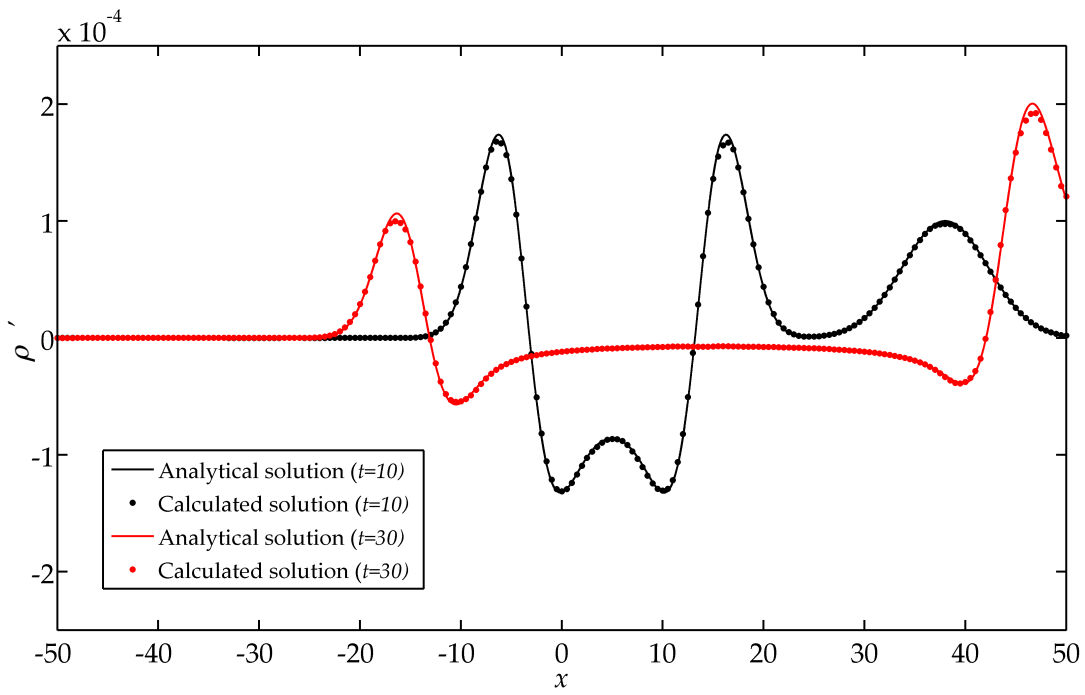
(b) Fluctuation of u at $t = 10$.



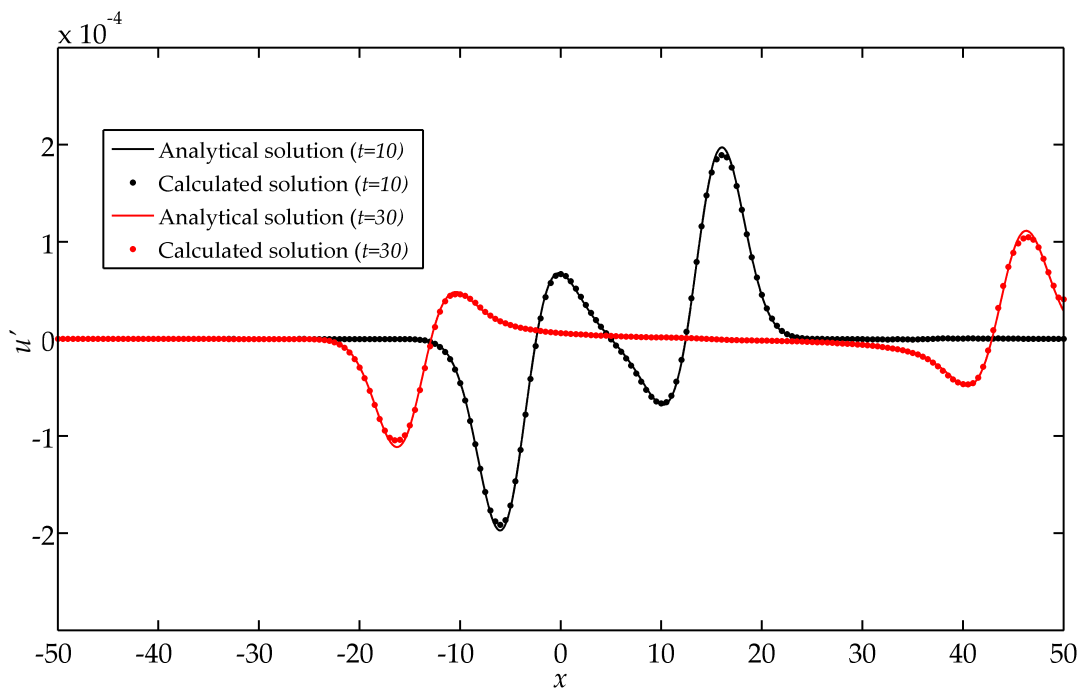
(c) Density fluctuation at $t = 30$.

(d) Fluctuation of u at $t = 30$.

Figure 3.20: Snapshots of results from CE/SE at different time.



(a) Density fluctuation.



(b) Fluctuation of u .

Figure 3.21: Comparison of CE/SE results with analytical solution at $y = 0$.

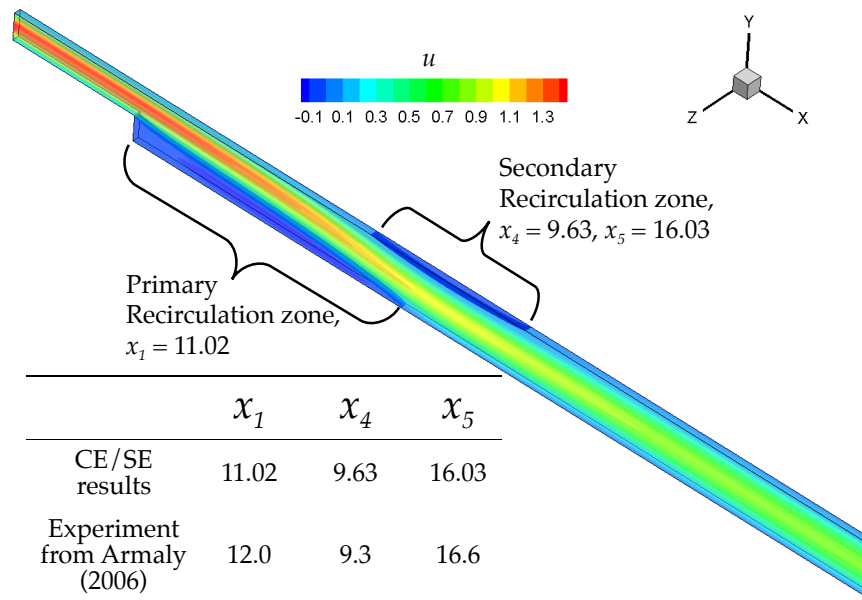


Figure 3.22: Streamwise velocity, u and recirculation zones from CE/SE calculations.

duct, H , and the mean velocity of the parabolic inlet profile, u_{av} . The Reynolds number, Re , and the Mach number, M , are calculated based on these parameters. In these studies, M is equal to 0.1 and the tested Re are taken to be 648. A parabolic velocity profile is applied to the left inlet boundary condition with density, $\rho = \rho_o = 1$ and pressure, $p = p_o = 1/M^2$. At the outlet boundary condition on the right of the domain, the density and pressure are fixed at their reference values while the velocities are taken as those in the boundary cells. All other boundary conditions are the NSWBC-NW. Buffer zones D_o of length 4.712 are applied to the inlet boundary and outlet boundary. Grid stretching is used in these zones. The applied boundary conditions are the same as those of the two dimensional backward facing step case except that the symmetric boundary condition is applied to the side boundaries. The time step Δt is 10^{-4} and the simulation is calculated until it reaches the steady state solution.

Figure 3.22 illustrates the time-stationary solution of this case and the comparison with the experimental results of Armaly et al. (1983). The calculated results are in a good agreement with the experimental results for the locations of both primary and secondary recirculation zones. The slight difference is most possibly due to the fact that only a slender central section

of the duct was simulated in the case, which may not accurately capture the original geometry used in experiment, and the two dimensional character still dominates the simulation. As claimed by [Armaly et al. \(1983\)](#), the flow past backward facing step exhibits three dimensional characteristics when $Re > 400$ and from their results, the three dimensionality mainly exists nearly the side wall, which is not simulated in the current calculation. Thus, it is reasonable to have some discrepancies in the calculation. However, the CE/SE method can still capture the recirculation zones extremely well.

3.4 CONCLUDING REMARKS

In the previous investigations of aeroacoustic problem, the CE/SE method is adopted in very few works, e. g., [Loh & Hultgren \(2006\)](#) and they mainly focused on the supersonic flow region, such as jet screeching. Therefore, the capability of the CE/SE method in dealing with the aeroacoustic problem, especially in the low Mach number flow such as the merging flow at duct junction, has not been assessed. In this chapter, the CE/SE method is vigorously assessed with carefully selected benchmark cases because DAS requires a highly accurate and low dissipative solver. The spatial resolution of CE/SE method is performed. It is observed that the CE/SE method performs very well when the number of cells per wavelength is at least 10. In the two dimensional situation, the chosen cases are i) flow past backward facing step, ii) acoustic propagation through duct junction, iii) aeolian tone generated by flow past a square cylinder and iv) acoustic absorption through in-duct orifice. Each case represents a situation frequently encountered in the DAS. Furthermore, the mesh is carefully designed to meet the requirement of resolving the flow and acoustic features in each case. The CE/SE method produced excellent results in good agreement with those of the corresponding experiments and numerical simulations. This shows that the CE/SE method

can accurately capture the interactions between the aerodynamic and acoustic field.

On the other hand, due to the high resolution of mesh requirement in the spanwise direction of these cases in three dimensions and the lack of computational resources, validation cases requiring less computational resources are considered. Since the DAS requires a solver that can correctly solve the N-S equations and can distinguish different signals of disparate scales, two cases are chosen for the validation in three dimensions, i. e., supersonic flow over wedge and the propagation of weak acoustic, vortex and entropy pulses in strong uniform flow. In addition, it is important to validate the method using a case similar to the merging flow at duct junction, so the flow past backward facing step is revisited, in which a thin section is simulated. Excellent agreements are obtained between the results from the CE/SE method and those of corresponding experiments and theory. All these validations have established the correctness of the CE/SE method in capturing the aeroacoustical physics. Therefore, it can be applied to investigate the aeroacoustics of merging flow at duct junctions in both two and three dimensions.

TWO DIMENSIONAL MERGING FLOW AT DUCT JUNCTIONS

In this chapter, the two dimensional investigation of the sound generation mechanism of merging flows at duct junctions is discussed. Although the flow development in the spanwise direction is ignored in the two dimensional simulation, it still serves as a good starting point to the problem investigation. The CE/SE method is applied for all the numerical studies hereafter. First of all, the merging flow at duct junctions is formulated for the two dimensional numerical investigations and its general aeroacoustic features will be discussed together with the fundamental physics about the flow. This includes the discussions on the mean field, the unsteady aerodynamics and finally the sound generation. Then, a parametric study on the aeroacoustics is carried out with two parameters - the velocity ratio between two inlet flows VR , and the merging angle θ .

4.1 FORMULATION OF THE PROBLEM

The computational domain of a main duct with a slanted side branch is illustrated in [Figure 4.1](#) and the reference parameters adopted are shown in [Table 4.1](#). The nondimensional length of each branch is 20 with the width being 1. Buffer zones, D_I and D_o of length 10 are applied to all duct inlets and outlet in the computational domain. The origin is located at the upstream corner of the duct junction and θ is the merging angle between the two branch center lines. The projection of side branch opening x_{dj} onto the opposite duct wall varies with θ as a result of constant duct width. [Table 4.2](#) shows the variation of x_{dj} with θ . The flow enters the domain through duct inlets I_1

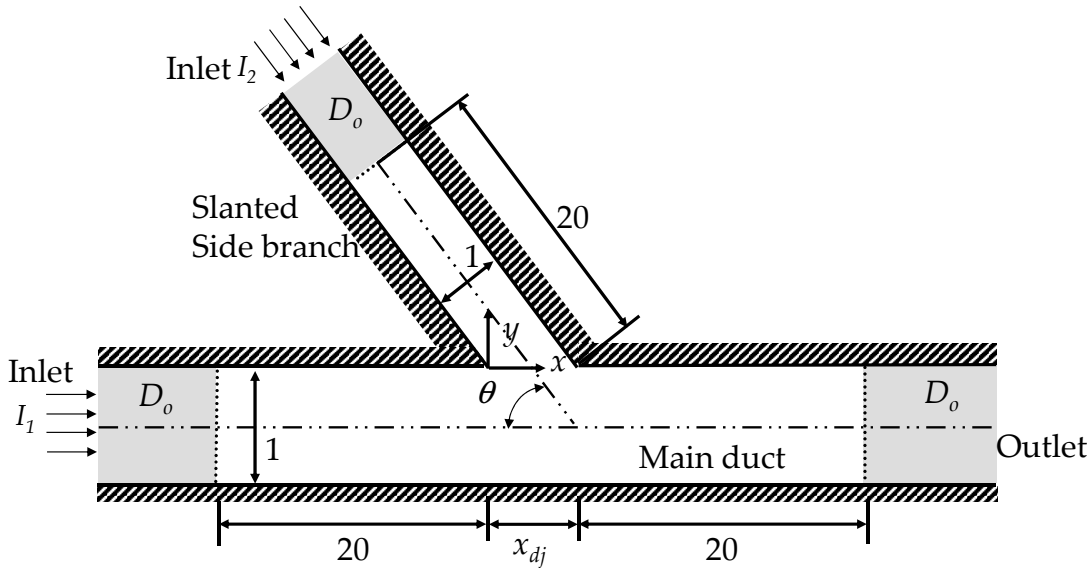


Figure 4.1: Schematic of the merging flow problem.

REFERENCE PARAMETERS	PHYSICAL VARIABLES
Length, \hat{L}_0	Width of duct, \hat{W}
Velocity, \hat{u}_0	Maximum velocity at I_2 , $\hat{u}_{2,max}$
Time, \hat{t}_0	$\hat{W} / \hat{u}_{2,max}$
Density, $\hat{\rho}_0$	Density at inlets, $\hat{\rho}_{in}$
Pressure, $\hat{\rho}_0 \hat{u}_0^2$	Inlet pressure, $\hat{\rho}_{in} \hat{u}_{2,max}^2$

Table 4.1: Reference parameters adopted in this chapter.

(main flow) and I_2 (side flow). The merged flow leaves the computational domain through outlet on the right. Furthermore, the Mach number M and the Reynolds number Re based on the reference parameters are 0.1 and 2.3×10^5 respectively.

The boundary conditions applied on all duct walls are the NSWBC-NW with wall modeling for turbulent flow (Section 2.5.2). NRBC-II is applied to duct outlet with outlet pressure taken as the reference pressure. The two inflow mean velocity profiles are assumed taking the shape of a fully developed turbulent velocity profile which is given by the classical logarithmic law, i. e.,

$$u^+ = \frac{1}{\kappa} \ln y^+ + C, \quad (4.1)$$

MERGING ANGLE θ	x_{dj}
30°	2.000
45°	1.414
60°	1.155
90°	1.000

Table 4.2: Variation of projection of side branch opening x_{dj} with θ .

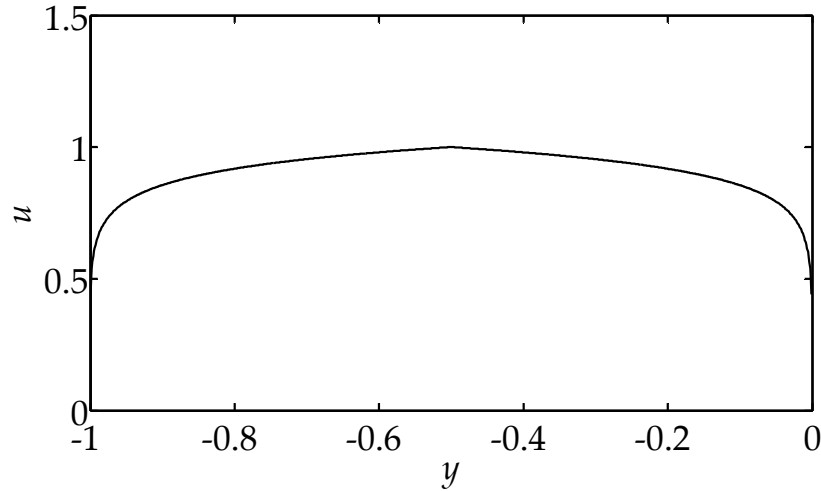


Figure 4.2: Mean velocity profile of the inflows at I_1 .

where $u^+ = u/u_\tau$, $y^+ = y\rho_w u_\tau Re/\mu_w$, u_τ is the friction velocity, ρ_w is the density at wall, μ_w is the viscosity at wall, $\kappa = 0.41$ and $C = 5.0$. u_τ is estimated by solving Eq.(4.1) with ρ_w , μ_w and u at $y = 0.5$. Figure 4.2 shows this velocity profile across the duct inlet section. Although this law is originally developed for the incompressible flow, it is still a good approximation for the present problem because the Mach numbers of the cases studied in this chapter are much below the compressibility limit ($M = 0.3$) (Babu 2008). No flow disturbance is imposed at the duct inlets.

The mesh is designed to meet the requirement for turbulent flow simulation. The mesh points are clustered near all the walls and relaxed towards the center line of the duct. The maximum mesh size $\Delta x_{max} = 0.015$ at the center of the duct and its minimum $\Delta x_{min} = 0.001$ at the walls, which corresponds to the wall unit, $y^+ = 16$ at the specified $M = 0.1$. There are roughly 20 meshes inside the turbulent boundary layer. When the flow speed is increased

CASE NUMBER	VR	θ
N-0.5-90	0.5	90°
N-0.67-90	0.67	90°
N-1.0-90	1	90°
N-2.0-90	2	90°
N-0.67-60	0.67	60°
N-1.0-60	1	60°
N-0.67-45	0.67	45°
N-1.0-45	1	45°
N-0.5-30	0.5	30°
N-0.67-30	0.67	30°
N-1.0-30	1	30°

Table 4.3: Description of simulated cases.

to $M = 0.2$, i. e., the maximum M in the present investigation, there are still about 16 meshes inside the boundary layers. Thus, the boundary layers are sufficiently captured by the mesh distribution.

For each calculation, an approximate steady state solution obtained from a separate calculation on a coarser mesh is taken as the initial condition. After the solution becomes steady with large time increment, the calculation proceeds up til a duration of 40 with the mesh defined above so as to obtain a time stationary solution. The time increment Δt is between 5×10^{-4} and 6.25×10^{-4} for all cases.

A series of cases are simulated with different combinations of velocity ratio VR and merging angles θ (Table 4.3). In the present study, the velocity ratio VR is defined as

$$VR = \frac{\widehat{u}_{2,max}}{\widehat{u}_{1,max}} = \frac{u_{2,max}}{u_{1,max}}, \quad (4.2)$$

$\theta \setminus VR$	0.5	0.67	1	2
30°	★		★	
45°		★		
60°				
90°	★		★	★

Table 4.4: Selected cases for illustrating the general aeroacoustic features.

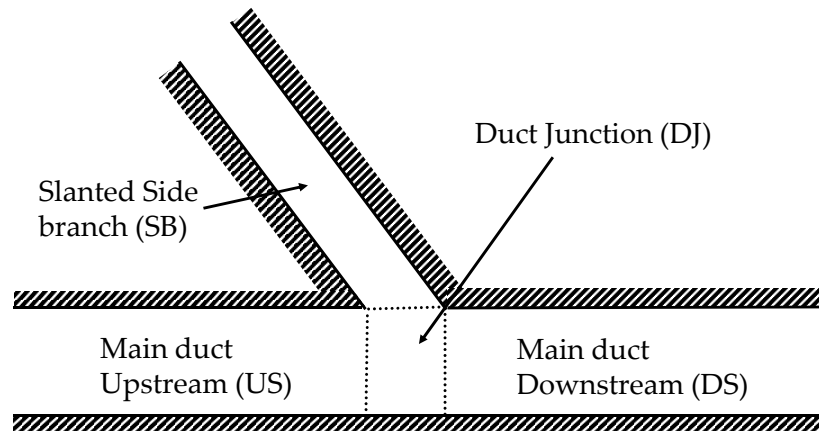


Figure 4.3: Different regions in the merging flow problem.

where $\hat{u}_{1,max}$ and $\hat{u}_{2,max}$ are the maximum velocity at inlet I_1 and I_2 respectively.

4.2 AEROACOUSTICS OF MERGING FLOW

In order to better understand the flow dynamics and aeroacoustics of the merging flow, the solutions of cases marked in Table 4.4 are analyzed and discussed. These cases are chosen because their numerical results altogether reveal the distinct aeroacoustic features of the merging flows at duct junction. Thus, we will focus on these selected cases in this part. On the other hand, in order to ease the forthcoming discussions, the computational domain is separated into four regions, namely US, DJ, SB and DS, as demonstrated in Figure 4.3.

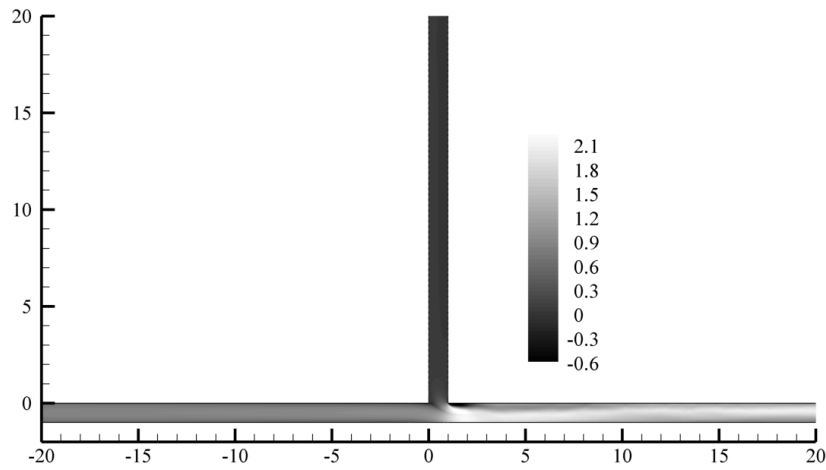
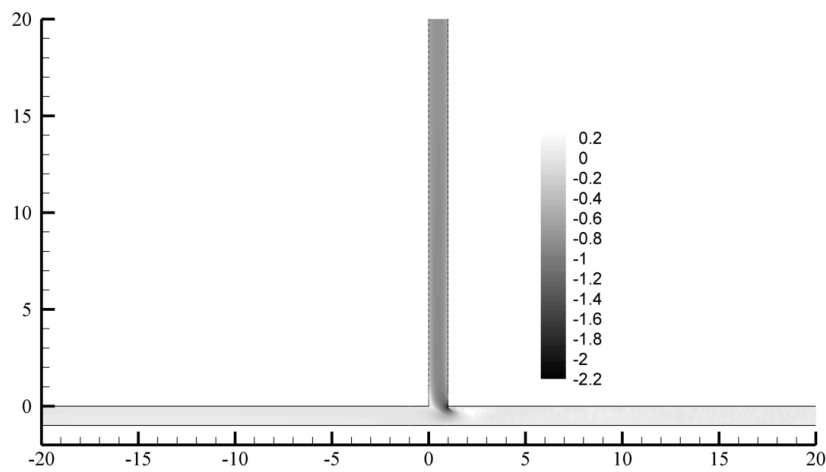
(a) u_{mean} .(b) v_{mean} .

Figure 4.4: Mean flow for N-1.0-90.

4.2.1 Mean Flow

When the information of a mean flow is available, its instability behavior can be predicted using classical linear stability theory such as the methods described in [Betchov & Criminale \(1967\)](#). Although it does not tell directly how the unsteadiness evolves in the flow, it is still able to reveal the locations where the flow unsteadiness emerges. Therefore, the mean flow is discussed here first. In all cases mentioned, the mean flow is obtained by averaging the results within a time period of 20 counting back from the end of calculation with an time increment of 0.2.

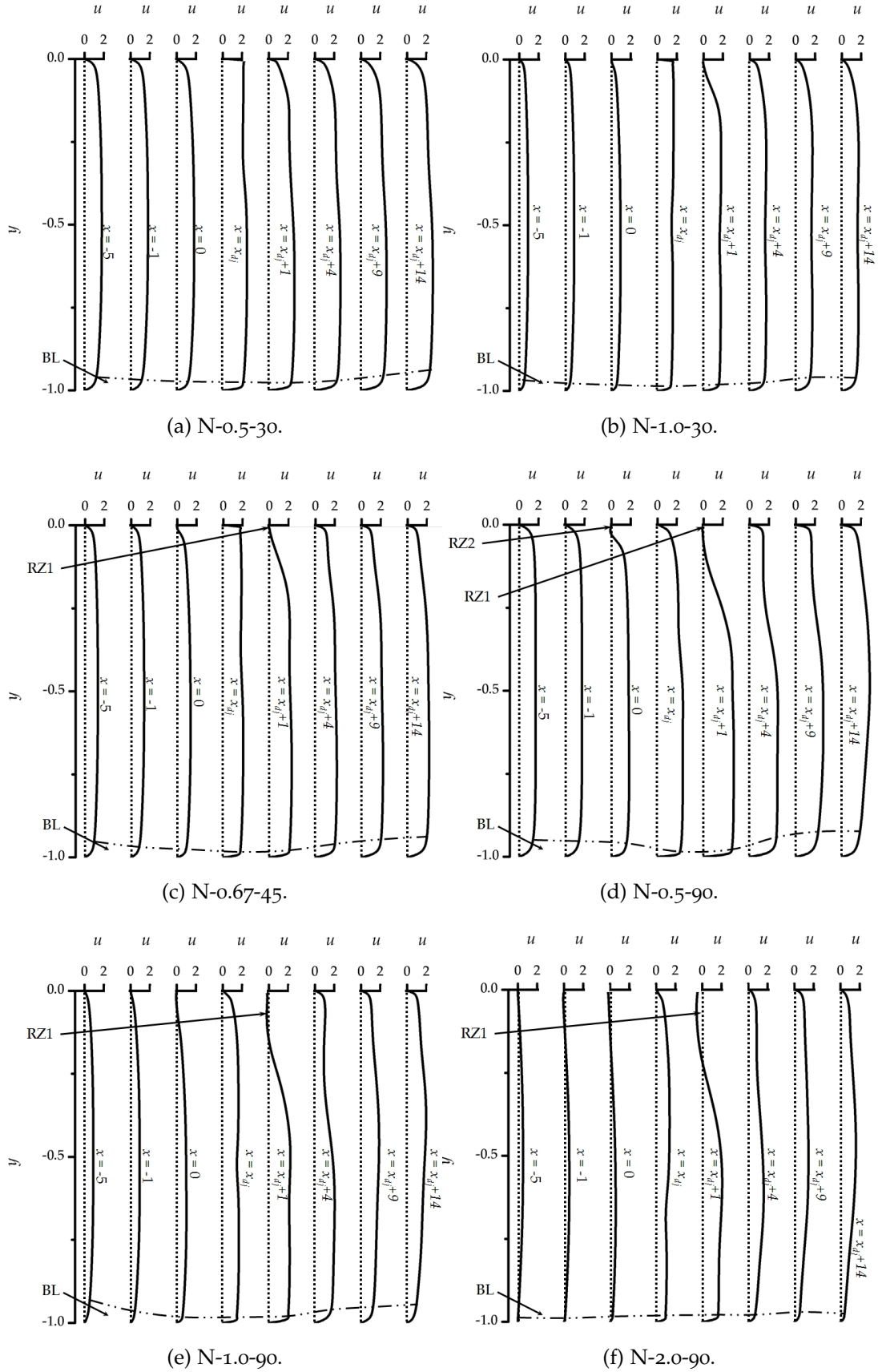


Figure 4.5: Profile of u_{mean} over the domain for different cases. BL denotes the approximated boundary layer. RZ1 and RZ2 denote the first and second recirculating zones respectively.

Flow Velocity

The mean flow velocity fields (u_{mean} and v_{mean}) for case N-1.0-90 is shown in [Figure 4.4](#). The velocity distributions almost keep unchanged in US and SB and flow features start to evolve near DJ. Similar behavior is observed in all the simulated cases. [Figure 4.5](#) illustrates u_{mean} along different cross-sections of main duct for the selected cases. In general, as the flow approaches to the duct junction ($x = 0$), its velocity profiles in the main duct are gradually distorted due to the merging of the two flows and a small recirculating region is formed at the upstream corner. At $x \geq 0$ (DJ), the flows from inlets I_1 and I_2 merge together and accelerate to a speed higher than the sum of speed at the two inlets due to the restriction imposed by recirculating zones RZ1 and RZ2. The velocity profile then recovers to a symmetric profile when the flow further convects downstream. Furthermore, the boundary layer near the lower wall (BL) is squeezed to very thin at the beginning of the downstream branch and then recovers further downstream.

Vorticity

In order to further illustrate the distinct flow features of this problem near DJ, the mean vorticity is discussed in this section.

[Figure 4.6](#) shows the mean vorticity, ω_{mean} , near DJ on which streamlines are also plotted in white. Illustrated from these cases, the flow near DJ generally consists of three key features. The first one is the recirculating zone RZ1 formed at the downstream corner of DJ; the second one is the recirculating zone RZ2 formed at the upstream corner of DJ while the last one is the thin, curved shear layer SL generated between these two flows at DJ. Such kind of distinct pattern is also observed in the work of [Hirota et al. \(2006\)](#), although he studied the merging flow with two different temperatures at a lower Re ($\approx 10^4$) than the present investigation.

In [Figure 4.6](#), the semi-oval RZ1 consists of two counter-rotating zones. It also contains the highest vorticity among the three key features of the flow.

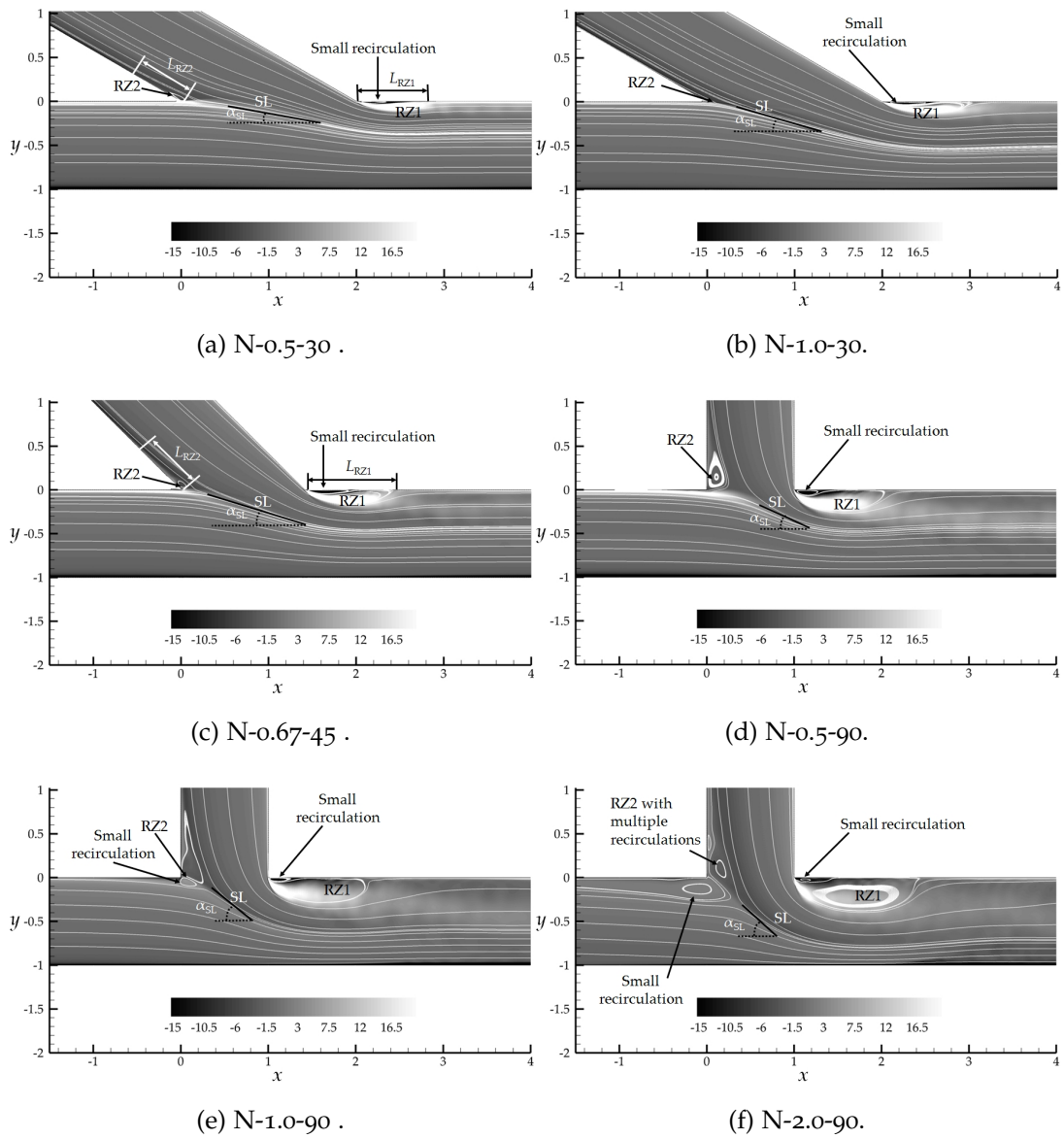


Figure 4.6: Mean vorticity ω_{mean} near the duct junction for different cases.

$\theta \setminus VR$	0.5	0.67	1	2
30°	0.734		1.03	
45°		1.025		
60°				
90°	1.089		1.170	1.469

Table 4.5: Reattachment length L_{RZ1} for selected cases.

When the non-parallel flows meet at the upstream edge of DJ (Figure 4.3), the y -momentum of the side flow presses the main flow downward and creates a separation from the edge. The flow then covers up this separation zone later and forms a recirculating zone. It can be characterized by the reattachment length L_{RZ1} ; its variation with VR and θ is tabulated in Table 4.5. An increase in VR will slightly increase L_{RZ1} . The merging angle θ also has the same influence on L_{RZ1} . This is because the increase in VR and θ both effectively increases the ratio of y -momentum to x -momentum of the merging flow.

The second key feature, RZ2 in Figure 4.6, consists of recirculating zones attached to the upstream edge of DJ. Sometimes in cases like N-1.0-90, a recirculating zone in US also exists as a result of the high flow velocity in the side branch. Generally, RZ2 is caused by an early separation of flow in SB and US before reaching DJ, which is induced by the impinging flow at DJ. This zone can also be characterized by the separation length of the flow in the slanted duct L_{RZ2} as shown in Figure 4.6. Its variations with VR and θ are tabulated in Table 4.6. In general, L_{RZ2} decreases with an increase in VR , but increases with θ .

The last feature of the merging flow is the thin, curved shear layer SL generated between these two separated flows at DJ. SL is formed downstream of RZ2. Its characteristics can be described with an inclined angle α_{SL} from main duct (Table 4.7). In general, α_{SL} increases with both VR and θ as a result of the increased ratio of y -momentum to x -momentum of the merging flow.

$\theta \setminus VR$	0.5	0.67	1	2
30°	0.495		0.3705	
45°		0.858		
60°				
90°	1.387		1.461	0.903

Table 4.6: Separation length L_{RZ2} for selected cases.

$\theta \setminus VR$	0.5	0.67	1	2
30°	9.69°		16°	
45°		16.46°		
60°				
90°	29.51°		38.15°	41.78°

Table 4.7: The initial angle between the shear layer and the main duct, α_{SL} .

4.2.2 Unsteady Flow Dynamics

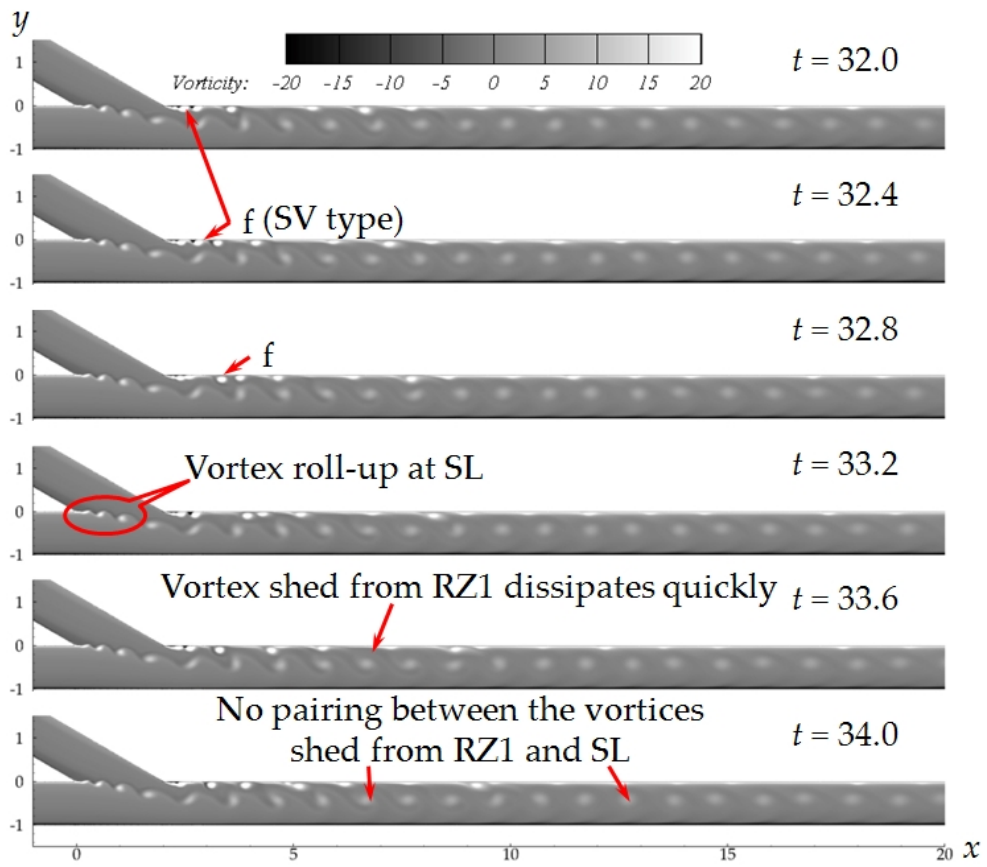
The previous section has demonstrated the three distinct flow features in the merging flow at duct junction. They all exhibit the strong velocity gradients developed at the vicinity of both upstream and downstream edge of DJ (Figure 4.5). According to classical linear stability theory (Browand 1966, Potter 1967), these locations are susceptible to the disturbances, which may cause the roll-up of vortex, leading to vortex shedding eventually. Since the present cases involve highly non-parallel flows, it is very difficult to determine the shedding frequency quantitatively by using linear stability theory. Therefore, it is not applied in the present study to predict the shedding frequency. Instead, this frequency is obtained through the inspection of instantaneous vorticity and the FFT analysis of pressure fluctuation at the selected locations. Thus, we will start at the observations on instantaneous vorticity for the discussion of the general unsteady flow dynamics.

Figure 4.7 to Figure 4.9 show the snapshots of instantaneous vorticity for the selected cases from time $t = 32$ to $t = 34$. Generally, vortex shedding phenomena near DJ can be classified into two scenarios. In the first one, the vortex shedding only occurs at RZ1 as shown in Figure 4.9a. In the second scenario, there is vortex roll-up at SL in addition to the vortex shedding at RZ1, as illustrated in Figure 4.7a. Thus, the flow unsteadiness only involves RZ1 and SL, but not RZ2. Furthermore, the vortex shedding at RZ1 occur at all cases while the vortex roll-up at SL can only be observed when $VR \leq 0.67$.

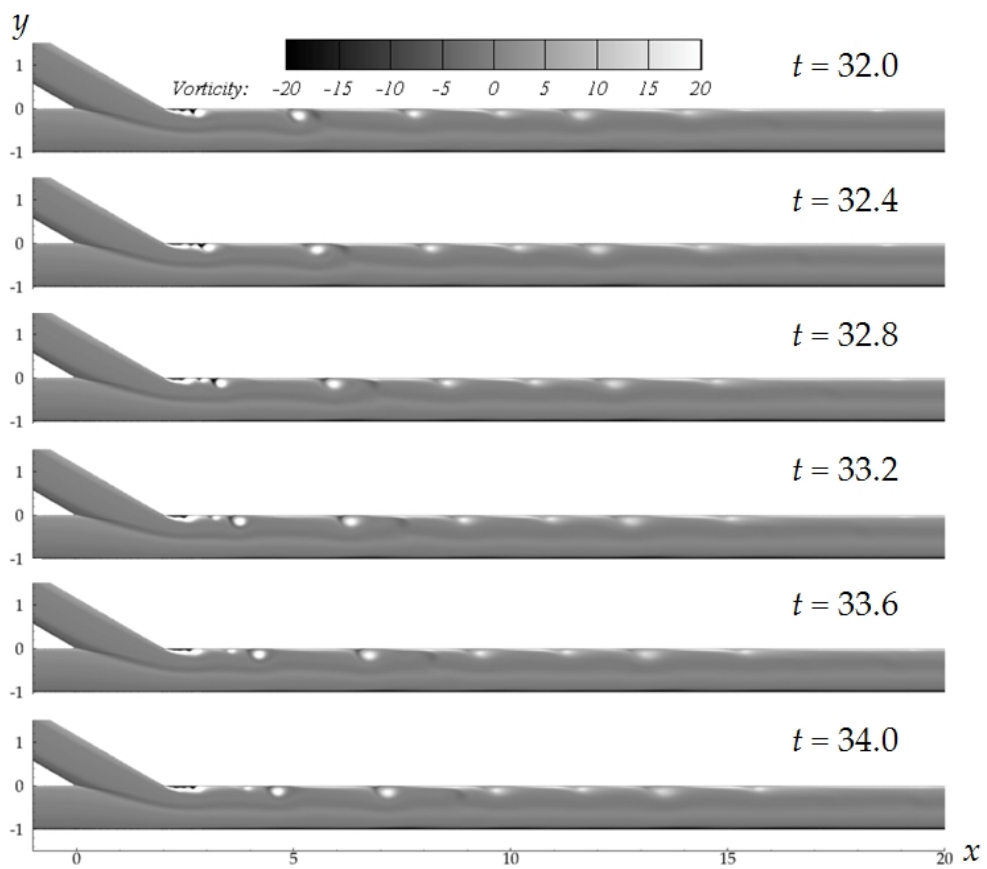
Based on these three figures, the interactions of the vortices from RZ1 and SL greatly depend on the path and the strength of vortices shed at RZ1. In N-0.5-30 (Figure 4.7a), the vortices from RZ1 stick to the upper wall and are dissipated rather quickly. No vortex pairing are observed between the vortices from RZ1 and SL. Their interaction is relatively weak. Thus, the flow pattern in DS is quite regular. On the contrary, in N-2.0-90, rather large vortices are shed at RZ1. Although they also suffer from turbulent dissipation, they are still sufficiently strong to engulf SL during propagating downstream such as Vortex a in Figure 4.9b, leading to intense interactions. The vortices shed at RZ1 also bounce between the walls and induce strong secondary vortices near the wall, e. g., Vortex b in Figure 4.9b. All these vortices undergo vigorous pairing further downstream in DS, e. g., Vortex c, d and e forming Vortex c+d+e in Figure 4.9b. Therefore, the flow in DS is less regular.

In general, the vortex shedding at RZ1 consists of two types. The first type, denoted by SV, is the primary vortex shedding, in which a single vortex is shed each time, such as Vortex f in Figure 4.7a. The second type, denoted by VP, is the shedding of a relatively large vortex, which is evolved from vortex pairing at RZ1 when the vortices just roll up. For example, Vortex g and h pair together to form Vortex g+h at RZ1 in Figure 4.9a. In each case, both types of shedding may occur, but its dominant type is case dependent.

As aforementioned, the frequency of vortex shedding $f_{s,RZ1}$ is obtained from the FFT analysis of the signals captured at selected location and inspecting the plots of instantaneous vorticity. The locations are chosen such that they

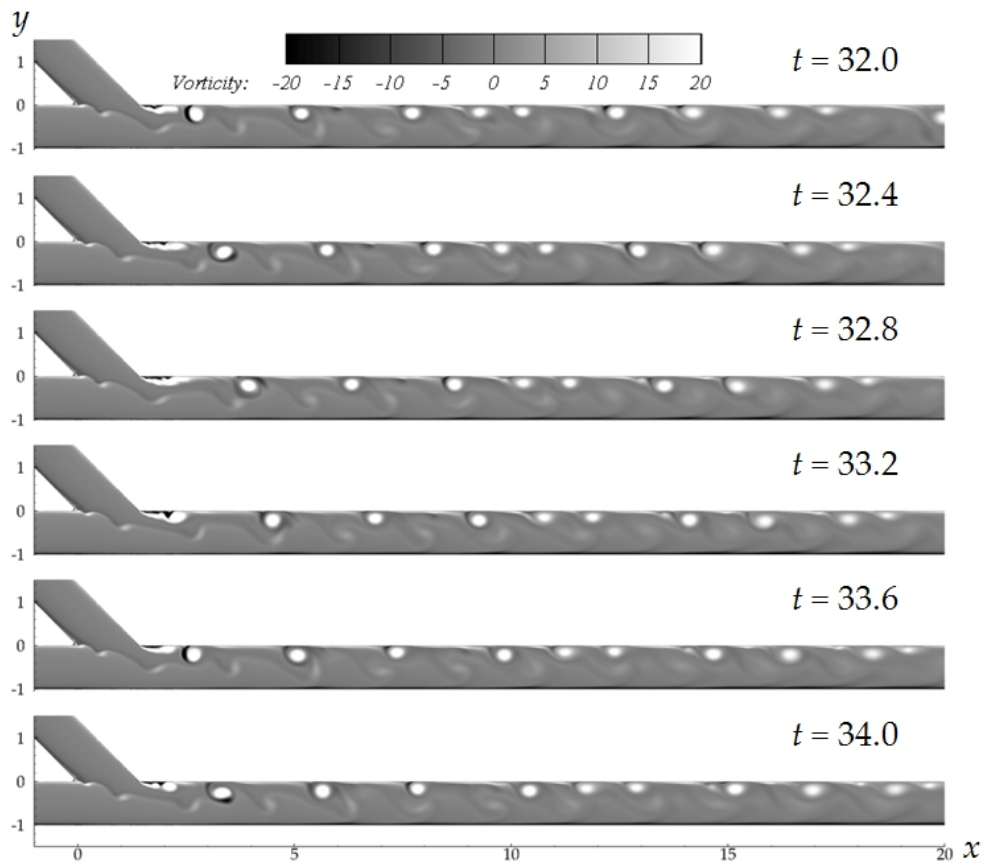


(a) N-0.5-30.

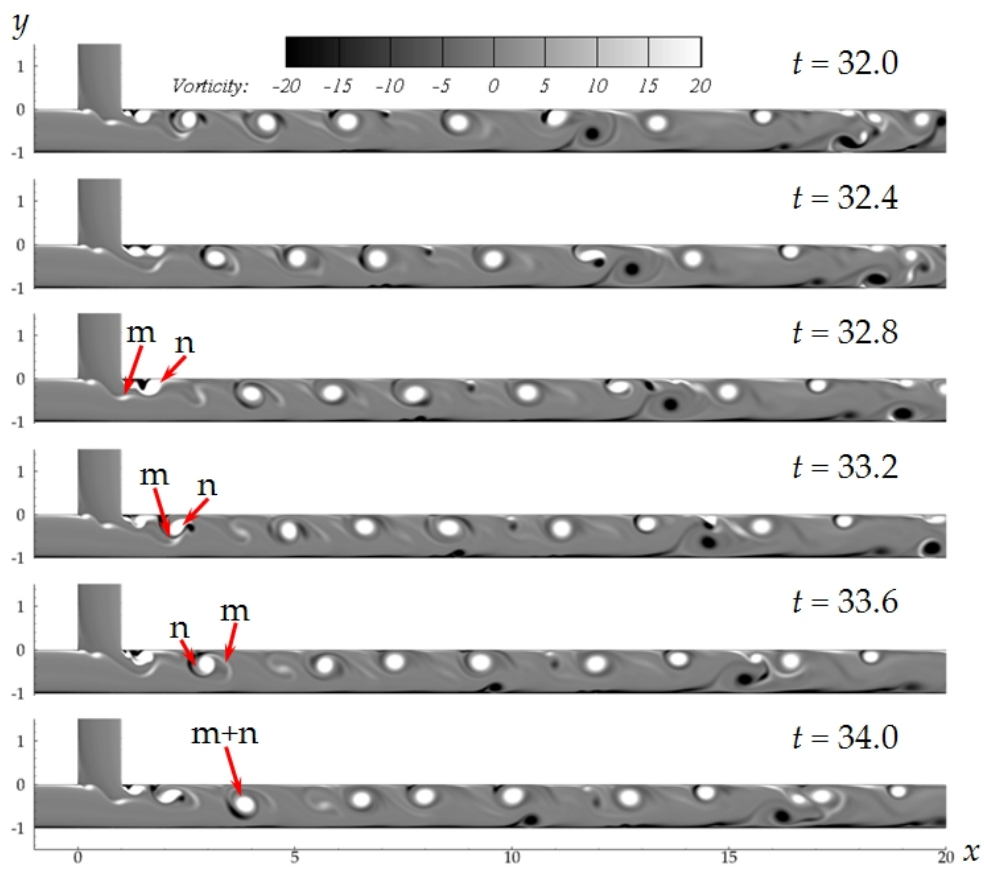


(b) N-1.0-30.

Figure 4.7: Snapshots of vorticity.

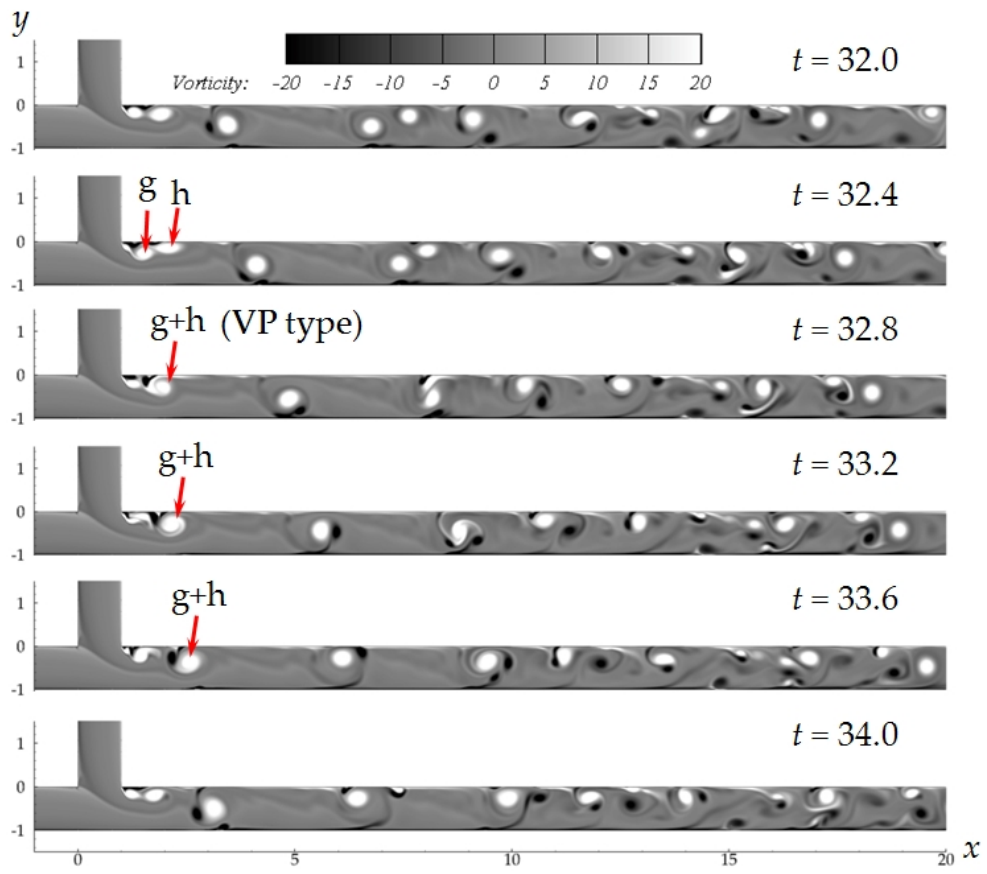


(a) N-0.67-45.

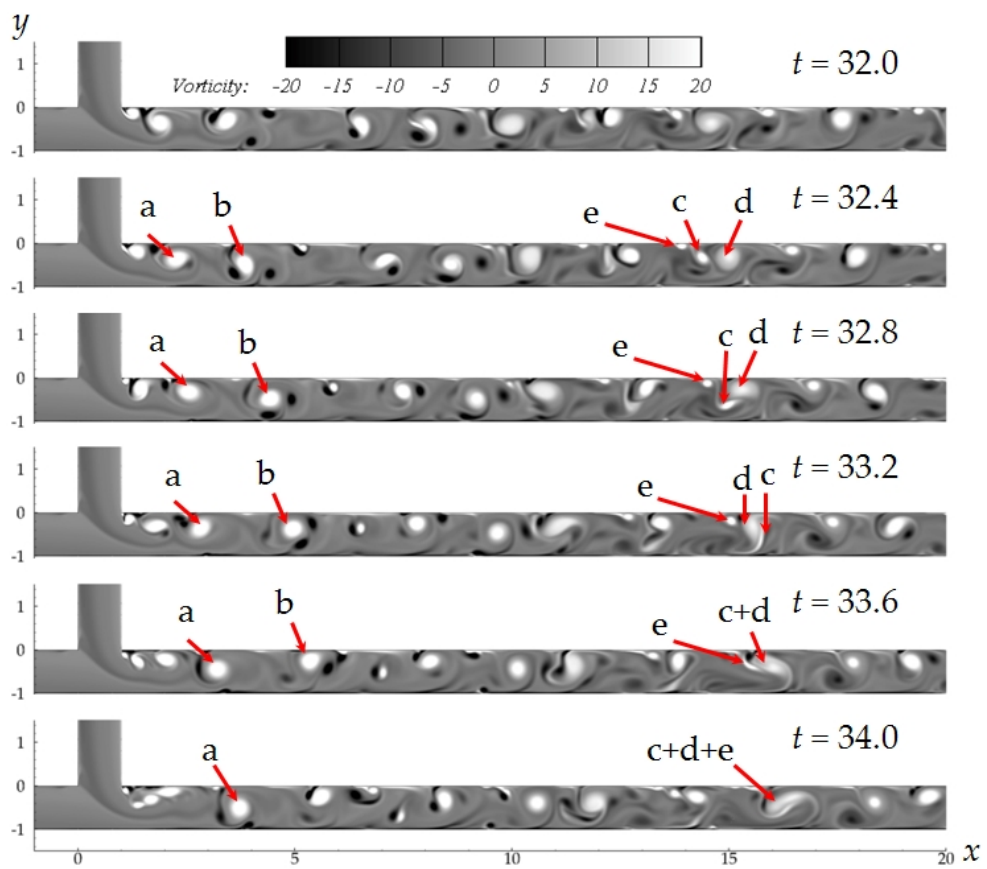


(b) N-0.5-90.

Figure 4.8: Snapshots of vorticity.



(a) N-1.0-90.



(b) N-2.0-90.

Figure 4.9: Snapshots of vorticity.

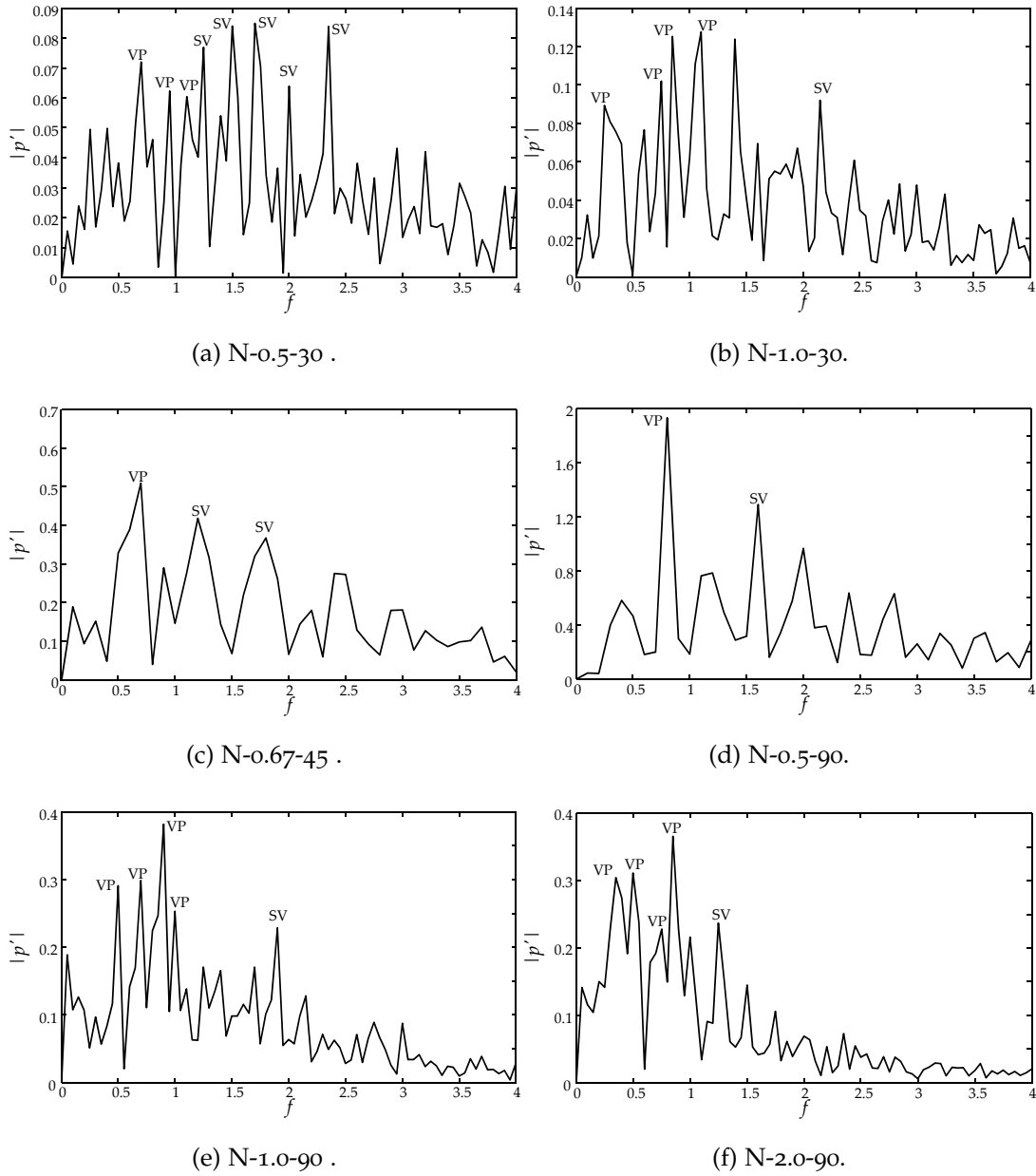


Figure 4.10: Spectra of pressure fluctuation calculated at a location between $(x_{dj} + 1, -0.2)$ and $(x_{dj} + 2, -0.2)$.

align along the path of vortex shedding. Based on this criterion, for each case attempted, a point lying between $(x_{dj} + 1, -0.2)$ and $(x_{dj} + 2, -0.2)$ is chosen for FFT analysis. Figure 4.10 shows all the spectra obtained. Multiple dominant peaks spread over $0 < f < 3$ and this indicates the complexity of the vortex shedding. The peaks associated with SV and VP are also marked in this figure. To illustrate clearly the dominant effect, each spectrum is normalized by its respective maximum amplitude, $|p'_{max}|$, and those normalized peaks with amplitude > 0.6 are plotted again in Figure 4.11. The shedding type is also determined from inspecting the plots of instantaneous vorticity in each case. $f \sim 1.1$ is observed to be the watershed of the shedding types. Generally, the frequency of SV is higher than that of VP because the pairing process occurs only after the roll-up of at least two single vortices. Thus, VP takes a longer time to evolve than SV does. Furthermore, while VR has little influence on the dominant type of shedding, the type changes with θ significantly. In cases with $\theta \leq 45^\circ$, SV dominates the vortex shedding at RZ1, but VP is the dominant type of vortex shedding when $\theta = 90^\circ$. On the other hand, VR may influence the shedding frequency of SV. Multiple frequencies are observed for SV especially when VR is small, e. g., N-0.5-30 in Figure 4.10a. This is caused by the interactions of the vortices rolled up at SL during their transports near RZ1. In the cases where vortices do not roll up at these two regions (N-1.0-30, N-1.0-90 and N-2.0-90), they usually exhibit single frequency for SV.

Regarding the case dependent vortex roll-up at SL such as N-0.67-45 in Figure 4.8a, the streamwise velocity profiles u at $x = 0.05$ (near the upstream edge of DJ) for the selected cases are plotted in Figure 4.12. Strong velocity gradient at SL may give rise to the Kelvin-Helmholtz instability (such as for the cases of N-0.67-45 and N-0.5-90). On the other hand, no vortices roll up when this velocity gradient is weak, e. g., in N-1.0-90. Instead SL oscillates in these cases and Hirota et al. (2010) suggested that this is caused by the fluctuation of streamwise velocity u .

After the vortices roll up at SL, they are convected downstream along SL and interact with the vortices shed from RZ1. The extent of interactions

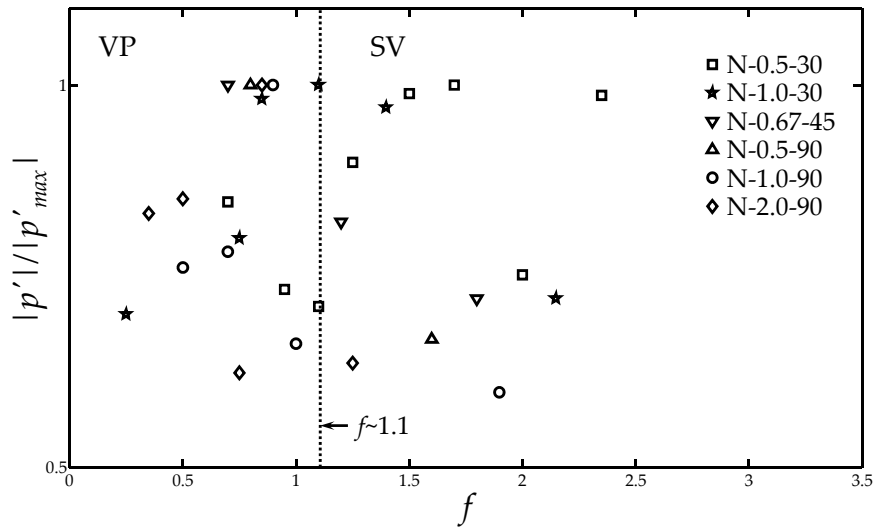


Figure 4.11: Vortex shedding frequency of different cases, $f_{s,RZ1}$. SL marks the frequency of vortex roll-up at SL respectively.

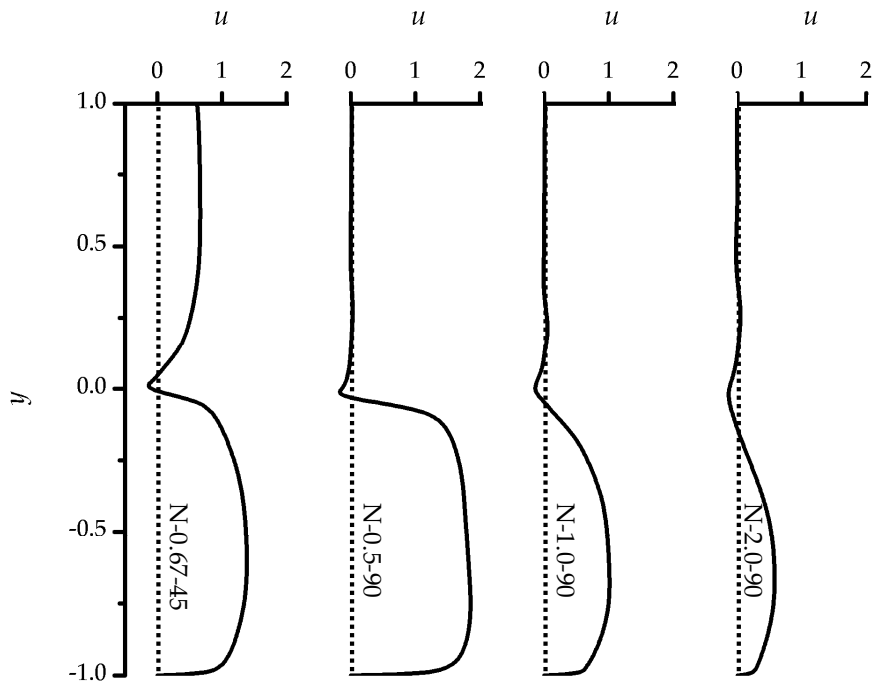


Figure 4.12: Streamwise velocity profile u along $x = 0.05$. Both N-0.67-45 and N-0.5-90 have large velocity gradient at SL (near $y = 0$), leading to vortex shedding at SL. The other two cases have a small velocity gradient at SL, thus no vortex shedding occurs at SL.

$\theta \setminus VR$	0.5	0.67	1	2
30°	2.35			-
45°		0.8		
60°				
90°	1.6		-	-

Table 4.8: The frequency of vortex rolling up at SL $f_{s,SL}$.

greatly depends on the sizes and the strengths of the vortices shed at RZ1. For example, in N-0.5-90 (Vortex m and n in Figure 4.8b), the vortices rolled up at SL (m) always pair with the strong vortices shed from RZ1 (n). On the other hand, in N-0.5-30, where the relatively weak vortices are shed from RZ1, vortex shedding is observed at SL but their interaction with those at RZ1 is insignificant.

The frequency of vortex roll-up at SL, $f_{s,SL}$, is listed in Table 4.8. It shows that both VR and θ affects $f_{s,SL}$. In contrast to the vortex shedding at RZ1, the pattern of vortex roll-up here is rather regular and the vortex pairing usually does not occur near the upstream edge of DJ. Although the vortex roll-up at SL may excite the vortex shedding at RZ1, $f_{s,SL}$ is generally not equal to $f_{s,RZ1}$ because $f_{s,RZ1}$ occurs at harmonic of forcing frequency closest to the most unstable frequency, rather than the forcing frequency as pointed out by Ho & Huang (1982).

Reynolds Stresses

The relative strengths of these flow unsteadiness can be illustrated by comparing their mean resolved Reynolds stresses. The Reynolds stresses expresses the level of intrinsic flow fluctuations, so they can indicate the extent of unsteady flow dynamics and its acoustics generated. Here they are defined by $\overline{u'u'}$, $\overline{v'v'}$ and $\overline{u'v'}$, where the bar overhead denotes the time averaged variable and the

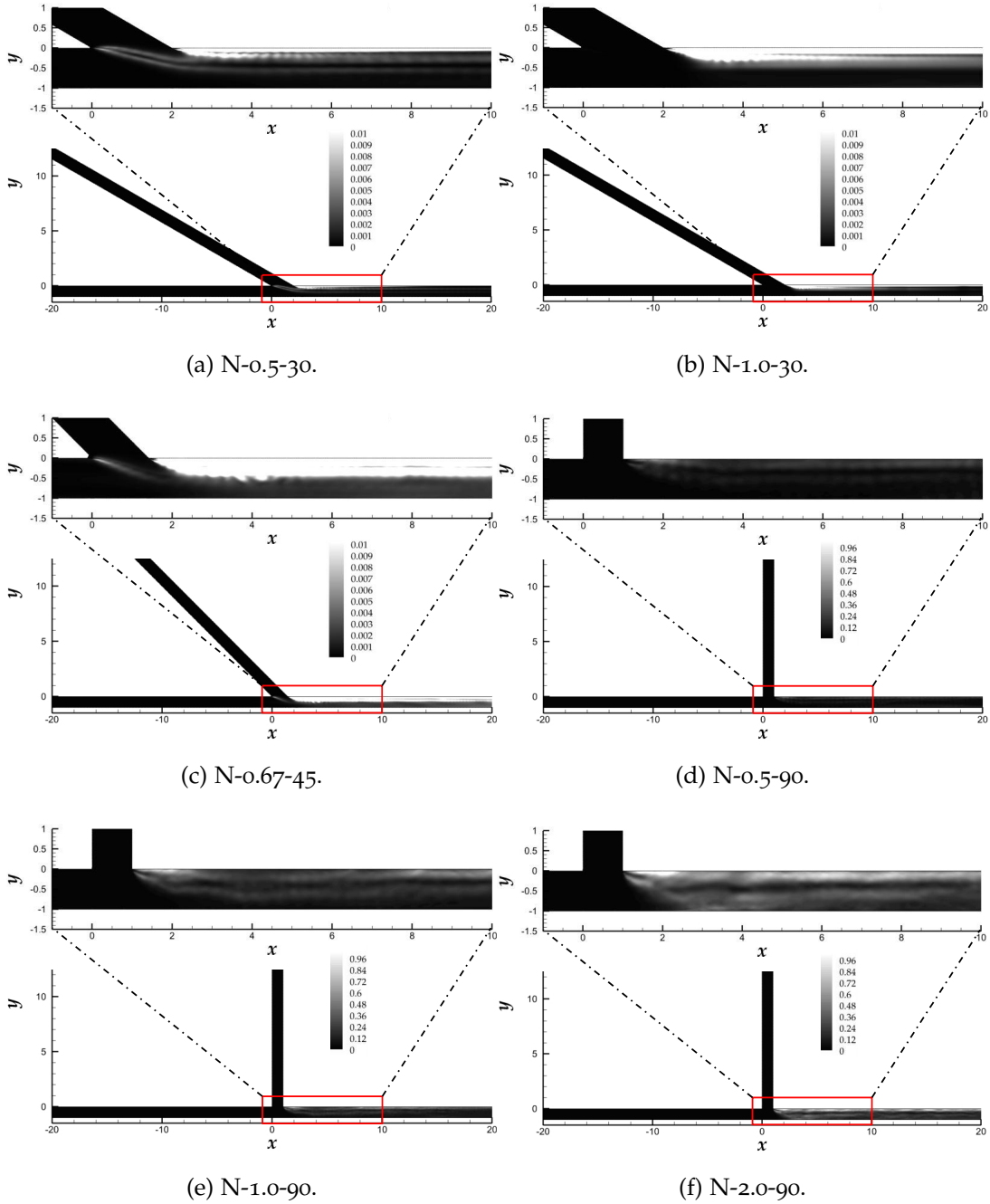


Figure 4.13: Distribution of $\overline{u'u'}/u_{eq}^2$ in different selected cases. The one with the smallest fluctuation is N-0.5-30 and the one with largest fluctuation is N-2.0-90.

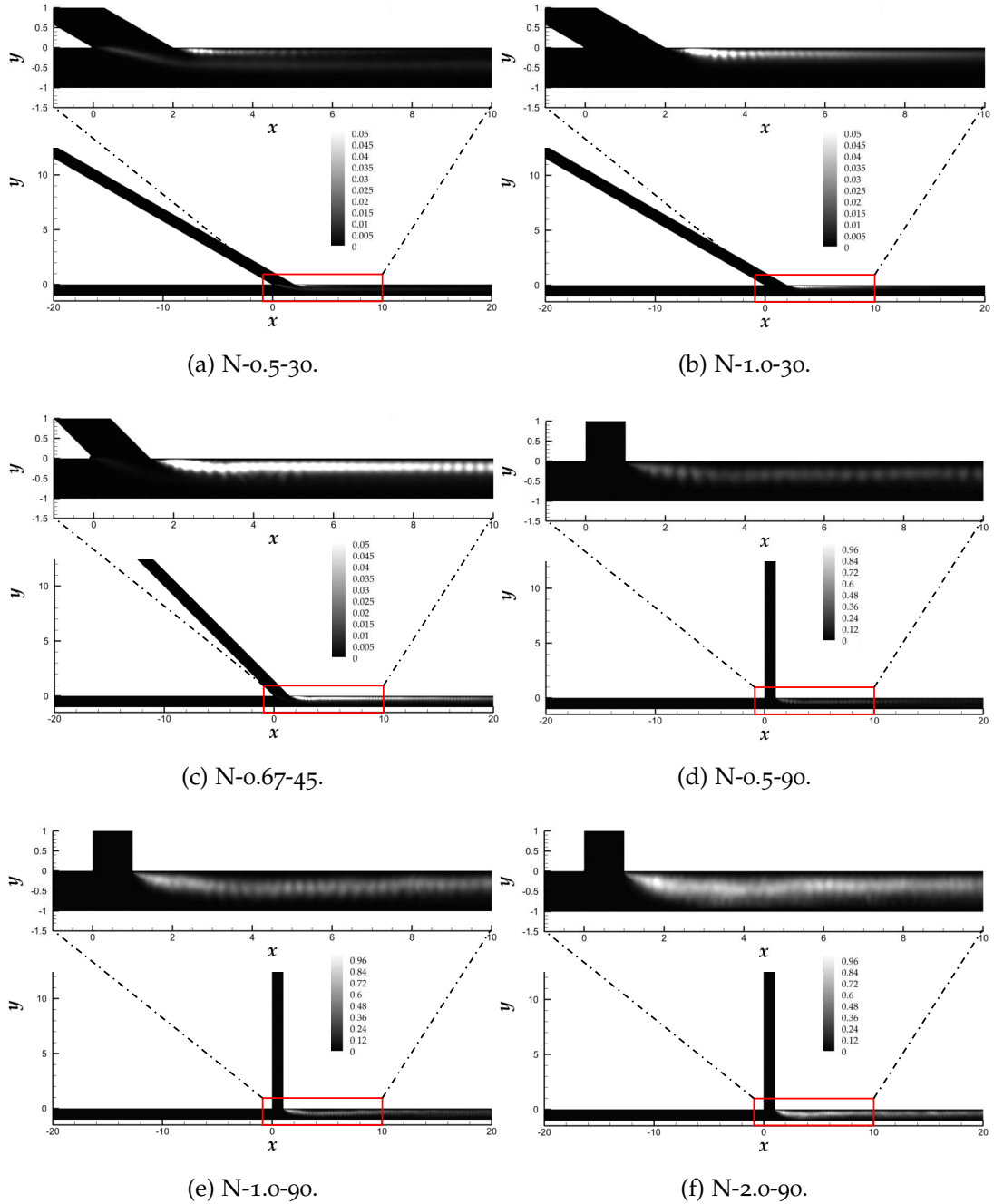


Figure 4.14: Distribution of $\overline{v'v'}/u_{eq}^2$ in different selected cases. The one with the smallest fluctuation is N-0.5-30 and the one with largest fluctuation is N-2.0-90.

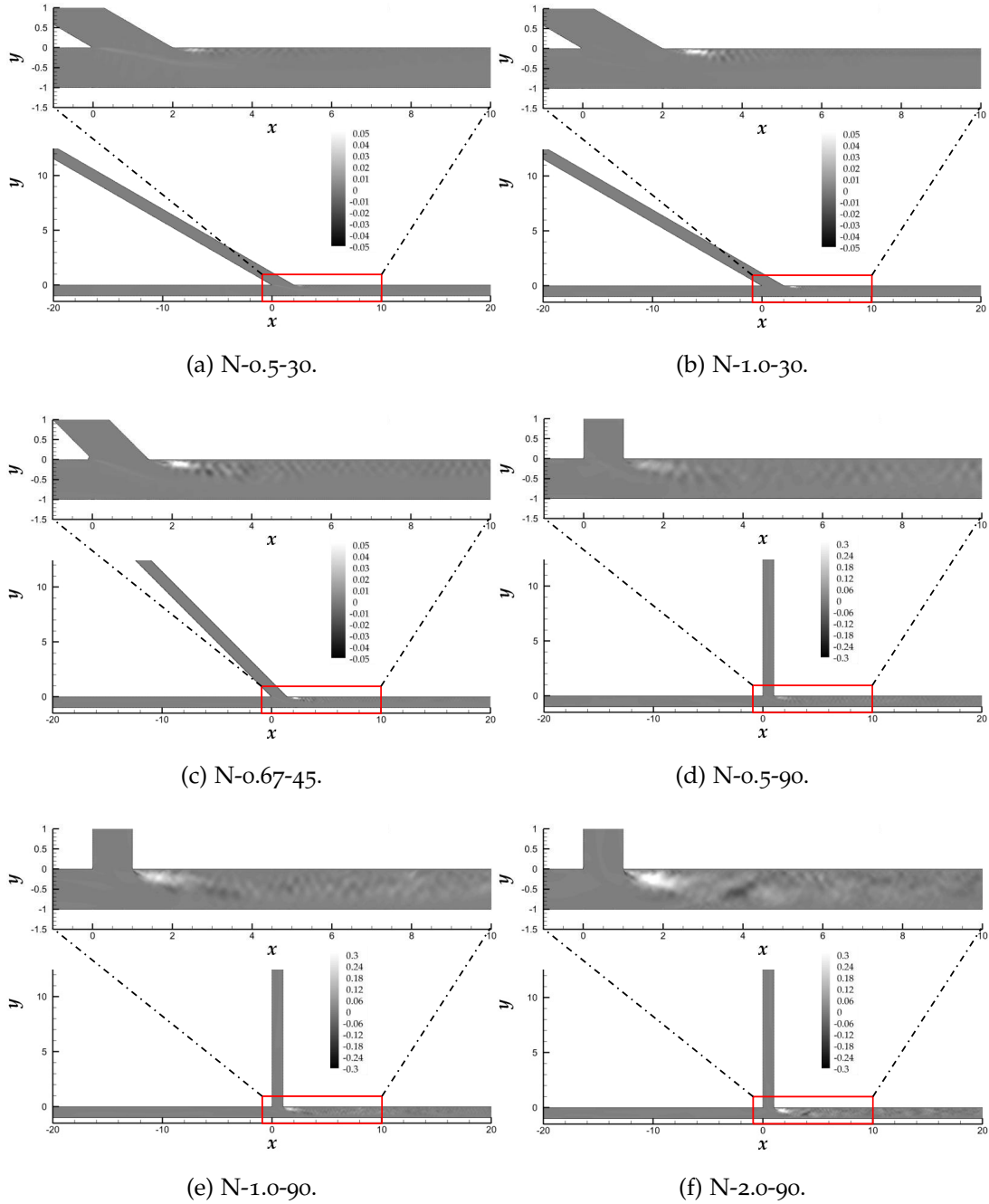


Figure 4.15: Distribution of $\overline{u'v'}/u_{eq}^2$ in different selected cases. The one with the smallest fluctuation is N-0.5-30 and the one with largest fluctuation is N-2.0-90.

superscript $'$ denote the fluctuating quantities. The fluctuating quantity is defined by

$$\phi'(x, y, t) = \phi(x, y, t) - \bar{\phi}(x, y) \quad (4.3)$$

where ϕ denotes the flow variables such as u , v , etc.. The mean values are obtained by performing time averaging.

The mean resolved Reynolds stresses $\overline{u'u'}$, $\overline{v'v'}$ and $\overline{u'v'}$ of the selected cases are shown in [Figure 4.13](#), [Figure 4.14](#) and [Figure 4.15](#) respectively. In order to compare these cases with different inlet velocities at I_1 , they are normalized by equivalent maximum velocity u_{eq}^2 defined by,

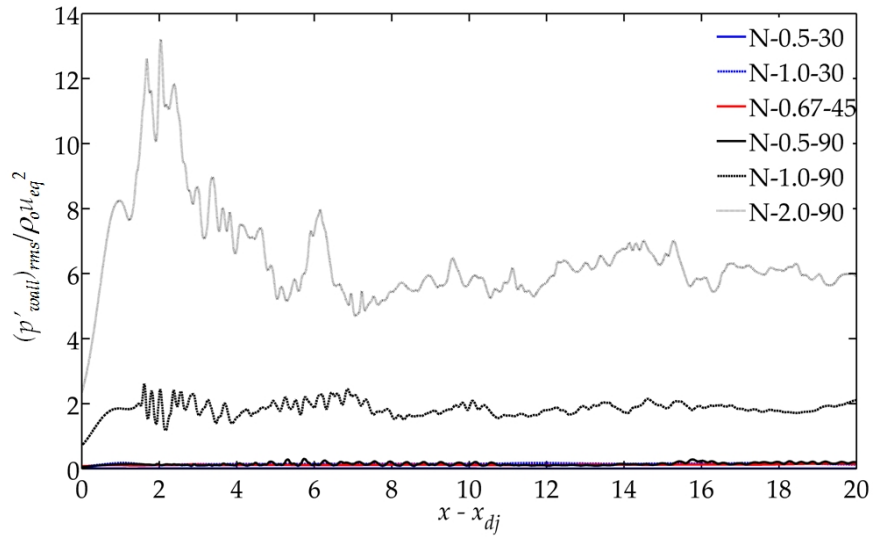
$$u_{eq}^2 = u_{1,max}^2 + u_{2,max}^2. \quad (4.4)$$

These figures show that high Reynolds stress levels are mostly concentrated near the upper wall in DS as a result of very strong but localized flow interactions. These interactions are originated mainly from the vortex shedding at RZ1. On the other hand, the levels of Reynolds stresses are quite low in US and SB. At SL, the Reynolds stresses are also relatively weak compared with those in DS. This suggests that the vortex shedding at RZ1 is the dominant physical process responsible for the fluctuations. Generally, the mean Reynolds stresses increase with θ and VR . Therefore, the highest level of stresses is found in the case N-2.0-90, whereas very strong flow/vortex interactions are observed.

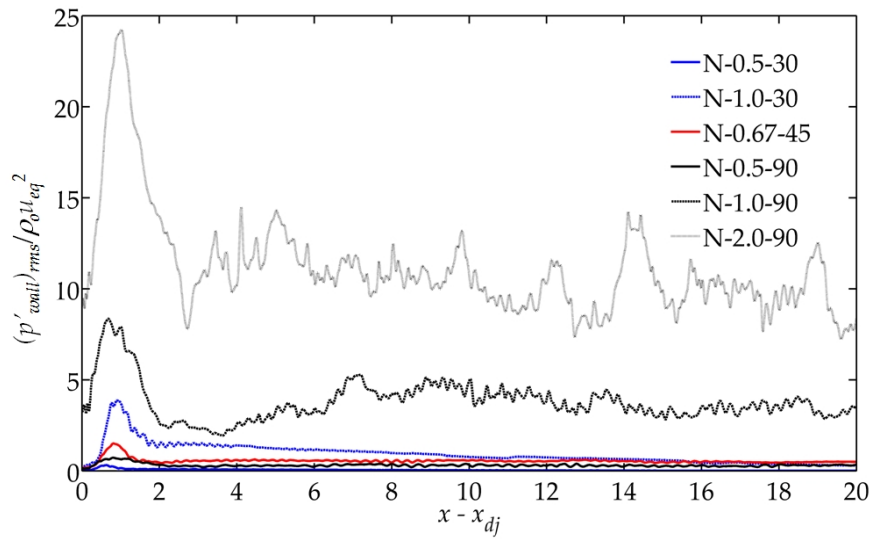
Fluctuating Wall Pressure

Another quantities that related to the acoustic generation is the fluctuating wall pressure, so it is discussed in this part. Since the major flow unsteadiness occurs in the DS ([Figure 4.7](#) to [Figure 4.9](#)), the fluctuating pressure on the lower and upper walls in DS are focused in this section.

The RMS values of fluctuating pressure $(p'_{wall})_{rms} / \rho_0 u_{eq}^2$ at both walls in DS are shown in [Figure 4.16](#). These values are calculated from the results



(a) Lower wall.



(b) Upper wall.

Figure 4.16: Distributions of $(p'_{wall})_{rms} / \rho_0 u_{eq}^2$ in various cases.

within a period of time 20 and a time increment of 0.2. Several observations can be made from this figure. First, this fluctuating pressure is induced by the vortical motions during their convection to downstream. Second, the fluctuating pressure exerted by the lower wall is smaller than that exerted by the upper wall. This is because the vortices shed are mainly convected near the upper wall, rather than the lower wall in most cases as shown in [Figure 4.7](#) to [Figure 4.9](#). Third, the peak location is at $x \sim 1$ and $x \sim 2$ of the upper wall and the lower wall (in some cases) respectively. These locations correspond to those of vortex shedding at the upper wall and the collision of vortices to the lower wall respectively. Fourth, the fluctuating pressure increases with VR and θ . Their details will be given in the corresponding section.

4.2.3 Sound Generation

In this section, the sound generation induced by the unsteady flow dynamics aforementioned is discussed. It first starts with the discussion on the sound sources in the merging flow at duct junction. Then the acoustic extraction from the DAS results is discussed followed by the discussion of the acoustics generated. Furthermore, in the previous section (Section [4.2.2](#)), it is observed that all the vortex shedding/roll-up frequency are below 3 in all these cases. This is much smaller than the cut-off frequency of the duct $f_{cutoff} = \frac{c_0}{2W} = 5$. Thus, the excitation of higher order duct mode is not expected. This implies the plane wave mode is dominant in the acoustic propagation.

Sound Sources in Merging Flow at Duct Junctions

[Lighthill \(1952, 1954\)](#) recasted the compressible Navier-Stokes equation and proposed the theory of acoustic generation by the unsteady flow dynamics, with Einstein's summation convention, as

$$\frac{\partial^2 \rho}{\partial t^2} - c_0^2 \nabla^2 \rho = \frac{\partial^2 T_{ij}}{\partial x_i \partial x_j}, \quad (4.5)$$

where c_o is the acoustic speed and $T_{ij} = \rho u_i u_j + p_{ij} - c_o^2 \rho \delta_{ij}$ is the instantaneous Reynolds stresses. At low Mach flows, $T_{ij} \approx \rho u_i u_j$. According to [Curle \(1955\)](#), the most general solution of Eq.(4.5) is

$$\rho - \rho_o = \frac{1}{4\pi c_o^2} \frac{\partial^2}{\partial y_i \partial y_j} \int_V \frac{T_{ij}(\mathbf{y}, \tau)}{r} d\mathbf{y} + \frac{1}{4\pi c_o^2} \frac{\partial}{\partial y_i} \int_S \frac{P_i(\mathbf{y}, \tau)}{r} d\mathbf{y}, \quad (4.6)$$

where \mathbf{y} is the location of source, τ is the retarded time, P_i is the force exerted on the fluid by the solid surface. The Reynolds stresses T_{ij} and the force P_i represent a volume distribution of quadruples and a surface distribution of dipoles respectively. Therefore, the mean Reynolds stresses obtained in the previous section can be, to a certain extent, a measure of overall contribution to the sound generation by the unsteady flow dynamics. However, at low Mach number flow, the surface distribution of dipoles usually dominates the sound generation ([Curle 1955](#)). Thus, the fluctuating wall pressure is the dominant sound source in the merging flow at duct junction at low Mach number.

According to [Figure 4.16](#), the fluctuating wall pressure at the upper wall is larger than that at the lower wall. This implies that the source strength of the upper wall is stronger than that of the lower wall. Furthermore, the fluctuating wall pressure is still quite high even at $x > 20$. This indicates that the walls in the whole DS section are the sound sources. Moreover, as stated in the previous section, the peak fluctuating wall pressure, i. e., source strength is located at those of vortex shedding at the upper wall and the collision of vortices to the lower wall respectively. This shows that two major mechanisms of the sound generation can be identified for the merging flow at duct junction based on Curle's analogy. One is the vortex shedding near the wall and the other one is the collision of the vortex on the wall. In addition, the source strength increases with VR and θ .

Disturbance

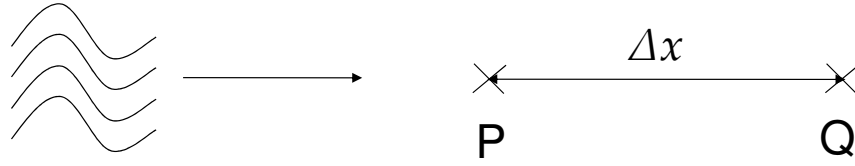


Figure 4.17: Setting of two point method.

Identification of Dominant Physics in Merging Flow

One should note that the calculated results in DAS combine the acoustic and flow dynamic fluctuations and their differentiation is not obvious. This renders great difficulties in determining the dominant physics in regions where the acoustics are always driven by the underlying unsteady flow dynamics.

To cope with this, a simple two microphone method is used to aid the identification of dominant physics in merging flow. Consider two locations P and Q separated by Δx in the flow (Figure 4.17), through them a disturbance is traveling. The phase difference ϑ_{PQ} between ϑ_P and ϑ_Q is defined by

$$\vartheta_{PQ} = \vartheta_P - \vartheta_Q, \quad (4.7)$$

where ϑ_P and ϑ_Q are the phases of disturbance obtained from FFT results. For a disturbance passing through PQ with speed v_o , the theoretical phase difference for this disturbance ϑ_{PQ,v_o} is given by

$$\vartheta_{PQ,v_o} = k_{v_o} \Delta x, \quad (4.8)$$

where $k_{v_o} = 2\pi f/v_o$ is the wave number of the disturbance and f is the frequency of the disturbance. The theoretical phase difference for an acoustic disturbance (c_o) and a flow disturbance (u_o) are given by

$$\vartheta_{PQ,c_o} = k_{c_o} \Delta x \quad (4.9)$$

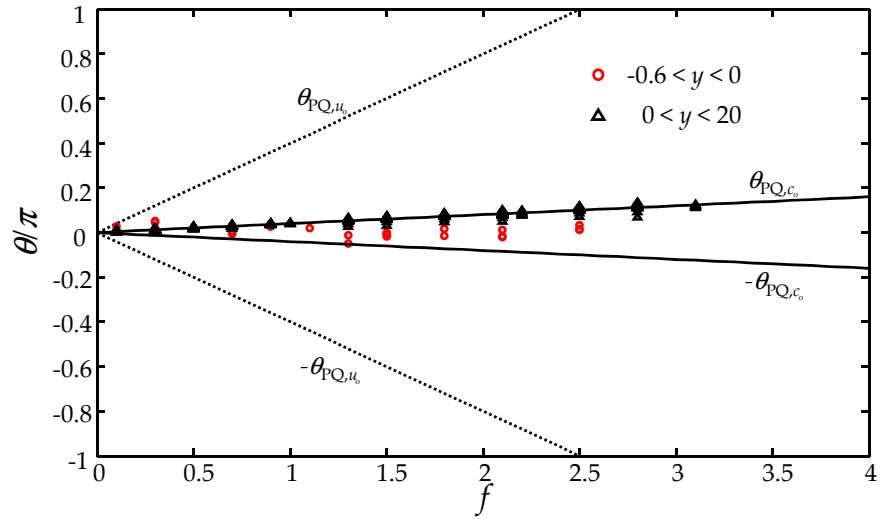
and

$$\vartheta_{PQ,u_0} = k_{u_0} \Delta x = \frac{1}{M} \vartheta_{PQ,c_0} \quad (4.10)$$

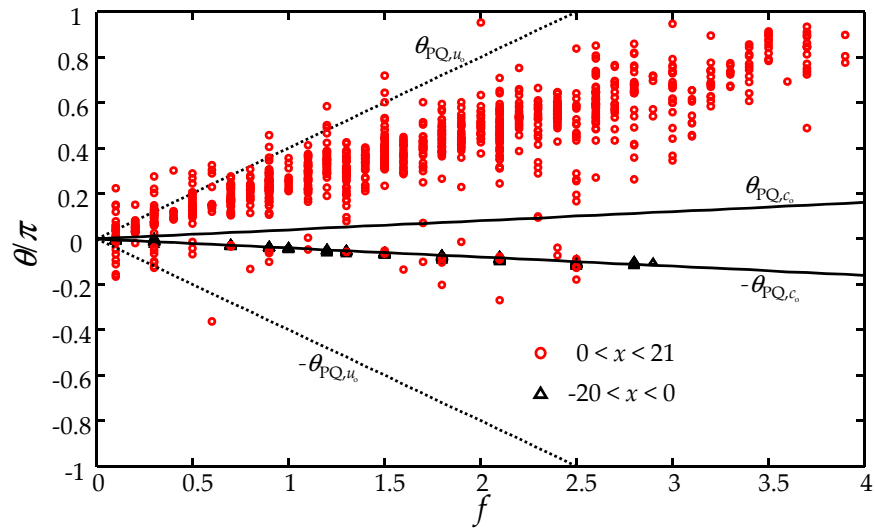
respectively. Eq.(4.10) also demonstrates that when $M \ll 1$, $\vartheta_{PQ,u_0} \gg \vartheta_{PQ,c_0}$. Thus, this method is suitable for applications in low Mach number flows like the present case due to their great difference. When a region is dominated by the acoustic disturbances, $\vartheta_{PQ} \rightarrow \vartheta_{PQ,c_0}$ and the acoustic effect is the dominant physics in that region. Similarly when the flow disturbance is dominant in a region, $\vartheta_{PQ} \rightarrow \vartheta_{PQ,u_0}$ and the flow unsteadiness dominates in that region.

The variations of ϑ are calculated along the centerlines of the main duct ($y = -0.5$) and SB (along $x = 0.5$), with a spatial separation of $\Delta x = \Delta y = 0.2$, for the case N-1.0-90. The distributions of ϑ with respect to frequency are shown in Figure 4.18. In this figure, all the positive and negative values of ϑ_{PQ,c_0} and ϑ_{PQ,u_0} are shown because the disturbances may travel in $\pm x$ direction. Furthermore, only ϑ of the dominant peaks in the spectra are calculated as they are the major disturbances in the flow. All the values of ϑ in SB ($x = 0.5, y > 0$) and US ($x < 0, y = -0.5$) are all lies on the lines of ϑ_{PQ,c_0} and this shows that the disturbances in SB and US are all acoustics in nature. This suggests that SB and US are dominated by acoustic physics. On the other hand, in DJ and DS ($x > 0$), the calculated ϑ fall between ϑ_{PQ,c_0} and ϑ_{PQ,u_0} . This indicates that both the flow dynamic and acoustic disturbances dominate in DS. All other cases also show the same behavior.

An interesting observation is the phase difference between the fluctuations of velocity and pressure ϑ_{p-u} , which is illustrated in Figure 4.19 with N-0.5-90 as the demonstration. The values of ϑ_{p-u} at the frequency peaks in its spectra are obtained at points $(-17, -0.5)$ in US, $(-0.6, -0.5)$ in DJ, $(x_{dj} + 17, -0.5)$ in DS and $(0.5, 17)$ in SB. Same peaks occur simultaneously in the spectra of u' and p' . The values of ϑ_{p-u} are very close to either 0 or $-\pi$ in US and SB while $0 > \vartheta_{p-u} > \pi$ in the other two regions, especially in DJ, whereas the ϑ_{p-u} at nearly all peaks are far from 0 and π . As mentioned by



(a) Along the centerline of SB ($x = 0.5$).



(b) Along the centerline of main duct ($y = -0.5$).

Figure 4.18: Variation of phase difference along the selected lines (N-1.0-90). Red circles denote the results in DS and the black triangles represent those in SB and US.

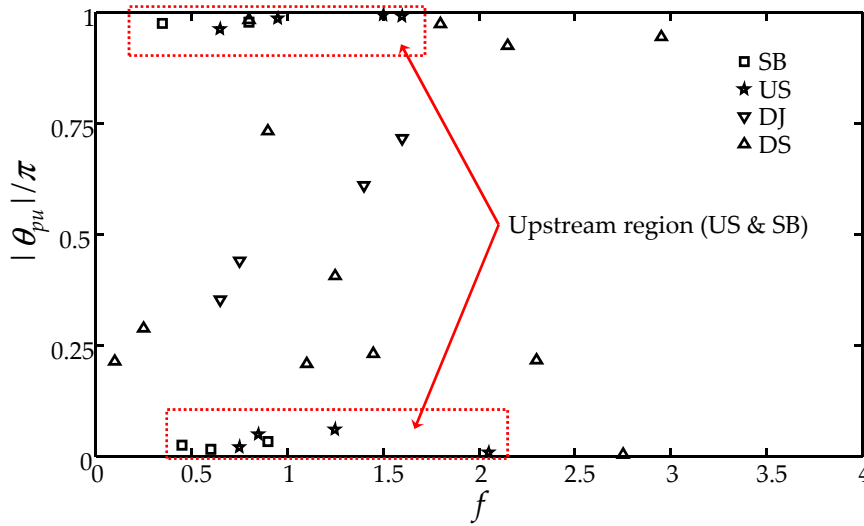


Figure 4.19: Typical phase difference between the streamwise velocity and pressure. The demonstration is N-0.5-90.

Morse (1986), for a simple harmonic point acoustic source, the velocity and the pressure are related by

$$u(x) = \frac{p}{\rho c_0} \left(1 + i \frac{\lambda}{2\pi x} \right), \tag{4.11}$$

where x is the distance from the source, λ is the wavelength of the source and c_0 is the acoustic speed. In the far field, where x is very large, i.e., $\left(\frac{\lambda}{2\pi x}\right) \rightarrow 0$, u and p are in phase. On the other hand, the values of ϑ_{p-u} are close to $\frac{\pi}{2}$ in the near field ($x \rightarrow 0$) because $\frac{\lambda}{2\pi r} \gg 1$ as $x \rightarrow 0$. Furthermore, when adopting Cartesian coordinate, $u = -\frac{p}{\rho c_0}$ if the propagating direction is negative x . Applying this argument to the present cases, it indicates that in US and SB, the fluctuations really reside in an acoustic far field, in which the linear acoustic theory can be applied, while in DJ and DS, the fluctuations are still in the near field. This is consistent with the aforementioned results derived from Figure 4.18. Similar phenomena are also observed in all other cases.

The time histories of pressure fluctuations at points $(-9, -0.4)$ in US, $(0.4, 9)$ in SB and $(10, -0.4)$ in DS of case N-1.0-90 are shown in Figure 4.20. They do not exhibit a very regular periodicity as a result of the existence of multiple dominant frequencies in the flow unsteadiness (Figure 4.10). The

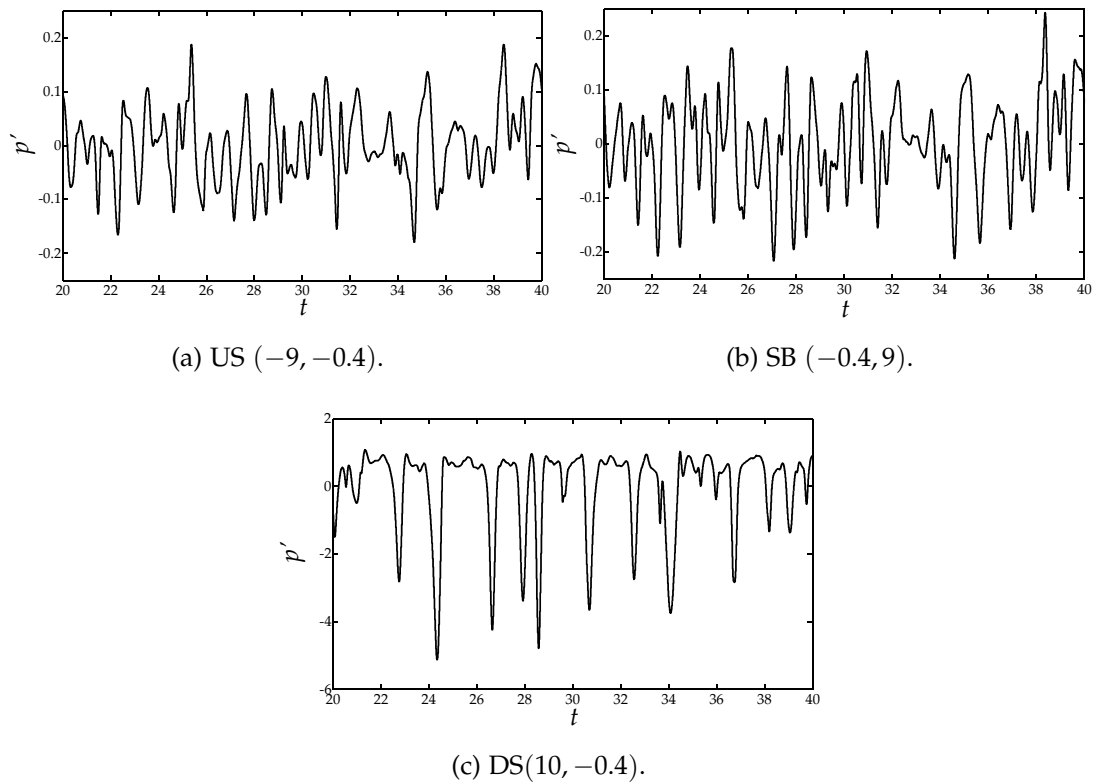


Figure 4.20: Time histories of pressure fluctuation at different points in US, SB and DS of case N-1.0-90.

amplitudes of fluctuations in US and SB are of the same order, but those in DS are larger than those in US and SB by a order of magnitude. This is because the acoustic disturbances dominate US and SB, but DS is dominated by the flow disturbances, which induce larger pressure fluctuations than acoustic disturbances do. Similar observations can be found in other cases.

Acoustic Propagation in SB and US

Figure 4.21 shows that the snapshots of density fluctuation of cases N-1.0-30 and N-1.0-90. Plane wave pattern is clearly shown in US and SB for both cases. No higher order mode is observed for both cases. Similar pattern is also observed for other cases. This confirms that the plane wave mode is dominant in the acoustic propagation due to the lack of mechanism exciting the higher order mode.

The overall acoustic power generated W_{acoust} by a flow through a duct cross-section can be determined from the instantaneous acoustic intensity along that section using the definition given in Morfey (2001). In the presence

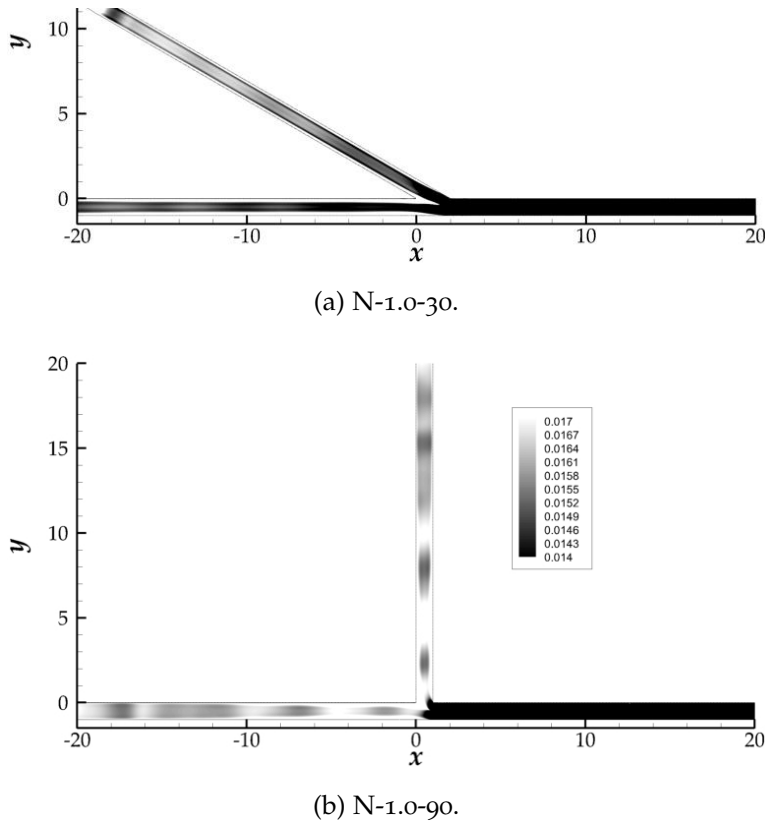


Figure 4.21: Snapshots of density fluctuations.

of a mean flow, the instantaneous acoustic intensity $\mathbf{I}_a(t)$ at a point is given by

$$\mathbf{I}_a(t) = p' \mathbf{u}' + (\mathbf{M} \cdot \mathbf{u}') (\mathbf{M} p' + \bar{\rho} c \mathbf{u}') + \mathbf{M} \left(\frac{p'^2}{\bar{\rho} c} \right), \quad (4.12)$$

where c is the local acoustic speed, $\mathbf{u}' = (u', v')$ is the fluctuating velocities, p' is the fluctuating pressure, $\mathbf{M} = |\bar{\mathbf{u}}| / c$, $|\bar{\mathbf{u}}|$ is the mean velocity and $\bar{\rho}$ is mean density. By taking integration across the cross-section, the instantaneous acoustic power $W_i(t)$ is given by

$$W_i(t) = \oint \mathbf{I}_a(t) \cdot \mathbf{n} ds, \quad (4.13)$$

where \mathbf{n} is the unit outward normal of the section. In two dimensions, unit thickness is often assumed in the z direction. Finally, the overall acoustic power W_{acoust} is calculated by

$$W_{acoust} = \frac{1}{T} \int_0^T W_i(t) dt, \quad (4.14)$$

where the duration T is usually chosen to cover at least one period of the lowest frequency of fluctuation. The calculation of W_i (Eq.(4.13)) should be done along a cross-section in the duct acoustic far field; otherwise the result will be contaminated with non-acoustic components. Thus, the chosen cross-sections are $x = -9$ in US and $y = 9$ in SB. The line integral only covers the locations from $y = 0.3$ to $y = 0.7$ along the chosen cross sections so as to exclude the influence of duct boundary layer.

The input flow kinetic energy into the system varies with VR . At high VR values, the flow unsteadiness at DJ, as well as the acoustic power generated there, are expected stronger due to the higher availability of flow kinetic energy. Therefore, in order to eliminate the bias of inlet flow variations on assessing acoustic generation capability in the different cases attempted, a term acoustic efficiency $\eta = W_{acoust}/W_{aero}$ is defined. W_{aero} can be calculated by

$$W_{aero} = \sum_i \oint \frac{1}{2} \rho (\mathbf{u} \cdot \mathbf{u}) \mathbf{n} \cdot \mathbf{u} ds, \quad (4.15)$$

where i is the number of inlet duct section, \mathbf{u} is the flow velocity, $\oint \frac{1}{2} \rho (\mathbf{u} \cdot \mathbf{u}) \mathbf{n} \cdot \mathbf{u} ds$ is the dynamic pressure supplied through the duct inlets. In essence, η indicates the level of acoustic generation per unit flow power injected into the system.

Table 4.9 and Table 4.10 show that an increase in VR and θ increases η in US and SB respectively. When VR is doubled, $O(\eta/\eta_{max})$ is increased by 1. On the other hand, $O(\eta/\eta_{max})$ is increased by 2 when θ is increased from 30° to 90° . The case N-2.0-90 has the largest η in both US and SB.

Acoustic Propagation in DS

Table 4.11 shows the variation of acoustic efficiency in DS, η_{DS} , obtained at $x = x_{dj} + 9$. It should be noted that Eq.(4.12) is originally applied to the far field (dominated with acoustic disturbances), rather than the near field (dominated with flow dynamic disturbances) like the present cases. In the latter,

$\theta \setminus \text{VR}$	0.5	0.67	1	2
30°	$6.87 \times 10^{-7},$ ($\sim 10^{-4}$)		$3.13 \times 10^{-6},$ ($\sim 10^{-3}$)	
45°		$1.4 \times 10^{-5},$ ($\sim 10^{-2}$)		
60°				
90°	$7.65 \times 10^{-5},$ ($\sim 10^{-2}$)		$4.48 \times 10^{-4},$ ($\sim 10^{-1}$)	$1.38 \times 10^{-3},$ (1)

Table 4.9: The acoustic efficiency η_{US} in US. Shown in the brackets are the relative order of difference $O(\eta/\eta_{\text{max}})$ when compared with the maximum η obtained.

$\theta \setminus \text{VR}$	0.5	0.67	1	2
30°	$5.08 \times 10^{-7},$ ($\sim 10^{-4}$)		$1.93 \times 10^{-6},$ ($\sim 10^{-3}$)	
45°		$1.2 \times 10^{-5},$ ($\sim 10^{-2}$)		
60°				
90°	$1.08 \times 10^{-4},$ ($\sim 10^{-2}$)		$4.6 \times 10^{-4},$ ($\sim 10^{-1}$)	$1.2 \times 10^{-3},$ (1)

Table 4.10: The acoustic efficiency η_{SB} in SB. Shown in the brackets are the relative order of difference $O(\eta/\eta_{\text{max}})$ when compared with the maximum η obtained.

$\theta \setminus VR$	0.5	0.67	1	2
30°	2.1×10^{-3} , ($\sim 10^{-3}$)		5.4×10^{-3} , ($\sim 10^{-2}$)	
45°		0.028, ($\sim 10^{-2}$)		
60°				
90°	0.12, ($\sim 10^{-1}$)		0.41, ($\sim 10^{-1}$)	0.45, (1)

Table 4.11: The acoustic efficiency η_{DS} in DS. Shown in the brackets are the relative order of difference $O(\eta/\eta_{max})$ when compared with the maximum η obtained. Note that the calculation of this acoustic efficiency actually includes the contribution of acoustic and flow dynamic disturbances in DS.

Eq.(4.12) represents the overall fluctuating power in the interested section, which consists of both acoustic and flow dynamic fluctuations. Based on this argument, $\eta_{DS} > \eta_{US}$ and $\eta_{DS} > \eta_{SB}$ as expected (Table 4.11). Furthermore, an increase in VR and θ also increase the acoustic efficiency, leading to the largest η_{DS} in N-2.0-90 among all cases.

As mentioned previously, the separation of the acoustic and flow disturbances in near field is a challenging task in analyzing DAS results. Conventional spectral analysis methods such as one dimensional FFT analysis, proper orthogonal decomposition are not able to differentiate the acoustic and flow disturbances as they are strongly coupled. Even worse is that they usually possess the same frequencies. Thus, an alternative method is proposed hereafter for the separation of the signals in DS.

Tinney & Jordan (2008) introduced a method in separating similar kinds of fluctuations by a two dimensional Fourier transformation of the pressure field $p(x, t) \rightarrow p(k_x, f)$. This is based on

$$p(k_x, f) = \frac{1}{2\pi} \iint p(x, t) W(x) e^{-i(k_x x + 2\pi f t)} dx dt, \quad (4.16)$$

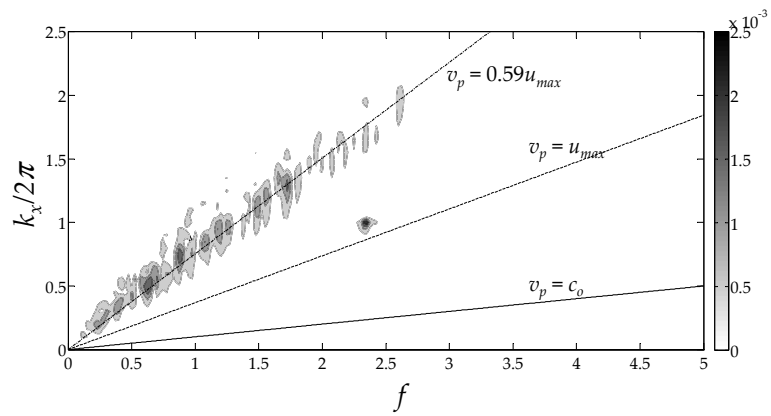
where $W(x)$ is the window function, f is the frequency, $k_x = 2\pi f/v_p$ is the wave number and v_p is the phase speed of the disturbances. Since the method makes use of the difference between the phase velocities of different disturbances, it is very suitable for use in the present low Mach number flow cases due to the large difference in phase speeds of acoustic and flow disturbances. The method starts with measuring pressure $p(x, t)$ along straight line mesh with uniform mesh size Δx . The mesh is aligned with the dominant traveling direction of disturbances. In their works, the locations of the receiver points were assumed at zero mean flow and no acoustic field was able to generate a subsonic phase velocity on the receiver points. According to Eq.(4.16), fluctuations of different propagating speeds are decomposed for the same frequency. The wave number of the disturbance k_x is given by

$$k_x = \frac{2\pi f}{v_p}. \quad (4.17)$$

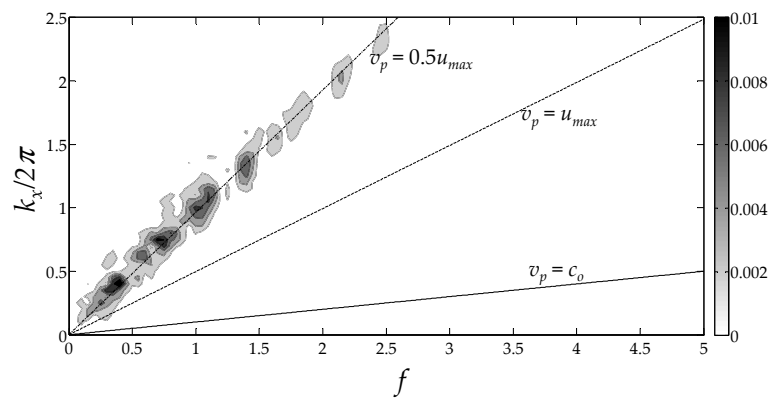
It shows that k_x decreases when the phase speed of that disturbance increases for the same frequency. They applied this to the investigation of aeroacoustics of a jet nozzle, which is a broadband noise in nature, and the disturbances with different phase speeds were successfully differentiated in the $p(k_x, f)$ spectra obtained.

In the present calculation, the time signals are recorded in a uniform straight line mesh at $y = -0.2$ with $\Delta x = 0.2$, through which the vortices pass. It also cuts through RZ1. Since the mesh is located inside the region with a strong mean flow, the effect of mean flow on the time signals is first eliminated by applying Eq.(4.3) before calculating the spectrum. The window function $W(x) = 1$ is arbitrarily chosen for the present case.

Figure 4.22 to Figure 4.24 shows the $p(k_x, f)$ spectra divided by u_{eq}^2 (Eq.(4.4)) for the selected cases. The theoretical variations of acoustic speed and different flow speeds in $p(k_x, f)$ spectra are also shown for reference. The region below the solid line is regarded as the supersonic zone because the disturbances propagate with a speed higher than the acoustic speed.

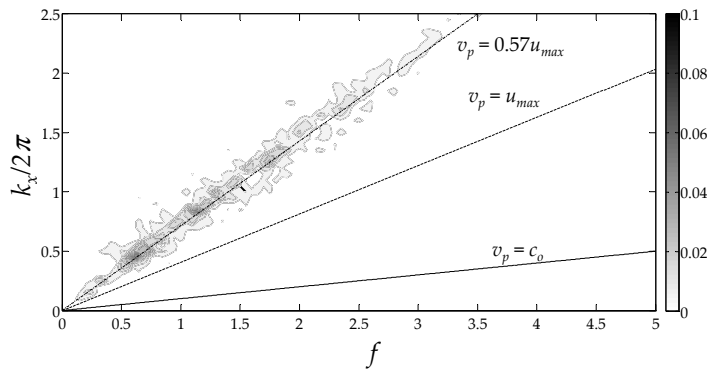


(a) N-0.5-30.

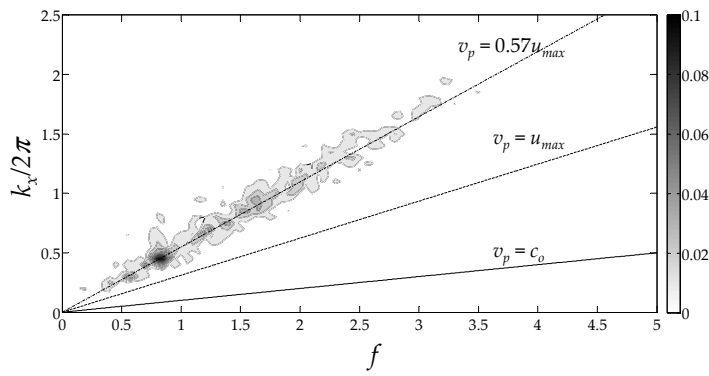


(b) N-1.0-30.

Figure 4.22: $p(k_x, f)$ spectrum at $y = -0.2$ in DS.

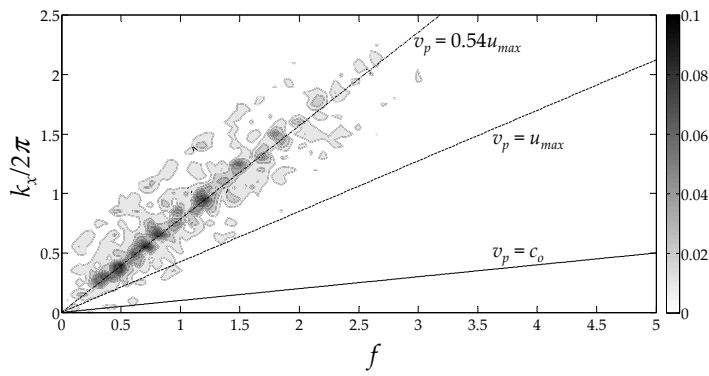


(a) N-1.5-45.

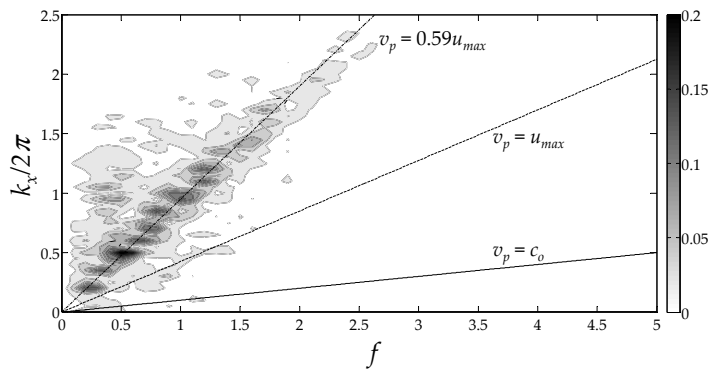


(b) N-0.5-90.

Figure 4.23: $p(k_x, f)$ spectrum at $y = -0.2$ in DS.



(a) N-1.0-90.



(b) N-2.0-90.

Figure 4.24: $p(k_x, f)$ spectrum at $y = -0.2$ in DS.

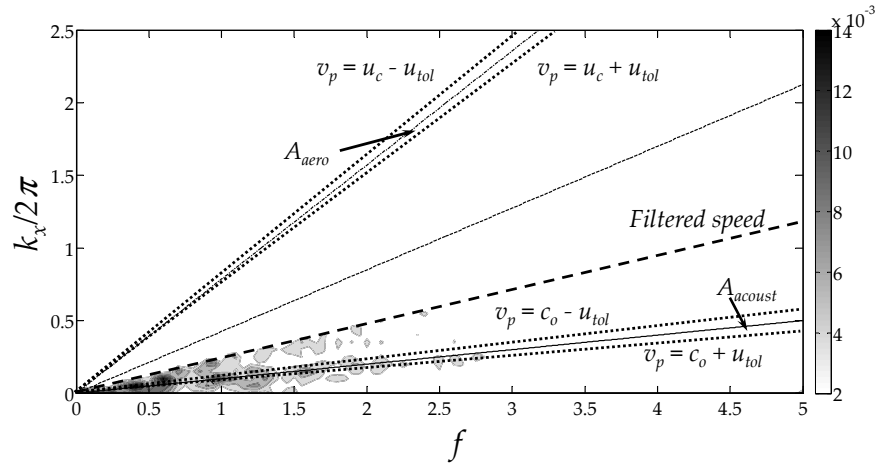


Figure 4.25: Acoustic disturbances shown in filtered $p(k_x, f)$ spectrum at $y = -0.2$.

On the contrary, the region above the solid line can be regarded as the subsonic zone. The figures clearly show that the dominant signals in DS travel with $v_p \sim 0.5 - 0.6u_m$, where $u_m = (u_{max} + u_{min}) / 2$ is the mean velocity of the separated flow at RZ1, u_{max} is the maximum velocity obtained at this separated flow and $u_{min} = 0$ for the present cases. This in general agrees with the previous experimental studies with mixing layer (Thomas 1991). Furthermore, Figure 4.22a also shows the flow disturbances generated by the vortex roll-up at SL (black spot at $f = 2.35$). This also indicates that the flow disturbances generated at SL travel at different speeds with those generated at RZ1. Moreover, when the dominating flow disturbances are filtered out, the acoustic disturbances appear in the spectra. One of the example is shown in Figure 4.25 with N-1.0-90. It clearly illustrates the acoustic disturbances in the spectra. Therefore, this method is capable to differentiate the mixed signals and helps us analyzing the effects of individual disturbances passing through the region.

The results of signal differentiation also facilitate the extraction of the acoustic contribution in the mixed disturbances inside DS. The $p(k_x, f)$ spectra along the centerline of DS (i. e., $y = -0.5$) with $\Delta x = 0.2$ are first calculated. Then, integrations are performed in the spectra at the area A_{aero} and A_{acoust} marked in Figure 4.25. They are bounded by $v_{p,aero} \pm v_{tol}$ and $v_{p,acoust} \pm v_{tol}$ respectively, where $v_{tol} = 0.1$ is the tolerance chosen, $v_{p,aero}$ and $v_{p,acoust}$ are the phase speeds of flow and acoustic disturbances respectively. Thus,

$\theta \setminus VR$	0.5	0.67	1	2
30°	2.4×10^{-7} , ($\sim 10^{-4}$)		1.2×10^{-6} , ($\sim 10^{-3}$)	
45°		1.37×10^{-5} , ($\sim 10^{-2}$)		
60°				
90°	2.6×10^{-5} , ($\sim 10^{-2}$)		1.3×10^{-4} , ($\sim 10^{-1}$)	8.1×10^{-4} , (1)

Table 4.12: The acoustic efficiency $\eta_{DS,acoustic}$ in DS. Shown in the brackets are the relative order of difference $O(\eta/\eta_{max})$ when compared with the maximum η obtained.

the contribution of acoustic component in mixed signals is estimated by $AR \equiv A_{acoust} / (A_{acoust} + A_{aero})$. Therefore, the acoustic contribution in DS $\eta_{DS,acoustic}$ is obtained by

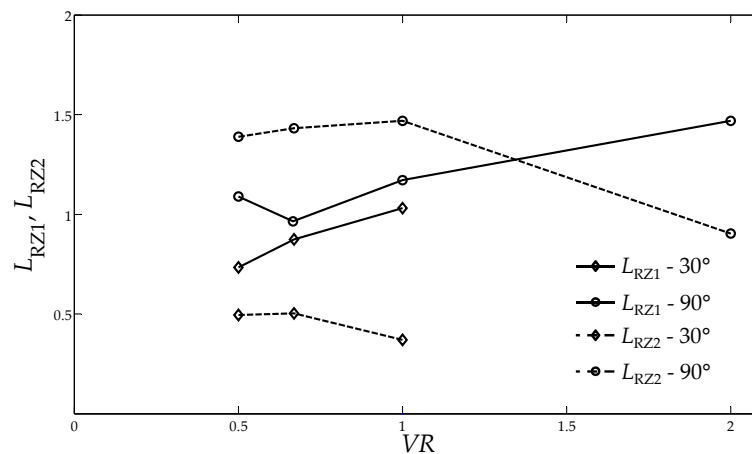
$$\eta_{DS,acoustic} = AR \times \eta_{DS}. \quad (4.18)$$

The calculated results are listed in Table 4.12. The orders of difference between cases are similar to η_{US} and η_{SB} . Furthermore, $\eta_{DS,acoustic} < \eta_{US} \approx \eta_{SB}$ and this may imply a upstream preference in the acoustic propagation (Åbom & Bodén 1995). In general, $\eta_{DS,acoustic}$ increases with VR and θ , which is the same as η_{US} and η_{SB} shown in Table 4.9 and Table 4.10 because the strength of dipole (fluctuating wall pressure) increases with VR and θ .

4.3 INFLUENCE OF VELOCITY RATIO, VR

The velocity ratio VR has already been shown a key influence in the aeroacoustics of merging flows at duct junction. In this section, the influence is further discussed. Modifying the velocity ratio VR effectively changes the

$\theta \setminus VR$	0.5	0.67	1	2
30°	★	★	★	
45°				
60°				
90°	★	★	★	★

Table 4.13: Selected cases for illustrating the effect of the velocity ratio, VR .Figure 4.26: Variation of reattachment length L_{RZ1} and separation length L_2 with VR ($\theta = 30^\circ, 90^\circ$).

ratio of x and y component of flow momentum merging at DJ. To illustrate this, all the cases with $\theta = 30^\circ$ and 90° are selected for this purpose as shown in Table 4.13.

4.3.1 Mean Flow

Increasing VR lengthens the zone of the streamwise velocity profile to recover fully developed turbulent profile. For instance, comparing Figure 4.5d and Figure 4.5e, the streamwise velocity profile has recovered to nearly fully developed state at $x = x_{dj} + 14$ for N-0.5-90, while the flow is still biased upwards at $x = x_{dj} + 14$ for N-1.0-90.

The variations of reattachment length L_{RZ1} and separation length L_{RZ2} are shown together in Figure 4.26. A nonlinear relationship is observed for VR

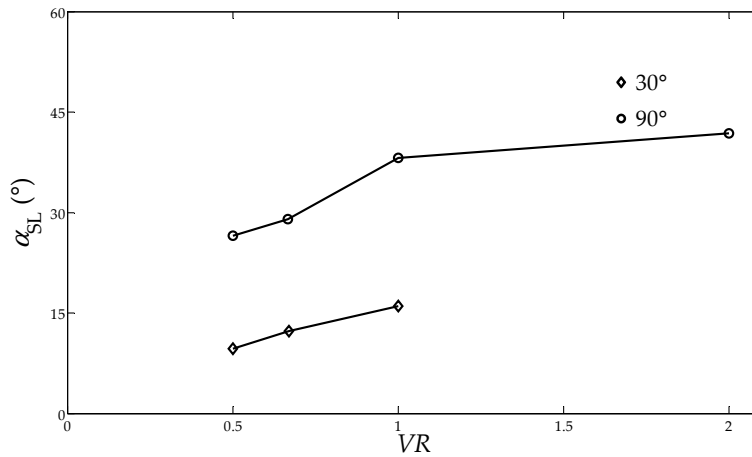


Figure 4.27: Variation of α_{SL} with VR ($\theta = 90^\circ$).

and L_{RZ1} . Generally, L_{RZ1} increases with VR except for $VR = 0.5$ at $\theta = 90^\circ$. The general trend of L_{RZ1} with VR may be owing to the increasing force exerted on the main flow by the side flow when VR is increased. Although L_{RZ1} of $VR = 0.5$ at $\theta = 90^\circ$ is larger than that of $VR = 0.67$, the area of RZ1 of $VR = 0.67$ ($Area = 0.238$) is larger than that of $VR = 0.5$ ($Area = 0.236$). Thus, the actual area of RZ1 is increased when VR is increased generally.

Furthermore, the separation length L_{RZ2} generally shows a maximum value with the variation of VR . It reaches maximum at $VR = 1$ for $\theta = 90^\circ$ while it does at $VR = 0.67$ for $\theta = 30^\circ$. The effect of θ has a greater effect than VR in this case.

In addition, the angle between SL and x axis, α_{SL} , is also changing with VR as illustrated in Figure 4.27. It generally increases with VR . When the momentum flux from side flow is increased as VR increases, the area occupied by side flow is increased in DS due to the nearly incompressible nature of the present flow. Thus, this leads to an increase in α_{SL} .

4.3.2 Unsteady Flow Dynamics

Variation of VR changes significantly the vortex shedding behavior in duct junction, which not only includes the shedding frequency, but also the pattern of vortex shedding/roll-up. This change in the pattern also occurs at other θ , such as $\theta = 30^\circ$ in Figure 4.7. Figure 4.28 recaptures the snapshots of vorticity

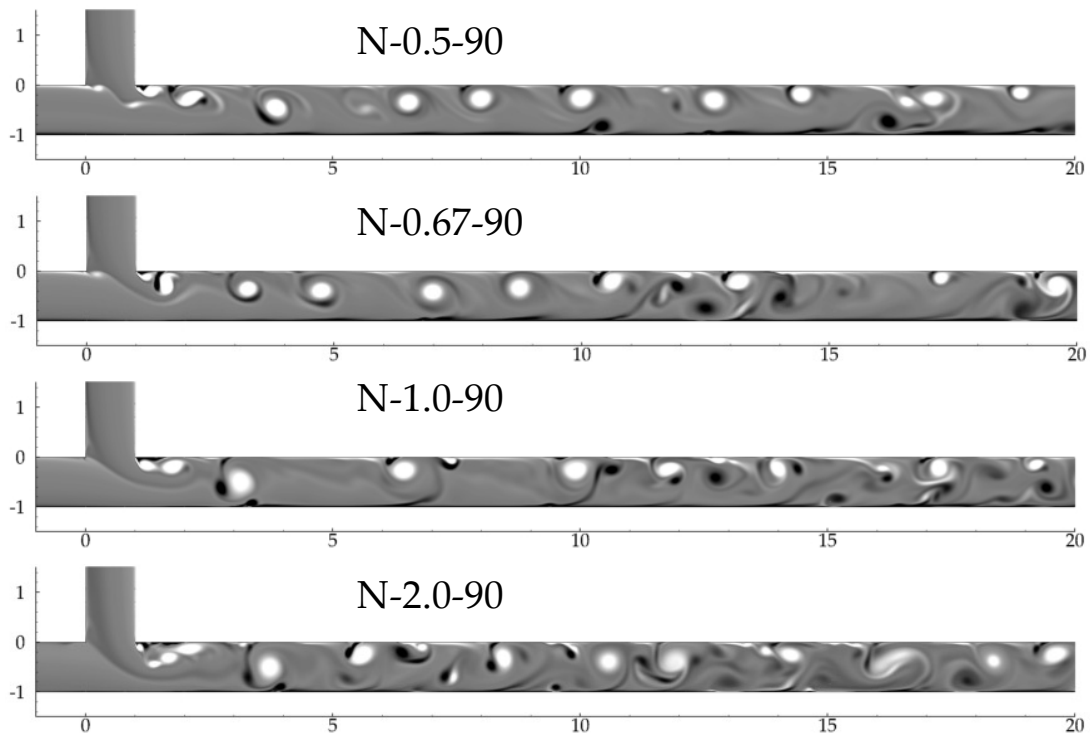


Figure 4.28: Snapshots of vorticity at $t = 34$ in all $\theta = 90^\circ$ cases.

at $t = 34$ for $\theta = 90^\circ$ cases. The common event of these cases is the vortex shedding from RZ1. This shedding is induced by the separated flow at RZ1 due to the sudden expansion encountered by the side flow at entering DJ. [Figure 4.28](#) also shows that it is the dominant flow unsteadiness based on its highest circulation. One of the major changes associated with variation of VR is the vanishing of vortex roll-up at SL as VR increases shown in [Figure 4.28](#). This can be explained by the fact that when VR increases, the recirculating zone at the upper wall of US near DJ grows as illustrated in [Figure 4.6](#), which in turn smears the streamwise velocity profile and thus suppresses the vortex shedding of SL.

Furthermore, from [Figure 4.28](#), the flow pattern becomes much more chaotic with increasing VR . When VR is at 0.5, the vortices shed seldom hit the bottom wall inducing secondary vortices there. However, when VR is increased, the path of vortex is shifted towards the bottom wall and the vortices bounce between the upper and lower walls. Thus, this increases the interaction between the vortices and the wall.

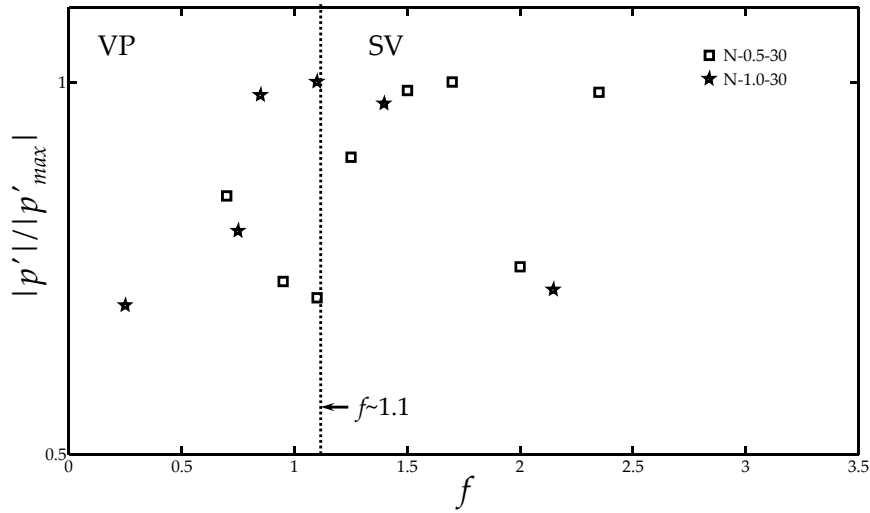


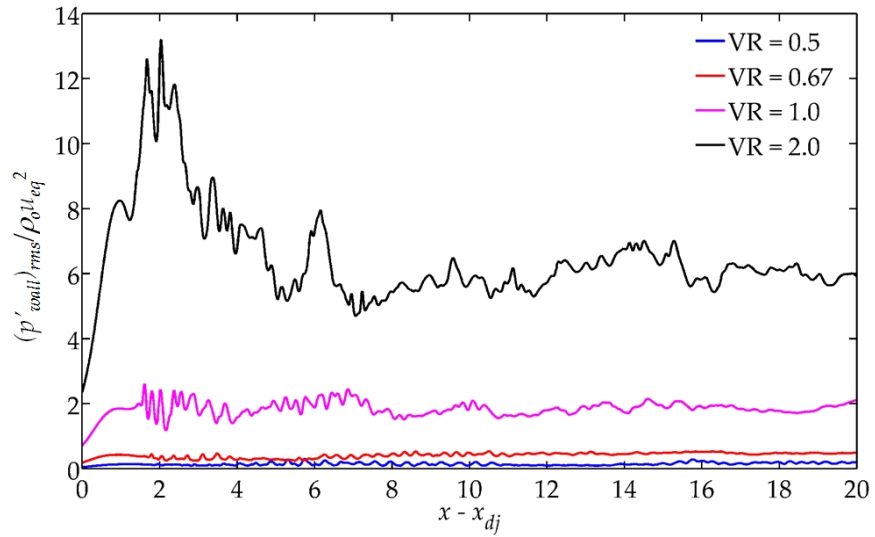
Figure 4.29: Variation of vortex shedding frequency $f_{s,RZ1}$ with VR ($\theta = 30^\circ$).

The variation of the dominant vortex shedding frequency $f_{s,RZ1}$ with VR is shown in Figure 4.29. The effect of VR can be observed from the cases with $\theta = 30^\circ$, whereas the dominant frequency is below $f < 1.1$ for low VR . This suggests that the flow is dominated by the vortex pairing during the process of vortex shedding when VR is small. When VR is increased, vortices at RZ1 are shed without pairing. However, no general trend in the variation of $f_{s,RZ1}$ is observed by varying VR .

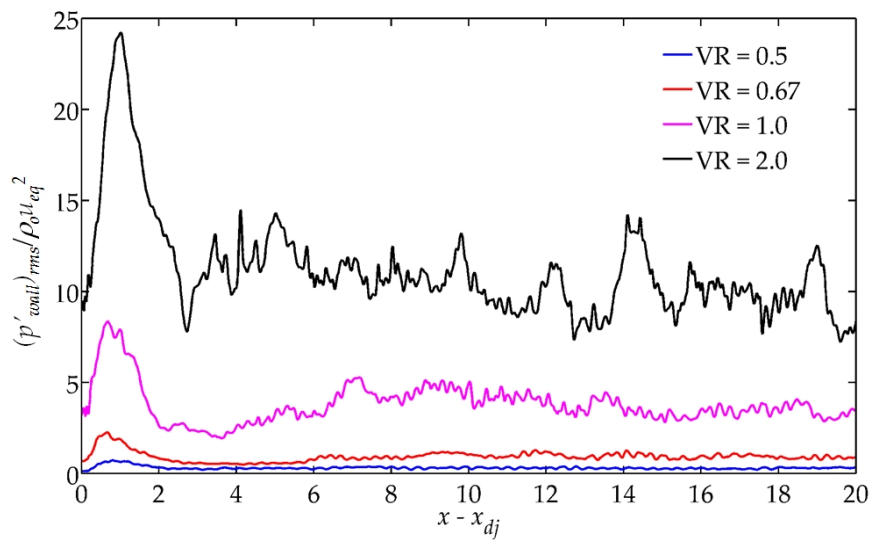
The vortex roll-up at SL is weakened as VR increases. The amplitude of the vorticity at the SL in N-0.5-90 is greater than that in N-0.67-90 from Figure 4.28. Furthermore, the roll-up frequency, $f_{s,SL}$ also decreases from 1.6 to 0.7 when VR increases from 0.5 to 0.67. This is because the streamwise velocity (u) in the main duct decreases, which suppresses the the velocity gradient required for the vortex shedding.

The relative strength of these flow unsteadiness can be indicated by the mean Reynolds stresses (Figure 4.13 to Figure 4.15). The stresses generally increase with VR , which implies increasing the extent of interaction in the flow. Although the vortex shedding also occurs at SL in N-0.5-90 and N-0.67-90, the Reynolds stresses are not produced substantially near SL like that in RZ1.

Figure 4.30 shows the RMS values of fluctuating pressure $(p'_{wall})_{rms} / \rho_0 u_{eq}^2$ at both walls in DS for various VR . As VR increases, $(p'_{wall})_{rms} / \rho_0 u_{eq}^2$ also in-



(a) Lower wall.



(b) Upper wall.

Figure 4.30: Distributions of $(p'_{wall})_{rms} / \rho_0 u_{eq}^2$ for various VR at $\theta = 90^\circ$.

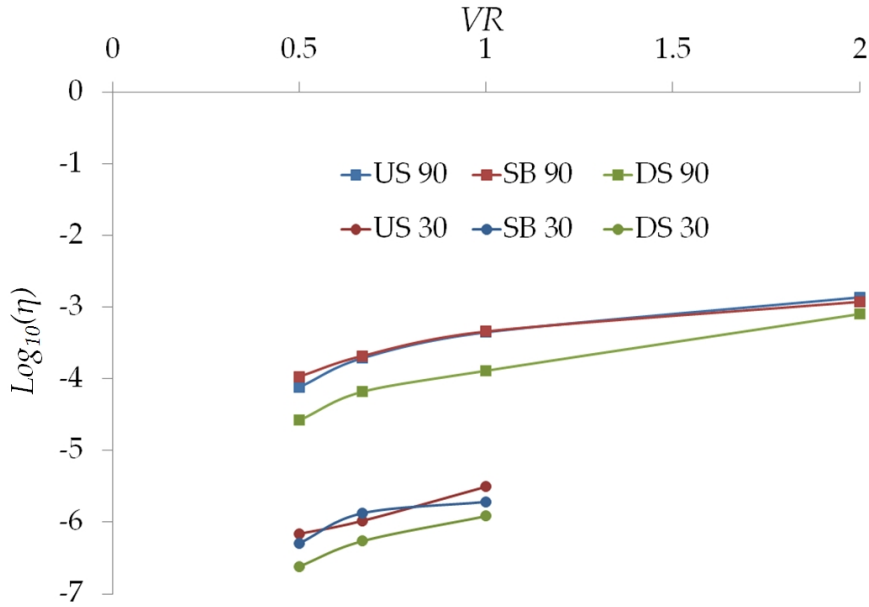


Figure 4.31: The variation of acoustic efficiency η with VR ($\theta = 30^\circ$ and 90°).

creases due to the stronger flow unsteadiness occurred. On the other hand, the distribution of $(p'_{wall})_{rms} / \rho_0 u_{eq}^2$ does not change significantly for both lower and upper wall when VR increases. The peak locations shown in Figure 4.30 are nearly the same.

4.3.3 Sound Generation

The acoustic efficiency in SB (η_{SB}), US (η_{US}) and DS ($\eta_{DS,acoustic}$) as determined from Eq.(4.12) to Eq.(4.15) are shown in Figure 4.31. $\eta_{a,DS}$ is also calculated by the method mentioned in Section 4.2.3. When VR is increased, η_{SB} , η_{US} and $\eta_{DS,acoustic}$ are increased. This is due to the increase in the source strength observed, i. e., the fluctuating wall pressure.

4.4 EFFECT OF MERGING ANGLE, θ

In this section, the effects of the merging angle θ on the aeroacoustics of the flow are discussed. Changing θ not only modifies the ratio of x and y momentum of the flow impinging at DJ, similar to VR , but also the geometry at DJ. To illustrate this, all the cases with $VR = 0.67$ and 1 are selected for this

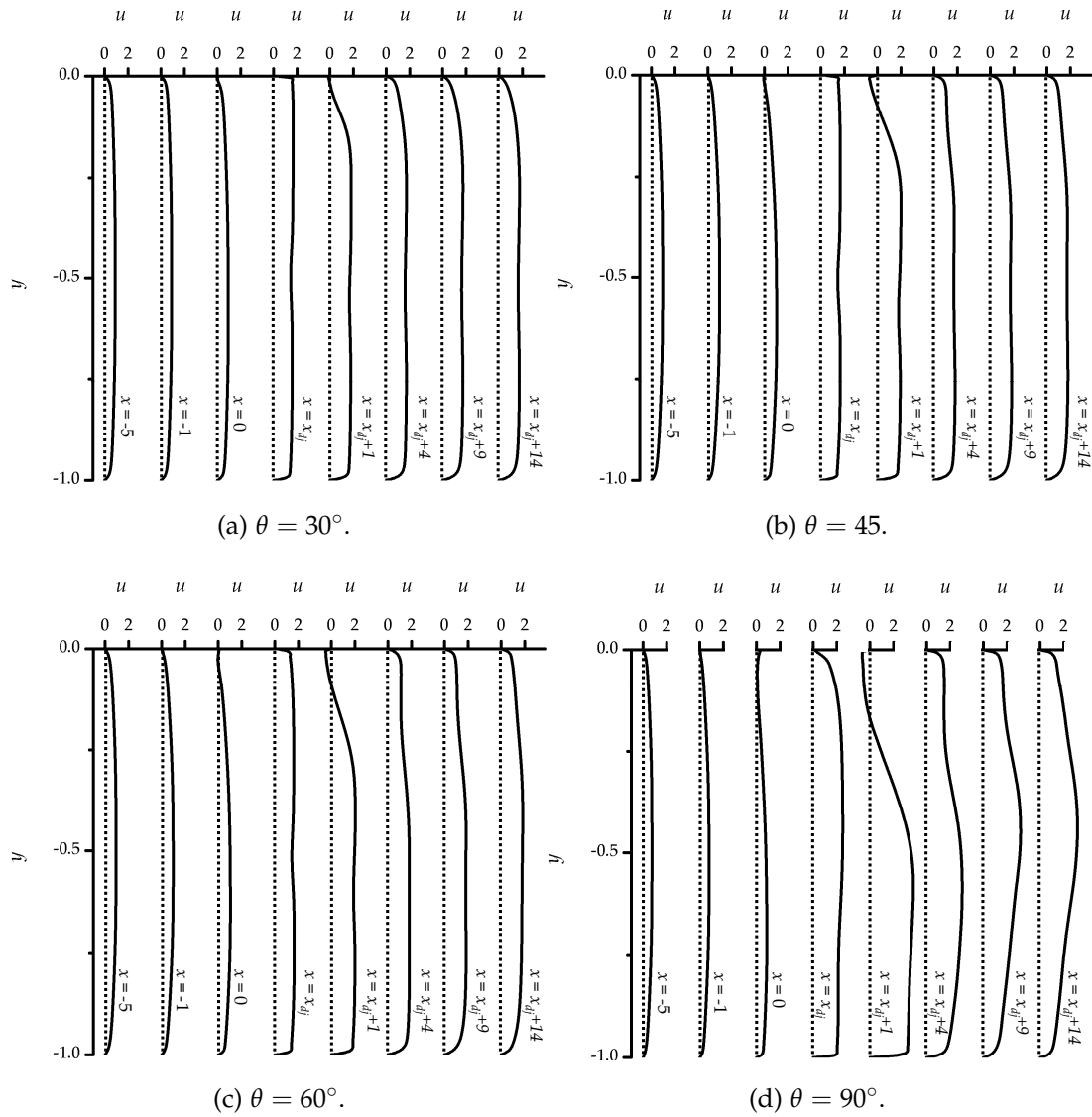


Figure 4.32: Mean streamwise velocity profile (u) at $VR = 1$.

purpose. However, $VR = 1$ is the primary focus of the discussion as vortex shedding only occurs at RZ1.

4.4.1 Mean Flow

The mean streamwise velocity profile (u) in Figure 4.32 illustrates that an increase in θ tends to the increase in the length required to recover to the fully developed velocity profile. This observation is similar to those for VR .

The mean vorticity and streamlines of these four cases are shown in Figure 4.33. RZ1 increases in size when the merging angle θ increases. θ mainly affects its thickness, rather than the reattachment length L_{RZ1} . In general, L_{RZ1}

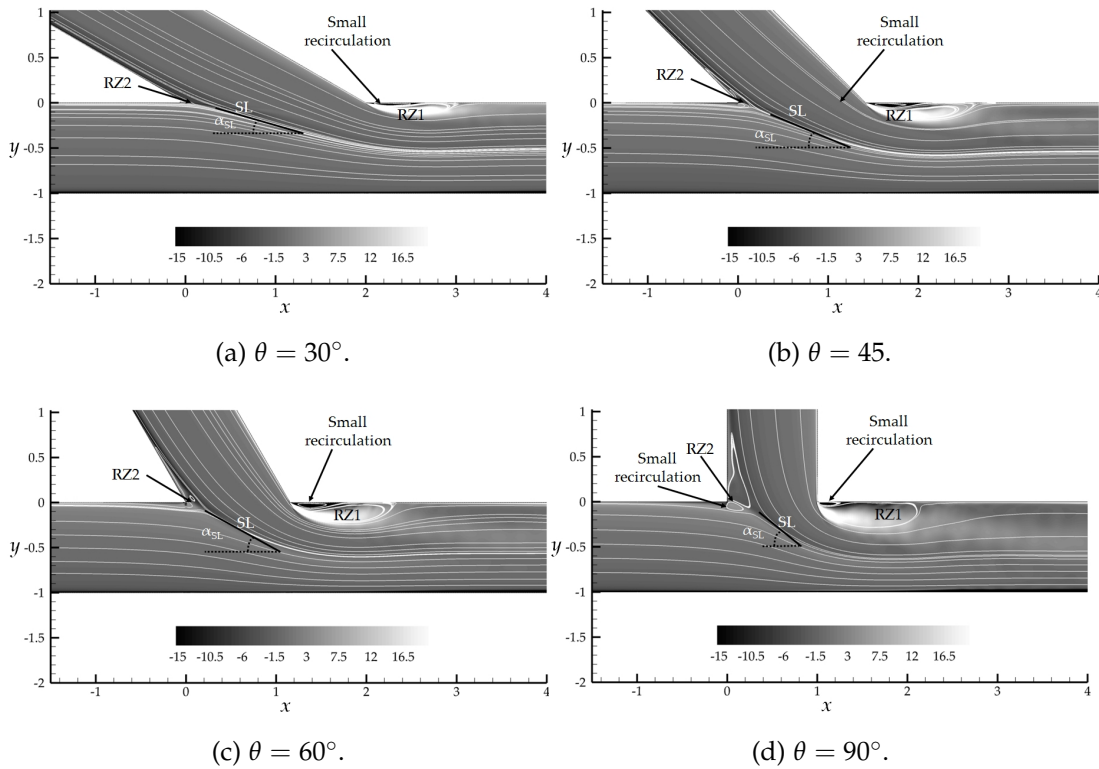


Figure 4.33: Mean vorticity with streamlines at $VR = 1$.

is comparable to the width of the duct but shows slight variation with θ . For $VR = 0.67$, L_{RZ1} attains its maximum at $\theta = 60^\circ$ (Figure 4.34). However, at a higher $VR = 1.0$, the maximum L_{RZ1} occurs at a smaller merging angle $\theta = 45^\circ$. The thickness of RZ1 decreases with an increase in θ due to the increasing y component of flow momentum at DJ.

Regarding the recirculating zone RZ2, the separation length L_{RZ2} increases almost linearly with θ illustrated in Figure 4.35. On the other hand,

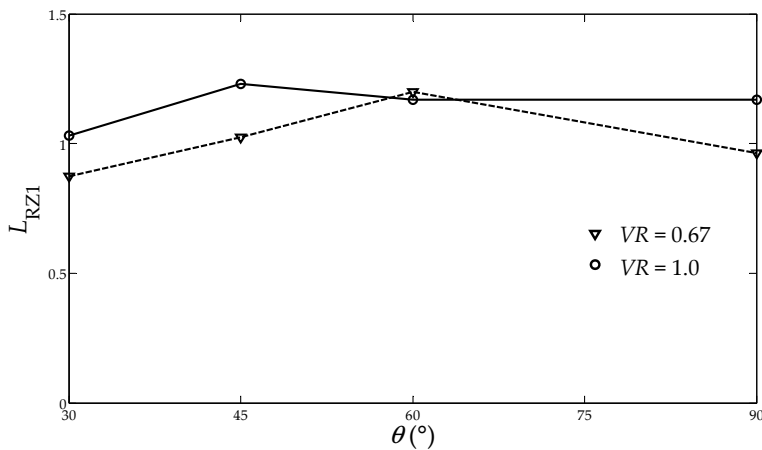


Figure 4.34: Variation of reattachment length L_{RZ1} with θ .

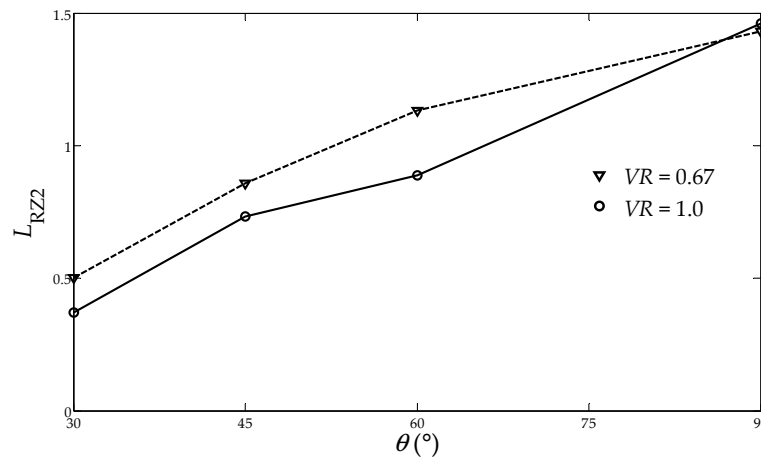


Figure 4.35: Variation of separation length L_{RZ2} with θ .

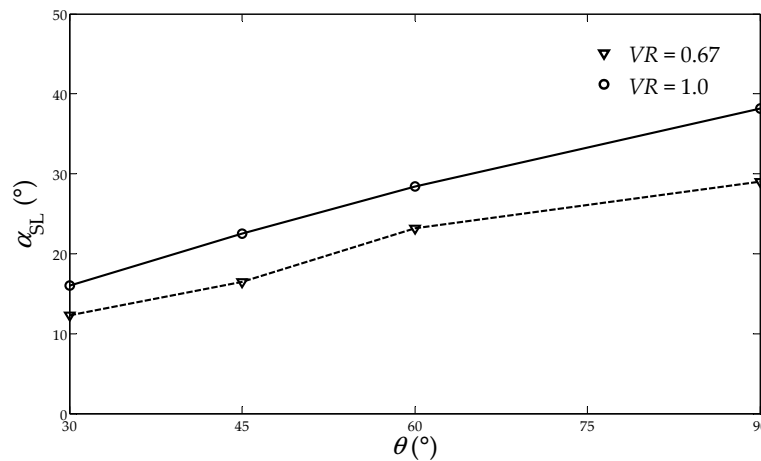


Figure 4.36: Variation of α_{SL} with θ .

the thickness of RZ2 increases greatly with the increase in θ (Figure 4.33). RZ2 further extends to the upper wall in US near DJ as θ increases perhaps because the downward force exerted on the main flow is increased, pressing the main flow further downward. Thus, this induces the earlier separation from the upper wall.

Furthermore, the angle of SL, α_{SL} , increases linearly basically with θ as illustrated in Figure 4.36. It should be noted that for $VR = 1$, α_{SL} is almost equal to half of the merging angle θ . This may be because the momentum fluxes from both upstreams (US and SB) are the same.

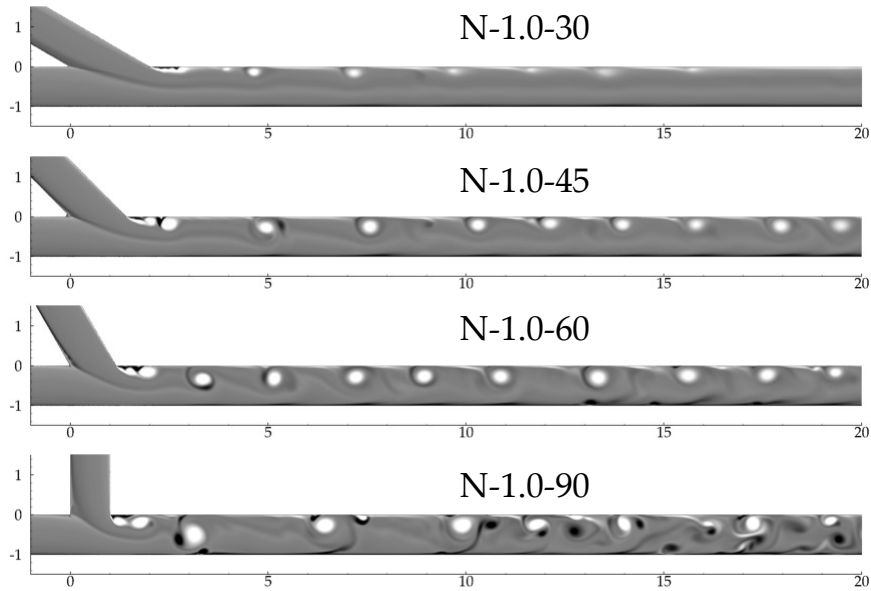


Figure 4.37: Snapshots of vorticity in all $\theta = 90^\circ$ cases at $t = 34$.

4.4.2 Unsteady Flow Dynamics

With the same velocity ratio, the pattern of vortex shedding does not change significantly by adjusting θ . Figure 4.37 presents the snapshots of vorticity at $t = 34$ for $VR = 1$ cases. It shows that the shedding locations are the same from RZ1 and this is different from the effect of VR (Figure 4.28). Therefore, the influence of θ on the shedding pattern is less than that of VR .

The major effect of θ on the vortex shedding at RZ1 is the size and the strength of the shed vortices. Both quantities increase greatly from $\theta = 30^\circ$ to $\theta = 90^\circ$. Furthermore, the trajectories of the vortices are also shifted towards the lower wall as θ increases. Figure 4.37 clearly shows the bouncing of the vortices at $x \sim 3$ in DS for N-1.0-90 but similar vortices stick to the upper wall in cases N-1.0-30 and N-1.0-45. The vortex bouncing also induces stronger secondary vortices for the $\theta = 90^\circ$ case. Therefore, the flow pattern in DS becomes less regular when θ increases.

Similar to Figure 4.29, the variation of the vortex shedding frequency, $f_{s,RZ1}$, with θ is shown in Figure 4.38. For $\theta < 45^\circ$, the type of dominant shedding is the single type SV. When θ is increased further, the dominant shedding type is changed to the pairing type VP. As θ increases, the mutual induction

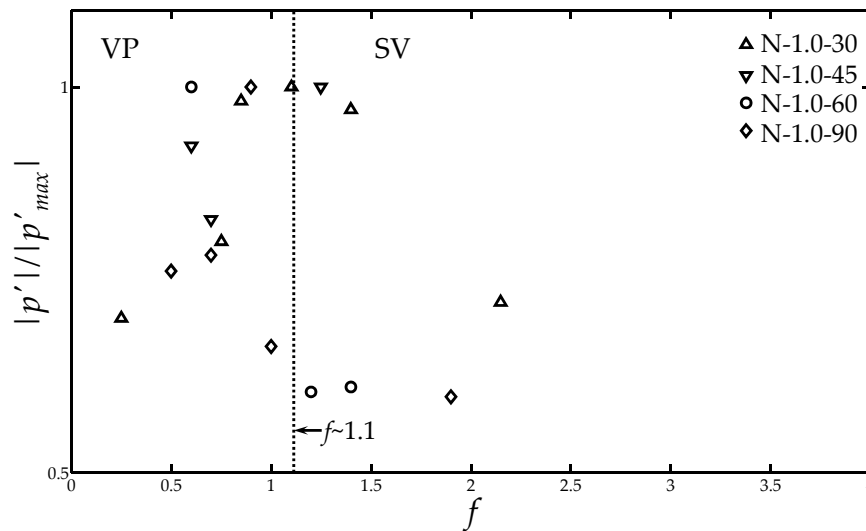


Figure 4.38: Variation of vortex shedding frequency, $f_{s,RZ1}$, with θ .

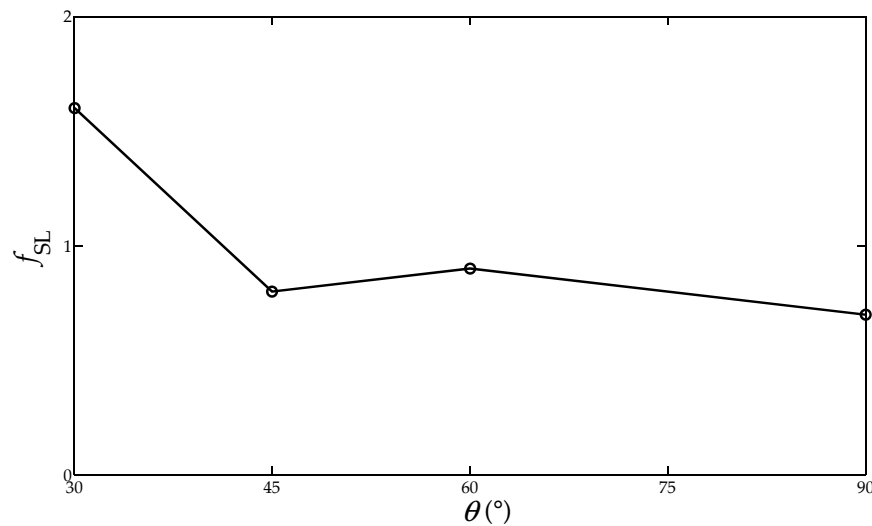


Figure 4.39: Variation of vortex shedding frequency, $f_{s,SL}$ with θ .

between shed vortices is increased due to the increased size and strength of vortices shed. This leads to the early vortex pairing near downstream edge of DJ, and consequently the dominant shedding process.

Another location of vortex roll-up is SL and all the cases for $VR = 0.67$ are evaluated to study the effect of θ . Figure 4.39 illustrates the vortex shedding frequency at SL $f_{s,SL}$ with different θ . Unlike $f_{s,RZ1}$, it usually contains a single vortex shedding frequency. $f_{s,SL}$ is decreased by increasing θ , whereas the decrease is much faster initially. This is perhaps because the y momentum, which is related to $\sin(\theta)$, is increased greatly from $\theta = 30^\circ$ to $\theta = 45^\circ$.

Furthermore, the mean Reynolds stresses $\overline{u'v'}/u_{eq}^2$ for $VR = 1$ is illustrated in Figure 4.40. It shows that the relative strength of the flow unsteady-

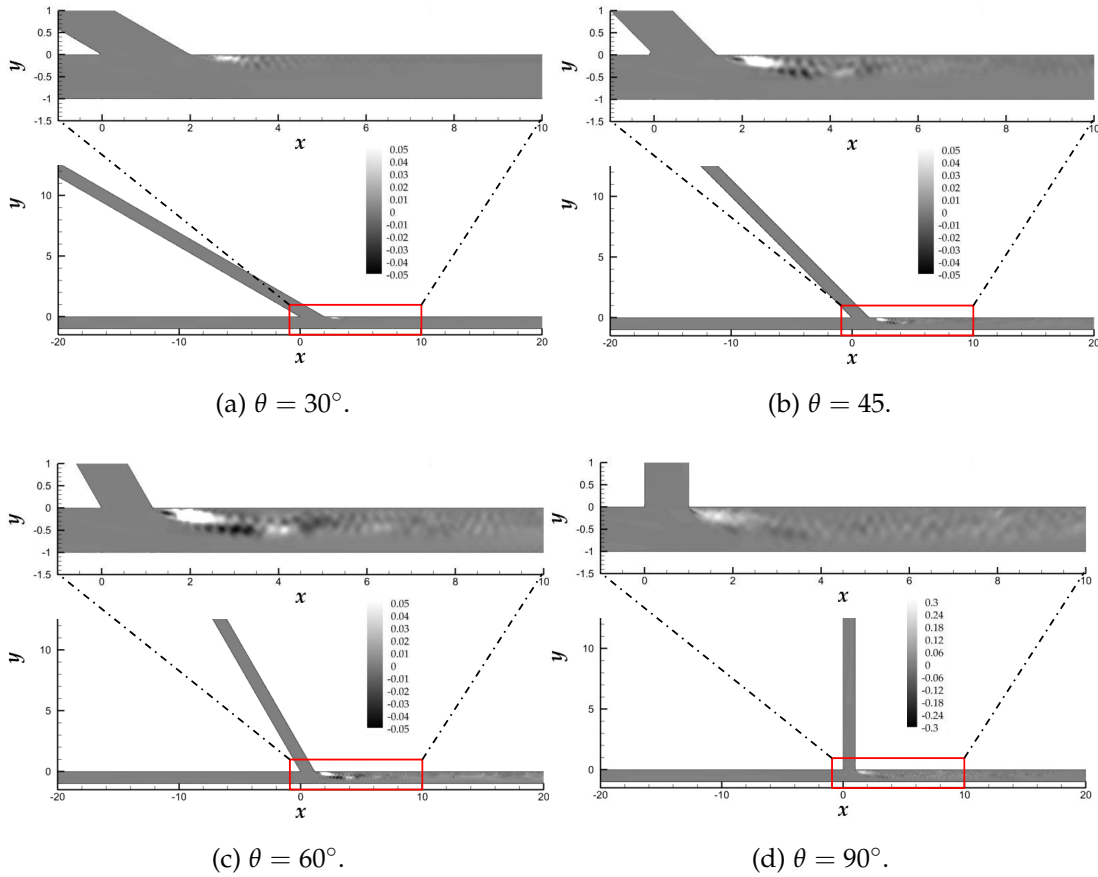
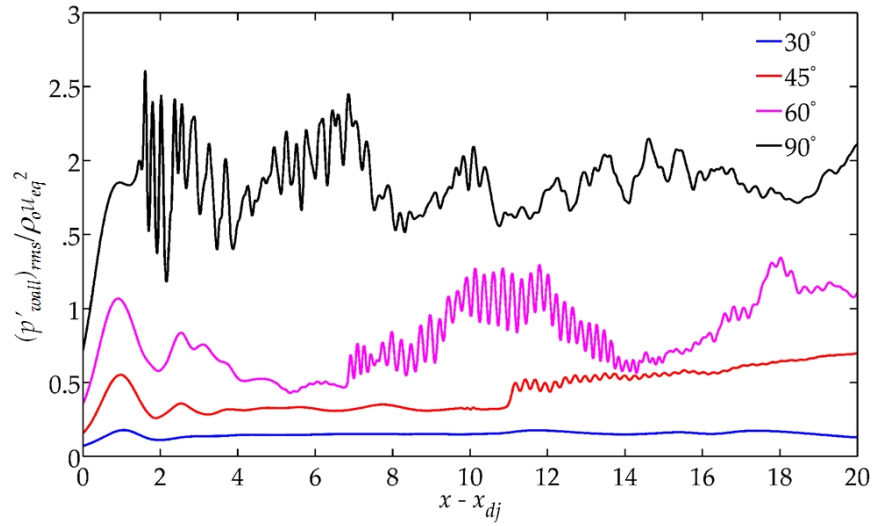


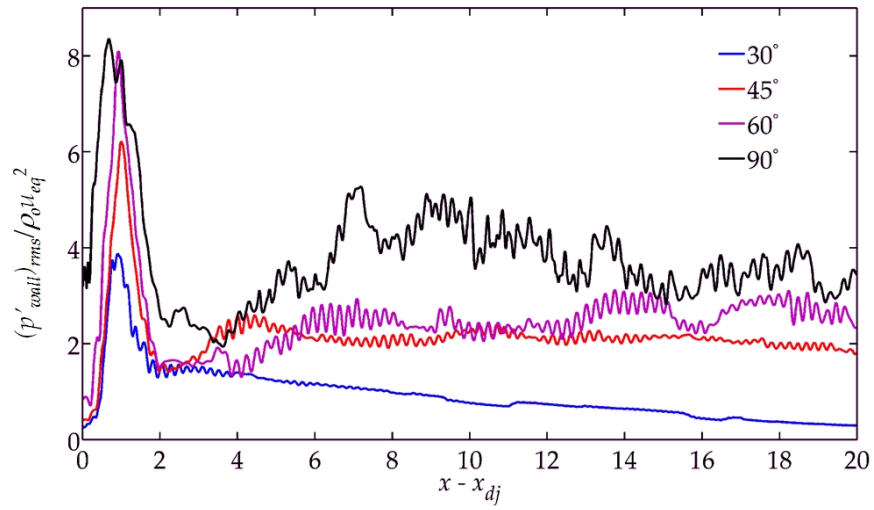
Figure 4.40: Mean Reynolds stress $\left(\overline{u'v'}/u_{eq}^2\right)$ at $VR = 1$.

ness increases with θ not only in its levels, but also its size. Similar behavior is also observed for $VR = 1.5$. This implies that the extent of interaction increases with θ as the flow becomes less regular in DS.

Figure 4.41 shows the RMS values of fluctuating pressure $(p'_{wall})_{rms} / \rho_0 u_{eq}^2$ at both walls in DS for various θ ($VR = 1.0$). It shows that θ increases $(p'_{wall})_{rms} / \rho_0 u_{eq}^2$ due to the increased flow unsteadiness occurring. It also shows a great increase in $(p'_{wall})_{rms} / \rho_0 u_{eq}^2$ from $\theta = 60^\circ$ to $\theta = 90^\circ$. In addition to the amplitude of the fluctuating wall pressure, its distribution also changes with θ . At the lower wall, the distribution in the lower wall is rather uniform at $\theta = 90^\circ$, implying a rather uniform interactions between the vortices and the walls in DS. When $\theta = 45^\circ$ or 60° , sudden jumps in the wall fluctuating pressure occur at the lower wall. This corresponds to the roll-up of secondary vortices at the lower wall. When $\theta = 30^\circ$, the distribution is very uniform indicating little occurrence of the interactions. On the other hand, at



(a) Lower wall.



(b) Upper wall.

Figure 4.41: Distributions of $(p'_{wall})_{rms} / \rho_0 u_{eq}^2$ for various θ ($VR = 1.0$).

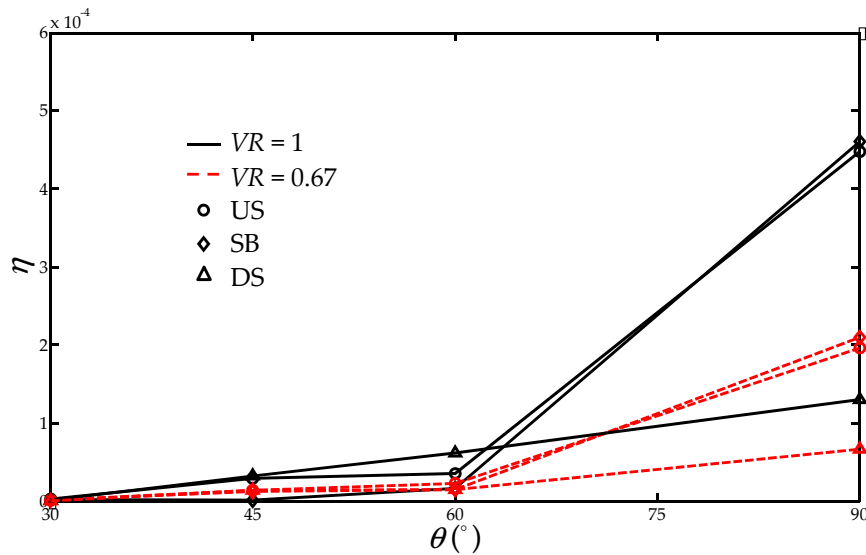


Figure 4.42: Variation of η_{SB} , η_{US} and $\eta_{DS,acoustic}$ with different θ .

the upper wall, a sharp decrease following the peak locations indicates the leaving of vortices shed from the upper wall. The fluctuating wall pressure then increases again showing the approach of the vortices after its bouncing from the lower wall.

4.4.3 Sound Generation

The previous section shows that the source strength is increased with increasing θ . This can be indicated by the variation of the acoustic efficiency in different θ . The acoustic efficiency η across the duct cross-section is calculated from Eq.(4.12) to Eq.(4.15) while $\eta_{DS,acoustic}$ is also calculated by the method mentioned in Section 4.2.3. The results η_{SB} , η_{US} and $\eta_{DS,acoustic}$ are shown in Figure 4.42. When θ is increased, all of them are increased due to the increased source strength. Furthermore, they have a huge increase from $\theta = 60^\circ$ to $\theta = 90^\circ$. Based on the flow dynamics shown in Section 4.4.2, such increase is probably due to the more vigorous interaction between the vortex and the walls in DS at $\theta = 90^\circ$. When $\theta \leq 60^\circ$, the vortices do not collide on the bottom wall in DS, so interaction between vortex and the wall is much less serious. The sound generation is increased significantly when this interaction is intensified.

4.5 CONCLUDING REMARKS

This chapter presents the findings in the two dimensional aeroacoustic investigation of merging flow at duct junctions. The effects of two parameters, VR and θ on its aeroacoustics have also been discussed. In general, three distinct flow features exist in the merging flow at duct junctions - the recirculating zone at downstream corner of duct junction RZ1, the shear layer between the two flows SL and another recirculating region upstreams to SL, RZ2. Another key finding is that the dominant flow unsteadiness is the vortex shedding at RZ1 due to the instabilities of the separated flow there. This implies that vortex shedding at RZ1 is also the dominant sound generation in this flow.

As the acoustic and flow disturbances are mixed in DS, a two dimensional spectral analysis is applied to differentiate the disturbances. Based on these results, an approach for extracting the acoustic contribution in DS is proposed. Generally, the acoustic power generated increase with VR and θ , thus N-2.0-90 is the noisiest case in the current study because of the intense vortex interactions in the unsteady flow dynamics. Furthermore, the acoustic efficiency η is directly proportional to VR . The sound generation is increased when the vortices from RZ1 interact vigorously with the vortices shed from wall. This is demonstrated by the sudden increase in sound generation from $\theta = 60^\circ$ to $\theta = 90^\circ$. Thus, this interaction plays an important role in the sound generation.

Generally, in the sound generation of aeroacoustics, a scaling law between the acoustic efficiency and a velocity scale is evaluated in order to aid the estimation of the sound power under different flow conditions. For example, [Lighthill \(1954\)](#) proposed a u^8 law for the sound power induced by the turbulence, which implies the acoustic efficiency $\eta \propto u^5$, where u is the speed of the flow. However, it is not obvious to derive such law for the merging flow at duct junction. Geometry effect also plays an important role in the sound generation. For instance, considering N-1.0-30 and N-1.0-90, same

inflow condition is applied for these two cases and their outflow velocities are nearly the same owing to the conservation of mass, but the difference between their acoustic efficiency is of 10^{-3} . It may not suggest a relation $\eta \propto u^n$. Another difficulty in evaluating a scaling law for the merging flow with the speed of the flow is the observed inverse relationship between the inflow speed and the acoustic efficiency. When VR is large, the average speed of the flow entering the duct junction is small, but it is observed that the acoustic efficiency is large. This contradicts with the general perception that higher speed input produces more sound as experienced in various aeroacoustic problems such as the sound generation from jet (Lighthill 1954). These show that the power law between the characteristic speed of the flow and the acoustic efficiency may not be established. Therefore, establishment of other relationship regarding the acoustic efficiency is considered.

According to Curle (1955), at the flow with low Mach number and the presence of solid boundary, the dominant sound source is the surface distribution of dipoles, i. e., the fluctuating wall pressure in the merging flow at duct junction. Thus, the force exerted on the fluid by the wall F is directly related to the acoustic efficiency suggesting a possible scaling law between them.

Following the argument adopted by Curle (1955). At the far field of a open, low Mach number flow ($M_o \ll 1$) with solid boundaries in three dimensional case, the acoustic fluctuation is given by

$$\rho - \rho_o \sim Fu_o c_o^{-3} L^{-1} x^{-1}, \quad (4.19)$$

where the subscript o denotes the reference state, L is a length scale and x is the distance to the source, c_o is the reference sound speed. The sound intensity I generated by the dipole can be expressed as $c_o^3 \rho_o^{-1} (\rho - \rho_o)^2$ is of order

$$I \sim \rho_o^{-1} F^2 u_o^2 c_o^{-3} L^{-2} x^{-2}. \quad (4.20)$$

This implies that the sound power W is of order

$$W \sim \rho_o^{-1} F^2 u_o^2 c_o^{-3} L^{-2}. \quad (4.21)$$

Since the total rate of supply $W_{in} \sim \rho_o u_o^3 L^2$, so the acoustic efficiency η is of order

$$\eta = \frac{W}{W_{in}} \sim \rho_o^{-2} F^2 u_o^{-1} c_o^{-3} L^{-4}. \quad (4.22)$$

Defining $\check{F} = F/\rho_o u_o^2 L^2$, it yields

$$\eta \sim \check{F}^2 M_o^3, \quad (4.23)$$

where $M_o = u_o/c_o$. One should note that this scaling law is obtained for open flow. In confined flow, [Davies & Ffowcs-Williams \(1968\)](#) found that the sound generation of the quadruple in confined flow is increased by order M_o^2 compared to the open flow case. In case of the dipoles in confined flow, [Bailly & Lafon \(1996\)](#), [Gloerfelt & Lafon \(2008\)](#) studied the sound generation of the flow through a diaphragm in a duct at low Mach number, which is also a dipole type of generation at diaphragm. It is found that its acoustic power generated varies with u^4 . This implies the acoustic efficiency $\eta \sim u_o \sim M_o$, which is also increased by order M_o^2 compared to the open flow case derived by [Curle \(1955\)](#) ($\eta \sim M_o^3$). Therefore, comparing the sound generation by dipoles in open and confined flow, the difference in their acoustic efficiency of order M_o^2 is expected. Based on this argument, the acoustic efficiency in the merging flow at duct junction, which is a dipole type of generation, should be of order

$$\eta \sim \check{F}^2 M_o. \quad (4.24)$$

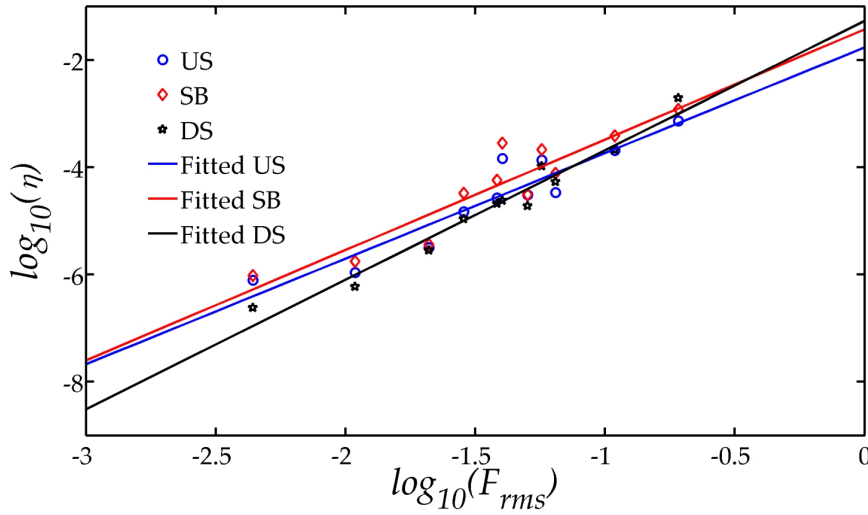


Figure 4.43: Scaling law of η and F_{rms} for all cases.

Furthermore, this equation is based on the three dimensional case. For two dimensional case, [Howe \(1998\)](#) suggested that the acoustic efficiency is increased by order M_0 compared to that in three dimensional case, i. e.,

$$\eta \sim \check{F}^2. \tag{4.25}$$

Here, the RMS values of the fluctuating force F_{rms} and the averaged speed $u_{flow} = \sqrt{W_{aero}/\rho u_{2,max}}$ are chosen as the scaling parameters. F_{rms} is estimated from integrating the RMS value of fluctuating wall pressure along the walls in DS. [Figure 4.43](#) shows the scaling law between the acoustic efficiency η and the fluctuating force F_{rms} . The exponential $n \approx 2$ for the region US and SB while $n \approx 2.4$ in DS. The proposed scaling law works quite well in the upstream region (US & SB), which has little flow disturbances. On the other hand, in the DS region, since the section taken for the calculation of the acoustic power is adjacent to the source region, the scaling law may not be applicable as it is based on the far field assumption, i. e., at least free from the flow unsteadiness.

EXPERIMENTAL INVESTIGATION OF MERGING FLOW AT DUCT JUNCTIONS

A three dimensional investigation of merging flow at duct junctions helps broadening our understanding of the three dimensional characteristics of the aeroacoustics. The investigation started with an experimental study. In this chapter, experiments of the merging flow at duct junctions are discussed. Because of the lack of non-intrusive technique such as particle image velocimetry (PIV) or Laser Doppler velocimetry (LDV), intrusive technique is applied in the experiment. The setup of this experiment is described first. Then the measurement results and their interpretations follow. Their results will also be compared with those obtained from the numerical simulations.

5.1 EXPERIMENTAL SETUP

According to the numerical study, the major aeroacoustic generation is located at the downstream of the duct junction especially the recirculating zone RZ1, so experimental investigation was focused around this region. The experiment aims at providing a comparison to the simulations especially for the mean flow and unsteady aerodynamics at this near field region. Measurements of the three dimensional velocities and the pressure fluctuation were performed in this region .

5.1.1 Test Rig Design and Instrumentations

A schematic of the test rig is shown in [Figure 5.1](#) and [Figure 5.2](#). Two centrifugal fans ([Figure 5.2a](#) and [Figure 5.2b](#)) were used to drive two inlet flows. In the main duct, a silencer with 25-mm-thick absorptive lining was used to reduce the noise radiated from the fan 1. A converging zone was then added downstream of the silencer to fit the test section, which was a duct junction with cross section size $100 \times 100\text{mm}^2$. In the side branch, due to the unmatched size of exit and the duct section, a converging zone ([Figure 5.2c](#)) was connected to the fan 2, followed by a duct work with absorptive lining of 50mm. Since the flow in side branch experienced two turns in flow direction, an expansion chamber of cross section $200 \times 200\text{mm}^2$ was added to enhance the flow regularity before entering the test section. All the duct work with absorptive lining and converging zones were made of 1.5-mm sheet metal. The duct junction test section was made of 19-mm acrylic sheet. They also had the cross sectional area of $100 \times 100\text{mm}^2$. There were two types of test section; one was with merging angle $\theta = 45^\circ$ whereas another one was $\theta = 90^\circ$ ([Figure 5.3](#)). A probe sliding mechanism shown in [Figure 5.3c](#) was designed for taking measurements in the duct junction. An acrylic duct work of 19-mm thick sheet was attached to the duct junction downstream and ends with a $160 \times 160\text{mm}^2$ outlet cone ([Figure 5.2d](#)). It was then extended further outside the test room, which was opened to release the pressure inside.

The velocity field in test section was measured by using a Turbulent Flow Instrumentation (TFI) Series-100 four-hole cobra probe ([Figure 5.4a](#)). It consisted of pressure tap holes with 0.5mm diameter. Instantaneous three dimensional velocities at a location could be obtained from the difference in the pressure captured at these tap holes. Thus, the mean and fluctuating velocities of the location could then be derived. Detailed theory and response of this probe could be referred to the work of [Hooper & Musgrove \(1997\)](#). The cobra probe has a limitation in the oncoming flow direction, which can only

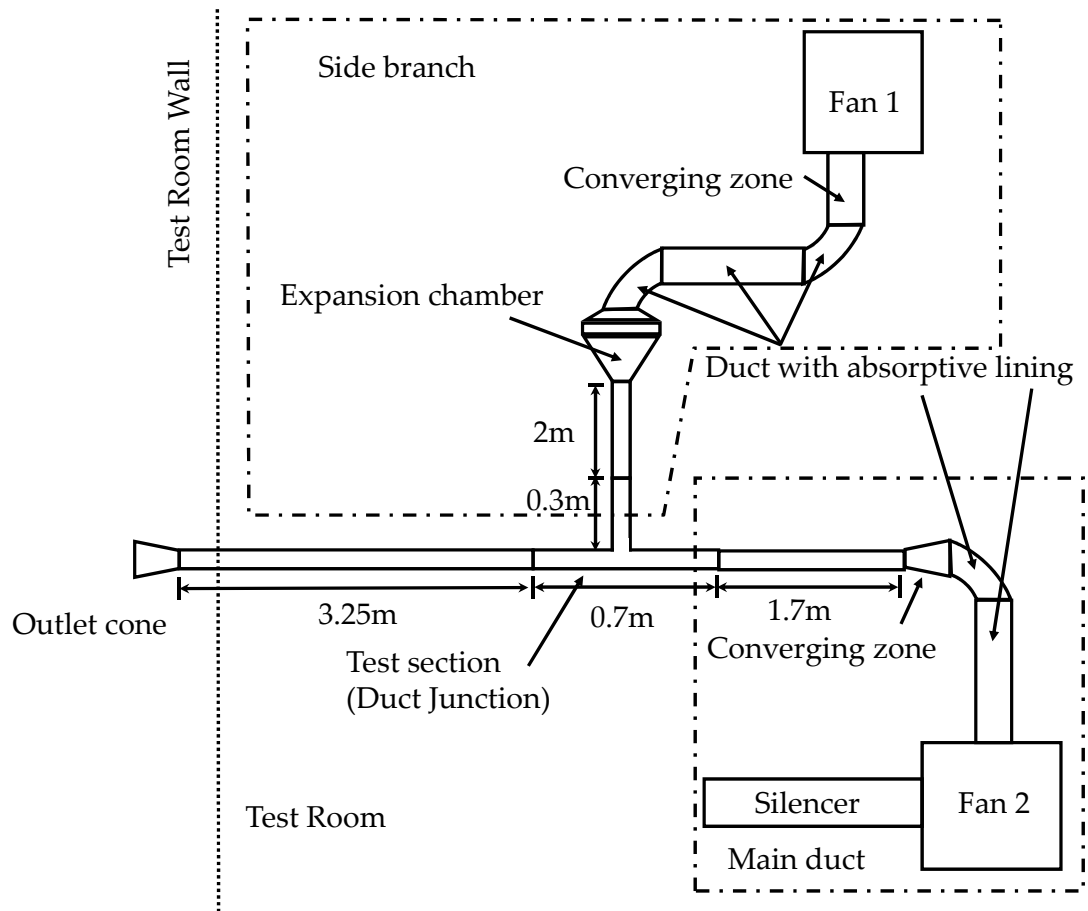


Figure 5.1: Schematic of duct system used. Two turns are required in the side branch due to the limitation of space available in laboratory, so an expansion chamber is added before the flow entering the junction.



(a) Fan with silencer (Main duct).



(b) Fan (Side branch).



(c) Converging zone (Side branch).

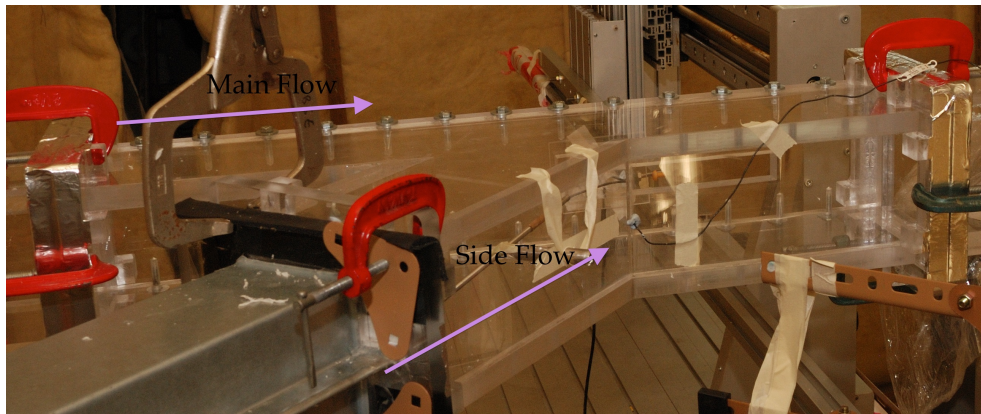


(d) Outlet cone.

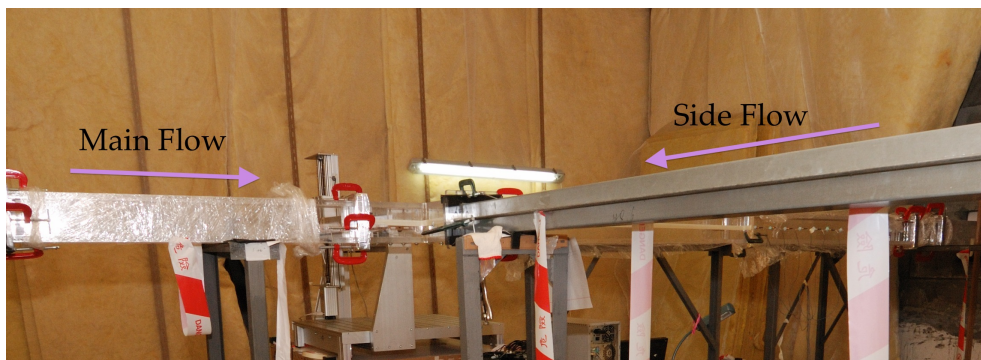


(e) Overall duct work used.

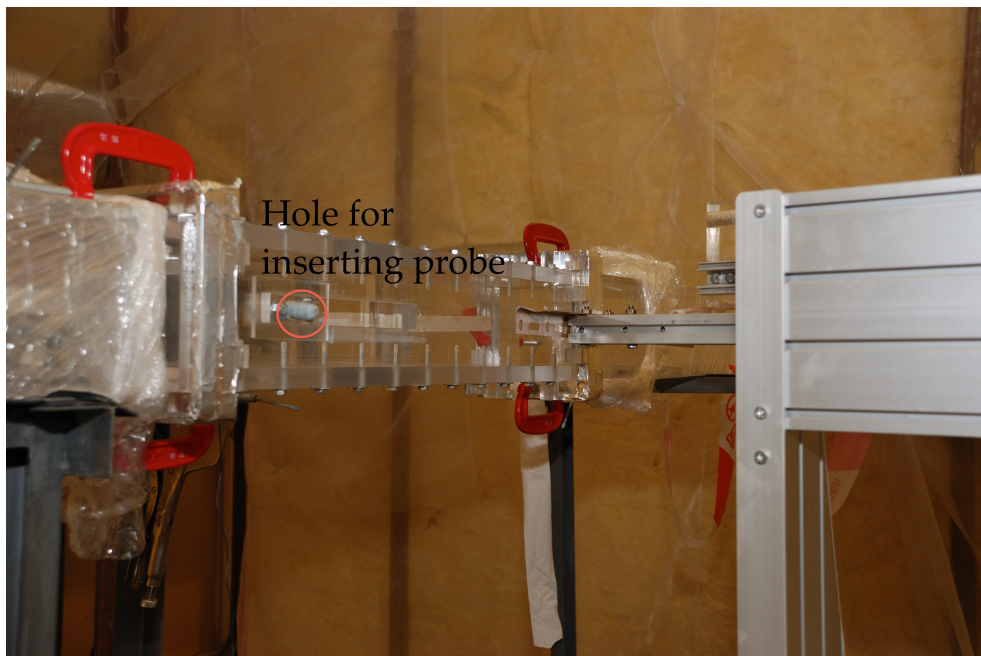
Figure 5.2: Various components of duct system used.



(a) 45° duct junction.



(b) 90° duct junction.



(c) Probe sliding mechanism for taking measurement. The hole is for inserting the probe to access the measurement zone.

Figure 5.3: Duct junction applied in experimental setup.

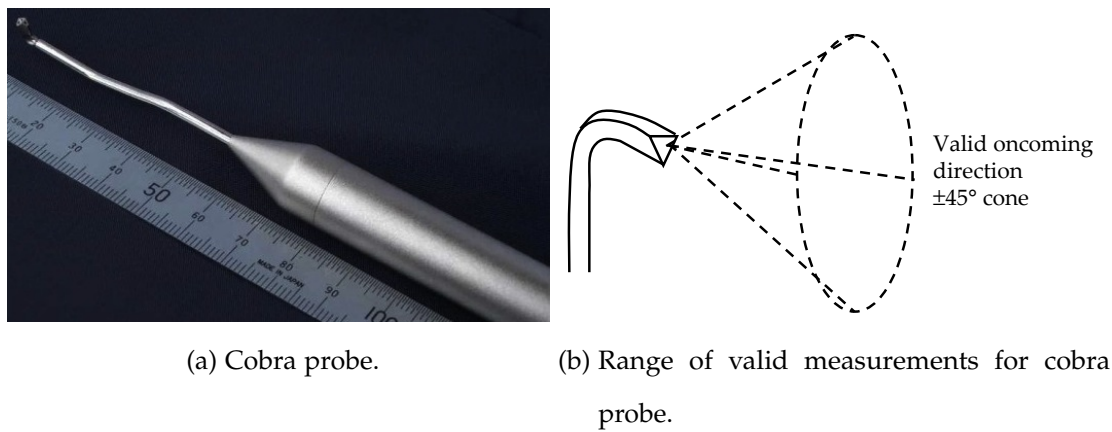


Figure 5.4: Cobra probe used in experimental study.

measure the oncoming flow within $\pm 45^\circ$ cone to its facing axis (Figure 5.4b). The data measured outside this range were rejected as it may not be accurate enough due to the flow separation from the tap holes of the probe.

The pressure field inside test section was measured by a Brüel & Kjær probe microphone (Model no. 4182) with a frequency response ranging from 20 Hz to 20k Hz. The data acquisition system as that mentioned later was adopted in this measurement. In both kinds of measurements, the sampling frequency was set at 5k Hz. This choice of sampling frequency should be sufficiently high for capturing the aeroacoustic signals generated in merging flow as the highest frequency of sound generated was less than 500 Hz as derived from numerical results in last chapter.

Figure 5.5 shows the schematic of data acquisition in measurements. The measurement area with size of $146 \times 48 \text{ mm}^2$ was located at the central section downstream of the duct junction, where the dominant aeroacoustic sources reside according to the numerical results reported in the last chapter. In these two measurements, the measuring probe, i. e., the cobra probe or the probe microphone, was connected to a data acquisition system, which was composed of a NI PCI – 6220M 16-channel analog-to-digital card connected to a computer and a data acquisition software, TFI Device Control. An ENDEVCO model no. 8507C – 2 pressure transducer was mounted at a wall location 8mm downstream from the duct junction for capturing the reference signal. This reference location was chosen such that it was able to detect the

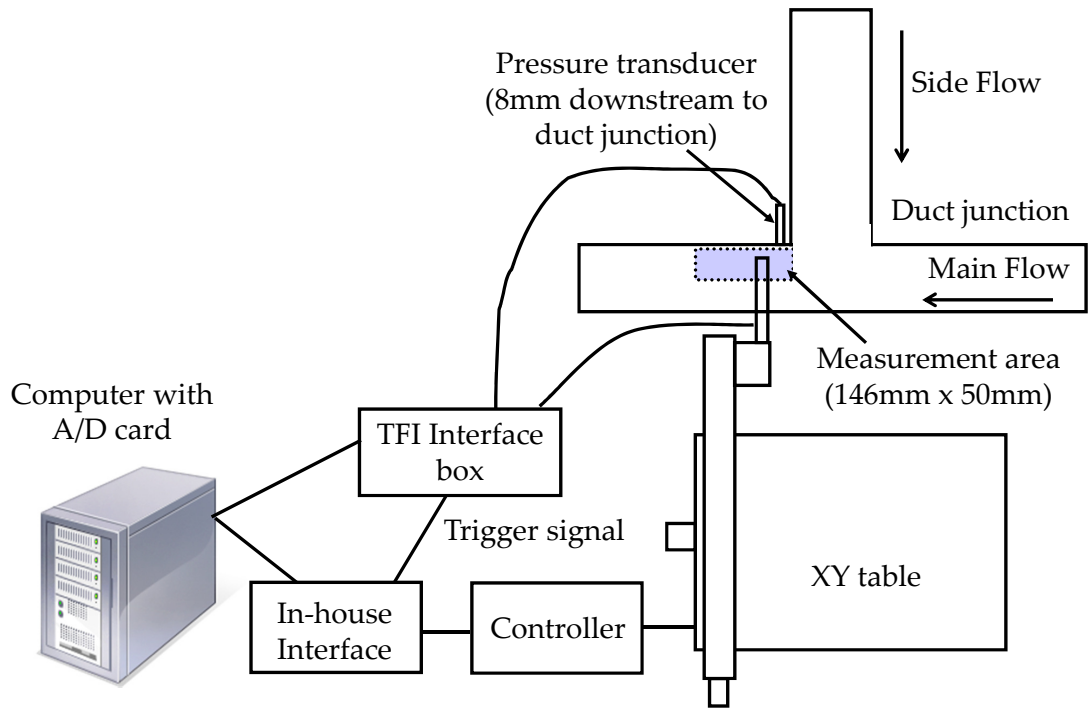
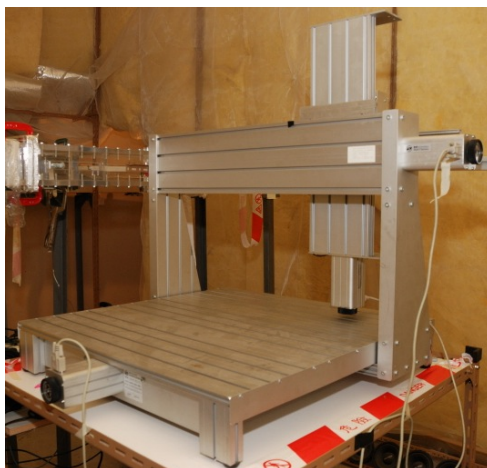


Figure 5.5: Schematic of data acquisition system in measurements.



(a) XY table used.



(b) Controller for XY table.

Figure 5.6: XY table.



Figure 5.7: Snapshot of measurement.

passage of the evolving coherent structures from duct junction. The cobra probe and the probe microphone were mounted on a XY table (Figure 5.6a) and inserted into the duct junction individually. The table motion was adjusted by a controller (Figure 5.6b), which is connected to the same computer used for data acquisition. A code was written to control the motion of XY table in the measurement. During every experiment, this code first moved the mounted probe to the desired location and then sent trigger signal to TFI Device Control to start the measurement. The measurement lasted for 5s and then the probe was driven to another measurement location. This procedure was repeated until all the measurements were completed. Figure 5.7 shows a snapshot during the measurement.

5.1.2 Flow Conditions

The reference parameters adopted in experiments are the same as those used in numerical study (Chapter 4). They are listed again in Table 5.1. Because of the limitation of the facilities, the highest flow speed attained was lower than

REFERENCE PARAMETERS	PHYSICAL VARIABLES
Length, \widehat{L}_o	Width of duct, \widehat{W}
Velocity, \widehat{u}_o	Maximum velocity at I_2 , $\widehat{u}_{2,max}$
Time, \widehat{t}_o	$\widehat{W} / \widehat{u}_{2,max}$
Density, $\widehat{\rho}_o$	Density at inlet, $\widehat{\rho}_{in}$
Pressure, $\widehat{\rho}_o \widehat{u}_o^2$	Inlet pressure, $\widehat{\rho}_{in} \widehat{u}_{2,max}^2$

Table 5.1: Reference parameters adopted in experiment.

CASE NUMBER	VR	θ	$\widehat{u}_{2,max}$	Re
E-0.5-90	0.5	90°	13.2	9.03×10^4
E-0.67-90	0.67	90°	13.2	9.03×10^4
E-1.0-90	1	90°	13.2	9.03×10^4
E-2.0-90	2	90°	12.4	8.48×10^4
E-0.5-45	0.5	45°	13.2	9.03×10^4
E-0.67-45	0.67	45°	13.2	9.03×10^4
E-1.0-45	1	45°	13.2	9.03×10^4
E-2.0-45	2	45°	14.5	9.91×10^4

Table 5.2: Description of experimental cases.

that adopted in the simulations. Therefore, the attained $Re = \widehat{\rho}_{in} \widehat{u}_{2,max} \widehat{W} / \widehat{\mu}_o$ was smaller than those used in the simulations. It is expected that viscous effects in the experiments were larger than those in simulations. Table 5.2 shows the settings of all experiments performed. Similar to the numerical investigation, no external acoustic source was applied to the flow. Furthermore, the temperature during the experiment was kept at room temperature.

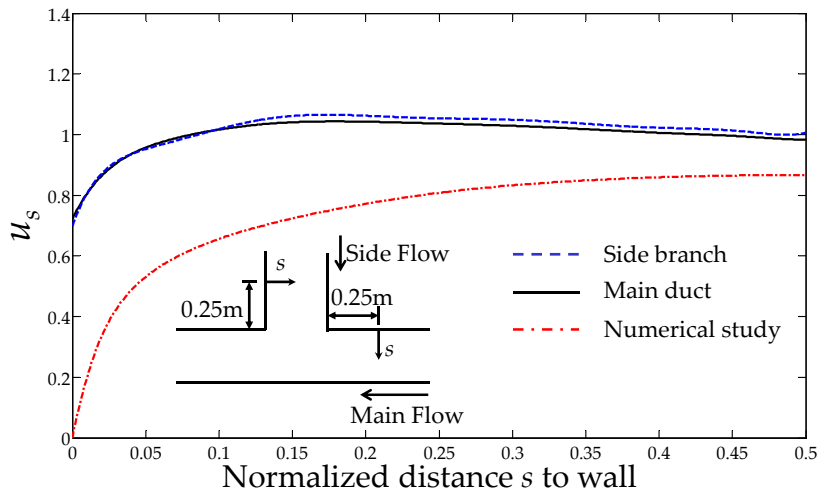


Figure 5.8: Streamwise velocity profile u_s before flows are merged for case E-1.0-90.

5.2 EXPERIMENTAL RESULTS

Similar to the numerical study, four cases are chosen for the discussions because they can represent the overall trend of the results. These cases are E-1.0-45, E-0.5-90, E-1.0-90 and E-2.0-90. Since the Reynolds number and the geometry applied in experimental study are different from those used in numerical simulations, their comparison in this chapter can only be interpreted in a qualitative rather than quantitative manner.

5.2.1 Inlet Flow Profile

Hot wire anemometer was used to measure the velocity profile inside the boundary layer on duct wall as the cobra probe was too large for serving this purpose. A hot wire with $5\mu\text{m}$ tungsten wire and a working length of 2mm was used. The nonlinear output was linearized using the method introduced by Bruun (1972). The measuring locations for both main duct and side branch were about 250mm ahead of duct junction.

Figure 5.8 shows a typical velocity profile using E-1.0-90 case. The flow profile is much steeper than the fully developed profile obtained using log law. Moreover, the flows in experiment are slightly biased in both branches. Table 5.3 shows both the displacement thickness δ_d and the momentum

CASE NUMBER	US δ_d	US δ_m	SB δ_d	SB δ_m
E-0.5-90	0.0087	0.0076	0.0130	0.0110
E-0.67-90	0.0094	0.0082	0.0138	0.0117
E-1.0-90	0.0114	0.0097	0.0139	0.0117
E-2.0-90	0.0131	0.0107	0.0107	0.0094
E-0.5-45	0.0086	0.0076	0.0374	0.0257
E-0.67-45	0.0107	0.0091	0.02	0.0166
E-1.0-45	0.0124	0.0105	0.0338	0.0209
E-2.0-45	0.0124	0.0106	0.0221	0.0182

Table 5.3: Boundary layer thickness δ_d and δ_m for different cases.

thickness δ_m for different cases. In general, both δ_d and δ_m increase with VR in US. No obvious trends are observed for them in SB. On the other hand, both δ_d and δ_m increase with θ in SB, but they are nearly constant in US with varying θ .

5.2.2 Mean Flow

Before the discussion of the experimental results, the coordinate system adopted in the coming discussion is described in [Figure 5.9](#).

[Figure 5.10](#) shows the velocities at the measurement region for different cases. Several observations can be made from these figures. Firstly, in all cases, the shaded regions represent the zones with rejected data more than 5% of total time data. This indicates that the direction of the flow is outside the applicable range of the cobra probe for more than 5% of total measuring time. This is reasonable because the recirculating zone is observed there in numerical study, in which the direction of flow near wall is definitely opposite to the orientation of the cobra probe. Secondly, the mean spanwise velocity w is very small compared with the other two velocity components for all cases.

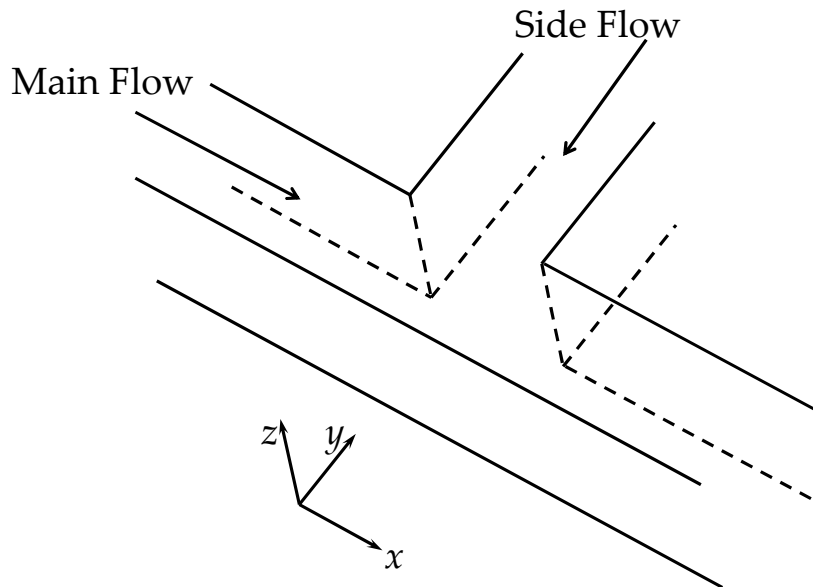


Figure 5.9: Coordinate system adopted in this discussion.

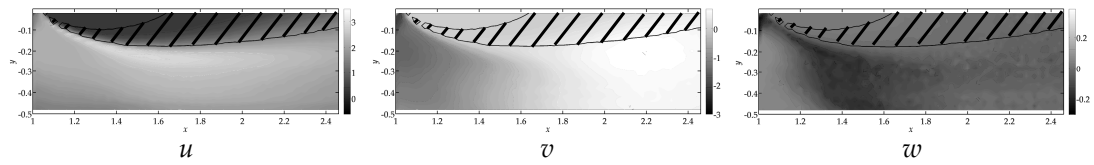
Thirdly, the size of rejected zone increases with both VR and θ . This size of this zone may be directly proportional to that of RZ1 observed in the last chapter as it also increases with both VR and θ in numerical study.

Figure 5.11 shows the comparison of the velocity profile to the two-dimensional numerical results. The rejected data are not shown in this figure. Generally, the numerical mean profiles outside the rejected zone agree with the experimental results quite well despite the difference in Re . For instance, in E-1.0-45, both results nearly overlap together. This may suggest that the mean flow field of merging flow is not sensitive to Re when $Re > 10^4$.

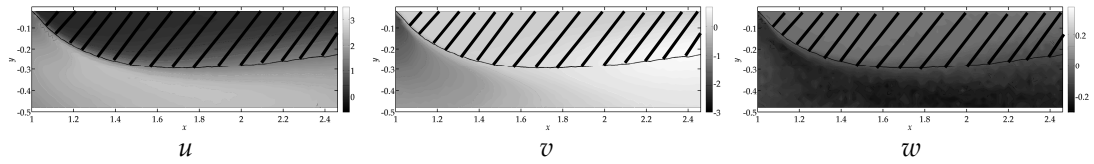
Owing to the existence of the rejected zones in all cases, the mean flow features cannot be obtained and compared.

5.2.3 Flow Unsteadiness

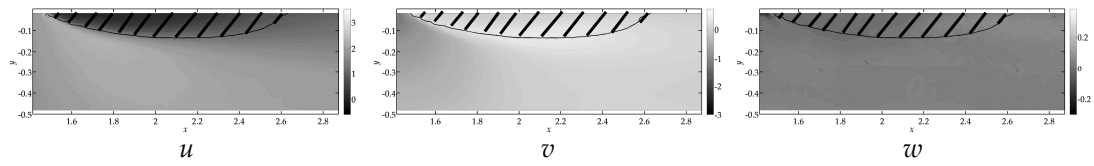
Since the velocity fluctuations can only be measured outside the rejected zone, it is very difficult to educe the evolution of coherent structures directly from the experimental results through any phase averaging technique e. g., adopted in Tang & Ko (1994a,b). However, the mean Reynolds stresses in the accepted zone can still provide some information about the fluctuations of



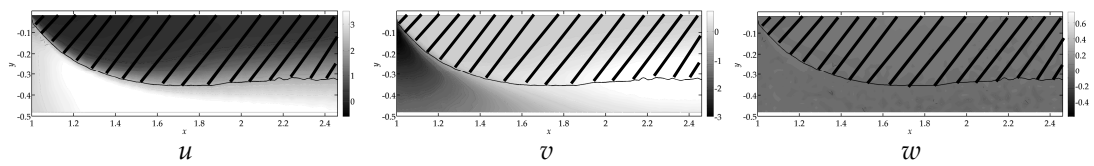
(a) E-0.5-90.



(b) E-1.0-90.



(c) E-1.0-45.



(d) E-2.0-90.

Figure 5.10: Velocity at the measurement region for different cases.

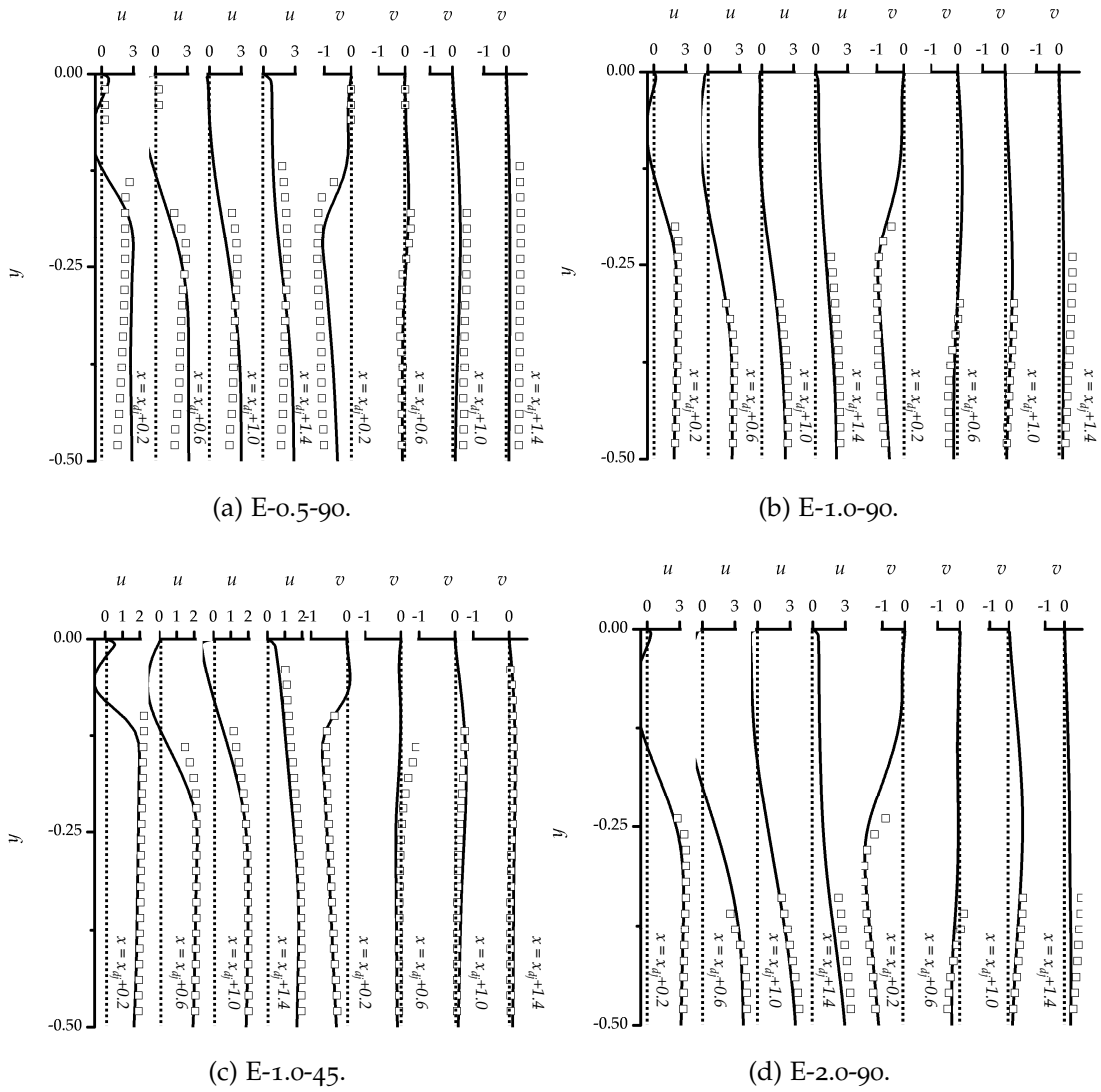


Figure 5.11: Comparison of velocity with 2D numerical study for different cases. (—) is the calculated results and (\square) represents the experimental results.

the flow. Therefore, it is discussed first and then the pressure fluctuations at the measurement zone are analyzed.

Reynolds Stresses

The mean Reynolds stresses normalized with u_{eq}^2 defined by Eq.(4.4) are shown in Figure 5.12 and only the shear stresses are shown here. This is because the normal stresses also show similar pattern. The rejected zone is also shown in this figure. All the figures show high values of Reynolds stresses near the rejected zones. This observation is consistent with the numerical results, in which regions with highest Reynolds shear stresses are found near RZ1 (Figure 4.15). Furthermore, the fluctuation in the spanwise direction is also comparable to those in the other two directions. This indicates a rather strong three-dimensional flow effect in this case. Moreover, the shear stresses also illustrate a increasing trend with the increase in VR and θ and this agrees with numerical study. This may be due to the more vigorous interaction of the flows when VR and θ increase.

Although the rejected zones exist for all cases, the mean flow in general agrees with the numerical study quite well including the predicted effect of the velocity ratio VR and merging angle θ . However, the three dimensionality of the flow shown in Reynolds shear stresses implies that the two dimensional numerical study have some differences in the unsteady flow dynamics.

Pressure Fluctuations

The root-mean-square (RMS) pressure fluctuations p_{rms} measured in selected cases are shown in Figure 5.13. They are all normalized by u_{eq}^2 (Eq.(4.4)). The RMS value is the highest outside the boundary of rejected zone but it is quite small near the wall. This suggests that most of the flow unsteadiness in the measurement zone occurs at the separated flow originated at the downstream edge of the duct junction, i.e., RZ1. This is also consistent with the results from numerical study shown in Figure 5.14. The difference between the experimental and numerical results is quite pronounced at the

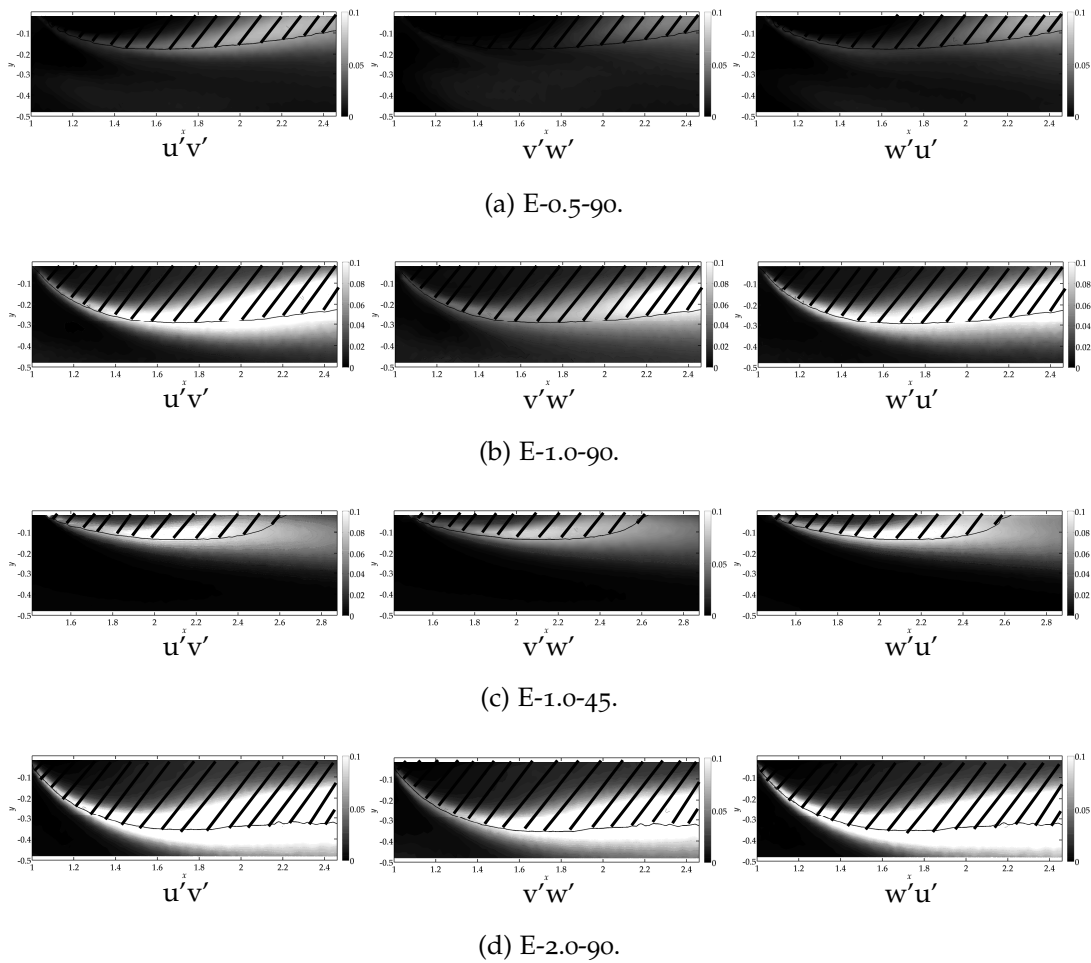


Figure 5.12: Reynolds shear stresses at the measurement region for different cases.

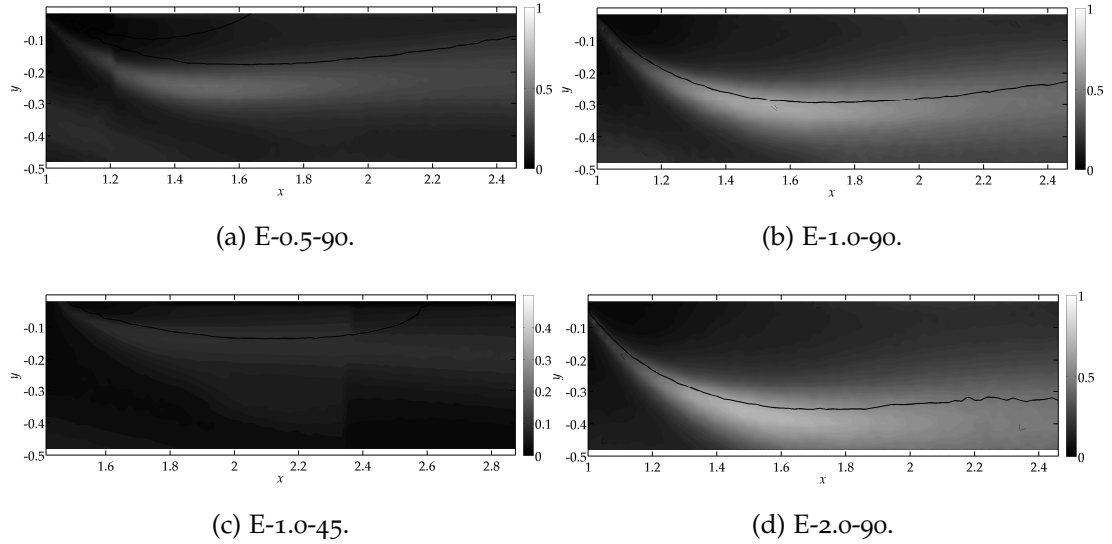


Figure 5.13: Root mean square of pressure fluctuation p_{rms} of experimental study in selected cases. The solid lines shown are the contours of rejected zone obtained from velocity measurements.

region near wall. In numerical study, the pressure fluctuations near wall are still comparable to those near RZ1 but the same quantities observed in experimental results are quite low near wall. Despite this difference, the experimental results show a trend of variation with VR and θ similar to those obtained in numerical study. The RMS of pressure fluctuation increases with both VR and θ .

5.2.4 Acoustic Propagation

The auto-spectra of these cases are obtained by applying the FFT analysis with Welch method to minimize the random noise in the signals. The time data is split into 3 pieces and their FFT results are averaged. Figure 5.15 shows the normalized auto-spectra G_{pp}^u of E-0.5-90 and N-0.5-90 at $(x_{dj} + 1, -0.2)$. The frequency resolution of the spectrum in E-0.5-90 is higher than that in N-0.5-90. Similar observations are also found in other cases. In order to aid the comparison between the experimental and numerical results, the auto-spectra of experimental results are converted to spectra $G_{pp}(f)$ with uniform band.

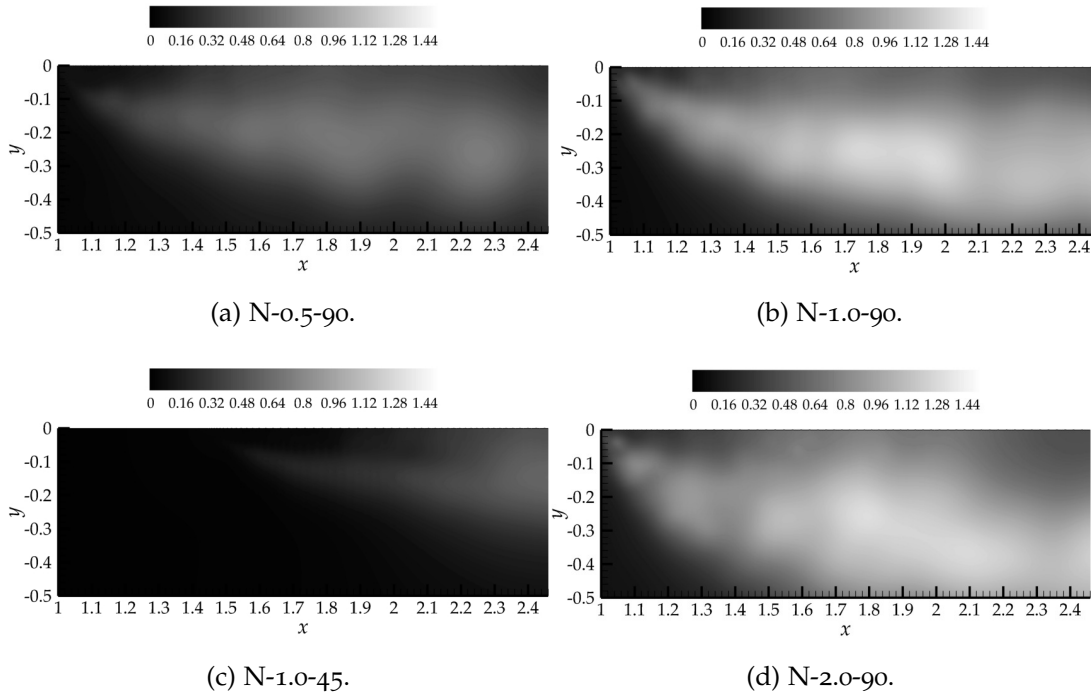


Figure 5.14: Root mean square of pressure fluctuation p_{rms} obtained from numerical study in selected cases.

The center frequency of each band is the same as the frequency axis obtained in 2D simulations. In other words, for each band in the spectra,

$$G_{pp}(f) = \sum G_{pp}^u(f_L < f < f_H),$$

where $G_{pp}^u(f)$ is the original spectra, $f_L = f_c - 0.5\Delta f$, $f_H = f_c + 0.5\Delta f$, f_c is the central frequency and Δf is the frequency resolution. Both f_c and Δf are obtained from the pressure spectra of the corresponding 2D simulations.

Figure 5.16 illustrates the comparison of normalized auto-spectra of the experimental results at $(x_{dj} + 1, -0.2)$ with the corresponding numerical results in the selected cases. The experimental results are converted to uniform band as aforementioned. All the spectra are scaled with their own maximum amplitudes. Although not shown in this figure, the amplitudes of numerical spectra are slightly less than those obtained in experiment. This implies that the unsteady flow interactions predicted by the numerical study are comparable to those from the experimental results. Furthermore, the experimental results illustrate a slower decay in the amplitudes of fluctuations than the

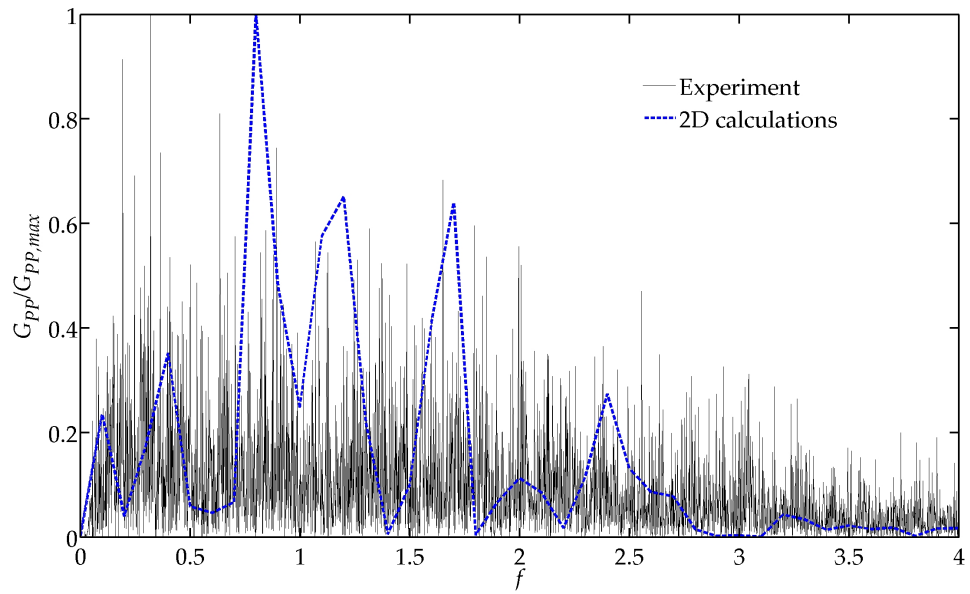


Figure 5.15: Auto-spectra of pressure fluctuations for E-0.5-90 and N-0.5-90.

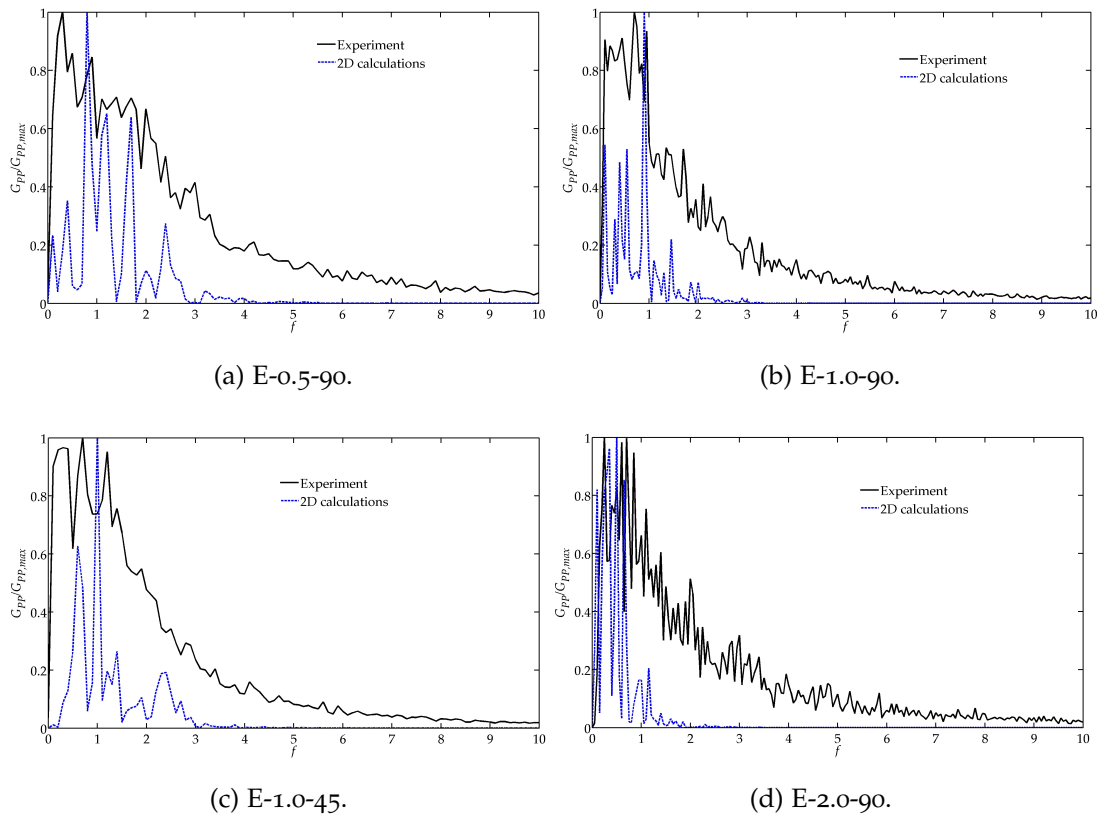


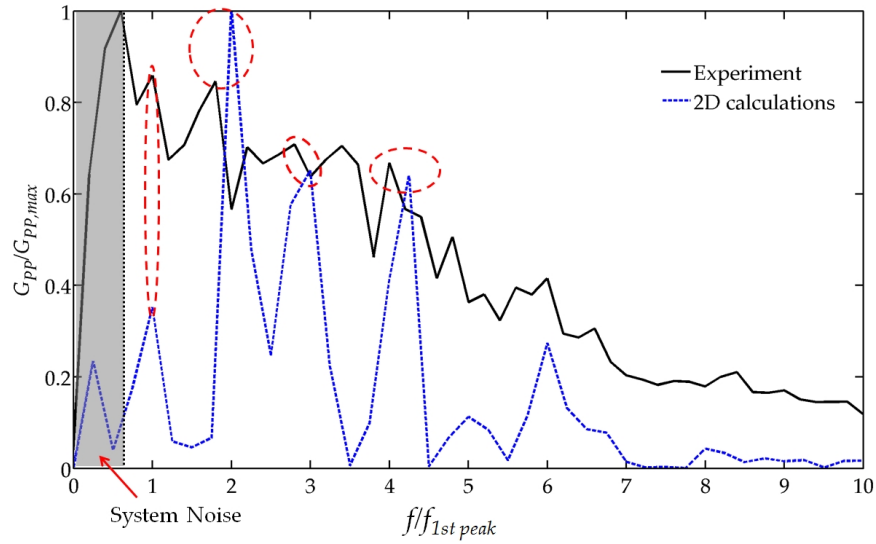
Figure 5.16: Auto-spectra of pressure fluctuations, G_{pp} , at $(x_{d_j} + 1, -0.2)$ of both experimental and 2D numerical study for different cases.

numerical results. The amplitudes of the experimental spectra decrease to 50% at $f \sim 3$ but those from numerical results drop to 50% at $f < 2$. In general, both results show a similar dominant frequency range, i. e., $0 \leq f \leq 2$.

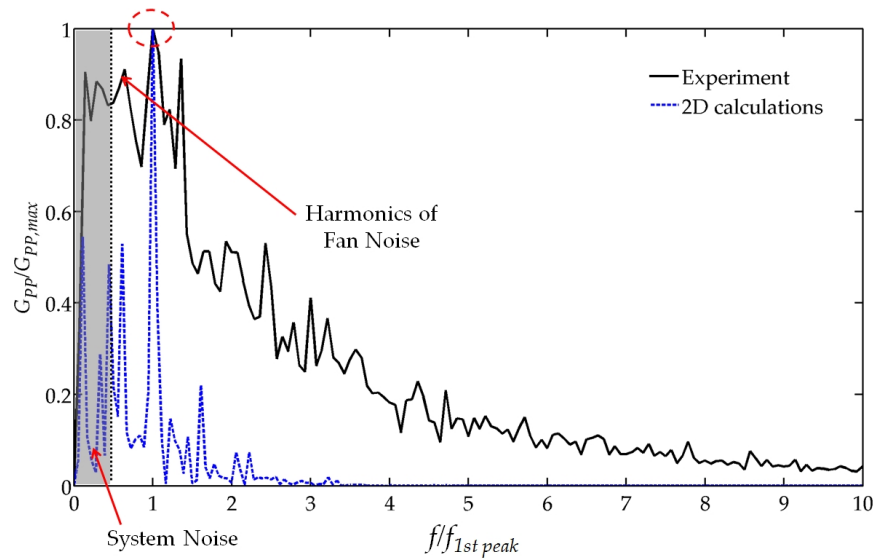
In order to capture the similarity between the experimental and numerical results, a frequency scaling is applied. In each case, the first peak in each auto-spectrum is chosen as the reference frequency, $f_{1st\ peak}$, for frequency axis scaling. Since the noise from the fans contaminates the flow in the very low frequency region ($f_{system} > 0$), its contribution is ignored as indicated in this figure (Shaded region). [Figure 5.17](#) and [Figure 5.18](#) show these auto-spectra again with this frequency scaling. In general, the numerical results match the experimental results reasonably well in the number of dominant peaks. Although the peaks of the corresponding pairs do not overlap entirely, the deviations of peak frequency for the selected cases are smaller than 30% compared with experimental results. This indicates that the numerical simulations may largely capture the key unsteadiness of the flow as observed in the experiments. The deviation in frequency peaks might be probably due to the difference in Reynolds number. However, due to the limitation of experimental facilities and background flow turbulence, further investigations are required to confirm this.

5.3 CONCLUDING REMARKS

In this chapter, the design of experiment for merging flow at duct junction is discussed. It is observed that strong three dimensional effects exist at RZ1, leading to the formation of rejected zone with flow sample rejection rate $> 5\%$ in its proximity. However, outside the rejected zone, the experimental measurements generally agree with the two dimensional numerical results. These two results show good agreement in the mean Reynolds shear stresses and the pressure fluctuations. The numerical results also agree reasonably with the experimental results in the dominant frequencies in the pressure

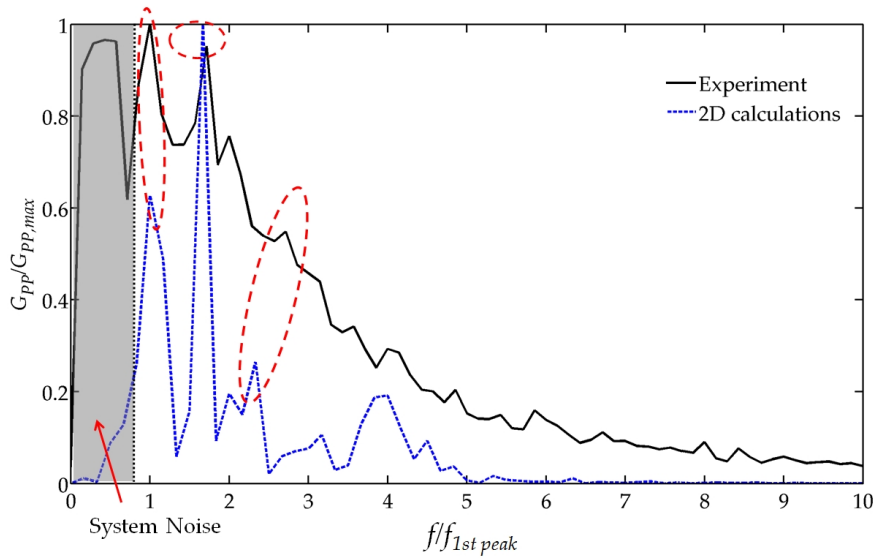


(a) E-0.5-90.

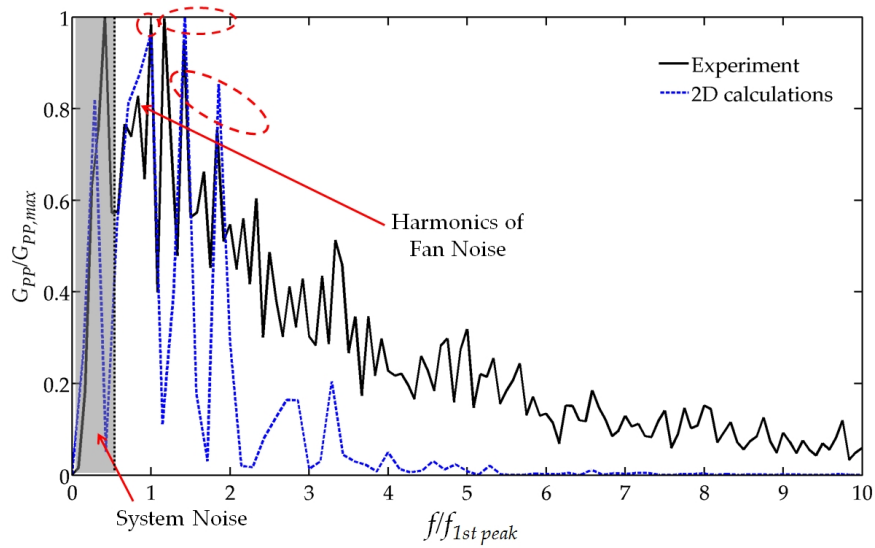


(b) E-1.0-90.

Figure 5.17: Auto-spectra of pressure fluctuations, G_{pp} , at $(x_{dj} + 1, -0.2)$ of both experimental and 2D numerical simulations with frequency scaling for different cases. Red dashed lines highlight the corresponding pairs of the dominant peaks in experimental and 2D numerical results. Shaded region: system noise dominant. a) $f_{system} / (f_{1st\ peak})_{experiment} = 0.6$; b) $f_{system} / (f_{1st\ peak})_{experiment} = 0.428$.



(a) E-1.0-45.



(b) E-2.0-90.

Figure 5.18: Spectra of pressure fluctuations, G_{pp} , at $(x_{dj} + 1, -0.2)$ of both experimental and 2D numerical simulations with frequency scaling for different cases. Red dashed lines highlight the corresponding pairs of the dominant peaks in experimental and 2D numerical results. Shaded region: system noise dominant. a) $f_{system} / (f_{1st\ peak})_{experiment} = 0.75$; b) $f_{system} / (f_{1st\ peak})_{experiment} = 0.5$.

spectra after the fan noise is ignored. Nevertheless, this requires further investigation because of the uncertainty imposed by limited quality of experimental facilities and background flow turbulence. Furthermore, the effect of VR and θ on the mean Reynolds stresses predicted by the numerical simulations are also consistent with those obtained from experiments.

THREE DIMENSIONAL MERGING FLOW AT DUCT JUNCTIONS

As a result of the rejected data at RZ1 in the experiments mentioned in the previous chapter, flow structures cannot be correctly captured by the experiments; thus their relationships with the acoustic generation cannot be thoroughly studied through experiments. In order to investigate this relationship, a three dimensional simulation of the problem is performed, which is discussed in this chapter. It is carried out with the CE/SE method, an extension of the two dimensional CE/SE method ([chapter 2](#)) to three dimensions. The numerical results are compared with their two dimensional counterparts, which has already given us some initial understanding of the aeroacoustics occurred in this flow. This study should provide us some ideas on the effect of three dimensionality on the flow. Due to the limited computational resources available, only the case $VR = 1$ with $\theta = 90^\circ$ (N-1.0-90) is repeated in the three dimensional simulation. For ease of discussion, this calculation is denoted as N-1.0-90-3D.

6.1 FORMULATION OF THE FLOW PROBLEM

The computational domain of N-1.0-90-3D is illustrated in [Figure 6.1](#) and the reference parameters adopted are shown in [Table 6.1](#). Since the computational resources are very limited, the domain size calculated has to be reduced and only a slender spanwise section is included. Thus, the flow simulated is still dominantly two dimensional, but it allows a more appropriate modeling of the effects of turbulence, which is intrinsically three dimensional. As the aeroacoustic generation in the two dimensional simulations mainly occurs

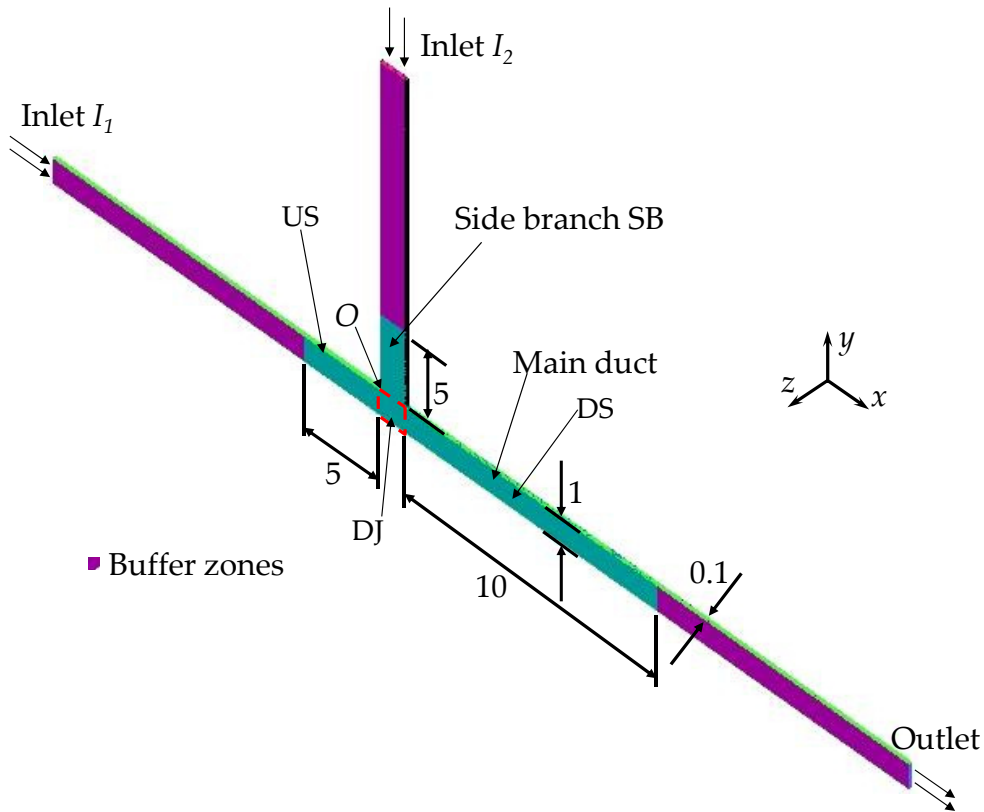


Figure 6.1: Schematic of the merging flow problem in three dimensional case.

in DJ and upstream part of DS, all branches are shortened in the three dimensional calculations. Therefore, the nondimensional lengths of US, SB and DS are 5 , 5 and 10 respectively. The widths of all duct sections are equal to 1. Buffer zones D_I and D_o , of length 10, are applied to all duct inlets and outlet. Furthermore, the duct width in the spanwise direction has chosen to be 0.1 under the compromise between available resources and solution accuracy, i. e., $0 \leq z \leq 0.1$. The origin is located at the upstream corner of DJ and $\theta = 90^\circ$. Same as in the previous two dimensional simulations, the flows enter the domain through duct inlets I_1 (main flow) and I_2 (side flow). Based on the reference parameters, the Mach number M and the Reynolds number Re of the problem are 0.1 and 2.3×10^5 respectively.

The boundary conditions applied on all the walls are NSWBC-NW with the wall modeling for turbulent flow (Section 2.5.2) while a slip wall condition SLWBC (Section 2.4.2) is applied to the wall normal to the spanwise direction. NRBC-II is applied to duct outlet with outlet pressure taken as the reference pressure. Fully developed turbulent velocity profile is applied at the two inlets

REFERENCE PARAMETERS	PHYSICAL VARIABLES
Length, \hat{L}_o	Width of duct, \hat{W}
Velocity, \hat{u}_o	Maximum of centerline velocity at $I_2, \hat{u}_{2,max}$
Time, \hat{t}_o	$\hat{W} / \hat{u}_{2,max}$
Density, $\hat{\rho}_o$	Density at inlets, $\hat{\rho}_{in}$
Pressure, $\hat{\rho}_o \hat{u}_o^2$	Inlet pressure, $\hat{\rho}_{in} \hat{u}_{2,max}^2$

Table 6.1: Reference parameters adopted in this research.

as in the two dimensional study as shown in [Figure 4.2](#). Moreover, no flow disturbance is imposed at the duct inlets.

The requirement of mesh design for turbulent flow simulation is the same as that in two dimensional simulation. Again the mesh points are clustered near the walls and then extended to the center of the duct. The maximum mesh size, Δx_{max} and Δy_{max} , are 0.015 at the center of the duct and its minimum, Δx_{min} and Δy_{min} , are 0.001, at the walls, which corresponds to the wall unit, $y^+ = 16$ at the specified M . There are roughly 20 meshes inside the turbulent boundary layer for $Ma = 0.1$. This mesh should be able to capture the change in boundary layer. In the spanwise direction, there are 20 cells with uniform meshes of size $\Delta z = 0.005$. The time increment Δt is set at 2.5×10^{-4} .

6.2 AEROACOUSTICS OF THREE DIMENSIONAL MERGING FLOW

In this section, the discussions of three dimensional merging flow numerical results are focused on three aspects: the mean flow, unsteady flow dynamics and the aeroacoustics.

6.2.1 Mean Flow

In N-1.0-90-3D, the mean flow is obtained by averaging the results within time period of 20 counting back from the end of calculation with an time increment of 0.2. In all the figures shown in this section, the z -axis is stretched with a scale of 70 for ease in illustration. In other words, $L_x : L_y : L_z = 1 : 1 : 70$ where L_x , L_y and L_z are the length scales in x , y and z axes respectively.

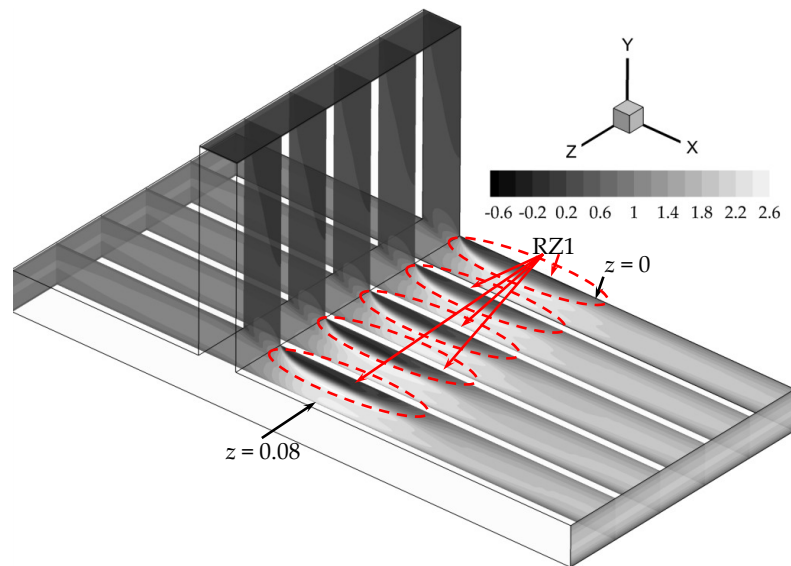
Flow Velocity

Figure 6.2 shows the mean velocity u , v and w in N-1.0-90-3D. Five streamwise cross sections at $z = 0, 0.02, 0.04, 0.06, 0.08$ are plotted for illustration. Similar to N-1.0-90, a fully developed turbulent profile is observed in SB and US. When the two inlet flows reach near DJ ($x = 0$), they merge together and accelerate downstream of DJ due to the restriction of RZ1 to a speed $u > u_{1,max} + u_{2,max}$. The merged flow profile then recovers to the symmetric profile further downstream. Furthermore, the magnitude of spanwise velocity w is much smaller than those of u and v . The highest magnitude of w concentrates in DS ($2 \leq x \leq 6$).

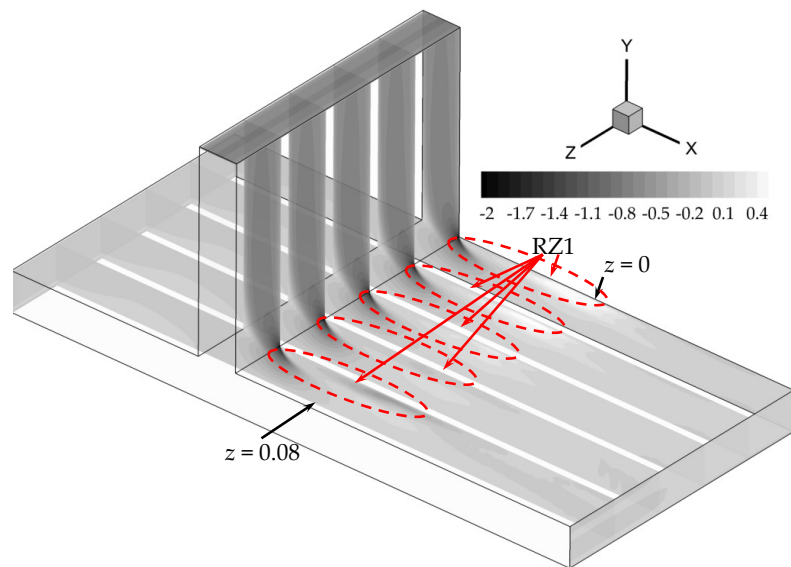
A comparison of u between two and three dimensional simulations is given in Figure 6.3. Here u on the $z = 0.05$ plane is taken. The red dashed line represents the profile of u obtained in N-1.0-90. From this figure, the profiles of u nearly overlaps completely for $x < 0$ and $x > x_{dj} + 5$. Their major difference is observed near the downstream edge of DJ ($x = x_{dj}$). RZ1 occurs earlier in N-1.0-90-3D than it does in N-1.0-90 from the profiles at $x = x_{dj}$. Moreover, the velocity gradient at the boundary layer attached to the lower wall in N-1.0-90-3D is less stiff than that in N-1.0-90.

Flow Features

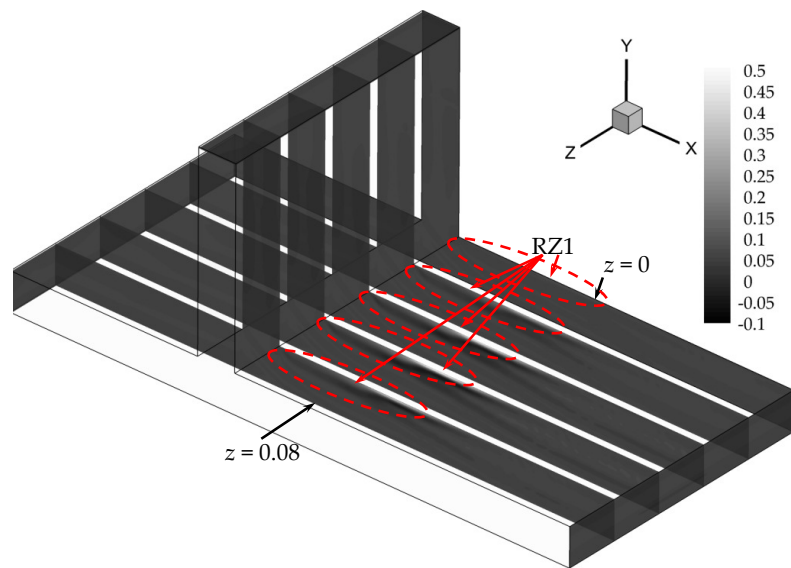
The three distinct flow features observed in the two dimensional study can also be found in N-1.0-90-3D, as shown in Figure 6.4. The pattern is still in good agreement with Hirota et al. (2006). All of them also show similar magnitude



(a) u_{mean} .



(b) v_{mean} .



(c) w_{mean} .

Figure 6.2: Mean flow over the domain for N-1.0-90-3D (Not to scale in z axis).

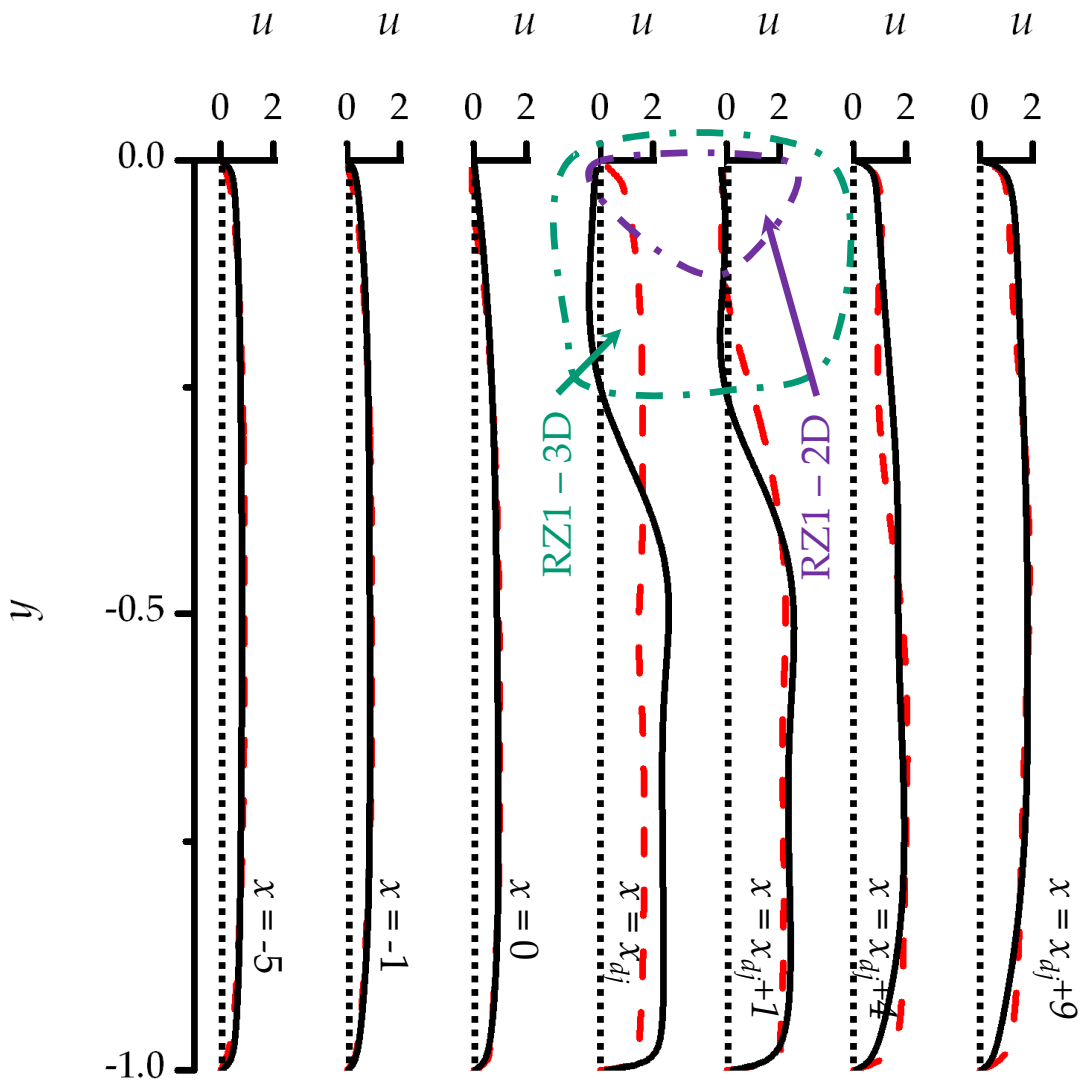


Figure 6.3: Comparison of u in N-1.0-90 (red dashed line) and N-1.0-90-3D (black solid line).

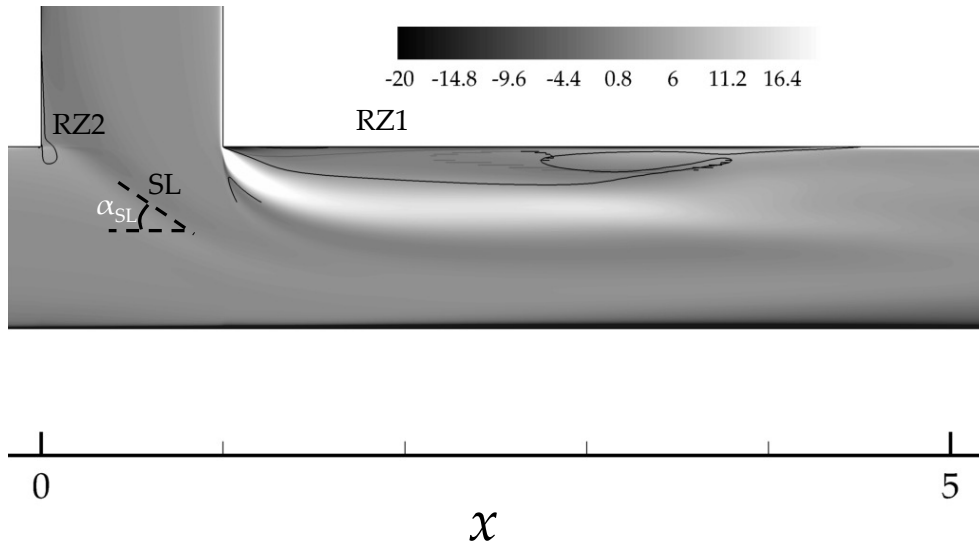


Figure 6.4: $\omega_{mean,z}$ in N-1.0-90-3D on $z = 0.05$.

SIZES OF FEATURES	N-1.0-90-3D	N-1.0-90
L_{RZ1}	3.241	1.170
L_{RZ2}	0.527	1.461
α_{SL}	34.88°	38.15°

Table 6.2: Sizes of various flow features for N-1.0-90 and N-1.0-90-3D.

of $\omega_{mean,z}$ compared with N-1.0-90 (Figure 4.6e) and RZ1 still contains the highest vorticities among the three distinct flow features. Furthermore, the highest vorticities occurs near the downstream edge of DJ inside RZ1. This observation is still the same as that observed in two dimensional simulations. However, the three dimensionality of the flow does affect the sizes of the these flow features. A comparison between two and three dimensional simulations is given in Table 6.2.

Here the length L_{RZ1} and L_{RZ2} are obtained from the locations at wall where the streamwise velocity gradient normal to the wall equals 0 (Nie & Armaly 2003). From Table 6.2, RZ1 is lengthened in N-1.0-90-3D by nearly 177%. On the contrary, RZ2 becomes smaller in the figure. Moreover, α_{SL} also decreases slightly in N-1.0-90-3D by $\sim 8.6\%$.

Figure 6.5 illustrates the mean vorticity calculated in N-1.0-90-3D for five streamwise sections at $z = 0, 0.02, 0.04, 0.06, 0.08$. The results at these sections

are very similar. The vorticity about x ($\omega_{mean,x}$) and y axes ($\omega_{mean,y}$) are much lower than that in z axis ($\omega_{mean,z}$). Starting from the downstream edge of DJ, $\omega_{mean,x}$ and $\omega_{mean,y}$ at RZ1 also grows further downstream and maximizes near the upper wall in DS at $x \approx 5$. This indicates that the flow there has significant three dimensionality. On the other hand, both $\omega_{mean,x}$ and $\omega_{mean,y}$ are relatively low near SL and bottom wall for all five sections. This shows that three dimensional effect is relatively weak in these locations.

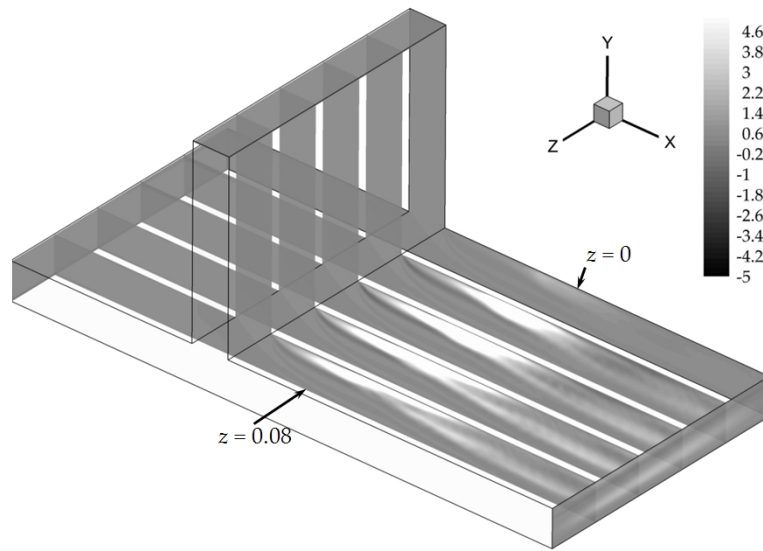
6.2.2 Unsteady Flow Dynamics

Owing to the complexity in the three dimensional flow unsteadiness, it is difficult to educe the vortical structures by the vorticity only. Therefore, in order to illustrate the flow structures, λ_2 -criterion suggested by Jeong & Hussain (1995) is chosen to educe these structures. Based on this method, the velocity gradient tensor $\nabla \mathbf{u}$ is first decomposed into two parts, i. e.,

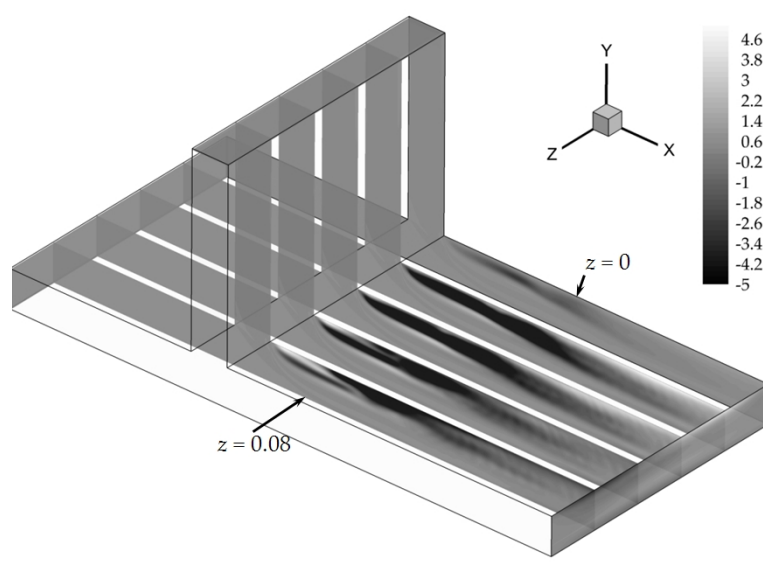
$$\nabla \mathbf{u} = \mathbf{S} + \mathbf{\Omega}, \quad (6.1)$$

where $\mathbf{S} = \frac{1}{2} (\nabla \mathbf{u} + \nabla \mathbf{u}^T)$ and $\mathbf{\Omega} = \frac{1}{2} (\nabla \mathbf{u} - \nabla \mathbf{u}^T)$ are the symmetric and the anti-symmetric parts respectively with \mathcal{T} denoting the transpose. Then another symmetric tensor $\mathbf{S}^2 + \mathbf{\Omega}^2$ is formed. According to this criterion, vortical structures are the region where the second eigenvalues of $\mathbf{S}^2 + \mathbf{\Omega}^2$, i. e., $\lambda_2 < 0$, after all its eigenvalues are sorted. One should note that this criterion does not exist in the two dimensional case.

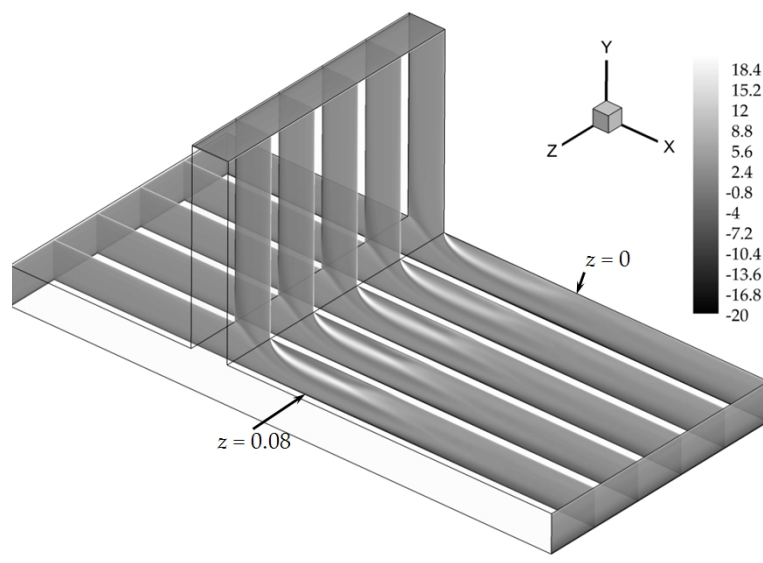
Figure 6.6 shows the flow structures educed by vorticity in z (ω_z) and λ_2 on the central plane of the duct ($z = 0.05$) at time $t = 50$. It clearly demonstrates that λ_2 -criterion is more appropriate for educing the flow structures in three dimensional cases. The flow structures at the bottom wall near $x = 5$ is clearly educed by λ_2 -criterion in Figure 6.6b, but they are masked by the boundary layer by observing ω_z in Figure 6.6a.



(a) $\omega_{mean,x}$



(b) $\omega_{mean,y}$



(c) $\omega_{mean,z}$

Figure 6.5: Mean vorticity ω_{mean} obtained in N-1.0-90-3D (Not to scale in z axis).

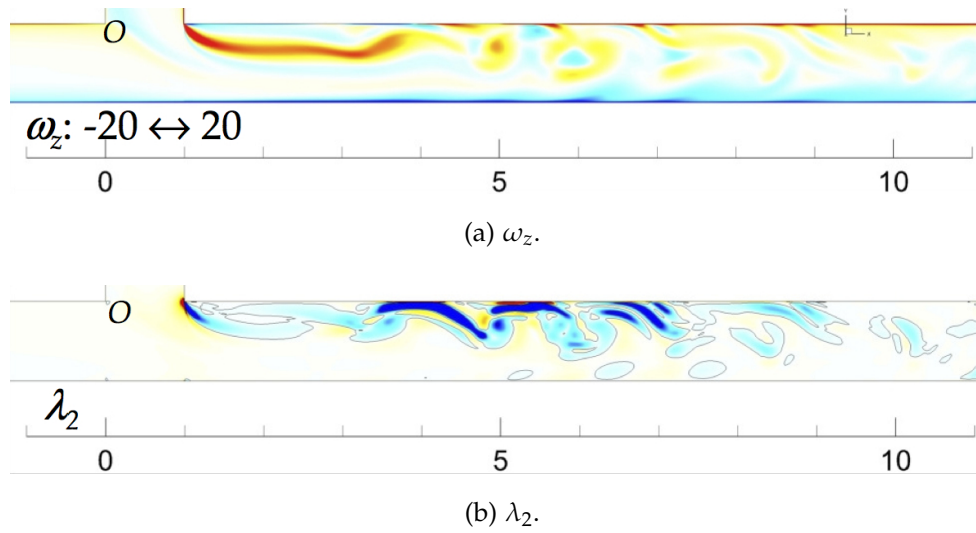


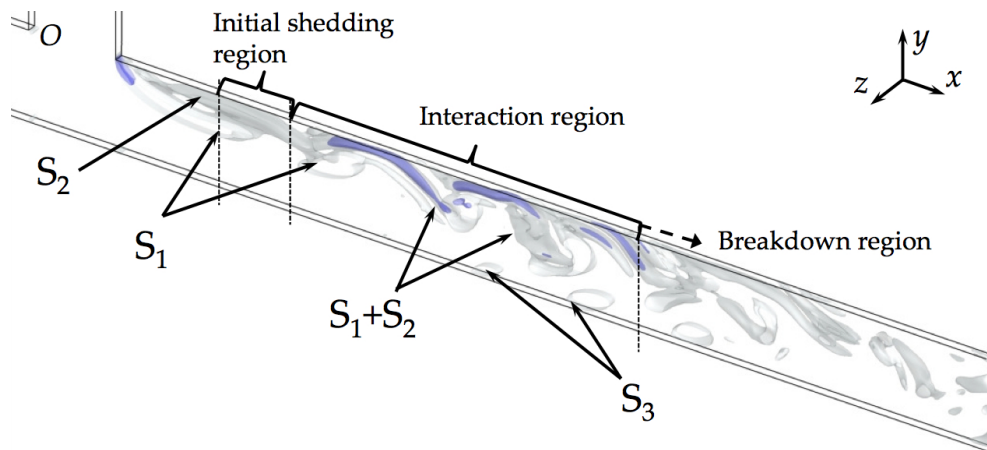
Figure 6.6: Snapshots of ω_z and λ_2 on $z = 0.05$ at $t = 50$.

Figure 6.7 and Figure 6.8 shows the snapshots of vortical structures educed by λ_2 -criterion from time $t = 50$ to 52 with $\Delta t = 0.4$. The iso-surfaces with $\lambda_2 = -10$ (gray surfaces) and -50 (deep blue surfaces) are illustrated.

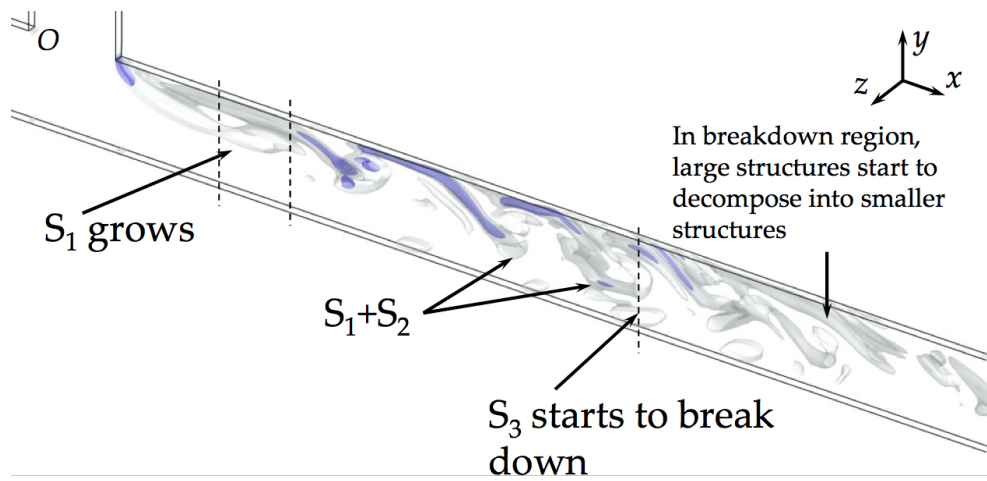
The vortical structures shown are somewhat different from those of the two dimensional cases. In general, the major vortical structures can be classified into three types and they are marked in Figure 6.7a. The first one is a line vortex (S_1) shed due to the roll-up of the shear layer of RZ1. It is characterized by the ring of λ_2 iso-surface aligned with z axis. The second one is the longitudinal vortex tube (S_2 , aligned with y axis) formed inside RZ1, which does not exist in N-1.0-90 due to the lack of three dimensionality in the simulation. The last one is the secondary vortex (S_3) induced at the bottom wall of DS. It is also a line vortex aligned with z axis and is characterized by the ring of λ_2 iso-surface.

A more detailed observation of Figure 6.7a reveals that generally, the vortex shedding inside DS can be split into three regions. The first region is initial shedding region within $x_{dj} + 1 \leq x \leq x_{dj} + 2$. The second region is the interaction region within $x_{dj} + 2 < x \leq x_{dj} + 6$ and the last one is the breakdown region in $x > x_{dj} + 6$. They are all marked in Figure 6.7a.

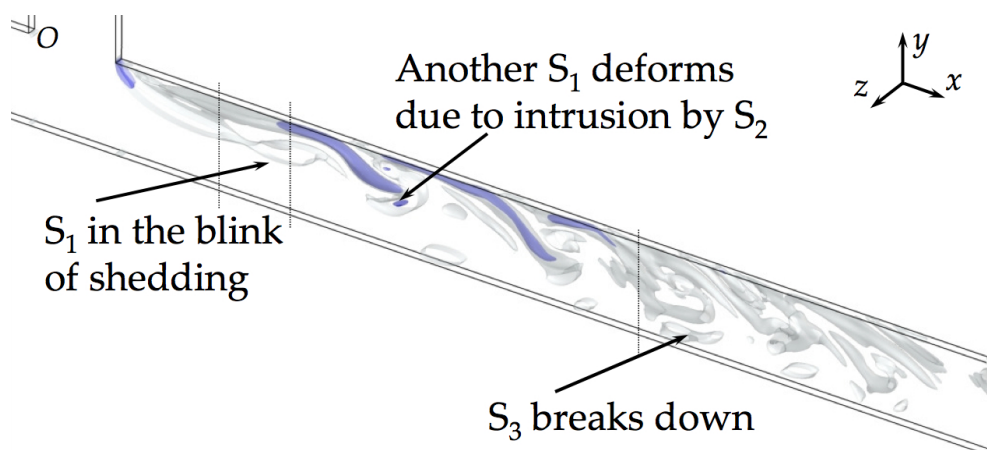
In the initial shedding region ($x_{dj} + 1 \leq x \leq x_{dj} + 2$), the vortices shed (S_1) at the shear layer originated from the downstream edge of DJ. Although it is sometimes affected by the vortex tube S_2 above, S_1 is shed rather regu-



(a) Time = 50.0.

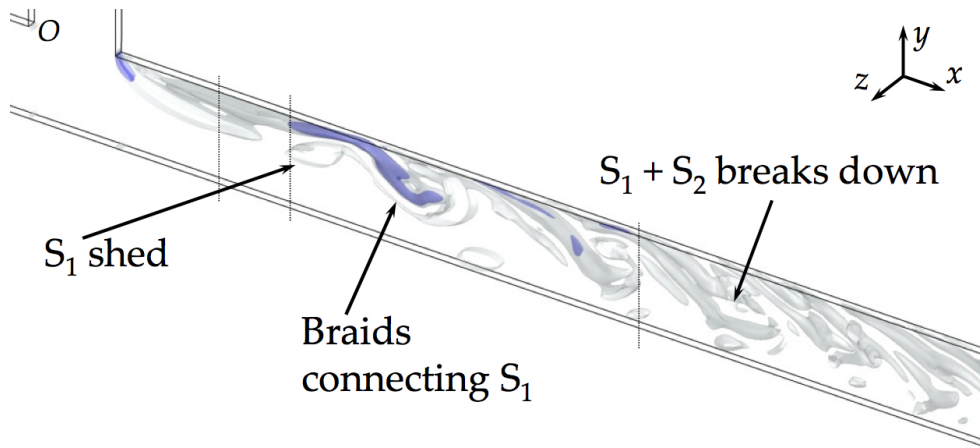


(b) Time = 50.4.

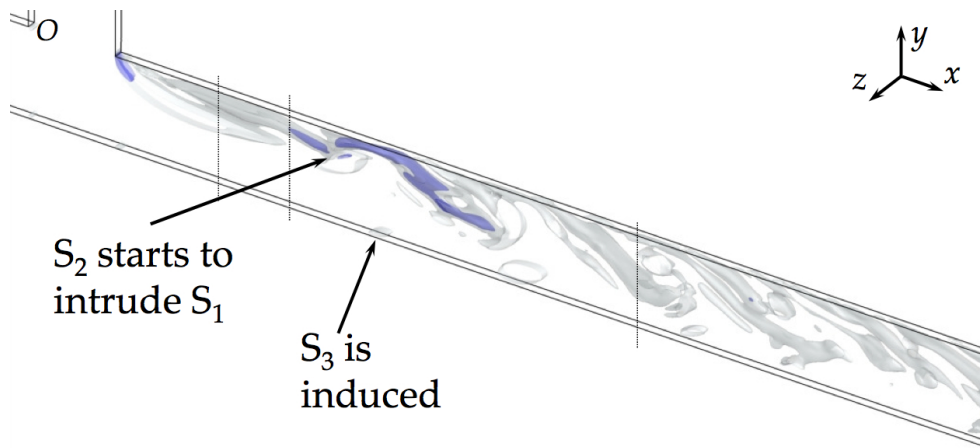


(c) Time = 50.8.

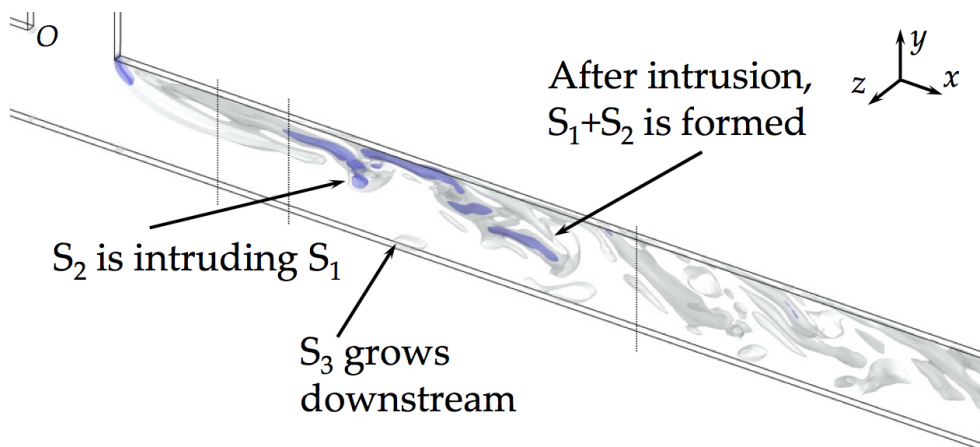
Figure 6.7: Snapshots of vortical structures educed by λ_2 -criterion.



(a) Time = 51.2.



(b) Time = 51.6.



(c) Time = 52.0.

Figure 6.8: Snapshots of vortical structures educed by λ_2 -criterion.

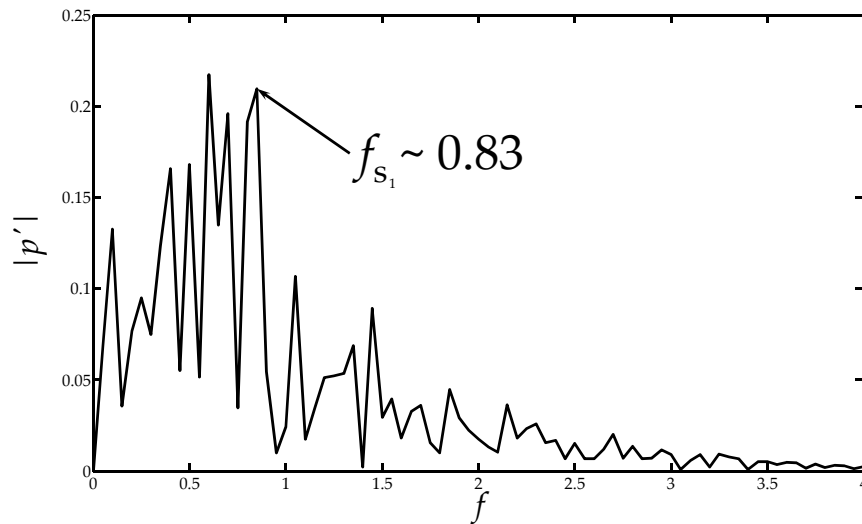


Figure 6.9: Spectrum of pressure fluctuation at $(x_{dj} + 3, -0.5)$.

larly inside RZ1. From the pressure fluctuation spectrum at $(x_{dj} + 3, -0.5)$ (Figure 6.9) and the snapshots of λ_2 , it is found that the dominant convection frequency for S_1 , f_{S_1} , is equal to 0.83. Figure 6.7b, Figure 6.7c and Figure 6.8a clearly show the shedding process of S_1 while S_2 does not have intense interaction with it in this region. Thus, the flow structures are rather organized in this region.

In the interaction region $x_{dj} + 2 < x \leq x_{dj} + 6$, significant interactions between the line vortex S_1 and the vortex tube above it S_2 are observed. To illustrate this, Figure 6.8 is referred. When S_1 is shed, the strong S_2 intrudes it from its behind. S_1 then deforms and merges with S_2 , forming a large flow structure $S_1 + S_2$. This large structure is also elongated when convected downstream with its tail attached to the upper wall. Its dominant convection frequency can be deduced from the pressure spectrum at $(x_{dj} + 6, -0.5)$ shown in Figure 6.10. At the same time, the secondary line vortex (S_3) is induced by S_1 or $S_1 + S_2$ at $x \sim x_{dj} + 3$ as shown in Figure 6.8. The frequencies of S_2 and S_3 are also shown in Figure 6.10 and they are all different.

Finally, the breakdown region ($x > x_{dj} + 6$) shows the gradual breakdown of $S_1 + S_2$ by viscous dissipation. This is indicated by the vanishing of deep blue surface in this region (Figure 6.8a). The breakdown of S_3 and $S_1 + S_2$ can be found in Figure 6.7c and Figure 6.8a respectively. Small vortical

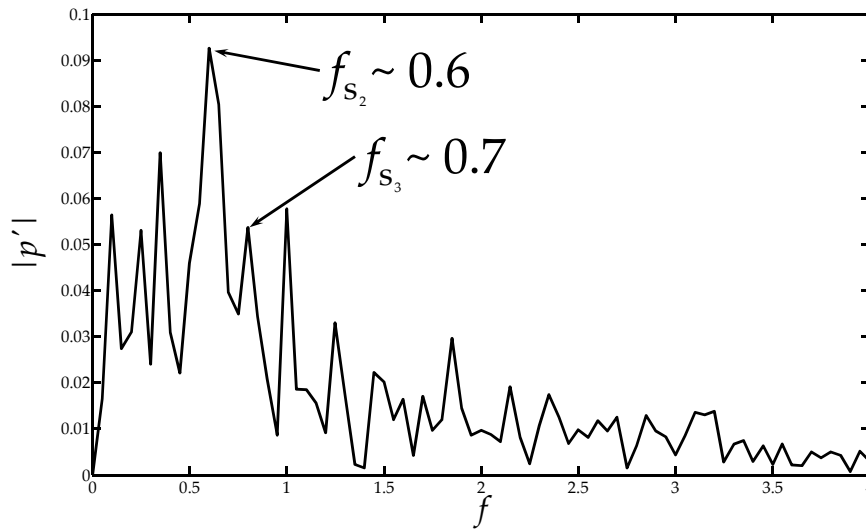


Figure 6.10: Spectrum of pressure fluctuation at $(x_{dj} + 6, -0.5)$.

structures are also evolved from the breakdown, leaving the flow in more homogeneous state here.

In short, the major difference between N-1.0-90 and N-1.0-90-3D is the existence of a three dimensional flow structure S_2 . Nevertheless, both two and three dimensional results show that the dominant flow structures are evolved from RZ1. The location of S_3 roll-up also agrees with the N-1.0-90 ($x \sim x_{dj} + 3$).

Figure 6.11 shows the auto-spectra of E-1.0-90, N-1.0-90 and N-1.0-90-3D at $x_{dj} + 1$. In each case, the first peak in each spectrum is chosen as the reference frequency, $f_{1st\ peak}$, for frequency axis scaling. Similarly, the contribution of the fan noise is ignored as indicated by the shaded region in this figure. Figure 6.11 shows that the 3D numerical results agree reasonably with the experimental results in the number of dominant peaks. This demonstrates that the key unsteadiness of the flow observed in experiment is captured by the 3D simulation. The difference in Reynolds number might be the cause of the discrepancy in frequency peak. Furthermore, the actual peak in the spectrum of 3D simulation ($f \approx 0.85$) is close to that of 2D simulation ($f \approx 0.9$) as a result of the dominant two dimensional character in the current 3D simulation. This is because only a slender section is simulated and SLWBC is applied on the spanwise direction in the 3D simulation. The three dimensional characteristics may require a larger width in the spanwise direction to develop. This also

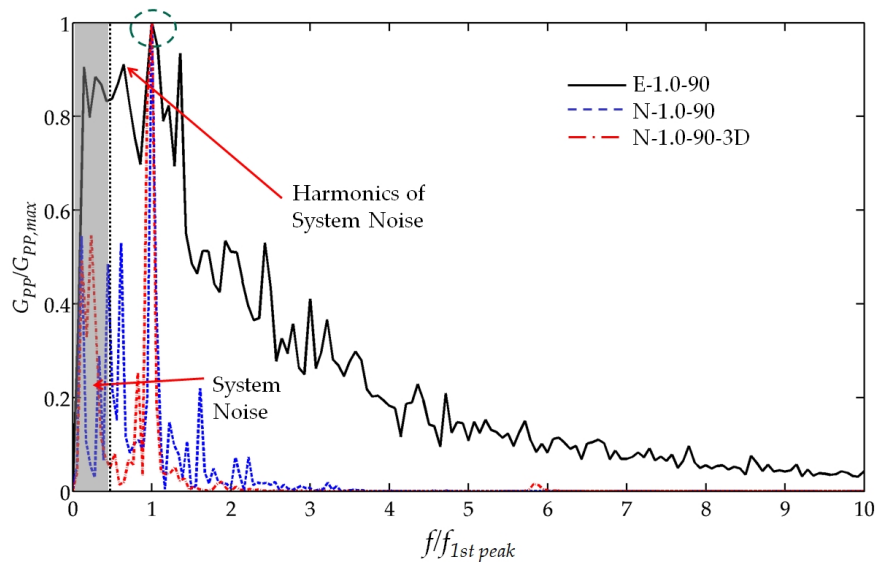


Figure 6.11: Comparison of the auto-spectra of pressure fluctuations between the experimental, 2D and 3D numerical simulations with frequency scaling for $VR = 1$, $\theta = 90^\circ$. Green dashed lines highlight the corresponding groups of the dominant peaks in experimental, 2D and 3D numerical results. Shaded region: fan noise dominant. $f_{fan} / (f_{1st\ peak})_{experiment} = 0.428$.

shows that the 2D simulations can capture the key unsteadiness of the flow. However, further investigations are required to confirm this as a result of the limitation of experimental facilities.

Reynolds Stresses

The relative strength of these structures can be illustrated by the mean Reynolds stresses shown in Figure 6.12. These stresses attain their highest value near the upper wall in the interaction region of DS. On the other hand, the stresses are quite low not only in the US and SB, but also at SL. This indicates that significant three dimensional flow occurs in the interaction region. Furthermore, they also implies that the dominant sound-producing flow is the vigorous interaction of S_1 and S_2 in the interaction region (downstream of RZ1) while SL is rather silent. This is also consistent with the flow dynamics revealed in two dimensional study, which shows that the dominant acoustic source is also the vortical structures generated at RZ1 in DS.

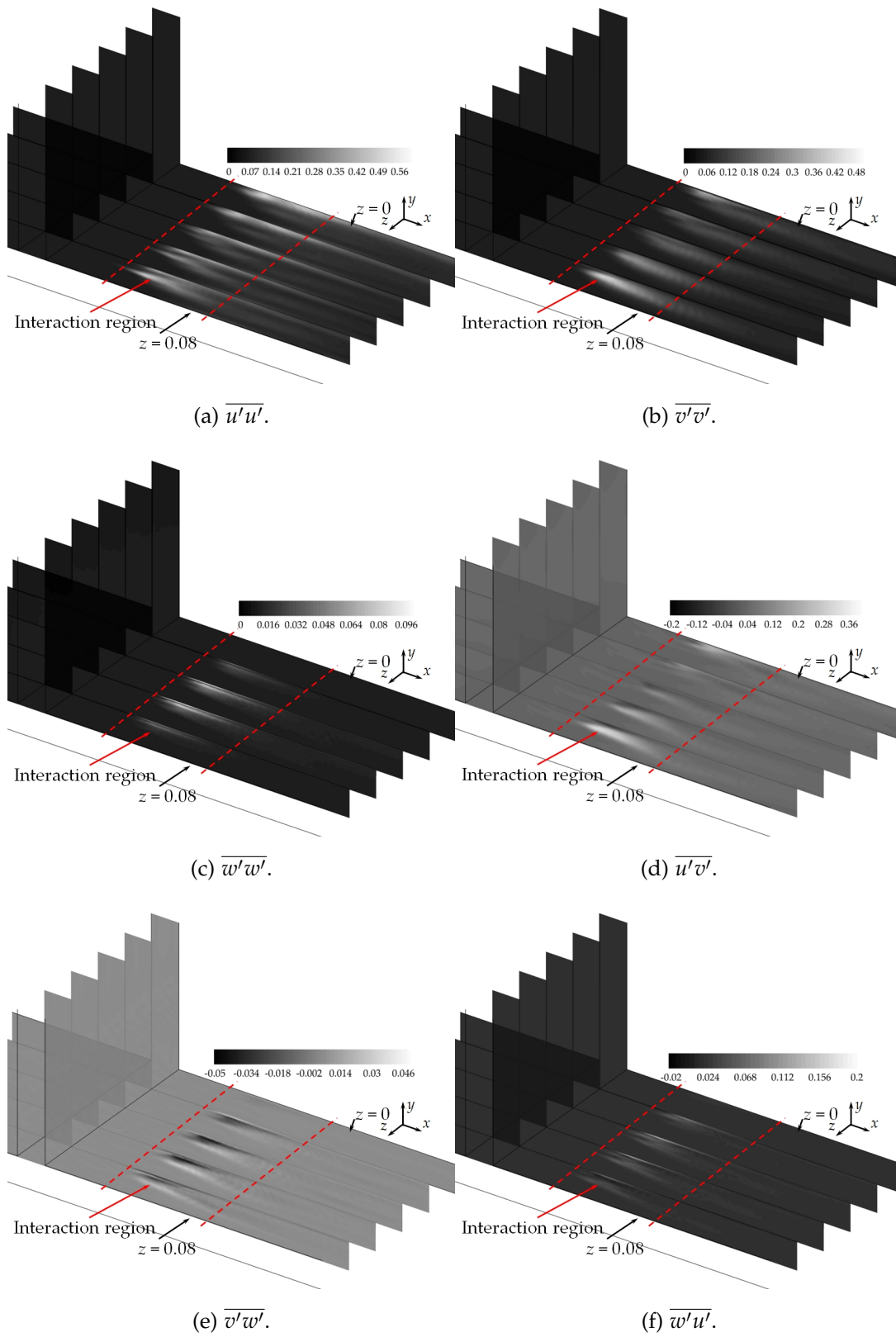
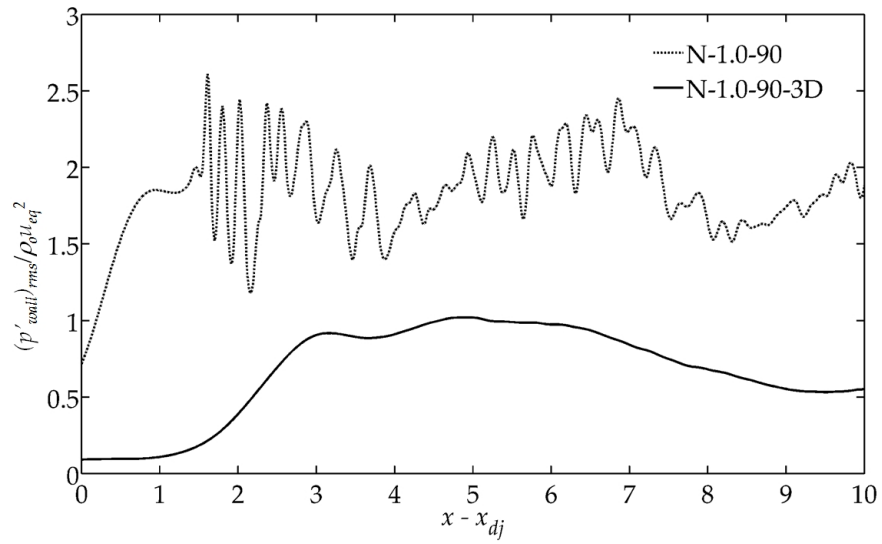
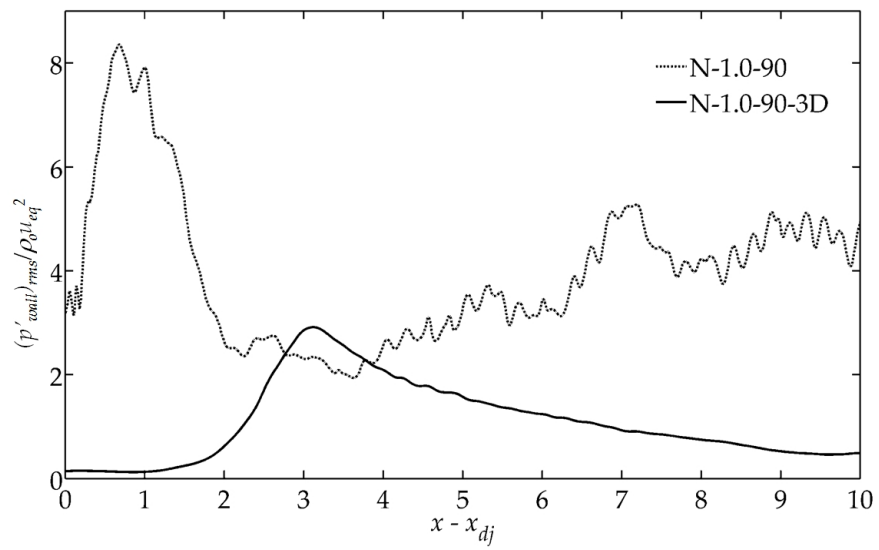


Figure 6.12: Reynolds stresses over the domain for N-1.0-90-3D.



(a) Lower wall.



(b) Upper wall.

Figure 6.13: Distributions of $(p'_{wall})_{rms} / \rho_0 u_{eq}^2$ in 2D and 3D cases.

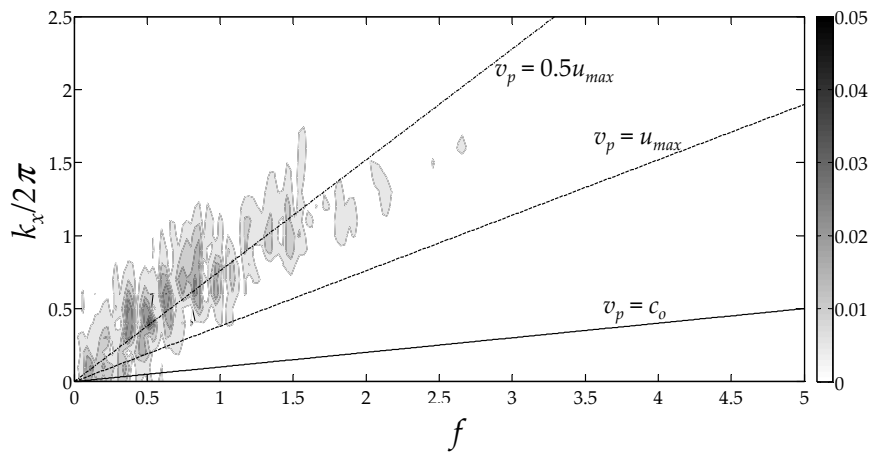


Figure 6.14: $p(k_x, f)$ spectrum at centerline of DS.

Fluctuating Wall Pressure

The comparison of fluctuating pressure $(p'_{wall})_{rms} / \rho_0 u_{eq}^2$ at both walls in DS between N-1.0-90 and N-1.0-90-3D is shown in Figure 6.13. These values are calculated from the results within a period of time 20 and a time increment of 0.2. The fluctuating pressure in 3D case is smaller than that in 2D case for both walls. Furthermore, the distributions of $(p'_{wall})_{rms} / \rho_0 u_{eq}^2$ also changes in 3D case. This corresponds to the changes of the vortex shedding location in 3D case.

6.2.3 Sound Generation

The previous section shows that the fluctuating wall pressure is smaller in the 3D case compared to the 2D case. This implies that the source in 3D case is weaker than that in 2D case. In this part, the acoustic generated will be extracted from the DAS results and discussed.

In order to extract the acoustic contribution in DS, $p(k_x, f)$ spectrum is obtained at the centerline of DS ($y = -0.5$) on $z = 0.05$ with $\Delta x = 0.2$. It is shown in Figure 6.14. The propagating speed of these vortical structures in DS is also roughly equal to $0.5 \sim 0.6u_m$, where u_m is the mean velocity of shear layer at RZ1. This agrees very well with the findings in two dimensional study.

SIZES OF FEATURES	N-1.0-90-3D	N-1.0-90	RATIO
η_{US}	7.20×10^{-5}	4.48×10^{-4}	6.22
η_{SB}	6.90×10^{-5}	4.60×10^{-4}	6.66
η_{DS}	2.45×10^{-5}	1.30×10^{-4}	5.32

Table 6.3: Acoustic efficiency η for N-1.0-90 and N-1.0-90-3D.

The acoustic efficiency η is evaluated by Eq.(4.14) and Eq.(4.15). Since the computational domain is reduced, the chosen cross sections for calculating η are changed to $x = -1$ in US, $y = 1$ in SB and $x = 9$ in DS. The integrals in these two equations are first carried out at the central cross-section of length 0.4 on $z = 0.05$ to exclude the boundary layer. Then, by dividing these integral with the spanwise width 0.1, the acoustic efficiency (per unit width) η can be obtained for three dimensional case.

Table 6.3 lists the calculated η in the three branches. The values, in general, are smaller than those calculated in N-1.0-90 by a factor of $5 \sim 6$ for all branches. Similar observations are also found in other aeroacoustic problem. For instance, [Sohankar et al. \(1999\)](#) calculated the flow past cylinder in both two and three dimensional cases. Comparing their calculated results in two types of cases, the fluctuating pressures on the cylinder showed a reduction by a factor of 4 in three dimensional cases. Since the acoustic power is highly related to the fluctuating pressure, so it is reasonable to expect such difference in the current calculation. Furthermore, according to [Howe \(1998\)](#), the acoustic efficiency generated aerodynamically in 2D manner is different from that in 3D manner by order of $1/M$, i. e., $\eta_{2D}/\eta_{3D} \sim O(1/M)$. This corresponds to a decrease of $1/M = 1/0.2 = 5$ in the acoustic efficiency compared to the 2D case.

Despite the reduced values, η of N-1.0-90-3D shows a trend similar to that of N-1.0-90. The acoustic efficiency in US, η_{US} , is more or less the same as that in SB, η_{SB} , while η_{DS} is smaller than those in US and SB. This observation is similar to two dimensional cases. Therefore, the two dimensional results

can be used to estimate the three dimensional case by applying a factor of reduction.

6.3 CONCLUDING REMARKS

In this chapter, a three dimensional simulation of merging flow with $VR = 1$ at $\theta = 90^\circ$ is discussed. It shows some changes in the flow features as compared with the corresponding two dimensional simulation. RZ1 exhibits strong three dimensional flow characteristics, the bounding volume of which is formed is consistent with the rejected zone found in the experimental results.

Furthermore, the flow dynamics observed in three dimensional simulation is somewhat different from those in two dimensional study. Three dimensional effects are observed in the vortex shedding at RZ1. It consists of the significant interaction between the vortices shed as a result of flow separation in RZ1 (rotating about z axis) and a vortex tube formed inside RZ1 (rotating about y axis). These two kinds of structures undergo pairing and then break down when convected downstream in DS. Its dominant frequency in the spectrum is slightly decreased in the three dimensional case. Meanwhile, secondary vortices are induced at the bottom wall in DS by the former structures. However, the vortex shedding at RZ1 is still the dominant flow unsteadiness, which is the same as the conclusion obtained using two dimensional approach. The prediction of dominant frequency peaks by the 3D simulation also shows good agreement with its counterparts in 2D simulation and the experiment when the contribution of fan noise is ignored. However, since the quality of the experiment is limited by the facility, further investigations are required. Moreover, the propagating speed of these vortical structures is nearly the same as that in two dimensional case. Although the acoustic efficiency η is reduced in N-1.0-90-3D, the distribution of η among each branch is still nearly the same as that obtained in two dimensional case. These findings show that the two dimensional calculation is capable to give a

reasonable overview in the aeroacoustics of the merging flow at duct junction.

CONCLUSIONS

In this chapter, some of the important achievements in the present investigation of the merging flow at duct junctions are presented. Suggestions for future investigations are also discussed.

7.1 SUMMARY OF IMPORTANT ACHIEVEMENTS

The investigation of the aeroacoustics of the merging flow at duct junctions is carried out because it seldom receives sufficient attentions while such flow is always encountered in many engineering applications. The investigation is performed using a combined numerical and experimental approach, but most achievements arise from two dimensional numerical simulations due to limited resources in computation and instrumentation available.

The numerical approach adopted is the direct aeroacoustic simulation (DAS) approach, which solves the compressible Navier-Stokes equations and the gas equation of state simultaneously. As such, the flow dynamics and the acoustics of the problem are solved together, thus enabling the calculation of their interactions without any modeling in the wave equation. The CE/SE method is chosen as the solver due to its elegant feature of strong conservation preservation. Its spatial resolution has been studied and it is observed that at least 10 cells per wavelength are required to represent the interested acoustics. Furthermore, validation cases have proven the capability of this method in capturing the aeroacoustics of various flow problems.

Based on both two and three dimensional numerical simulations the dominant flow unsteadiness in this flow is the vortex shedding from the separated flow at RZ1. The dominant sound source in this flow is the fluc-

tuating wall pressure induced by the interaction between vortices shed and the walls according to the [Curle \(1955\)](#) because this dipole (fluctuating wall pressure) is more efficient than the quadruple (Reynolds stresses) in the low Mach number flow. Since both the acoustic and flow disturbances are mixed in the near field of the flow, an acoustic extraction approach utilizing the wave number - frequency spectrum is proposed. The acoustic signals are successfully extracted with this approach. Furthermore, two parameters velocity ratio VR and merging angle of the duct θ are investigated for their influences on the aeroacoustics of the merging flows. Both parameters are found to be directly proportional to the acoustic efficiency η , which relates the production of acoustic energy and the flow input energy. This is probably a result of the increased interactions of the vortices and the walls when VR and θ increase. Furthermore, although the scaling law relating the acoustic efficiency and the speed of the flow may not be derived like other sound generation by flow, e. g., the works of [Lighthill \(1954\)](#), [Curle \(1955\)](#), [Gloerfelt & Lafon \(2008\)](#), a scaling law between the acoustic efficiency η and the RMS value of fluctuating force by the walls F_{rms} is proposed in 2D case, i. e., $\eta \propto F_{rms}^2$. It is observed that the present 2D numerical results match this proposed relationship quite well especially for the upstream part of the duct junction.

Although some flow data in the experiment are rejected due to the limitation of the instrumentation, both the mean Reynolds stresses in the accepted zone and the root mean square value of the pressure fluctuation show a trend in velocity ratio VR and merging angle of the duct θ similar to those predicted by the numerical simulations. Furthermore, the predictions of dominant frequency peaks by the two and three dimensional simulations agree reasonably with the experiments when the contribution of fan noise is ignored. This shows that two and three dimensional simulations can capture the key unsteadiness of the flow as observed in experiments. Nevertheless, due to the uncertainty imposed by the experiment facilities, further investigations are required.

7.2 SUGGESTIONS FOR FUTURE WORK

It is observed that the dominant flow unsteadiness of the merging flow is related to the separated flow originated at the downstream edge of duct junction in all investigations. However, the evolution of these flow structures is still not clearly understood. According to the three dimensional simulation, a longitudinal vortex tube (S_2) is shown near the wall downstream of the edge of duct junction. It is also the strongest vortical structure found in this flow instead of the line vortex (S_1) evolved at this shear layer. Nevertheless, two dimensional character prevails in this calculation as a result of the slender geometry adopted. Therefore, it is enlightening to see how these structures evolve in a truly three dimensional flow. The production of acoustic energy from these structures is also not clear. Regarding these issues, some future investigations are suggested.

In the aspect of numerical modeling and its implementation, a more sophisticated turbulence modeling such as dynamic subgrid model (Najjar & Tafti 1996) can be applied to further improve this modeling. Furthermore, one of the most important issue in DAS is the speed of calculation. In order to achieve a large scalability, Message Passing Interface (MPI) should be implemented in the CE/SE code.

Concerning the two dimensional investigation of merging flow at duct junctions, the proposed extraction of acoustic signals in DS can also be extended such that the contribution of any different dominant frequency, thus different mechanisms, can be determined in the near field of the flow. Furthermore, the scattering effect of the merging flow is not investigated in the present research, so it is not clear if there is any whistling when sound is introduced to the duct junction. This can be investigated by adopting system identification technique (Polifke et al. 2001) to study the reflection and transmission coefficient at the duct junction. This technique has been successfully applied to the Large Eddy Simulation (LES). For example, Föller

et al. (2010) applied this technique to their LES results in investigating the aeroacoustics of T-junction and showed good agreement to the experiments by *Karlsson & Åbom* (2010). Another methodology for investigating the scattering effect is based on the linearized Navier-Stokes equation in frequency domain (*Kierkegaard et al.* 2012), which uses the mean flow solution obtained from Reynolds Averaged Navier-Stokes computations as input. This method is more efficient as less flow details are required. *Kierkegaard et al.* (2012) demonstrated its success in determining the scattering effect of the acoustic absorption by orifice and the prediction in whistling of an orifice.

In order to reveal the evolution of the coherent vortical structures, experiments utilizing non-intrusive techniques such as PIV should be carried out. This can help us understand the underlying physics of this flow and help in predicting sound generation. Furthermore, the measurement of the sound generation is also a challenging task as it is usually masked by the unsteady flow in a confined environment. N-Port analysis such as the work of *Holmberg et al.* (2011) can help to evaluate the strength of the sound generated by the unsteady flow accurately.

In addition, a sophisticated three dimensional simulation of the problem can also help study the evolution of coherent vortical structures because the instrumentation required for experiment may not be readily available. Such simulations should be performed in full spanwise manner, i. e., the whole spanwise width. This allows the evolution of the flow structures to further three dimensional evolution of the flow structures.

BIBLIOGRAPHY

- Åbom, M. & Bodén, H. (1995), 'A note on the aeroacoustic source character of in-duct axial fans', *Journal of Sound and Vibration* **186**(4), 589–598.
- Abou-Haidar, N. I. & Dixon, S. L. (1992), 'Pressure losses in combining subsonic flows through branched ducts', *Journal of Turbomachinery* **114**(1), 264–270.
- Anagnostopoulos, J. S. & Mathioulakis, D. S. (2004), 'Unsteady flow field in a square tube T-junction', *Physics of Fluids* **16**(11), 3900–3910.
- Armaly, B. F., Durst, F., Pereira, J. C. F. & Schönung, B. (1983), 'Experimental and theoretical investigation of backward-facing step flow', *Journal of Fluid Mechanics* **127**, 473–496.
- Babu, V. (2008), *Fundamentals of Gas Dynamics*, 1st edn, CRC Press.
- Bailly, C. & Lafon, P. (1996), 'Computation of noise generation and propagation for free and confined turbulent flows', *AIAA Paper* (96-1732).
- Betchov, R. & Criminale, W. O. (1967), *The Stability of Parallel Flows*, Academic, New York.
- Blaisdell, F. W. & Manson, P. W. (1963), *Loss of Energy at Sharp-Edged Pipe Junctions in Water Conveyance Systems*, US Department of Agriculture, Technical Bulletin No. 1283.
- Bogey, C. (2004), 'A family of low dispersive and low dissipative explicit schemes for flow and noise computations', *Journal of Computational Physics* **194**(1), 194–214.
- Boris, J. P., Grinstein, F. F., Oran, E. S. & Kolbe, R. L. (1992), 'New insights into large eddy simulation', *Fluid Dynamics Research* **10**(4-6), 199–228.

- Browand, F. K. (1966), 'An experimental investigation of the instability of an incompressible, separated shear layer', *Journal of Fluid Mechanics* **26**(02), 281–307.
- Brücker, C. (1997), 'Study of the three-dimensional flow in a T-junction using a dual-scanning method for three-dimensional scanning-particle-image velocimetry (3-D SPIV)', *Experimental Thermal and Fluid Science* **14**(1), 35–44.
- Bruggeman, J. C. (1987), 'The propagation of low-frequency sound in a two-dimensional duct system with T joints and right angle bends: Theory and experiment', *The Journal of the Acoustical Society of America* **82**(3), 1045–1051.
- Bruggeman, J. C., Hirschberg, A., van Dongen, M. E. H., Wijnands, A. P. J. & Gorter, J. (1991), 'Self-sustained aero-acoustic pulsations in gas transport systems: Experimental study of the influence of closed side branches', *Journal of Sound and Vibration* **150**(3), 371–393.
- Bruun, H. H. (1972), 'Hot wire data corrections in low and in high turbulence intensity flows', *Journal of Physics E: Scientific Instruments* **5**(8), 812–818.
- Chang, C. L. (2006), Time-accurate, unstructured-mesh Navier-Stokes computations with the space-time CESE Method, in '42nd AIAA Joint Propulsion Conference and Exhibit AIAA', Sacramento, CA, pp. 1–20.
- Chang, C. L. (2007), Three-dimensional Navier-Stokes calculations using the modified space-time CESE Method, in '43rd AIAA/ASME/SAE/ASEE Joint Propulsion Conference & Exhibit', pp. 1–19.
- Chang, S. C. (1995), 'The method of space-time Conservation Element and Solution Element-A new approach for solving the Navier-Stokes and Euler equations', *Journal of Computational Physics* **119**(2), 295–324.
- Chang, S. C. (1999), 'The space-time Conservation Element and Solution Element Method: A new high-resolution and genuinely multidimensional

- paradigm for solving conservation laws: I. The two dimensional time marching schemes', *Journal of Computational Physics* **156**(1), 89–136.
- Chang, S. C. (2002), 'Courant number insensitive CE/SE schemes', *AIAA Paper* (2002-2890).
- Chang, S. C., Zhang, Z. C., Yu, S. T. J. & Jorgenson, P. C. (2001), 'A unified wall boundary treatment for viscous and inviscid flows in the CE / SE method', *Computational Fluid Dynamics* **4**, 671–676.
- Cheng, M., Whyte, D. & Lou, J. (2007), 'Numerical simulation of flow around a square cylinder in uniform-shear flow', *Journal of Fluids and Structures* **23**(2), 207–226.
- Colonus, T., Lele, S. K. & Moin, P. (1993), 'Boundary conditions for direct computation of aerodynamic sound generation', *AIAA Journal* **31**(9), 1574–1582.
- Curle, N. (1955), 'The influence of solid boundaries upon aerodynamic sound', *Proceedings of the Royal Society A: Mathematical, Physical and Engineering Sciences* **231**(1187), 505–514.
- Davies, H. G. & Ffowcs-Williams, J. E. (1968), 'Aerodynamic sound generation in a pipe', *Journal of Fluid Mechanics* **32**, 765–778.
- Dequand, S., Hulshoff, S. J. & Hirschberg, A. (2003), 'Self-sustained oscillations in a closed side branch system', *Journal of Sound and Vibration* **265**(2), 359–386.
- Dubos, V., Kergomard, J., Khettabi, A., Keefe, D. H. & Nederveen, C. J. (1999), 'Theory of sound propagation in a duct with a branched tube using modal decomposition', *Acta Acustica united with Acustica* **85**(2), 153–169.
- Fernholz, H. H. & Finley, P. J. (1980), 'A critical commentary on mean flow data for two-dimensional compressible turbulent boundary layers', *AGARD-AG-253*.

- Föller, S., Polifke, W. & Tonon, D. (2010), Aeroacoustic characterization of T-junctions based on large eddy simulation and system identification, in '16th AIAA/CEAS Aeroacoustic Conference', pp. 1–13.
- Freund, J. B. (2001), 'Noise sources in a low-Reynolds-number turbulent jet at Mach 0.9', *Journal of Fluid Mechanics* **438**, 277–305.
- Fureby, C. (2002), 'Large eddy simulation of high-Reynolds-number free and wall-bounded flows', *Journal of Computational Physics* **181**(1), 68–97.
- Germano, M., Piomelli, U., Moin, P. & Cabot, W. H. (1991), 'A dynamic subgrid-scale eddy viscosity model', *Physics of Fluids A: Fluid Dynamics* **3**(7), 1760–1765.
- Gloerfelt, X., Bailly, C. & Juvé, D. (2003), 'Direct computation of the noise radiated by a subsonic cavity flow and application of integral methods', *Journal of Sound and Vibration* **266**(1), 119–146.
- Gloerfelt, X. & Lafon, P. (2008), 'Direct computation of the noise induced by a turbulent flow through a diaphragm in a duct at low Mach number', *Computers Fluids* **37**(4), 388–401.
- Guj, G. & Stella, F. (1988), 'Numerical solutions of high-Re recirculating flows in vorticity-velocity form', *International Journal for Numerical Methods in Fluids* **8**(4), 405–416.
- Guo, Y., Hsu, A. T., Wu, J., Yang, Z. & Oyediran, A. (2004), 'Extension of CE/SE method to 2D viscous flows', *Computers & Fluids* **33**(10), 1349–1361.
- Hardin, J. C., Ristorcelli, J. R. & Tam, C. K. W. (1994), 'ICASE/LaRC Workshop on benchmark problems in computational aeroacoustics (CAA)', NASA-CP3300 .
- Hirota, M., Asano, H., Nakayama, H., Asano, T. & Hirayama, S. (2006), 'Three-dimensional structure of turbulent flow in mixing T-junction', *JSME International Journal Series B* **49**(4), 1070–1077.

- Hirota, M., Mohri, E., Asano, H. & Goto, H. (2010), 'Experimental study on turbulent mixing process in cross-flow type T-junction', *International Journal of Heat and Fluid Flow* **31**(5), 776–784.
- Ho, C. M. & Huang, L. S. (1982), 'Subharmonics and vortex merging in mixing layers', *Journal of Fluid Mechanics* **119**, 443–473.
- Holmberg, A., Åbom, M. & Bodén, H. (2011), 'Accurate experimental two-port analysis of flow generated sound', *Journal of Sound and Vibration* **330**(26), 6336–6354.
- Hooper, J. D. & Musgrove, A. R. (1997), 'Reynolds stress, mean velocity, and dynamic static pressure measurement by a four-hole pressure probe', *Experimental Thermal and Fluid Science* **15**(4), 375–383.
- Howe, M. S. (1998), *Acoustics of Fluid-Structure Interactions*, Cambridge University Press, Cambridge.
- Hu, F. Q., Li, X. D. & Lin, D. K. (2008), 'Absorbing boundary conditions for nonlinear Euler and Navier-Stokes equations based on the perfectly matched layer technique', *Journal of Computational Physics* **227**(9), 4398–4424.
- Huang, P. G., Bradshaw, P. & Coakley, T. J. (1993), 'Skin friction velocity profile family for compressible turbulent boundary layers', *AIAA Journal* **31**(9), 1600–1604.
- Huang, P. G. & Coleman, G. N. (1994), 'Van Driest transformation and compressible wall-bounded flows', *AIAA Journal* **32**(10), 2110–2113.
- Inoue, O. & Hatakeyama, N. (2002), 'Sound generation by a two-dimensional circular cylinder in a uniform flow', *Journal of Fluid Mechanics* **471**(1), 285–314.
- Ito, H. & Imai, K. (1973), 'Energy losses at 90° pipe junctions', *Journal of the Hydraulics Division* **99**(9), 1353–1368.

- Jan, Y. & Sheu, T. W. H. (2004), 'A numerical confirmation of the dual body vortex flowmeter design', *Computers & Fluids* **33**(9), 1157–1174.
- Jeong, J. & Hussain, F. (1995), 'On the identification of a vortex', *Journal of Fluid Mechanics* **285**, 69–94.
- Jing, X. & Sun, X. (2002), 'Sound-excited flow and acoustic nonlinearity at an orifice', *Physics of Fluids* **14**(1), 268–276.
- Karlsson, M. & Åbom, M. (2010), 'Aeroacoustics of T-junctions - An experimental investigation', *Journal of Sound and Vibration* **329**(10), 1793–1808.
- Kelso, R. M., Lim, T. T. & Perry, A. E. (1998), 'New experimental observations of vortical motions in transverse jets', *Physics of Fluids* **10**(9), 2427–2429.
- Kierkegaard, A., Allam, S., Efraimsson, G. & Åbom, M. (2012), 'Simulations of whistling and the whistling potentiality of an in-duct orifice with linear aeroacoustics', *Journal of Sound and Vibration* **331**(5), 1084–1096.
- Kim, J. & Moin, P. (1985), 'Application of a fractional-step method to incompressible Navier-Stokes equations', *Journal of Computational Physics* **59**(2), 308–323.
- Knuth, D. E. (1974), 'Computer Programming as an Art', *Communications of the ACM* **17**(12), 667–673.
- Krijger, J. K. B., Hillen, B., Hoogstraten, H. W. & Raadt, M. P. M. G. (1990), 'Steady two-dimensional merging flow from two channels into a single channel', *Applied Scientific Research* **47**(3), 233–246.
- Larchevêque, L., Sagaut, P., Mary, I., Labbé, O. & Comte, P. (2003), 'Large-eddy simulation of a compressible flow past a deep cavity', *Physics of Fluids* **15**(1), 193–210.
- Lele, S. K. (1992), 'Compact finite difference schemes with spectral-like resolution', *Journal of Computational Physics* **103**(1), 16–42.

- Lighthill, M. J. (1952), 'On sound generated aerodynamically. I. General theory', *Proceedings of the Royal Society A: Mathematical, Physical and Engineering Sciences* **211**(1107), 564–587.
- Lighthill, M. J. (1954), 'On sound generated aerodynamically. II. Turbulence as a source of sound', *Proceedings of the Royal Society A: Mathematical, Physical and Engineering Sciences* **222**(1148), 1–32.
- Loh, C. Y. (2003), 'On a non-reflecting boundary condition for hyperbolic conservation laws', *AIAA Paper* (2003-3975).
- Loh, C. Y. (2005), 'Computation of tone noise from supersonic jet impinging on flat plates', *AIAA Paper* (2005-0418).
- Loh, C. Y., Chang, S. C. & Hultgren, L. S. (2001), 'Wave computation in compressible flow using space time conservation element and solution element method', *AIAA Journal* **39**(5), 794–801.
- Loh, C. Y., Chang, S. C., Wang, X. Y. & Jorgenson, P. C. (2001), Gap noise computation by the CE/SE Method, in 'Proceedings of ASME Fluids Engineering Division Summer Meeting', New Orleans, Louisiana, pp. 1–6.
- Loh, C. Y., Himansu, A. & Wang, X. Y. (2001), 'Computation of an under-expanded 3-D rectangular jet by the CE / SE Method', *AIAA Paper* (2001-0986).
- Loh, C. Y. & Hultgren, L. S. (2006), 'Jet screech noise computation', *AIAA Journal* **44**(5), 992–998.
- Martínez-Lera, P., Schram, C., Föller, S., Kaess, R. & Polifke, W. (2009), 'Identification of the aeroacoustic response of a low Mach number flow through a T-joint.', *The Journal of the Acoustical Society of America* **126**(2), 582–586.
- McNown, J. S. (1954), 'Mechanics of manifold flow', *Transactions of the American Society of Civil Engineerings* **119**, 1103–1142.

- Miles, J. W. (1947), 'The diffraction of sound due to right-angled joints in rectangular tubes', *The Journal of the Acoustical Society of America* **19**(4), 572–579.
- Miller, D. S. (1971), *Internal Flow: A Guide to Losses in Pipe and Duct Systems*, British Hydromechanics Research Association.
- Miranda, A. I. P., Oliveira, P. J. & Pinho, F. T. (2008), 'Steady and unsteady laminar flows of Newtonian and generalized Newtonian fluids in a planar T-junction', *International Journal for Numerical Methods in Fluids* **57**(3), 295–328.
- Morfey, C. L. (2001), Acoustic Power, in 'Dictionary of Acoustics', Academic Press, London, p. 199.
- Morse, P. M. (1986), *Theoretical Acoustics*, Princeton University Press.
- Moshkin, N. & Yambangwi, D. (2009), 'Steady viscous incompressible flow driven by a pressure difference in a planar T-junction channel', *International Journal of Computational Fluid Dynamics* **23**(3), 259–270.
- Najjar, F. M. & Tafti, D. K. (1996), 'Study of discrete test filters and finite difference approximations for the dynamic subgrid-scale stress model', *Physics of Fluids* **8**(4), 1076–1088.
- Nelson, P., Halliwell, N. & Doak, P. (1983), 'Fluid dynamics of a flow excited resonance, Part II: Flow acoustic interaction', *Journal of Sound and Vibration* **91**(3), 375–402.
- Nie, J. H. & Armaly, B. F. (2003), 'Reattachment of three-dimensional flow adjacent to backward-facing step', *Journal of Heat Transfer* **125**(3), 422–428.
- Okajima, A. (2006), 'Strouhal numbers of rectangular cylinders', *Journal of Fluid Mechanics* **123**, 379–398.

- Pérez-García, J., Sanmiguel-Rojas, E. & Viedma, A. (2010), 'New coefficient to characterize energy losses in compressible flow at T-junctions', *Applied Mathematical Modelling* **34**(12), 4289–4305.
- Poinsot, T. & Lele, S. K. (1992), 'Boundary conditions for direct simulations of compressible viscous flows', *Journal of Computational Physics* **101**(1), 104–129.
- Polifke, W., Poncet, A., Paschereit, C. O. & Döbbling, K. (2001), 'Reconstruction of acoustic transfer matrices by instationary computational fluid dynamics', *Journal of Sound and Vibration* **245**(3), 483–510.
- Popescu, M. & Shyy, W. (2002), 'Assessment of Dispersion-Relation-Preserving and space-time CE/SE schemes for wave equations', *Numerical Heat Transfer, Part B* **42**(February), 93–119.
- Potter, M. C. (1967), 'Linear stability of symmetrical parabolic flows', *Physics of Fluids* **10**(3), 479–482.
- Reynolds, W. (1989), The potential and limitations of direct and large eddy simulations, in J. L. Lumley, ed., 'Whither Turbulence? Turbulence at the Crossroads', 1st edn, Springer-Verlag, Ithaca, New York, chapter 4, pp. 313–343.
- Rowley, C. W., Colonius, T. & Basu, A. J. (2002), 'On self-sustained oscillations in two-dimensional compressible flow over rectangular cavities', *Journal of Fluid Mechanics* **455**, 315–346.
- Smagorinsky, J. (1963), 'General circulation experiments with the primitive equations I. The basic experiments', *Monthly Weather Review* **91**(3), 99–164.
- Sohankar, A., Norberg, C. & Davidson, L. (1998), 'Low Reynolds number flow around a square cylinder at incidence: study of blockage, onset of vortex shedding and outlet boundary condition', *International Journal for Numerical Methods in Fluids* **26**(1), 39–56.

- Sohankar, A., Norberg, C. & Davidson, L. (1999), 'Simulation of three-dimensional flow around a square cylinder at moderate Reynolds numbers', *Physics of Fluids* **11**(2), 288–306.
- Sohn, J. L. (1988), 'Evaluation of FIDAP on some classical laminar and turbulent benchmarks', *International Journal for Numerical Methods in Fluids* **8**(12), 1469–1490.
- Tam, C. K. W. (1993), 'Dispersion-Relation-Preserving finite difference schemes for computational acoustics', *Journal of Computational Physics* **107**(2), 262–281.
- Tam, C. K. W. (1995), 'Computational aeroacoustics - Issues and methods', *AIAA Journal* **33**(10), 1788–1796.
- Tam, C. K. W. (2006), 'Recent advances in computational aeroacoustics', *Fluid Dynamics Research* **38**(9), 591–615.
- Tang, S. K. (2004), 'Sound transmission characteristics of Tee-junctions and the associated length corrections.', *The Journal of the Acoustical Society of America* **115**(1), 218–227.
- Tang, S. K. & Ko, N. W. M. (1994a), 'Coherent structure interactions in an unexcited coaxial jet', *Experiments in Fluids* **17**(3), 147–157.
- Tang, S. K. & Ko, N. W. M. (1994b), 'Experimental investigation of the structure interaction in an excited coaxial jet', *Experimental Thermal and Fluid Science* **8**(3), 214–229.
- Tang, S. K. & Lam, G. C. Y. (2008), 'On sound propagation from a slanted side branch into an infinitely long rectangular duct.', *The Journal of the Acoustical Society of America* **124**(4), 1921–1929.
- Tang, S. K. & Li, F. Y. C. (2003), 'On low frequency sound transmission loss of double sidebranches: a comparison between theory and experiment.', *The Journal of the Acoustical Society of America* **113**(6), 3215–3225.

- Thangam, S. & Knight, D. (1990), 'A computational scheme in generalized coordinates for viscous incompressible flows', *Computers & Fluids* **18**(4), 317–327.
- Thomas, F. O. (1991), 'Structure of mixing layers and jets', *Applied Mechanics Reviews* **44**(3), 119–153.
- Thomas, S. & Ameel, T. A. (2010), 'An experimental investigation of moderate reynolds number flow in a T-Channel', *Experiments in Fluids* **49**(6), 1231–1245.
- Tinney, C. E. & Jordan, P. (2008), 'The near pressure field of co-axial subsonic jets', *Journal of Fluid Mechanics* **611**, 175–204.
- Tonon, D., Landry, B., Belfroid, S., Willems, J., Hofmans, G. & Hirschberg, A. (2010), 'Whistling of a pipe system with multiple side branches: Comparison with corrugated pipes', *Journal of Sound and Vibration* **329**(8), 1007–1024.
- Venkatachari, B., Cheng, G., Soni, B. & Chang, S. C. (2008), 'Validation and verification of Courant number insensitive CE/SE method for transient viscous flow simulations', *Mathematics and Computers in Simulation* **78**(5–6), 653–670.
- Vogel, G. (1928), 'Investigation of the loss in right-angled pipe branches', *Mitt. Hydraulischen Instituts der Tech. Hochschule Munchen* **2**, 61–64.
- Wang, X. Y. & Chang, S. C. (1999), 'A 2D non-splitting unstructured triangular mesh Euler solver based on the space-time Conservation Element and Solution Element Method', *Computational Fluid Dynamics Journal* **8**(2), 309–325.
- Wu, H. (2003), 'Influence of sleeve tube on the flow and heat transfer behavior at a T-junction', *International Journal of Heat and Mass Transfer* **46**(14), 2637–2644.

Yen, J. C. & Wagner, D. A. (2005), 'Computational aeroacoustics using a simplified Courant number insensitive CE/SE Method', *AIAA Paper* (2005-2820).

Yen, J. C., Wagner, D. A. & Martindale, W. (2006), CAA using 3D CESE method with a simplified Courant number insensitive scheme, *in* '12th AIAA/CEAS Aeroacoustics Conference (27th AIAA Aeroacoustics Conference)', Cambridge, Massachusetts, pp. 1-17.